

**Fabrication and Characterization of a Plasmonic Grating Platform for
Enhanced Fluorescence Biosensor Applications**

A Dissertation Presented to the Faculty of the Graduate School

University of Missouri-Columbia

In Partial Fulfillment

of the Requirements for the Degree

Doctor of Philosophy

by

AARON JENE WOOD

Dr. Sheila Grant, Dr. Shubhra Gangopadhyay,

Dissertation Supervisors

DECEMBER 2016

The undersigned, appointed by the dean of the Graduate School, have examined
the dissertation entitled

FABRICATION AND CHARACTERIZATION OF A PLASMONIC GRATING
PLATFORM FOR ENHANCED FLUORESCENCE BIOSENSOR
APPLICATIONS

presented by Aaron Jene Wood,

a candidate for the degree of doctor of philosophy,

and hereby certify that, in their opinion, it is worthy of acceptance.

Dr. Sheila Grant
Department of Bioengineering

Dr. Shubhra Gangopadhyay
Department of Electrical and Computer Engineering

Dr. Peter Cornish
Department of Biochemistry

Dr. Raghuraman Kannan
Department of Radiology

ACKNOWLEDGEMENTS

This dissertation would not have been possible without the guidance and the help of several individuals who contributed their assistance and expertise in the development and experiments of this project.

I would like to thank my co-advisor, Dr. Sheila Grant, for accepting me into her laboratory as an undergraduate researcher in my junior year and her encouragement for me to continue my education in graduate school. Her expertise and guidance throughout this project have been invaluable. I would like to thank my co-advisor, Dr. Shubhra Gangopadhyay, for her guidance throughout this project and for providing my lab group members and me with one of the best nanofabrication facilities in the state for this project. This project would not have been possible without the collaboration between my co-advisors and their support.

I would like to thank Dr. Sangho Bok for his hands-on guidance on experiment design, discussions on plasmonic theory, and general aid throughout this project. I would like to thank Dr. C. Joseph Mathai for his guidance as he worked with me to solve any grating fabrication difficulties, equipment issues, and for the countless metal depositions and ALD runs he performed for this project. I would like to thank Dr. Syed Barizuddin for his help trouble shooting the PMSSQ stamping process, for aiding me with the sensor experiments at all hours of the day and night, and the many metal and ceramic depositions he performed for this project. Without their help, it would not have been possible to accomplish any of the work required for this project.

I would like to thank my mom, Lisa, for her encouragement, for home educating me from 3rd grade through high school, and the countless hours she has invested in my future. I want to thank my dad, Warren, for his leadership, encouragement, patience, and for igniting my passion for engineering by including my brothers and me in the design and construction of many building projects around the house during my younger years.

I have formed many good memories during my undergraduate and graduate experience at the University of Missouri, and I would like to thank all of my friends and family for their encouragement and support throughout my time at Mizzou.

TABLE OF CONTENTS

ACKNOWLEDGEMENTS	ii
LIST OF FIGURES.....	viii
LIST OF TABLES	xx
CHAPTER 1: PLASMONICS	1
1.1. Introduction	1
1.2. Surface Plasmon Polaritons	2
1.3. SPP Excitation and Surface Plasmon Resonance	7
1.4. SPR Simulation	16
1.5. Principles of Fluorescence Microscopy	22
1.6. Fluorescent Dye and Metal Interactions.....	25
1.7. Angular Excitation and SPCE Capture.....	29
CHAPTER 2: PLASMONIC GRATING FABRICATION	34
2.1. Introduction	34
2.2. HD-DVD and Bluray Disc Preparation.....	35
2.3. Polydimethylsiloxane (PDMS) Stamp Fabrication	39
2.4. Polymethylsilsesquioxane (PMSSQ) Grating Fabrication.....	43
2.5. Metallization and Protective Capping of the Grating	53
2.6. Surface and Optical Characterization.....	61
2.7. Fluorescence Characterization.....	67

CHAPTER 3: INFLUENCE OF SILVER DEPOSITION METHOD ON PLASMONIC PROPERTIES	74
3.1. Abstract.....	74
3.2. Introduction	75
3.3. Silver Grating Fabrication.....	77
3.4. Surface and Optical Characterization.....	81
3.5. Fluorescent Dye Enhancement.....	83
3.6. Influence of Grating Properties on SPR	88
3.7. EM Field Simulations.....	92
3.8. Deposition Alignment Impact on Grating properties	99
3.9. Conclusion	102
3.10. Experimental Methods.....	103
CHAPTER 4: CORTISOLBIOSENSOR	107
4.1. Introduction	107
4.2. Cortisol Antibody Specificity	109
4.3. Sandwich Fluoroimmunoassay	112
4.4. Competitive Binding Fluoroimmunoassay	117
4.5. Bimetallic Gratings	132
4.6. Cortisol Binding Aptamer.....	140
4.7. Conclusion	144
4.8. Future Work	145

CHAPTER 5: ENHANCED DNA DETECTION THROUGH THE INCORPORATION OF NANOCONES AND CAVITIES INTO A PLASMONIC GRATING SENSOR PLATFORM.....	147
5.1. Abstract.....	147
5.2. Introduction	148
5.3. Materials and Methods.....	151
5.4. Grating Topography	154
5.5. Optical Properties.....	155
5.6. DNA Detection and Fluorescence Enhancement.....	157
5.7. Conclusion and Future Direction	159
CHAPTER 6: SINGLE-MOLECULE SURFACE PLASMON-COUPLED EMISSION WITH PLASMONIC GRATINGS.....	160
6.1. Introduction	160
6.2. Wide Concentration Range Fluorescence Imaging	160
6.3. SPCE Fluorescence Imaging	167
6.4. Conclusion	174
6.5. Experimental Methods.....	174
CONCLUSION.....	177
PUBLICATIONS AND PRESENTATIONS.....	179
Publications – Journal Articles	179
Publications – Conference Proceedings	180

Podium Presentations.....	181
REFERENCES.....	182
VITA.....	192

LIST OF FIGURES

- Figure 1-1.** (a) TM polarized EM wave incident on a metal/dielectric interface with electric field components in the x-z plane and magnetic components in the x-y plane. (b) Electric field lines of a surface plasmon at the metal/dielectric interface. An external EM field, such as a photon or electron, can induce a surface charge oscillation. The charge oscillation forms an EM wave that decays evanescently into the dielectric, where the EM intensity is strongest near the interface. 4
- Figure 1-2.** (a) Illustration of a photon impinging on a metal/dielectric interface and (b) Photon dispersion in a dielectric compared to the plasmonic dispersion at the dielectric/metal interface. Note that $k_{SP} > k_{||}$ for any frequency ω 7
- Figure 1-3.** (a) Otto and (b) Kretschmann configurations for prism-based SPR excitation. (c) Photon and SPR wavevector matching conditions for the Kretschmann configuration..... 8
- Figure 1-4.** (a) Illustration of the wavevector matching between incident EM radiation (transverse-magnetic (TM) light) on a grating and a propagating surface plasmon polariton. (b) Theoretical frequency vs. momentum plot for a metallic grating (red and black), and incident EM radiation (blue line). (c) Experimental frequency vs. momentum for a silver grating in air based on the SPR peak location from the reflectivity scans.[22, 23] 10
- Figure 1-5.** (a) Transmission ($\theta=0-15^\circ$) and (b) Reflectivity ($\theta=15-30^\circ$) measurements on a 40 nm thin silver grating immersed in oil..... 11
- Figure 1-6.** Illustration of the formation of (a) grazing diffraction mode interference, also known as wood's anomalies, and (b) SPR with an expansion of the two SPR frequency modes typically observed on a corrugated surface. (c) Overlaid reflectivity and transmission scans at $\theta=15^\circ$ with coupling modes indicated with arrows..... 13
- Figure 1-7.** (a) Coupling sensitivity to polarization angle illustration. (b) Polarized Reflectivity at $\theta=15^\circ$ onto a grating where polarization angle is rotated from TM to TE polarization ($\beta=0 - 90^\circ$). 14
- Figure 1-8.** (a) Coupling sensitivity to polarization angle illustration. (b) Polarized Reflectivity at $\theta=15^\circ$ onto a grating where polarization angle is rotated from P- to S-polarization ($\beta=0 - 90^\circ$). 15
- Figure 1-9.** 3-dimensional Yee cell for FDTD simulation of the electric and magnetic field vectors..... 17

- Figure 1-10.** (a) Simulation area for a silver-coated PMSSQ grating on a glass substrate in air, water, or oil. (b) Reflectivity results for simulation window (a) in air from $\theta=0, 5, 10, 15,$ and 20° . (c) E_z -field intensity plots for locations 1 and 2 indicated in (b) that correspond to the upper and lower ω_{SPR} solutions at $\theta=5^\circ$ 21
- Figure 1-11.** (a) Jablonski energy level diagram illustrating the typical excitation and emission steps in the generation of fluorescence as well as the transition time for each step.[33] (b) Various dyes dissolved in ethanol illuminated with (top) ambient light and (bottom) UV light..... 23
- Figure 1-12.** (a) BX51 Olympus epi-fluorescence microscope and the (b) excitation and emission illustration for fluorescence filter cube imaging..... 24
- Figure 1-13.** Jablonski diagram of Metal/Fluorophore interactions that lead to surface plasmon coupled emission or lossy surface plasmons. 1) An incident photon onto the grating will be converted into a surface plasmon. 2) the resulting generated dipole will interact with the fluorophore's dipole and non-radiatively transfer energy to the molecule. 3) the fluorescent molecule will undergo internal conversion and vibrational relaxation to dissipate energy. 4) the fluorophore will non-radiatively transfer the remaining energy to the grating surface via dipole/dipole interaction. 5a) the energy will either be converted to a radiative plasmon and emit a photon at the emission wavelength of the fluorophore at the SPR dispersion angle, or 5b) the energy will be converted into a non-radiative plasmon that dissipates into heat.[35, 43, 44] 27
- Figure 1-14.** Emission efficiency for a range of Förster distances ($R_0=5$ (blue), 6.2 (red), and 7 nm (green)) compared to the E-field intensity (black) of a silver plasmonic grating. The product of emission efficiency curve and the E-field intensity for each Förster distance (dashed lines). The peak in the resulting product of the two curves is 10 nm ($R_0=5$ nm), 12 nm ($R_0=6.2$ nm), and 13.3 nm ($R_0=7$ nm)..... 28
- Figure 1-15.** (a) Reflectivity measurements for a 100 nm thick silver grating in air and corresponding (b) SPR dispersion curve in air. (c) SPR dispersion in air (black), water (blue), and oil (red) mediums. 29
- Figure 1-16.** (a) Experimentally derived SPR dispersion of a 100 nm thick silver grating in air and water. The excitation and emission wavelength range for AF568 has been plotted as well as the convergence angle of three microscope objectives (10x, 20x, and 40x) calculated based on numerical aperture (N.A.) and the refractive index of the imaging medium.[42] (b) Objective lens emission/collection range for 10x, 20x, 40x, and 100x oil immersion objectives compared with the SPR

coupling angles of the excitation wavelength range for AF568 and the emission angle range for the emission wavelength range for AF568 via SPCE. (c) Convergence angle and SPR/SPCE intensity comparison between the 10x and 40x objective..... 32

Figure 1-17. (a) Minimum XY resolution and (b) depth of field for 10x, 20x, 40x, 60x WI, 60x OI, and 100x OI objective lenses..... 33

Figure 2-1. HDDVD and its underlying grating structure composed of repeating pits and ridges..... 34

Figure 2-2. (a) HDDVD and (b) Blu-ray disc cross-sections with the grating period (Λ) and height (H) listed. The laser-writable organic dye film found in LTH Blurays is soluble in IPA whereas HTL Blu-ray discs use an inorganic dye film typically made from copper and silicon. The metal films for Blu-ray discs are composed of silver and either aluminum or silver for HDDVDs. PC: Polycarbonate..... 35

Figure 2-3. 3D rendering of the surface of polycarbonate gratings and corresponding 2D topographical profiles below for (a) HD DVD and (b) 6x LTH Blu-ray disc obtained through AFM. 39

Figure 2-4. General hydrosilylation reaction diagram. 40

Figure 2-5. Tensile loading results for PDMS samples with different base:curing agent ratios. (b) Young’s modulus of elasticity for samples tested in (a)..... 41

Figure 2-6. (a) Chemical structure of PMSSQ.[1] Low-Humidity Stamping Chamber (b) illustration and (c) actual chamber..... 44

Figure 2-7. (a) Measured and modeled thicknesses and (b) refractive indices for spin-coated PMSSQ films at varying %wt. in pure ethanol with and without curing at 400^oC for 1 hour. 45

Figure 2-8. Soft lithography process diagram. 1) Cut and remove the PDMS stamp pieces from the disc mold; 2) spin coat PMSSQ “ink” solution onto the PDMS stamp; 3) stamp and peel off the PDMS onto a glass slide or silicon wafer.[42]..... 46

Figure 2-9. Stamp cut pattern for easy identification of grating alignment post stamping..... 48

Figure 2-10. (a) Vapor treatment chamber and (b) Illustration of the water and air traps connected to the vapor treatment chamber. 52

Figure 2-11. PMSSQ gratings on silicon wafer before loading onto the high-temperature annealing plate.....	53
Figure 2-12. (a) Kurt J. Lesker Nano38 thermal evaporation chamber with and (b) an image of the deposition chamber and (c) the resistive boats before and during heating (images courtesy of Kurt J. Lesker Company or Creative Commons BY-SA 4.0.) (d) Thermal evaporation illustration of the resistive heating, evaporation of the target material resulting in a plume of material that is deposited on the sample at distance L above the well.	55
Figure 2-13. (a) Stepped deposition rate (black) and the film thickness of a 40 nm thick silver film in contrast to a (red) rapid deposition rate and the film thickness of a 40 nm thick silver film. (b) Heat map of the deposition angle from the middle boat evaporated onto samples located at sample height = 270 mm.	56
Figure 2-14. Simplified illustrations of (a) DC sputtering and (b) RF sputtering.	59
Figure 2-15. 2D topography rendering of a (a) 100 nm Sputter-coated silver and (c) 100 nm thermally evaporated silver Blu-ray grating. Corresponding 3D extrapolation and surface profiles for (b) 100 nm sputter-coated and (d) 100 nm thermally evaporated silver gratings.....	64
Figure 2-16. Measured reflectance spectra for (a) sputter-coated and (b) thermal evaporated Blu-ray silver gratings as a function of wavelength for three different incident angles (15° , 30° , and 45° .) (c) Comparison between the 15° reflectivity scans from sputtered and thermal gratings. (d) Table of calculated values for the labeled peaks in (c). SPR dispersion curves (with Air and with a 33 nm thick PMSSQ film on the gratings) with overlaid excitation and emission spectrum location for FITC. .	65
Figure 2-17. Normalized epi-fluorescence micrograph of a 10 μ M FITC dye layer on sputter-coated silver (a) flat area and (b) blu-ray grating as well as thermally evaporated silver (c) flat area and (d) blu-ray grating using a 20 \times objective, 80 ms CMOS exposure and FITC filter set.....	68
Figure 2-18. Histogram of the mean and maximum enhancement factors of sputtered and thermally evaporated silver Blu-ray gratings coated with a FITC/PMSSQ film compared to flat silver areas next to the gratings.....	69
Figure 2-19. (a) HDDVD gratings with (left) and without (right) an epoxied coverslip with immersion oil for reflectivity measurement. (b) grating with coverslip mounted to the VSAE sample stage.....	71

- Figure 2-20.** SPR Dispersion curves based on coupling peak location from reflectivity data for silver and alumina coated (a) HD DVD and (b) Bluray gratings. The excitation and emission spectrum locations for fluorescein isothiocyanate (FITC), rhodamine 6G (R6G), Rhodamine 640 (R640), and cyanine 5 (Cy5) have also been provided. (c) Mean fluorescence enhancement factor of silver Bluray gratings with respect to dye-coated glass samples for the previously listed fluorophores using different microscope objectives and different imaging mediums including air (RI: 1.000), water (RI: 1.333), and immersion oil (RI: 1.5148). 72
- Figure 3-1.** Grain and island growth mechanisms for silver films deposited onto (a) germanium, (b) titanium, and (c) chromium adhesion layers. 79
- Figure 3-2.** Topographical AFM scans ($1.5 \mu\text{m} \times 1.5 \mu\text{m}$) of gratings with (a,b) sputtered germanium and silver, (c,d) sputtered titanium and silver, and (e,f) thermally evaporated chromium and silver. Oxygen plasma treated samples (b,d,f) on average exhibited larger average grain diameters than the (a,c,e) untreated counterparts. All scan heights have been plotted from 0 to 60 nm. (g) Grain diameter histograms from the previous AFM scans. (h) Real and (i) imaginary permittivity components were taken from flat silver films with the same deposition parameters and PMSSQ/APTES film surface energy with bulk silver values from Johnson and Christy.²⁵ 81
- Figure 3-3.** TM-polarized reflectivity plots for 15° and 45° angles of incidence of gratings with (a,b) sputtered germanium and silver, (c,d) sputtered titanium and silver, and (e,f) thermally evaporated chromium and silver. Oxygen plasma treated (b,d,f) and untreated counterparts (a,c,e). (g) TM-polarized reflectivity at 15° of silver gratings with plasma, P, and no plasma treatment, NP. (h) Dispersion plot of the $m = \pm 1$ SPR modes derived from reflectivity peak location of silver gratings in air. 83
- Figure 3-4.** (a) Illustration of SPR excitation and SPCE capture from a silver grating with a simple microscope objective. (b) SPR dispersion curve representing SPR coupling peak location with overlay of R6G excitation and emission spectrum. (c) Normalized objective illumination intensity vs. angle for $10\times$, $20\times$, and $40\times$ objectives with estimated SPR excitation and SPCE emission angle ranges from (b) for a silver grating coated in 35 nm PMSSQ. (d) Mean enhancement factor of R6G dye coated gratings with different grain sizes as compared to R6G-coated glass substrates using 20 ms CCD exposure. 84

Figure 3-5. Brightfield images and false-colored fluorescence images using a R6G filter taken with a 60x oil immersion objective (NA: 1.35) of R6G dye coated, plasma-treated silver gratings composed of (a,d) sputtered Ge/Ag, (b,e) sputtered Ti/Ag, (c,f) and thermally evaporated Cr/Ag. Bright field images were taken with an exposure time of 200 milliseconds and an Ocean Optics high power 455 nm LED light source. Fluorescence images were taken with a xenon arc lamp and ORCAflash2.8 CCD camera at different exposure times to capture the much lower fluorescence intensity of the sputtered gratings compared to the evaporated gratings: (d) 150 ms, (e) 90 ms, and (f) 50 ms. The fluorescence intensity range for each image has been provided in the top right corner of each image..... 90

Figure 3-6. Simulations of silver gratings: (a) reflectivity for silver gratings with small and large grain sizes at 15° angle of TM-polarized incidence in air, (b) simulated maximum electric field ($E_z/E_{z,0}$) vs. wavelength for 35 nm PMSSQ-coated silver gratings with small and large grain sizes at 5° angle of TM-polarized incidence in air, (c) simulated reflectivity plots for silver gratings with different grating heights from 10 nm to 60 nm (rectangular shape) at 15° angle of TM-polarized incidence in air.,(d) SPR wavelength and maximum electric field vary with grating heights at 15° and 40° angle of incidence, (e) SPR wavelength and (f) maximum electric field at reflectivity dips for gratings with duty cycles from 0.25 to 0.85 with a grating height of 30 nm, 40 nm, or 60 nm. 94

Figure 3-7. (a) Simulated reflectivity plots for silver gratings with small and large grain sizes at 15° angle of TM-polarized incidence in air, with and without conformal PMSSQ coating. (b) Maximum electric field ($E_z/E_{z,0}$) vs wavelength plots for silver gratings. Simulated profiles for (c) small grain size and (e) large grain size, the red region is air and the magenta region is silver and R6G excitation ranges. Electric field distribution for the wavelengths at reflectivity dips for (d) small grain size (538 nm) and (f) large grain size (536 nm), maximum $E_z/E_{z,0}$ is normalized at 10..... 95

Figure 3-8. Simulated electric field distribution ($E_z/E_{z,0}$) for silver gratings with small and large grain sizes at 15° angle of TM-polarized incidence in air under the wavelengths at reflectivity dips and 10 nm less or more than the SPR wavelength: (a) small grain size and (b) large grain size. 95

Figure 3-9. (a) 2D simulation window for Ag gratings with rectangular shape varying grating heights from 10 nm to 60 nm. Simulated (b,c) reflectivity and (d,e) electric field distribution ($E_z/E_{z,0}$) for silver

gratings with 0.5 of duty cycle at (b, d)15⁰ and (c, e) 40⁰angle of TM-polarized incidence in air under the wavelengths at reflectivity dips, maximum $E_z/E_{z,0}$ in scale bar is normalized at 10. 96

Figure 3-10. (a) Reflectance (R) vs. wavelength for varying grating duty cycles from 0.25 to 0.85 with a constant grating height of 30 nm, 40 nm or 60 nm under each condition. (b) Electric field distribution ($E_z/E_{z,0}$) for silver gratings with varying duty cycle from 0.25 to 0.75 with grating heights of 30 nm, 40 nm and 60 nm, at 15⁰ angle of TM-polarized incidence in air under the wavelengths at reflectivity dips, maximum $E_z/E_{z,0}$ in scale bar is normalized at 10. 99

Figure 3-11. (a) Grating orientation and plate position identification diagram on an 8 in. silicon wafer. C: Circumferential, R: Radial. (b) Fluorescence enhancement factors with respect to glass at for silver gratings deposited with (b) thermal evaporation and (c) RF sputtering at different positions and orientations. 101

Figure 4-1. (a) Cortisol molecule diagram and (b) cortisol serum concentration throughout a 24 hr. period. 107

Figure 4-2. Fluorescence images of various cortisol-binding antibodies bound to substrates with either Cortisol-3, CMO-BSA or Cortisol-21, HS-BSA. All fluorescence images were taken with a 20x objective and 2 sec. exposure..... 112

Figure 4-3. Illustration of the Sandwich fluoroimmunoassay for cortisol. 113

Figure 4-4. Antibody immobilization assay fluorescence images and intensity. All images were taken with a 20x objective and an exposure time of 700 msec..... 115

Figure 4-5. Sandwich assay fluorescence intensity results. Fluorescence imaged with the R6G fluorescence filter, 20x Obj., and 2 sec. CMOS exposure..... 117

Figure 4-6. Illustration of the Competitive binding fluoroimmunoassay for cortisol. 118

Figure 4-7. (a) Fluorescence Images of gratings, flat silver regions, and glass taken with a 10x objective lens and normalized to 300 ms exposure (Image dimensions: 700 μm x 520 μm .) (b) Fluorescence intensity from alumina-capped gratings, flat silver regions, and glass samples exposed to CO₂ plasma at 7W for 0, 30, 60, or 120 sec. and bound to BSA-FITC. 120

- Figure 4-8.** Normalized fluorescence images were taken with a 20x objective (350 μ m x 260 μ m) of FITC-BSA bound to plasmonic gratings that were exposed to CO₂ plasma with and without PDMS wells during exposure..... 121
- Figure 4-9.** (a) Glass samples during exposure to milk blocking solution. (b) Grating samples during exposure to XM210 solution. 124
- Figure 4-10.** Fluorescence intensity (normalized to an exposure time of 5 sec.) at varying XM210 binding concentrations for grating and glass sensors. The original image exposure times are listed by each data point. Fluorescence images were taken with the TRITC filter cube and 10x objective lens..... 125
- Figure 4-11.** (a) Fluorescence images of plasmonic gratings and the surrounding flat silver regions after exposure to different concentrations of cortisol. Images were taken with a 20x objective lens (350 μ m x 260 μ m FOV) with a CMOS exposure of 250 msec. (b) Average fluorescence intensity of the samples in (a). (c) Background subtracted fluorescence intensity plotted with respect to cortisol concentration for gratings and flat silver..... 128
- Figure 4-12.** (a) Fluorescence images of plasmonic gratings and the surrounding flat silver regions after exposure to different concentrations of cortisol. Images were taken with a 20x objective lens (350 μ m x 260 μ m FOV) with a CMOS exposure of 100 msec. Background-subtracted fluorescence intensity normalized to 2 sec. CMOS exposure plotted with respect to cortisol concentration for (b) gratings and (c) alumina-coated glass samples. 130
- Figure 4-13.** Normalized fluorescence intensity of estimated XM210 concentrations given specific binding ratios to cortisol in the patient sample before surface exposure plotted against the normalized fluorescence intensity of known surface-bound XM210 concentrations with a molecular weight estimate of (a) 150 kDa and (b) 120 kDa..... 131
- Figure 4-14.** (a) DNA-based Cortisol Detection mechanism. 1) Fluorescently-labeled aptamer immobilized onto surface and forms hairpin that brings dye within quenching domain of gold layer. 2) Aptamer binds to cortisol resulting in a conformation change that lifts dye out of quenching domain and into the plasmonic enhancement domain.132
- Figure 4-15.** Reflectivity measurements at $\theta = 15^\circ$, 30° , and 45° incident light on plasmonic gratings composed of (a) 100 nm thick silver and (b) 90 nm thick silver with 10 nm gold-capping layer. (c) SPR dispersion curves

for 100 nm gold grating, 90 nm silver with 10 nm gold capping layer, and 100 nm silver grating in air. 133

Figure 4-16. Fluorescence images of 30 nm thick silver plasmonic gratings with a (a) 5 nm or (b) 10 nm thick gold-capping layer coated in a 30 nm thick PMSSQ layer with 10 μ M Cy5. Note the metal was deposited via GLAD ($\alpha=76^\circ$). Images taken with 60x WI objective lens. Scale bar: 20 μ m. 134

Figure 4-17. Brightfield images of 30 nm thick silver plasmonic gratings 10 nm thick gold-capping layer (a) before and (b) after immersion in T50 buffer solution for 24 hrs. Fluorescence images of the same plasmonic grating after immersion in T50 buffer for 24 hours taken with the (c) DAPI and (d) FITC filter cubes. (e) Fluorescence image of a 40 nm thick silver grating without gold cap in the FITC filter after 1 hour of exposure to T50 buffer. Note the metal was deposited via GLAD ($\alpha=76^\circ$). All fluoresce images taken at with 60x WI objective and 2 sec. CMOS exposure time. Scale bar: 20 μ m..... 135

Figure 4-18. FDTD simulation windows for a (a) 90 nm thick silver grating, (b) 90 nm thick silver grating with 10 nm thick gold capping layer, and (c) 90 nm thick gold grating. The reflectivity measurements obtained from the simulation have been provided in (top row) air, (middle row) water, and (bottom row) immersion oil. 137

Figure 4-19. (a) Reflectivity measurements from 100 nm thick, flat silver and gold films. (b) SPR dispersion for all gratings simulation in all mediums (air, water, and oil) from the reflectivity measurements in Fig. 4-18. ... 138

Figure 4-20. E_z field intensities with maximum field intensity listed in each plot for the $\pm\omega$ SPR modes generated at $\theta=5^\circ$ on a 90 nm thick silver grating, 90 nm thick silver grating with 10 nm thick gold capping layer, and 90 nm thick gold grating immersed in (a) air, (b) water, and (c) immersion oil..... 139

Figure 4-21. (a) Cortisol molecule dimensions. Cortisol 3D model made via Accelrys DS Visualizer. (b) Aptamer sequence including cortisol binding sequence with the sequence sections that are similar to other cortisol binding aptamers highlighted and spacer sequence. 142

Figure 4-22. Minimum free energy structures (ΔG) predicted by IDTDNA OligoAnalyzer 3.1 for the (a) 58 bp aptamer and (b) the spacer sequence of the aptamer alone. The 58 bp aptamer exhibits very stable hairpin structures that should place the dye label within 3-4 bp ($\sim 2.1 - 2.8$ nm) of the gold surface. The 18 bp spacer sequence only exhibits one secondary structure but has very high free energy / low

melting temperature and thus has a low probability of self-hybridizing when unbound..... 143

Figure 4-23. (a) 8 cm x 11 cm plasmonic grating array with alignment markings for attachment to a bottomless 96-wellplate. (b) Gratings attached to a bottomless 96-wellplate..... 145

Figure 5-1. AFM rendering of a plasmonic grating with (a) nanocones and a (b) nanogap. (c) The plasmonic grating cross section with incorporated nanocones/gaps with immobilized fluorophores. 149

Figure 5-2. (a) Single-stranded DNA (ssDNA) aptamer 1) immobilized via thiol binding to a gold plasmonic grating with a fluorescent dye molecule on the 5' end that is quenched due to folding of the DNA and proximity to the gold surface; 2) exposure to a mismatched aptamer does not result in hybridization; 3) complementary ssDNA binds and hybridizes the DNA, extending the dye molecule out of the quenching region; 4) due to hybridization, the dye molecule is extended into the plasmonic enhancement region of the grating resulting in much more intense fluorescence. (b) ssDNA aptamer sequence compared to the mismatch and target oligomers. 151

Figure 5-3. (a) Reflectivity measurements on a plasmonic gold grating with nanocavities at difference angles of incidence. (b) Experimental and simulated SPR dispersion plot of plasmonic gold grating indicating the wavelength/angle pairs that result in high, SPR-based absorption as well as the excitation and emission spectrums for the Cy5 filter cube. (c) Objective illumination angle distribution for a 60x water-immersion objective with SPR excitation and SPCE emission ranges from the overlap between Cy5 filter cube spectrum and SPR dispersion of the gold grating in water from (b)..... 153

Figure 5-4. (a) Bright-field micrograph of nanocones/gap-embedded gold gratings using a 60x water-immersion objective. (b-d) Normalized epifluorescence micrographs (0.1 second CCD exposure time) of 0.5 μ M immobilized ssDNA aptamer samples incubated with: (b) no complement (negative control) and perfect DNA complement on (c) gratings and (d) flat gold..... 157

Figure 5-5. Fluorescence enhancement factors of gold gratings, nanocones, and nanogaps with respect to flat gold after exposure to the mismatched and complementary DNA sequences. 158

Figure 6-1. Decreasing concentration of R6G dissolved in ethanol under (a) ambient illumination and (b) UV excitation. Top (L to R): 100 μ M,

10 μ M, 1 μ M, 100 nM, 10 nM, 1 nM, 100 pM. Bottom (L to R): 10 pM, 1 pM, 100 fM, 10 fM, 1 fM, 100 aM, 10 aM, 1 aM..... 162

Figure 6-2. (a) False-colored fluorescence images taken with a 100x (1.4 NA) oil-immersion objective of the plasmonic gratings with decreasing concentrations of R6G at different exposure times. 100 μ M–0.012s, 10 μ M–0.05s, 1 μ M–0.5s, 100 nM – 1.5s , 10 nM–4s, 1 nM–8s, 10 pM–10s, and 1 fM–10s. Scale bar: 4 μ m. (b) Fluorescence intensity of R6G dye films at different concentrations normalized to 10 second exposure on plasmonic gratings, flat silver, and glass with a 20x (0.45 NA) objective. 163

Figure 6-3. Raw fluorescence images of a SM of R6G exhibiting a split-emission pattern from an image sequence (a) before (frame 9) and (b) after photobleaching (frame 33). Each frame had an exposure time of 10 sec. and were taken with a 100x OI objective. (c) Mean background-subtracted fluorescence image where the mean background signal of 1201 was subtracted from the image in (a). (d) The photobleached sample image in (b) was subtracted from (a). 164

Figure 6-4. (a) Normalized fluorescence intensity of single molecules imaged with a 100xOI objective and 10 sec. exposure time on silver gratings, flat silver, and glass samples coated with R6G over the SM behavior concentration range. (b) Calculated quantity of dye mol. μ m⁻² for various R6G dye concentrations. The estimated upper detection limit is 30 mol./ μ m² where the SM emission is too overlapped to separate. The estimated lower limit is less than 0.02 mol./ μ m² and is primarily limited by the field of view of the objective rather than the objective’s resolution and CMOS sensitivity..... 165

Figure 6-5. Single molecule SPCE on a plasmonic grating. (a) Formation of SM SPCE 1) Excitation light is incident on the grating. 2) Photons converted into SPR evanescent field that excites a nearby fluorescent molecule 3) Excited fluorescent molecule vibrates and non-radiatively transfers remaining energy to the grating 4) Radiative plasmon emitted from grating at the SPCE emission angle (θ_{SPCE}). (b) Calculated θ_{SPCE} range for FITC, R6G, and Cy5 fluorescent dyes based on SPR dispersion, emission wavelengths of each dye, and emission filter transmission spectrum..... 167

Figure 6-6. SPR Dispersion of the plasmonic grating with light incident in air (black) and oil (red) and excitation (SPR) /emission (SPCE) wavelength ranges for (a) Cy5, (b) R6G, and (c) FITC, respectively. 168

- Figure 6-7.** Bright field and false-colored fluorescence image (100xOI objective, 10 sec. exposure) of a plasmonic grating with a spin-casted 33 nm thin fluorescent PMSSQ film (10^{-14} M R6G) with expansions of the same location. 169
- Figure 6-8.** Polarization and Emission Angle of Single Molecules. (a) Fluorescence images of single R6G molecules with a polarized emission analyzer rotated from S-P-S polarization. Separate dye molecules exhibiting (Top) P-polarized SM SPCE behavior and (Bottom) Dipole-oriented emission behavior that rotates with polarization angle. (b) Stacked fluorescence images taken at increasing focal plane height above the plasmonic grating. (Left) Angled SPCE and (Right) Airy disc pattern from the isotropic emission of a SM spreading with increasing focal height. Scale bar: 400 nm. Image exposure: 10 sec. 170
- Figure 6-9.** Fitted Intensity Profiles. Fluorescence intensity profiles with fitted points of interest (P: peak, C: center) at varying focal heights for (a) FITC, (b) R6G, and (c) Cy5. 171
- Figure 6-10.** Single molecule SPCE on a plasmonic grating. Overlaid brightfield and fluorescence images of PMSSQ coated gratings with 1 fM (a) FITC, (b) R6G, (c) and Cy5. The normalized emission angle range for each respective fluorescence image has been plotted with the emission range predicted by the SPR dispersion to the right of each image. Scale bar: 1 μ m. Grating Ridge (R) and Groove (G). 172
- Figure 6-11.** Background-subtracted Fluorescence images of single molecules of R6G on a plasmonic grating exhibiting a (a) diffraction-limited airy disc and (b) split emission due to SPCE. 100x Objective (NA 1.49), 10 sec. exposure, Scale bar: 400 nm. (c) Cross-section of the SM in (a) and (b) with calculated FWHM and separation distance of the split emission lobes. 173

LIST OF TABLES

Table 1-1. Microscope Objective Parameters for the BX51WI epifluorescence microscope.	30
Table 2-1. Optical Media Grating Parameters	35
Table 2-2. Mechanical properties of PDMS.....	42
Table 2-3. PMSSQ/APTES film surface energy summary.	50
Table 3-1. Summary of grating dimensions, roughness, and grain diameter.	81
Table 3-2. Grating-Based Fluorescence Enhancement Literature Summary	88
Table 3-3. Summary of simulated SPR peak parameters at $\theta_{\text{SPR}} = 15^\circ$ for silver gratings with different grain sizes.....	93
Table 3-4. Summary of simulated SPR peak parameters at $\theta_{\text{SPR}} = 15^\circ$ and 40° for silver gratings with different grating heights, with a constant duty cycle of 0.5.....	98
Table 3-5. Grating structure summary for various plate positions and orientations.	100
Table 4-1. Normal Adult Physiological Range of Cortisol and Sodium in Body Fluids	108
Table 4-2. Cortisol binding sequences with highlighted sequence similarities. [94]	141

CHAPTER 1: PLASMONICS

1.1. Introduction

Nanotechnology is the idea that we can create devices and machines all the way down to the nanometer scale, which is a billionth of a meter, about half the width of a human DNA molecule. – Prof. Paul McEuen, U.C. Berkeley

Since its discovery, nanotechnology has provided the tools necessary for scientists to study and even control the interaction of individual atoms and molecules. Despite the inherent challenges of manipulating nanoscale objects, scientists continue to learn about and add novel methods to an ever growing list of potential applications. One field in particular, plasmonics, has grown out of nanotechnology and encompasses the study of the interaction between electromagnetic (EM) waves and their interaction with the free electrons in a metal film. This field has led to many incredible discoveries and applications in both electronics and medicine, the first of which was the discovery of a phenomenon known as surface plasmon resonance (SPR.) R. W. Wood made the first recorded observation of the SPR phenomenon in 1902. Wood observed that the transmission/reflection of light would decrease in intensity at specific angles of incidence on metallic gratings when the wavelength of the illuminating light was similar to the grating spacing. At the time he was unable to provide an interpretation of the phenomenon and was called "singular anomalies," later termed "Wood's anomalies." In 1920, Sir Walter Rayleigh conducted a thorough analysis of Wood's results and theorized that the anomalies occur at specific wavelengths where the scattered wave emerges

tangentially to the plane of the grating surface. The physics behind this phenomenon was not well understood until the theory of SPR was postulated by U. Fano in 1941 and expanded on by A. Hessel in 1965.[2, 3] Thanks to their work and many others, we now know that these dips in intensity are the result of the light being converted to surface plasmon polaritons (SPP) at the grating surface. The underlying physics behind the generation of SPP and SPR will be explored in much further detail, theoretically and experimentally, in the following sections as well as the application of this technology as a fluorescence enhancement platform.

1.2. Surface Plasmon Polaritons

SPR-based research has grown substantially over the past several years and led to many substantial discoveries in nanotechnology including plasmonic nanoantennas and nanoresolution imaging techniques.[4-9] SPR is a phenomenon where light can be coupled into a metal/dielectric interface to form a propagating charge oscillation called a surface plasmon polariton (SPP). A better theoretical understanding of the dispersion relation is required to understand how a SPP is generated at a metal/dielectric interface. The electromagnetic behavior of surface plasmons can be described using Maxwell's equations (1.1) which are a combination of Faraday's law of induction (1.1a), Ampere's law amended to include displacement current $\partial \mathbf{D} / \partial t$ (1.1b), and Gauss's law for electric (1.1c) and magnetic fields (1.1d).[10, 11]

$$\nabla \times \mathbf{E} = -\frac{\partial \mathbf{B}}{\partial t} \quad (1.1a)$$

$$\nabla \times \mathbf{H} = -\frac{\partial \mathbf{D}}{\partial t} \quad (1.1b)$$

$$\nabla \cdot \mathbf{D} = 0 \quad (1.1c)$$

$$\nabla \cdot \mathbf{B} = 0 \quad (1.1d)$$

Where \mathbf{D} is the electric field displacement (C/m^2), \mathbf{B} is the magnetic field strength ($N/A/m$), \mathbf{E} is the electric field (V/m), and \mathbf{H} is the magnetic field (A/m). The electric and magnetic quantities are also related to each other through the material equations (1.2):

$$\mathbf{D} = \epsilon_0 \epsilon(\omega) \mathbf{E} \quad (1.2a)$$

$$\mathbf{B} = \mu_0 \mu(\omega) \mathbf{H} \quad (1.2b)$$

Where ϵ_0 is the electric permittivity of free space, μ_0 is the magnetic permittivity of free space, $\epsilon(\omega)$ is the dielectric constant, and $\mu(\omega)$ is the relative permeability. For the sake of this derivation, we assume that the dielectric and metal are homogenous, isotropic materials and are linearly polarized and magnetized in response to external fields. This reduces $\epsilon(\omega)$ and $\mu(\omega)$ to scalar quantities but complex functions dependent on the angular frequency ω of the exciting field. With these conditions Maxwell's equations can be solved by electric plane wave to give:

$$\mathbf{E}(\mathbf{r}, t) = \mathbf{E}_0 e^{i(\mathbf{k} \cdot \mathbf{r} - \omega t)} \quad (1.3)$$

Where \mathbf{r} is the position vector in free space, t represent the time, \mathbf{E}_0 is the electric field amplitude, and \mathbf{k} is the wavevector. Note that \mathbf{k} is aligned parallel to the direction of propagation and orthogonal to \mathbf{E}_0 due to the transverse nature of light.

The photonic dispersion relation can then be used to relate k and ω : [12]

$$\frac{\omega^2}{|k|^2} = \frac{1}{\mu_0 \mu(\omega) \epsilon_0 \epsilon(\omega)} \quad (1.4)$$

If we assume a non-magnetic media ($\mu(\omega) = 1$) and the free space permittivity is related to the speed of light in a vacuum:[13]

$$c^2 = \frac{1}{\mu_0 \epsilon_0} \quad (1.5)$$

Equation (1.4) can be simplified to provide the wavevector magnitude $|\mathbf{k}|$:

$$|\mathbf{k}| = \omega \sqrt{\mu_0 \epsilon_0 \epsilon(\omega)} = \frac{\omega}{c} \sqrt{\epsilon(\omega)} \quad (1.6)$$

While equation (1.6) describes $|\mathbf{k}|$ in a single medium, the conditions become more complicated when applied to the interface of two materials with different permittivities. First, consider an EM plane wave with transverse magnetic (TM) polarization that is incident at the interface of two materials such as seen in Fig. 1-1(a). The electric component of the TM wave in the x-z plane can generate a charge oscillation due to the discontinuity at $z=0$, i.e. the material interface. Unlike TM, an EM wave with transelectric polarization (TE) would not generate a charge oscillation as there is not discontinuity in the x-y plane.

The charge oscillation, i.e. surface plasmon, formed by the TM wave will correspond to solutions of Maxwell's equation which satisfy the interfacial

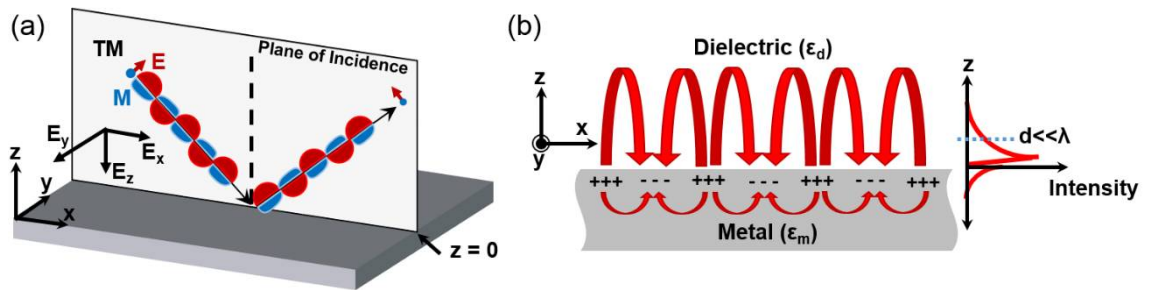


Figure 1-1. (a) TM polarized EM wave incident on a metal/dielectric interface with electric field components in the x-z plane and magnetic components in the x-y plane. (b) Electric field lines of a surface plasmon at the metal/dielectric interface. An external EM field, such as a photon or electron, can induce a surface charge oscillation. The charge oscillation forms an EM wave that decays evanescently into the dielectric, where the EM intensity is strongest near the interface.

boundary conditions and the magnitude will vary in a wave-like manner in the x direction, but decay evanescently in the z-direction in both media.[14] The electric and magnetic fields at the interface at the interface can be described by:

$$\mathbf{E}_1 = \mathbf{E}_1^0 e^{i(k_{x1}x - \omega_1 t)} e^{ik_{z1}z}; \quad z > 0 \quad (1.7a)$$

$$\mathbf{H}_1 = \mathbf{H}_1^0 e^{i(k_{x1}x - \omega_1 t)} e^{ik_{z1}z}; \quad z > 0 \quad (1.7b)$$

$$\mathbf{E}_2 = \mathbf{E}_2^0 e^{i(k_{x2}x - \omega_2 t)} e^{ik_{z2}z}; \quad z < 0 \quad (1.7c)$$

$$\mathbf{H}_2 = \mathbf{H}_2^0 e^{i(k_{x2}x - \omega_2 t)} e^{ik_{z2}z}; \quad z < 0 \quad (1.7d)$$

Where $\mathbf{E}_1^0 = (E_{x1}^0, E_{y1}^0, E_{z1}^0)$, $\mathbf{E}_2^0 = (E_{x2}^0, E_{y2}^0, E_{z2}^0)$, $\mathbf{H}_1^0 = (H_{x1}^0, H_{y1}^0, H_{z1}^0)$, and $\mathbf{H}_2^0 = (H_{x2}^0, H_{y2}^0, H_{z2}^0)$ are vector fields at the interface of medium 1 and 2, respectively.

The wavevector components in z, $k_{z1} = k'_{z1} + ik''_{z1}$ and $k_{z2} = k'_{z2} + ik''_{z2}$, are perpendicular to the interface and the wavevector components in x, $k_{x1} = k_{x2} = k_x = k'_x + ik''_x$, are the components parallel to the interface. The frequency is common to both media and thus $\omega_1 = \omega_2 = \omega$. With the assumed field continuity conditions for \mathbf{E} and \mathbf{H} parallel to the interface, we obtain:

$$E_{x1} = E_{x2} = E_x \quad (1.8a)$$

$$H_{y1} = H_{y2} = H_y \quad (1.8b)$$

$$k_{x1} = k_{x2} = k_x \quad (1.8c)$$

By substituting equations (1.7a-d) into Maxwell's equations (1.1a-d) we obtain the following relations:

$$k_{z1}H_y = \frac{\omega}{c} \epsilon_1 E_{x1} \quad (1.9a)$$

$$k_{z2}H_y = \frac{\omega}{c} \epsilon_2 E_{x2} \quad (1.9b)$$

By dividing equations (1.9a) and (1.9b), we can relate the wavevector to the media permittivities:

$$\frac{k_{z1}}{k_{z2}} = -\frac{\varepsilon_1}{\varepsilon_2} \quad (1.10)$$

The only condition where this relation is satisfied is if ε_1 and ε_2 are of opposite signs, which is only true if the interface is between a metal ($-\varepsilon_m$) and a dielectric ($+\varepsilon_d$) such as the illustration in Fig. 1-2(b.) The wavevector components k_z and k_x can be related using the total wavevector k_i in each medium using equation (1.6):

$$k_{zi}^2 = |k_i|^2 - k_{xi}^2 = \left(\frac{\omega}{c}\right)^2 \varepsilon_i - k_{xi}^2 \quad (1.11)$$

As found in (1.8c), the x-components are equal in both media and thus (1.11) can be reduced to:

$$\left(\frac{\omega}{c}\right)^2 \varepsilon_1 - k_x^2 = \left(\frac{\varepsilon_1}{\varepsilon_2}\right)^2 \left[\left(\frac{\omega}{c}\right)^2 \varepsilon_2 - k_x^2 \right] \quad (1.12)$$

By solving for k_x , we can obtain the plasmonic dispersion relation that describes the propagation of a SPP along the interface two media [15]:

$$k_x = \frac{\omega}{c} \sqrt{\frac{\varepsilon_1 \varepsilon_2}{\varepsilon_1 + \varepsilon_2}} \quad (1.13)$$

To find k_z of the SPP, the right side of (1.7) can be solved to separate the complex term of $k_z = k'_z + ik''_z$:

$$e^{i((k'_z - ik''_z)z - \omega t)} = e^{i(k'_z z - \omega t)} e^{-k''_z z} \quad (1.14)$$

Based on (1.14), the SPP will decay exponentially in the z direction, $e^{-k''_z z}$, with a decay length of $d = \frac{1}{k''_z}$. We can also expect that E_x and H_y will also decay

evanescently along the respective axis as all of the (1.7a-d) equations share (1.14).

1.3. SPP Excitation and Surface Plasmon Resonance

The plasmonic dispersion relation derived in the previous determines the SPP wavevector for any given metal and dielectric interface. In this section, we will explore the theory and methods of generating SPPs and the formation of surface plasmon resonance (SPR) using incident light. Consider that a photon of a specific frequency ω is propagating through a dielectric medium with refractive index (RI) $n = \sqrt{\epsilon}$, at an angle θ to the normal, and impacting on a planar metal surface. The in-plane wavevector can be described as:

$$k_x = k_{\parallel} = \frac{\omega}{c} \sqrt{\epsilon} \sin\theta \quad (1.15)$$

Subsequently, the SPP with a corresponding wavevector k_{SP} in equation (1.15) will always be larger than k_{\parallel} and as a result, free photons are unable to couple to SPP. This can be observed in the illustration provided in Fig. 1-2(a) and the frequency and momentum plot of the light line and plasmonic dispersion in Fig. 1-2(b).

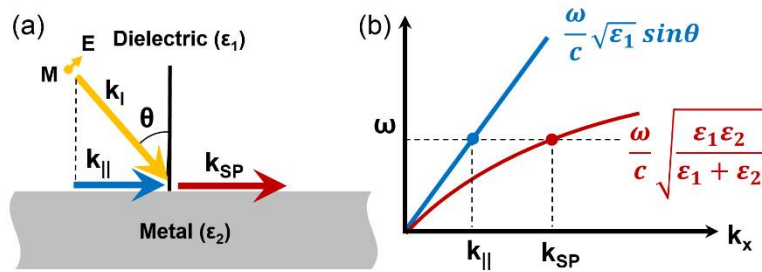


Figure 1-2. (a) Illustration of a photon impinging on a metal/dielectric interface and (b) Photon dispersion in a dielectric compared to the plasmonic dispersion at the dielectric/metal interface. Note that $k_{SP} > k_{\parallel}$ for any frequency ω .

Additional momentum is needed for the photon's wavevector to match the SPR wavevector and couple to form a SPP. Two methods have been discovered that can provide the momentum necessary to achieve wavevector matching conditions. The first method uses the combination of a high RI prism n_p and a thin noble metal film while the second method use the diffraction of metallic gratings. Variations of this method was developed by Otto and Kretschmann in 1968.[16, 17] Wavevector matching with method follows the equation below:

$$k_{SP} = \frac{\omega}{c} \sqrt{\frac{\epsilon_d \epsilon_m}{\epsilon_d + \epsilon_m}} = n_p \frac{\omega}{c} \sin \theta_{SP} \quad (1.16)$$

Where ϵ_d and ϵ_m and the permittivities of the dielectric, typically air or water, and metal film, typically gold or silver, respectively; θ_{SP} is the SPR resonance angle for a specific wavelength λ . In the Otto configuration (Fig. 1-3(a)), light in the form of a laser, is transmitted through a prism onto a thin dielectric film over a thick metal layer. Total internal reflection (TIR) occurs at critical angles between the prism and the dielectric which generates an evanescent field. This field can subsequently interact with the metal/dielectric interface to generate SPR.

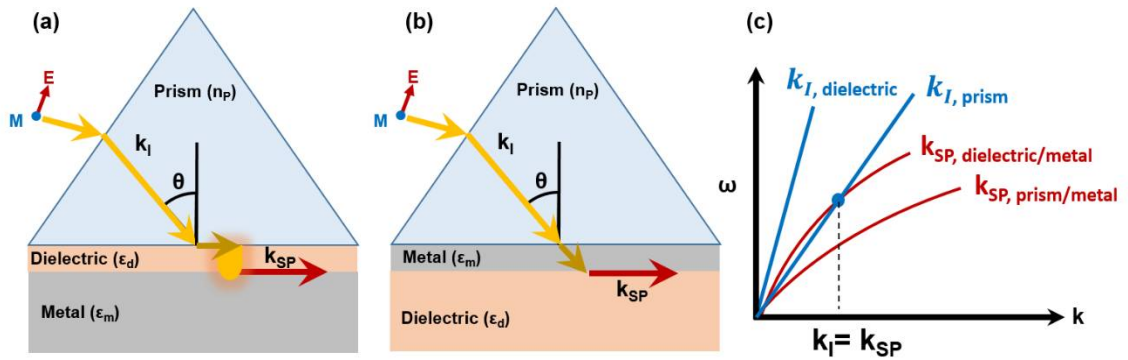


Figure 1-3. (a) Otto and (b) Kretschmann configurations for prism-based SPR excitation. (c) Photon and SPR wavevector matching conditions for the Kretschmann configuration.

Similarly, in the Kretschmann configuration (Fig. 1-3(b)), laser light is transmitted through a prism onto a thin metal film. The majority of the laser light is transmitted through the metal film and diffracts along the metal/dielectric interface such that the resulting photon wavevector k_I matches k_{SP} (Fig. 1-3(c)). While both configurations can effectively couple light to a SPP, three major drawbacks are: 1) both systems rely on the thickness of either the dielectric or the metal films; 2) light can only couple at very specific angles of incidence; and 3) these systems are typically very expensive to operate. An alternative solution to the Otto and Kretschmann configuration lies in the use of diffraction of metallic gratings to generate SPR.

A grating is defined as a periodic structure that is typically composed of fine, parallel grooves and ridges with a period or pitch Λ . The distance from the bottom of the groove to the top of the ridge is the grating height h . When a photon impinges perpendicularly to lines of a metal grating at θ_I with a pitch similar to the photon wavelength, it is diffracted at a specific angle θ_D and defined by the diffraction equation (1.17).

$$\sin\theta_D = \frac{m\lambda}{\Lambda} - \sin\theta_I \quad (1.17)$$

Where $m = 0, \pm 1, \pm 2, \dots$ is the diffraction order and λ is the photon wavelength. The Bragg's diffraction condition is defined for a surface grating as :[18] [19]

$$k_x + m\mathbf{G} = k'_{xm}; \quad |\mathbf{G}| = \frac{2\pi}{\Lambda} \quad (1.18)$$

Where \mathbf{G} is the grating vector, k_x is the component of the incident wavevector parallel to the grating surface, and k'_{xm} is the wavevector of the diffracted wave.

In order for the photon to couple to the SPP, the incident photon must be diffracted parallel to the grating surface as seen in Fig. 1-4(a). In this case, the momentum matching condition becomes [19, 20]:

$$k_{SP} = \frac{\omega}{c} \sqrt{\frac{\epsilon_d \epsilon_m}{\epsilon_d + \epsilon_m}} = \frac{\omega}{c} \sqrt{\epsilon_d} \sin \theta_{SPR} + m \frac{2\pi}{\Lambda}; \quad m = \pm 1, \pm 2, \dots \quad (1.19)$$

The range of values at which proper coupling conditions occur can be visualized in frequency vs. momentum plots, seen theoretically in Fig. 1-4(b) and experimentally in Fig. 1-4(c).[21]

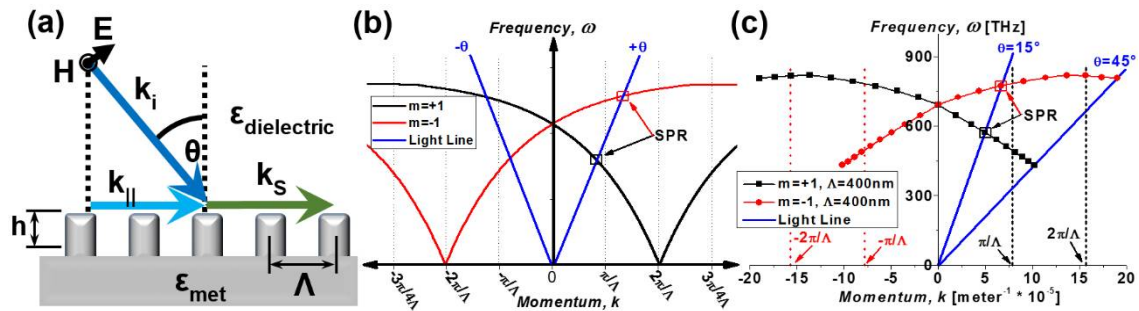


Figure 1-4. (a) Illustration of the wavevector matching between incident EM radiation (transverse-magnetic (TM) light) on a grating and a propagating surface plasmon polariton. (b) Theoretical frequency vs. momentum plot for a metallic grating (red and black), and incident EM radiation (blue line). (c) Experimental frequency vs. momentum for a silver grating in air based on the SPR peak location from the reflectivity scans.[22, 23]

The momentum added by diffraction shifts the plasmonic dispersion curve by $\pm m \frac{2\pi}{\Lambda}$ and creates a unique situation where two frequencies ω can now couple at a single θ_{SPR} . [24] Furthermore, it can be observed that these two modes converge as the angle of incidence of light approaches $\theta=0^\circ$. The ability to excite SPR at a low illumination angle on gratings has led to the development of systems that, for example, use microscope objectives to excite SPR instead of single angle, laser based systems.

The coupling of light to the grating at specific angles to the grating can be probed using reflectivity/transmission measurements taken with systems such as a variable angle spectroscopic ellipsometry (VASE). For example, a 40 nm thin silver film sputter-deposited over an HDDVD grating immersed in oil (RI: 1.518) exhibits the transmission intensity seen in Fig. 1-5(a) and the reflected intensity seen in Fig. 1-5(b).

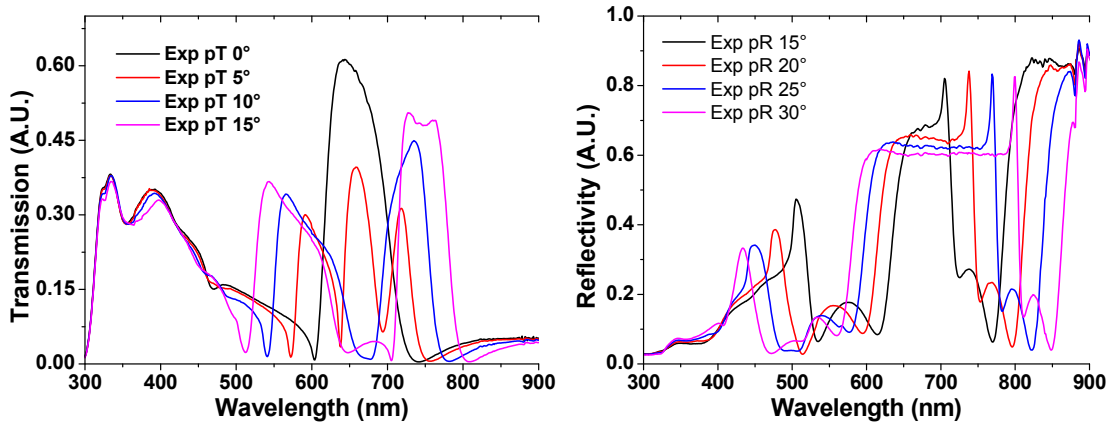


Figure 1-5. (a) Transmission ($\theta=0-15^\circ$) and (b) Reflectivity ($\theta=15-30^\circ$) measurements on a 40 nm thin silver grating immersed in oil.

This data is consistent with many of the observations made by R. W. Wood in 1902. Due to substantial progress SPR research and obtaining a better understanding of this phenomenon, we now understand that light can interact with a metallic grating in more ways than just SPR. One such interaction that light can occur upon incidence on a grating is a specific diffraction mode, known as a “grazing” mode, and was calculated by Sir Walter Rayleigh, and later expanded upon by Fano, to be:[3, 25]

$$\sin(\theta_n) = \sin(\theta) + \frac{n\lambda}{d} \quad (1.20)$$

Where θ is the angle of incidence, θ_n is the angle of diffraction, λ is the wavelength in vacuum, and d is the grating period. The grazing mode is located on the order n when $\sin(\theta_n) = \pm 1$, and thus the equation can be simplified to equation (1.21) to provide the wavelength of different grazing modes at various diffracted orders and incident angles for a specific grating pitch.

$$\lambda = -\left(\frac{d}{n}\right) * \sin(\theta) \pm 1, \quad n = \pm 1, \pm 2 \dots \quad (1.21)$$

As the grazing mode is tangential to the grating plane and forms on every period of the grating in phase with the period next to it, it constructively interferes to form the sharp increase in reflected intensity seen in Fig. 1-6(a). The increase in reflected intensity and a corresponding decline in transmission intensity at specific angles indeed matches half of Wood's results. However, the data not fitted by equation (1.21) are observed as declines in both reflected and transmitted data and always occur at slightly longer wavelengths than the location of the grazing mode.

The wavelengths at which a loss in both reflectivity and transmission occur can be predicted using the previously-derived wavevector-matching equation (1.19) and correspond to specific SPR modes. We also understand from Barnes that two frequency solutions exist for this equation and these solutions correspond to the two coupling wavelengths for each angle of incidence seen in Fig. 1-6(b).[9] In the case of a thin silver film (< 60 nm), transmitted light through the silver film can attain diffract in the underlying PMSSQ to form SPR. All of these coupling modes

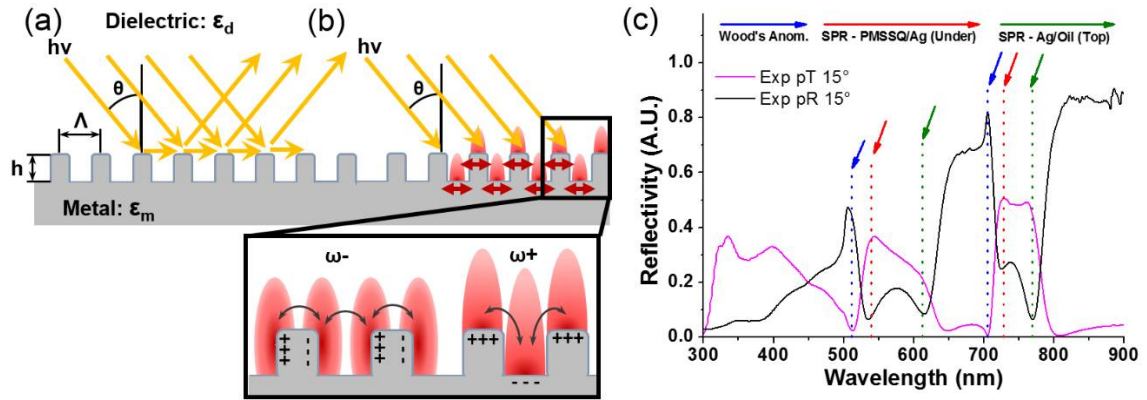


Figure 1-6. Illustration of the formation of (a) grazing diffraction mode interference, also known as wood’s anomalies, and (b) SPR with an expansion of the two SPR frequency modes typically observed on a corrugated surface. (c) Overlaid reflectivity and transmission scans at $\theta=15^\circ$ with coupling modes indicated with arrows.

are present in the reflectivity and transmission scan results obtained in Fig. 1-5, and have been indicated with blue, red, and green arrows in Fig. 1-6(c).

In the case of very thin, continuous films (< 30 nm), SPR formed on both interfaces of the film can also destructively interfere and reduce the propagation length or constructively interfere to form what is known as “long-range SPR” or LRSPR as was observed by Toma, Wang, Dostalek, and others.[26-28] The refractive index of the dielectric above and below the metal film must match to form constructive interference. Due to the increased sensitivity of LRSPR to the metal properties, thickness/refractive index of the PMSSQ, and the inherent fragility of such films the primary focus of the research within this project will be on thicker silver films (≥ 40 nm).

Sensitivity to Polarization: Two critical assumptions were made in the previous derivation of the wavevector matching conditions between the incident light and surface plasmon resonance. First, the electric component of the incident EM wave is parallel to the plane of incidence (TM polarization) and, second, that the EM

wave is incident perpendicular to the grating orientation. The sensitivity of coupling based on these two assumptions was tested experimentally using reflectivity measurements from a 100 nm thick silver grating. For the sake of consistency, incident light perpendicular to grating orientation refers to incident light that travels across the grating ridges ($\alpha=0^\circ$), whereas, parallel to grating orientation refers to light traveling with the grating ridge orientation ($\alpha=90^\circ$). If the polarization of light is rotated from TM ($\beta=0^\circ$) to TE ($\beta=90^\circ$) polarization, as seen in Fig. 1-7(a), the magnitude of the electric component into the grating decreases. As a result, this diminishes the ability of the incident light to excite SPR properly and can be observed in Fig. 1-7(b) as a loss in SPR peak area in reflectivity measurements with no peak wavelength shift.

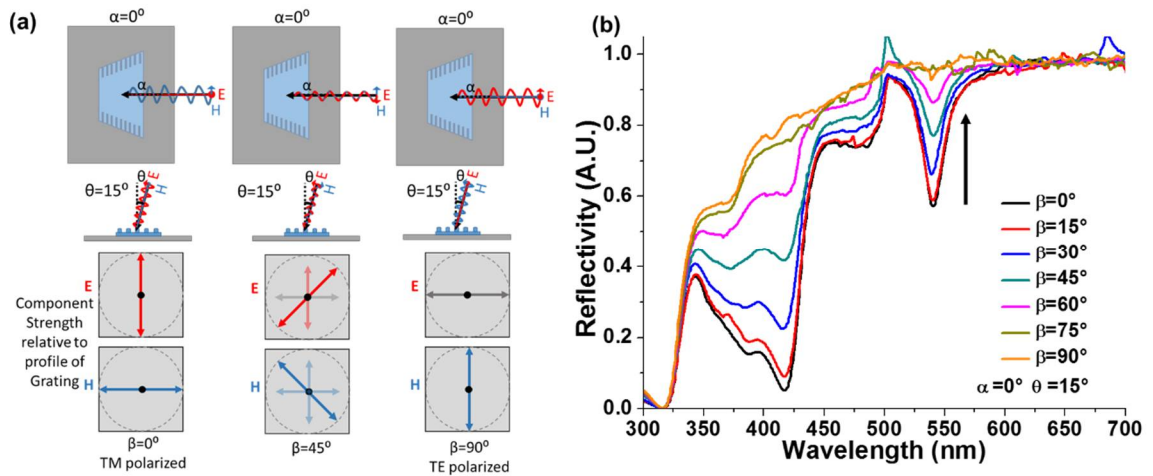


Figure 1-7. (a) Coupling sensitivity to polarization angle illustration. (b) Polarized Reflectivity at $\theta=15^\circ$ onto a grating where polarization angle is rotated from TM to TE polarization ($\beta=0 - 90^\circ$).

Sensitivity to Grating rotation: As derived in section 1.3, grating diffraction provides the additional momentum needed to obtain matching wavevectors of incident light and SPR on a grating of a specific pitch. Under ideal conditions, i.e.

incident light is perpendicular to the grating orientation, the entirety of incident light is diffracted resulting in the highest magnitude wavevector being coupled. However, any component of incident light parallel to grating orientation is not diffracted perpendicular to the grating. This results in a wavevector reduction that can be observed experimentally as a blue-shift in the SPR peak location, Fig. 1-8, where the grating orientation is rotated from $\alpha=0^\circ$ to 90° relative to the incident light. The peak location blue-shifts to compensate for the reduction in the perpendicular component of the photon wavevector with increasing grating orientation misalignment. In other words, higher energy light is necessary to obtain the same perpendicular wavevector component matching conditions as fully perpendicular incident light. It can also be seen in Fig. 1-8 that SPR peak area reduces with grating rotation. As discussed during coupling sensitivity to polarization rotation, peak area reduction is the result of increasing misalignment of the electric component in Fig. 1-8(b).

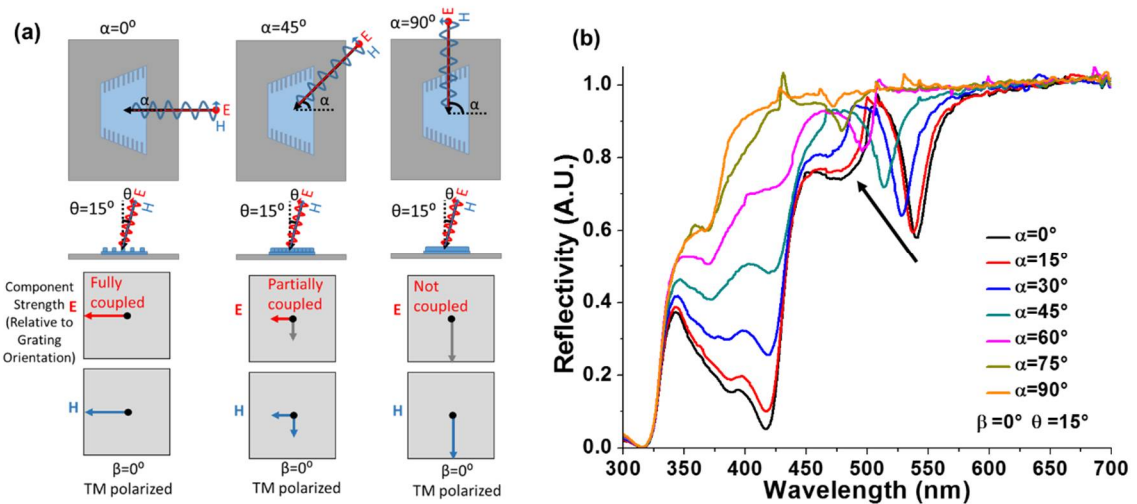


Figure 1-8. (a) Coupling sensitivity to polarization angle illustration. (b) Polarized Reflectivity at $\theta=15^\circ$ onto a grating where polarization angle is rotated from P- to S-polarization ($\beta=0 - 90^\circ$).

1.4. SPR Simulation

While much of the research on the fundamentals of SPR has depended on experimental measurements, theoretical simulations such as finite difference time domain (FDTD) simulation have provided a much easier and less expensive method for determining the effect of various parameters on the formation of SPR. An explanation of how FDTD simulations can be used to model SPR has been provided in this section.

FDTD is incredibly useful in determining the effect of nanostructure changes to an applied EM field. While FDTD can be used across the entire EM spectrum, the focus of this project will be primarily on the spectrum located between near UV, Visible, and near IR region. FDTD is an algorithm that can be used to provide a rigorous solution to Maxwell's equations. As Maxwell's equations are expressed in the differential form, FDTD solves the equations through first temporal and spatial discretization of the computational domain followed by numerical solutions for all of the equations. For linear, spatial discretization, the computational domain is divided into a grid of equally spaced points by Δx and Δy for a 2-dimension domain or plane and by Δx , Δy , and Δz for 3-dimensional domains as illustrated in Fig. 1-9. This spatial and temporal discretization was developed by K. Yee in 1966. [29, 30]

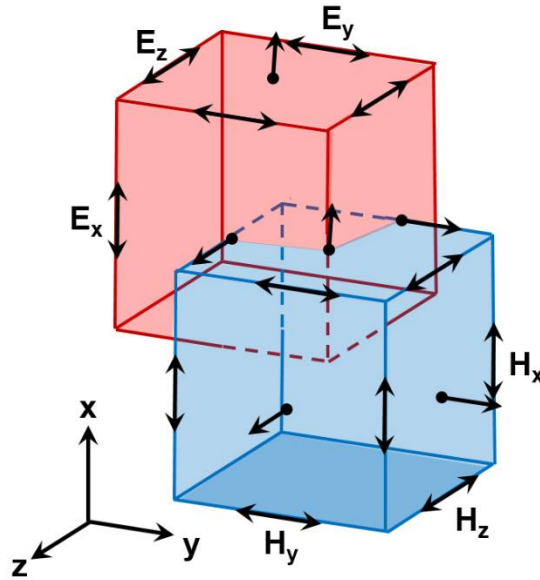


Figure 1-9. 3-dimensional Yee cell for FDTD simulation of the electric and magnetic field vectors. Many software packages for FDTD simulation, such as FullWave© by Synopsys, include capabilities for non-linear discretization to reduce computational time for larger objects. The temporal computational domain is also divided into time steps Δt . The electric field (E-field) vector components are then calculated at multiples of the time step $t = n\Delta t$ and the magnetic field (H-field) is calculated at $t = (n+1/2)\Delta t$. This time offset is introduced such that the magnetic field is updated halfway between each time step. This eliminates the need to simultaneously solve equations for the E- and H-fields, eliminates any dissipation from the wave propagation, and allows for the addition of the spatial variation, or curl, into both of the field calculations. However, this $\frac{1}{2}$ offset may greatly increase the number of time steps required for a simulation to reach steady state.

Using the Yee's cube, we can obtain an equation for each field component, E_x , E_y , E_z , H_x , H_y , and H_z . These equations, listed below and derived by K. Yee in 1966,

provide the field at any point and time step.[30] Typically, the equations are iteratively solved by the software package alternating between the E and H components with the $\frac{1}{2}$ offset per time step.

$$E_{x(i,j,k)}^{n+1} = E_{x(i,j,k)}^n + \frac{\Delta t}{\varepsilon \Delta y} \left(H_{z(i,j+1,k)}^{n+\frac{1}{2}} - H_{z(i,j,k)}^{n+\frac{1}{2}} \right) - \frac{\Delta t}{\varepsilon \Delta z} \left(H_{y(i,j,k+1)}^{n+\frac{1}{2}} - H_{y(i,j,k)}^{n+\frac{1}{2}} \right) \quad (1.22a)$$

$$E_{y(i,j,k)}^{n+1} = E_{y(i,j,k)}^n + \frac{\Delta t}{\varepsilon \Delta z} \left(H_{x(i,j+1,k)}^{n+\frac{1}{2}} - H_{x(i,j,k)}^{n+\frac{1}{2}} \right) - \frac{\Delta t}{\varepsilon \Delta x} \left(H_{z(i,j,k+1)}^{n+\frac{1}{2}} - H_{z(i,j,k)}^{n+\frac{1}{2}} \right) \quad (1.22b)$$

$$E_{z(i,j,k)}^{n+1} = E_{z(i,j,k)}^n + \frac{\Delta t}{\varepsilon \Delta x} \left(H_{y(i,j+1,k)}^{n+\frac{1}{2}} - H_{y(i,j,k)}^{n+\frac{1}{2}} \right) - \frac{\Delta t}{\varepsilon \Delta y} \left(H_{x(i,j,k+1)}^{n+\frac{1}{2}} - H_{x(i,j,k)}^{n+\frac{1}{2}} \right) \quad (1.22c)$$

$$H_{x(i,j,k)}^{n+\frac{1}{2}} = H_{x(i,j,k)}^{n-\frac{1}{2}} + \frac{\Delta t}{\mu \Delta z} \left(E_{y(i,j,k)}^n - E_{y(i,j,k-1)}^n \right) - \frac{\Delta t}{\mu \Delta y} \left(E_{z(i,j,k)}^n - E_{z(i,j-1,k)}^n \right) \quad (1.22d)$$

$$H_{y(i,j,k)}^{n+\frac{1}{2}} = H_{y(i,j,k)}^{n-\frac{1}{2}} + \frac{\Delta t}{\mu \Delta x} \left(E_{z(i,j,k)}^n - E_{z(i,j,k-1)}^n \right) - \frac{\Delta t}{\mu \Delta z} \left(E_{x(i,j,k)}^n - E_{x(i,j-1,k)}^n \right) \quad (1.22e)$$

$$H_{z(i,j,k)}^{n+\frac{1}{2}} = H_{z(i,j,k)}^{n-\frac{1}{2}} + \frac{\Delta t}{\mu \Delta y} \left(E_{x(i,j,k)}^n - E_{x(i,j,k-1)}^n \right) - \frac{\Delta t}{\mu \Delta x} \left(E_{y(i,j,k)}^n - E_{y(i,j-1,k)}^n \right) \quad (1.22f)$$

For TE polarized waves ($E_z, H_x, H_y = 0$), the equation set is reduced to:

$$E_{x(i+\frac{1}{2},j)}^{n+1} = E_{x(i+\frac{1}{2},j)}^n + \frac{\Delta t}{\varepsilon \Delta y} \left(H_{z(i,j+1)}^{n+\frac{1}{2}} - H_{z(i,j,k)}^{n+\frac{1}{2}} \right) \quad (1.23a)$$

$$E_{y(i,j,k)}^{n+1} = E_{y(i,j,k)}^n - \frac{\Delta t}{\varepsilon \Delta x} \left(H_{z(i,j,k+1)}^{n+\frac{1}{2}} - H_{z(i,j,k)}^{n+\frac{1}{2}} \right) \quad (1.23b)$$

$$H_{z(i,j,k)}^{n+\frac{1}{2}} = H_{z(i,j,k)}^{n-\frac{1}{2}} + \frac{\Delta t}{\mu \Delta y} \left(E_{x(i,j,k)}^n - E_{x(i,j,k-1)}^n \right) - \frac{\Delta t}{\mu \Delta x} \left(E_{y(i,j,k)}^n - E_{y(i,j-1,k)}^n \right)$$

Likewise, for TM polarized waves ($E_x, E_y, H_z = 0$):

$$H_{x(i,j,k)}^{n+\frac{1}{2}} = H_{x(i,j,k)}^{n-\frac{1}{2}} - \frac{\Delta t}{\mu \Delta y} \left(E_{z(i,j,k)}^n - E_{z(i,j-1,k)}^n \right) \quad (1.23c)$$

$$H_{y(i,j,k)}^{n+\frac{1}{2}} = H_{y(i,j,k)}^{n-\frac{1}{2}} + \frac{\Delta t}{\mu \Delta x} \left(E_{z(i,j,k)}^n - E_{z(i,j,k-1)}^n \right) \quad (1.23d)$$

$$E_{z(i,j,k)}^{n+1} = E_{z(i,j,k)}^n + \frac{\Delta t}{\varepsilon \Delta x} \left(H_{y(i,j+1,k)}^{n+\frac{1}{2}} - H_{y(i,j,k)}^{n+\frac{1}{2}} \right) - \frac{\Delta t}{\varepsilon \Delta y} \left(H_{x(i,j,k+1)}^{n+\frac{1}{2}} - H_{x(i,j,k)}^{n+\frac{1}{2}} \right)$$

The EM field must not change significantly between grids to obtain meaningful results. As such, the grid dimensions must be much smaller than the wavelength simulated. The time increment, related to the grid resolution by the Courant condition, must also be satisfied for simulation stability.[30]

$$\frac{1}{\sqrt{\left(\frac{1}{\Delta x^2}\right) + \left(\frac{1}{\Delta y^2}\right) + \left(\frac{1}{\Delta z^2}\right)}} > c_{max} \Delta t \quad (1.24)$$

Where c_{max} is the maximum speed of light in the simulated region. Based on equation (1.24), the time increment must be selected based on Δx , Δy , and Δz .

Boundary conditions: These conditions are also a necessary component in FDTD simulations as they describe the field as it interacts with the edge of the simulated domain. Commonly used boundary conditions include a perfectly matched layer (PML), perfect electric conductor (PEC), and periodic.

A PML condition incorporates an absorbing layer at the boundary, whose thickness is defined in the simulation. This condition typically eliminates unwanted reflections that could interfere with simulated domain and cause simulation instability. It is utilized when simulations include open boundaries such as a simulation where an interface with a bulk dielectric material is present in the simulated domain, but the material extends far beyond the simulated domain.

While a PEC boundary condition is similar to the layer added by a PML condition, the PEC layer is highly reflective instead of absorbing. This condition is useful for simulations including a reflective material, such as a thick metallic film.

A periodic boundary condition is a useful boundary condition when attempting to simulate repetitive structures such as a metallic grating. This condition essentially transmits the waves passing through a boundary to the opposite boundary of the simulated domain. This enables simulations of a single periodic structure to behave as part of a much larger structure with several periods and can drastically reduce the size of a simulated domain and the computation duration.

Launch conditions: In most simulations, an external wave must be applied to perturb a simulated system. However, the method of applying or launching the wave into the system depends on the desired result, whether it be achieving a steady state or determining the interaction with a single excitation wave. In this research, continuous wave (CW) excitation was used to simulate the plasmonic gratings to obtain the EM fields present on the grating at steady state. A sinusoidal plane wave with either TM or TE polarization is utilized in CW excitation and is governed by:

$$g(t) = \alpha(t)\beta(t) \sin \left[\frac{2\pi}{\lambda} + At^2 \right] \quad (1.25)$$

Where α and β are functions that provide a steady increase from 0 to 1 and steady decreasing from 1 to 0, respectively. The excitation wavelength is λ and A represents a function where the frequency increases or decreases with time, also known as chirped excitation. The following example has been provided to illustrate how these parameters, various boundary conditions, and launch conditions previously described can be applied to a plasmonic grating.

A 100 nm thick silver grating over a 100 nm thick PMSSQ film layered over a pure silica (quartz) substrate (Fig. 1-10(a).) The surrounding environment was selected to be air; however, the refractive index could just as easily be modified to match water or immersion oil. A reflected intensity monitor was placed just above the excitation source bar where both were >550 nm from the grating surface. The upper and lower boundaries of the simulation were given a PML boundary condition whereas the side boundaries were given a periodic boundary condition due to the inherent repetitive structure of the grating. The simulation was performed using TM polarized light over an incident angle range of $\theta=0-20^\circ$. The resulting reflected intensity can be observed in Fig. 1-10(b). One of the many advantages of using simulations is that physical system limitations can be completely avoided, such as the restriction of the VASE that reflectivity measurements cannot be taken at $\theta < 15^\circ$. Simulations can also provide the EM

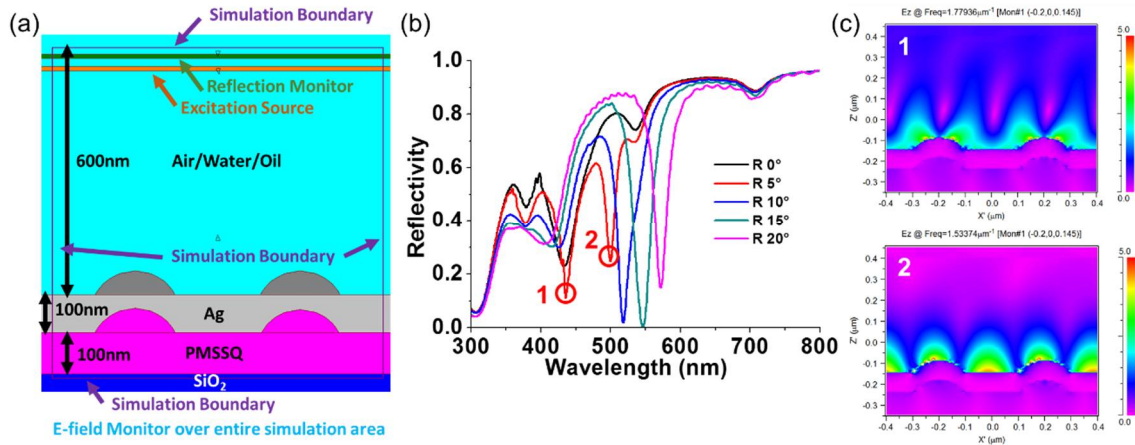


Figure 1-10. (a) Simulation area for a silver-coated PMSSQ grating on a glass substrate in air, water, or oil. (b) Reflectivity results for simulation window (a) in air from $\theta=0, 5, 10, 15,$ and 20° . (c) E_z -field intensity plots for locations 1 and 2 indicated in (b) that correspond to the upper and lower ω_{SPR} solutions at $\theta=5^\circ$.

field vectors for a given incident angle of light which enables users to observe the two SPR modes at $\theta=5^\circ$ (Fig. 1-10(c).)

1.5. Principles of Fluorescence Microscopy

Fluorescence is the emission of radiation, typically in the visible spectrum, by a substance after exposure to radiation of higher energy or shorter wavelength. This term was first phrased by G. G. Stokes in 1852 after observing the emerald green light emitted by the mineral fluorspar after absorbing deep sapphire blue light.[31] Fluorescence excitation and emission are typically illustrated using a Jablonski energy level diagram such as the diagram seen in Fig. 1-11. In a Jablonski diagram, there are three electronic singlet states S_0 , S_1 , and S_2 that represent the ground and first two excited states. For each the states there are several vibrational energy states 0, 1, 2, etc. and the population of each state follows the Boltzmann distribution.[32] As a result, only the S_0 is expected to be populated at room temperature.

Upon exposure to external radiation such as an incident photon, fluorescent molecules, such as those that make up the impurities present in fluorspar or calcium fluorite, are excited to higher electronic states. Following excitation, the molecule will undergo internal conversion and vibrational relaxation to dissipate energy. The molecule will then emit a photon with energy equivalent to the difference from the previous energy state to the ground or lower vibrational energy

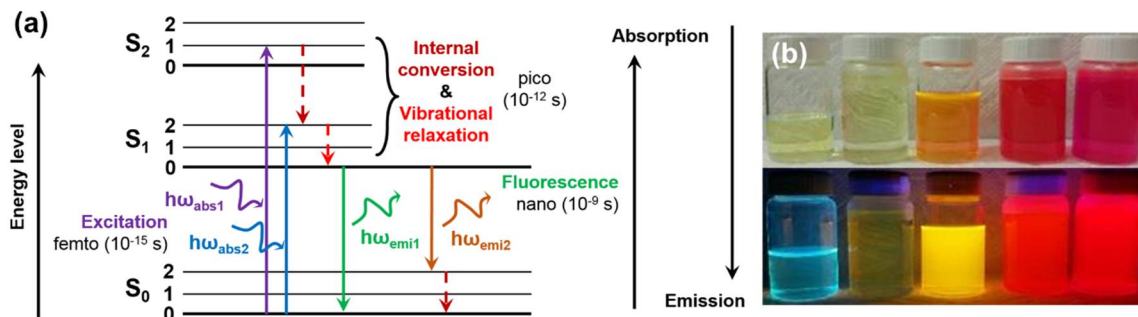


Figure 1-11. (a) Jablonski energy level diagram illustrating the typical excitation and emission steps in the generation of fluorescence as well as the transition time for each step.[33] (b) Various dyes dissolved in ethanol illuminated with (top) ambient light and (bottom) UV light.

state. The electronic transition between states occurs much faster than changes in the nuclei position according to the Frank-Condon principle and, as such, the energy state transitions are vertical and the same energy diagram can be used for both absorption and emission.[34]

We can see in Fig. 1-11(a) that the energy of the absorbed photon ($h\omega_{abs}$) is higher than the fluorescently emitted photon ($h\omega_{emi}$). The loss in energy is called Stoke's shift, and it enables the separation of the two photons using the optical filters found in fluorescence microscopy. Fluorescence microscopes, such as the BX51 Olympus epifluorescence microscope seen in Fig. 1-12(a), enable easy separation of the excitation and emission light and provide highly magnified imaging of fluorescent samples. These microscopes typically utilize a set of filter cubes that are specifically designed for either a particular fluorophore or wavelength range. Filter cubes are composed of an excitation filter, a dichroic mirror, and an emission filter (Fig. 1-12(b)). The emission filter, typically a short pass or bandpass filter, chops the wide spectrum of light from the light source, typically a xenon arc or halogen lamp, such that only the excitation wavelength range is transmitted. Next,

the dichroic mirror, typically a long pass filter, reflects the excitation wavelengths down towards the objective lens and sample. The sample is excited and emits fluorescence which is captured by the objective lens. The combination of reflected excitation light and the sample emission impinges upon the dichroic mirror which transmits all of the wavelengths longer than the excitation wavelength range. The light is then filtered through the emission filter such that only the emission wavelength range is transmitted to the detector. The emission filter is useful for removing longer wavelengths of light that may be due to either external light sources or fluorescent molecules with longer emission spectrums present in the same sample. The next section will explore the possible interactions between fluorescent molecules and plasmonic gratings.

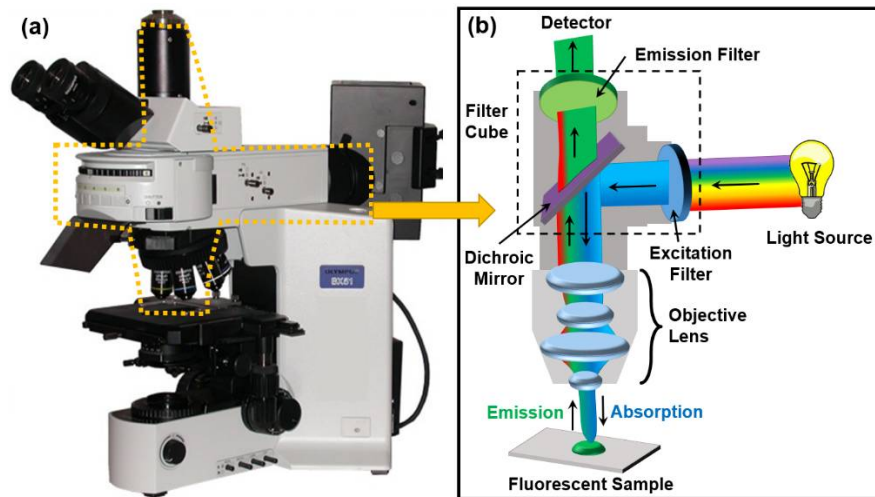


Figure 1-12. (a) BX51 Olympus epi-fluorescence microscope and the (b) excitation and emission illustration for fluorescence filter cube imaging.

1.6. Fluorescent Dye and Metal Interactions

As a better understanding of SPR has been obtained, a unique interaction was observed between the evanescent electromagnetic (EM) field formed during SPR and nearby fluorescent molecules. It was also observed that the emission intensity of fluorophores could be drastically enhanced when located between 10 – 100 nm to the metal surface and a phenomenon later called metal enhanced fluorescence.[35] If the frequency of the surface charge oscillation matched the excitation frequency of the fluorophore, the fluorophore would be excited to a higher energy state. However, due to the proximity to the metal surface, the fluorophore would non-radiatively transfer energy to the metal and form a radiative plasmon with directed photon emission, also known as surface plasmon-coupled emission (SPCE).[36] Alternately, fluorescent molecules at <10 nm from the metal surface were found to have no emission and thus the spacing of the dye molecule from the grating plays a key role in determining whether the dye is quenched and enhanced.

The interaction between a fluorescent molecule and a metal surface can be treated as a dipole/dipole interaction as described in the Förster model with minor modification.[37-39] In the Förster model, the efficiency of energy transfer, E , between two point-like dipoles is determined based on the separation distance, r , and the Förster distance, R_0 , defined as the distance at which the energy transfer efficiency is 50% as seen below in equation (1.26).

$$E = \frac{k_{ET}}{k_f + k_{ET} + \sum k_i} = \frac{1}{1 + \left(\frac{r}{R_0}\right)^6} \quad (1.26)$$

The Förster distance depends on the integral of the overlap of the donor emission spectrum and acceptor absorption spectrum and their respective molecular orientation exhibited in equation (1.27).

$$R_0^6 = \frac{9(\ln 10)}{128\pi^5 N_A} \frac{\kappa^2 Q_D}{n^4} J \quad (1.27)$$

Where Q_D is the quantum yield of the donor, κ^2 is the dipole orientation factor (assumed to be 2/3), n is the refractive index of the medium, N_A is Avogadro's number, and J is the spectral overlap integral. The Förster distance typically ranges from 5-7 nm for most Förster resonance energy transfer (FRET) pairs of fluorescent molecules. However, the transfer efficiency is different in the case of a metallic grating and a single fluorophore. The width of the metallic surface (>100 nm) is much larger than the size of molecule (1-2 nm) so the metal can be treated as a metal plane. Integration over the metal plane converts the model from a point-like dipole and compensates the distance term by a factor of r^2 . The resulting relation of emission efficiency, i.e., the efficiency of a fluorophore not transferring energy to the metal or $\eta_{eff} = 1 - E_{FRET}$, from a fluorophore near the metal plane can then be determined by: [40, 41]

$$\eta_{eff} = \frac{I(d)}{I_\infty} = \frac{1}{1 + \left(\frac{R_0}{r}\right)^4} \quad (1.28)$$

Where at infinity the dye will not interact with the metal and emit at intensity I_∞ . At a finite distance from the metal, d , the emission intensity is $I(d)$. At the Förster distance between the metal and the fluorophore the emission intensity is equal to 0.5, assumed to be between 5-7 nm, and is largely dependent on the permittivity

of the metal. The maximum emission efficiency would thus be when the separation distance is more than one Förster distance apart. For example, the spacing with minimal emission efficiency was estimated to be from 5-10 nm for silver and gold surfaces.[35] Several articles describe the energy transfer and resulting loss in fluorescent emission as generic “quenching” at this distance. However, for plasmonic systems, it is hypothesized that the transferred energy is converted into a lossy surface plasmon below 8-10 nm as the charge spacing is too close to form a radiative plasmon.[35] Above 10 nm, the charge spacing is wide enough to form a radiative plasmon in a process illustrated in Fig. 1-13. Using SPCE, the fluorescent emission intensity on gratings was previously demonstrated to be up 126x that of fluorophores on glass substrates.[42]

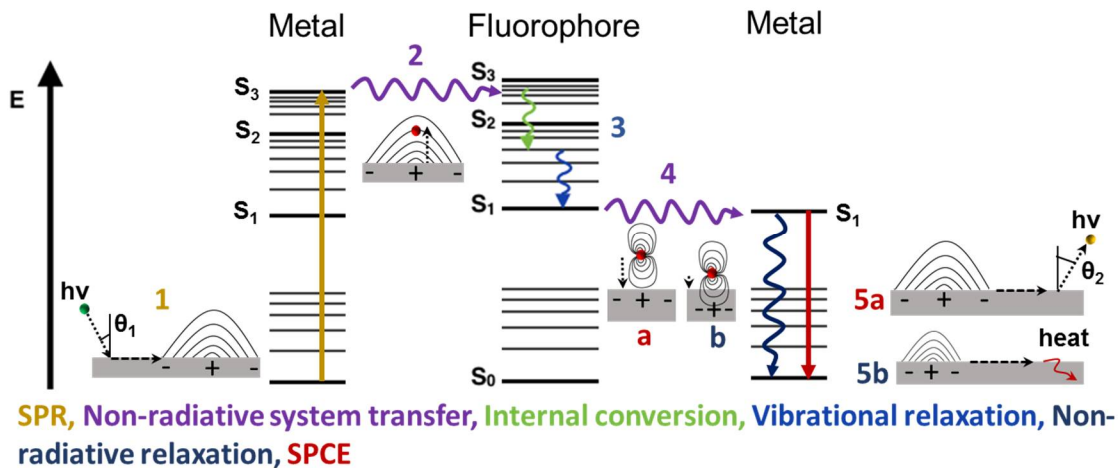


Figure 1-13. Jablonski diagram of Metal/Fluorophore interactions that lead to surface plasmon coupled emission or lossy surface plasmons. 1) An incident photon onto the grating will be converted into a surface plasmon. 2) the resulting generated dipole will interact with the fluorophore’s dipole and non-radiatively transfer energy to the molecule. 3) the fluorescent molecule will undergo internal conversion and vibrational relaxation to dissipate energy. 4) the fluorophore will non-radiatively transfer the remaining energy to the grating surface via dipole/dipole interaction. 5a) the energy will either be converted to a radiative plasmon and emit a photon at the emission wavelength of the fluorophore at the SPR dispersion angle, or 5b) the energy will be converted into a non-radiative plasmon that dissipates into heat.[35, 43, 44]

Based on this information, the optimal spacing of the fluorophore from the metal to obtain maximum emission intensity can be determined by comparing the fluorescence emission efficiency, equation (1.26), to the evanescent field strength of the plasmonic grating as seen in Fig. 1-10(c-2). A 100 nm thick silver plasmonic grating was simulated using FullWave® by RSoft to obtain the evanescent field strength into an aqueous medium ($n = 1.333$) at SPR coupling angle $\theta_1 = 0^\circ$ and the excitation wavelength AF568 ($\lambda = 579$ nm.) The fluorescence emission efficiency was calculated using equation 1.28 for three Förster distances (5, 6.2, and 7 nm).

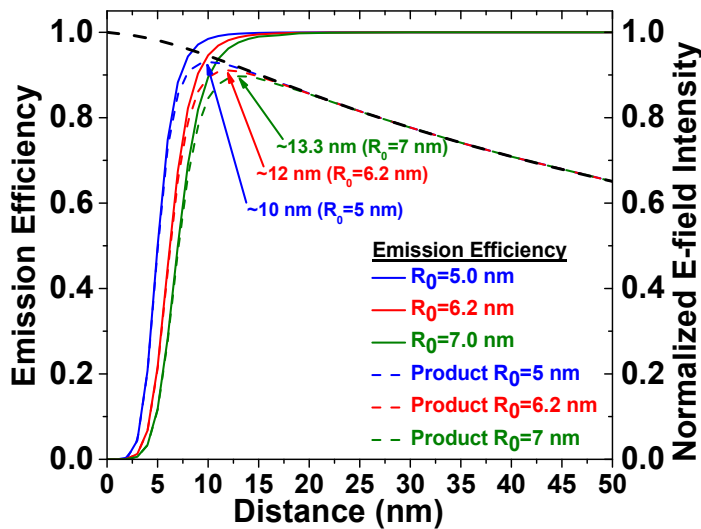


Figure 1-14. Emission efficiency for a range of Förster distances ($R_0 = 5$ (blue), 6.2 (red), and 7 nm (green)) compared to the E-field intensity (black) of a silver plasmonic grating. The product of emission efficiency curve and the E-field intensity for each Förster distance (dashed lines). The peak in the resulting product of the two curves is 10 nm ($R_0 = 5$ nm), 12 nm ($R_0 = 6.2$ nm), and 13.3 nm ($R_0 = 7$ nm).

The product of the E-field intensity and the emission efficiency (Fig. 1-14) peaks between 10 – 13.3 nm from the surface of the grating which should correspond to the maximum fluorescence emission intensity. Below 3 nm, the emission efficiency is less than 4% for all three Förster distances. Thus, a dye molecule spaced 3 nm

or less from the metal surface is completely quenched and completely emissive at distances greater than 10 nm from the metal surface.

1.7. Angular Excitation and SPCE Capture

In Section 1.3 we found that the SPR dispersion is highly angle dependent and this is also true for SPCE. SPR and SPCE are, in essence, opposite processes of one another where SPR is the coupling of light at a specific angle to the grating and SPCE is the radiation of light at a specific angle from the grating. The angles at which coupling or emission of light can both be observed using the SPR dispersion curve in either frequency (ω) vs. momentum (k) as seen in Fig. 1-4 or wavelength (λ) vs. incidence angle (θ) in specific mediums plots as seen in Fig. 1-15. The advantage of using λ vs. θ curves is that the coupling angles can be found easily using reflectivity measurements (Fig. 1-15(a)) in different mediums (Fig. 1-15(b,c)). However, these curves are true for only one dielectric/interfacial condition, whereas the ω vs. k curve is true for all dielectric and interfacial conditions.

Single angle, monochromatic illumination is the most common form of SPR excitation found today. While this may be optimal for prism-based systems with

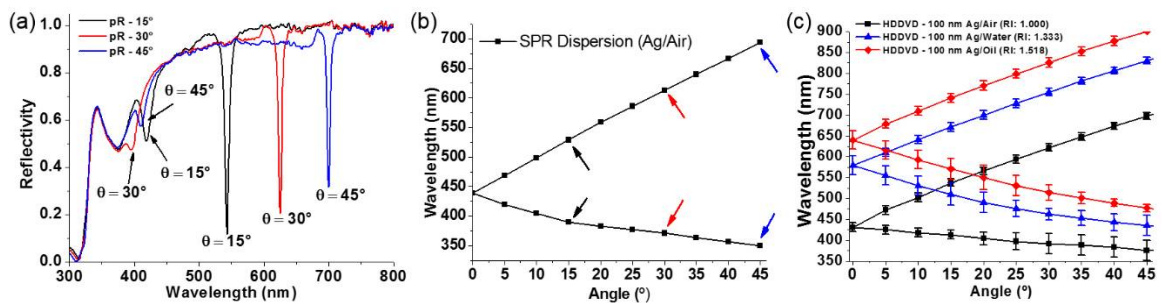


Figure 1-15. (a) Reflectivity measurements for a 100 nm thick silver grating in air and corresponding (b) SPR dispersion curve in air. (c) SPR dispersion in air (black), water (blue), and oil (red) mediums.

narrow coupling ranges, it is much less efficient for systems with wider coupling ranges, such as plasmonic gratings. By exciting SPR on wide coupling range systems with a single wavelength and angle, a significant portion of the SPR coupling range is underutilized. The plasmonic grating must be illuminated with polychromatic light that matches the excitation spectrum of the desired fluorophore at a range of angles that can couple to form SPR to take full advantage of the wide coupling range. This type of illumination can already be found in the objective of a simple fluorescence microscope as objectives focus light into a cone with a particular convergence angle. The convergence angle of a particular objective can be calculated using equation (1.29), a variation of Snell's Law:

$$NA = n \sin(\pm\theta_{CA}) \quad (1.29)$$

Where $\pm\theta_{CA}$ is the maximum convergence angle of the objective from sample normal, NA is the numerical aperture, and n is the refractive index of the imaging medium. A range of convergence angles and other objective parameters has been provided in Table 1-1 for the objectives used in this research.

Magnification	10x	20x	40x	60x	100x
Corrections	UPLFLN	LUCPLFLN	LUCPLFLN	UPLSAPO	UAPON
Beam Spot Diam. (mm)	2.65	1.1	0.55	0.44	0.22
Immersion Medium	-	-	-	Water	Oil
NA	0.3	0.45	0.6	1.2	1.49
FN (Field number)	26.5	22	22	26.5	22
WD (mm)	10	6.6-7.8	2.7-4	0.28	0.1
θ_{CA}	17.45 ⁰	26.74 ⁰	36.87 ⁰	64.19 ⁰	79.62 ⁰

Additionally, the intensity of light emitted by the objective lens follows a Gaussian distribution that peaks at $\theta = 0^\circ$ and decays towards the convergence angle. After SPR is excited using the oblique illumination provided by the objective and photons emitted via SPCE, the microscope objective must have a large enough convergence angle to capture the SPCE.

Using SPR dispersion curves, it is possible to predict the SPCE emission angle and optimize the emission intensity for a given microscope objective lens. For example, the optimal wavelength range for enhanced fluorescence is located between 550 nm and 650 nm for a silver grating immersed in water or a buffer solution of a similar refractive index. This wavelength range includes two fluorescent dyes: AlexaFluor 568 (AF568) and AlexaFluor 594 (AF594). AF568 has a higher quantum yield than most fluorescent dyes with longer wavelengths (0.69 vs. 0.66-0.12 for the AF594 - AF750 dye series) and thus will be used for this example. The excitation and emission wavelengths for AF568 have been plotted vs. the silver grating SPR dispersion curves in air (black) and water (blue) in Fig. 1-16(a). The overlap between the excitation and emission wavelengths and the SPR dispersion can be subsequently compared to the angular illumination/ capture curves for each microscope objective (Fig. 1-16(b)) to determine the objective with the most overlap between the illumination intensity and SPR excitation range. From Fig. 1-16(b), we find that the 10x objective will provide the highest fluorescent enhancement as it has the most overlap with the SPR excitation as well as a large enough convergence angle to include the angular SPCE range (Fig. 1-16(c).)

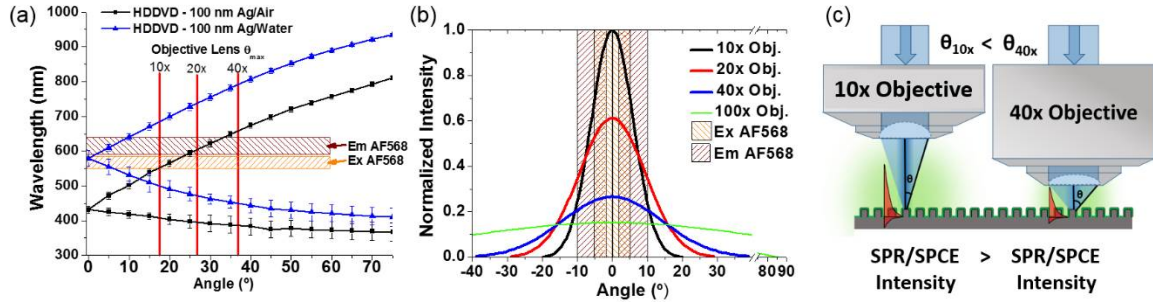


Figure 1-16. (a) Experimentally derived SPR dispersion of a 100 nm thick silver grating in air and water. The excitation and emission wavelength range for AF568 has been plotted as well as the convergence angle of three microscope objectives (10x, 20x, and 40x) calculated based on numerical aperture (N.A.) and the refractive index of the imaging medium.[42] (b) Objective lens emission/collection range for 10x, 20x, 40x, and 100x oil immersion objectives compared with the SPR coupling angles of the excitation wavelength range for AF568 and the emission angle range for the emission wavelength range for AF568 via SPCE. (c) Convergence angle and SPR/SPCE intensity comparison between the 10x and 40x objective.

The resolution of the images collected is another important factor in selecting a microscope objective, especially in high magnification, single molecule imaging applications. The minimum resolution of an objective lens is calculated based on the Rayleigh criterion which describes the interaction between diffraction and aberration that causes image blurring between two point sources in the image. The minimum XY resolvable distance, also known as the diffraction limited resolution can be found by:

$$R = \frac{\lambda}{2 * n * \sin(\theta_{CA})} = \frac{\lambda}{2 * NA} \quad (1.30)$$

Where λ is the imaging wavelength, R is the minimum XY resolution, M is the magnification of the objective, NA is the numerical aperture, and n is the refractive index. The minimum focal plane thickness or depth of field can be found by:

$$Z = \frac{\lambda * n}{NA^2} + \frac{n * R}{M * NA} \quad (1.31)$$

The two sides of equation (1.31) represent the two sources of resolution limitations. The left side dominates when NA is low and is due to the circle of confusion caused

by the concentration of light into a cone not combining to form a perfect focus. However, the right side dominates when the NA is high and is primarily caused by wave optics. Based on the objective lenses available with the microscopic used during this project, the minimum XY and depth of field (Z-resolution) has been provided in Fig. 1-17.

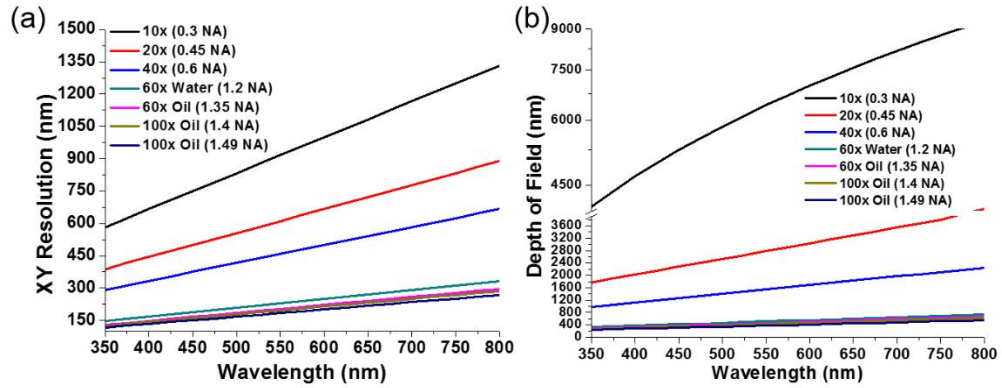


Figure 1-17. (a) Minimum XY resolution and (b) depth of field for 10x, 20x, 40x, 60x WI, 60x OI, and 100x OI objective lenses.

CHAPTER 2: PLASMONIC GRATING FABRICATION

2.1. Introduction

The expense of manufacturing platforms such as nanoscale gratings is currently cost prohibitive as it commonly involves the use of electron beam or interference lithography techniques.[45, 46] However, an inexpensive, mass-produced source of nanoscale gratings has been readily available for more than a decade in the form of optical media. Optical media, such as HD DVDs or Blu-ray discs, are an excellent source of inexpensive nanoscale gratings with a range of different pitches and heights.

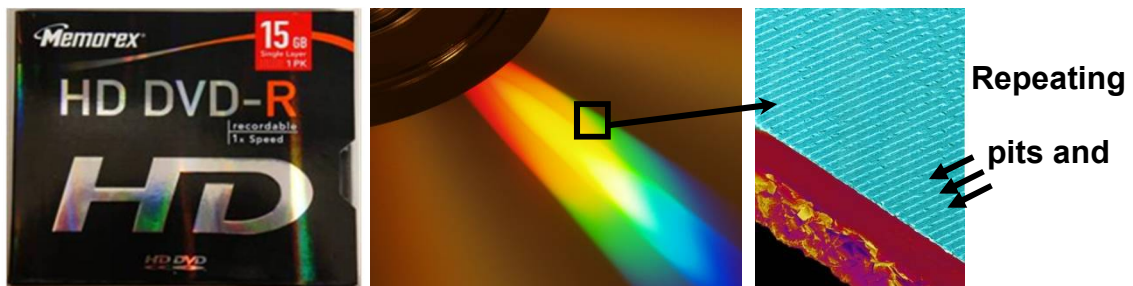


Figure 2-1. HDDVD and its underlying grating structure composed of repeating pits and ridges. Once exposed, the underlying gratings can be used as a master mold to transfer the grating structure to more research-friendly media, such as glass microscope slides and silicon wafers. As previously shown in equation (1.19), the coupling light to a plasmonic grating largely depends on the permittivity of the dielectric/metal layers as well as the grating period. If converted into plasmonic gratings, this wide range of grating periods available enables the coupling of light from deep ultraviolet (UV) through the visible spectrum to the infrared (IR). The robust design of optical media is such that it is typically difficult to gain access to the grating layer of the

disc. However, we have developed a method of quickly and efficiently gaining access to this layer which is described in the next section. Additionally, the process can be applied to other types of optical media, for example, CDs and DVDs, which provides a much greater selection of grating pitches for this research. Table 2-1 has been provided with the different gratings present in various optical media.

	CD [47]	DVD [48]	HDDVD	Bluray
Grating Period (Λ)	1600 nm	700 nm	400 nm	320 nm
Grating Height (H)	140 nm	140 nm	55 nm	33 nm

2.2. HD-DVD and Bluray Disc Preparation

For this project, HDDVDs and Bluray discs were selected as the optical media of interest as the shorter grating periods found on these discs can optimally couple light from UV to the near-IR. Due to the differences in disc construction as seen in Fig. 2-2, a separate method is needed to remove the dye and metal layers and leave behind the polycarbonate surface.

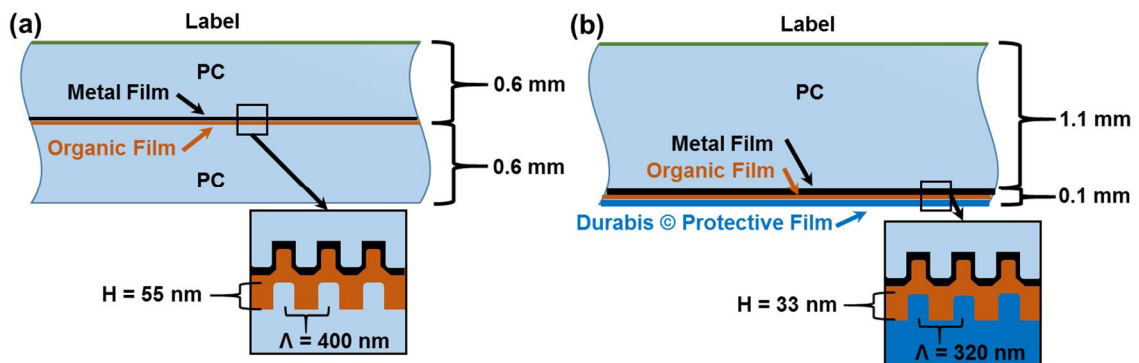


Figure 2-2. (a) HDDVD and (b) Bluray disc cross-sections with the grating period (Λ) and height (H) listed. The laser-writable organic dye film found in LTH Blurays is soluble in IPA whereas HTL Bluray discs use an inorganic dye film typically made from copper and silicon. The metal films for Bluray discs are composed of silver and either aluminum or silver for HDDVDs. PC: Polycarbonate.

The spacing of a grating structure or grating pitch used in surface plasmon resonance (SPR) plays a critical role in the formation of surface plasmon polaritons (SPP). In the previous report, we developed a process for replicating HD DVD gratings that have a 400 nm pitch. We have expanded the capabilities of our process to include the replication of Blu-ray discs that have a pitch of 320 nm. By decreasing the grating pitch to 320 nm, we can blue-shift the light coupling range to lower wavelengths than HD DVD gratings. This significant expansion in coupling range enables the use of UV, blue, and green fluorescent dyes, dyes that are commonly used in biological sensing. Additionally, the incorporation of Blu-ray gratings further reduces the expense of μ -contact stamping process as Blu-ray discs are ~\$1 per disc while HD DVD discs cost ~\$10/disc and are being phased out of the consumer market.

A Memorex HDDVD can be converted to a polycarbonate disc with exposed gratings via the following protocol.

- 1) A razor blade is held perpendicular to the edge of the disc and is scraped around the circumference of the disc to remove the protective sealant. The sealant forms a powder when scraped whereas the polycarbonate forms ribbons. Care should be taken to avoid removing too much polycarbonate or rounding the edge.
- 2) The razor blade is carefully inserted ~1 mm between the two halves of the disc and slid along the edge to separate the edges of the two halves.
- 3) The two halves are then peeled away from another in a circular motion working towards the center of the disc and pulled apart once the center is

all that remains attached. Care should be taken to ensure that the metal/reflective film remains on the disc half with the label.

- 4) The transparent half should then be placed grating side up in a recrystallization dish (125 mm diameter) and rinsed in ~50 mL of pure isopropanol for 2 min. The labeled half of the disc can be discarded.
- 5) The isopropanol should be drained away and replaced two times or until the rinse solution and disc are no longer orange in color.
 - a. If a large section of the transparent half of the disc is covered with the metal film, the disc can be soaked in 15% nitric acid in a sonicator for 10 min. Replace the solution after 10 min. or move to the next step if the metal film is no longer present. Note: higher concentrations of nitric acid may damage the polycarbonate disc.
- 6) The disc half should be rinsed with a copious amount of DI water and blown dry with a stream of nitrogen or compressed air. Visually inspect the disc to ensure no streaks of solvent or metallic particulate remain. Repeat the DI water rinse if streaks are present or repeat steps 4 and 5 if particulate is observed.

The result of this process is a ~0.6 mm thick polycarbonate disc with gratings exposed on one side that is ready for casting in PDMS (described in the following section). As previously noted above, the processing for a Blu-ray disc is different from that of an HDDVD as the metal layer must be chemically removed, as opposed to physical removal during the peeling of the HDDVD halves.

The protocol for the Bluray disc (6x LTH) process has been provided below. It should be noted that the process is designed for a 6x LTH Bluray, HTL Bluray discs have inorganic writable films that will not be removed in this process. Memorex 4x LTH Bluray discs have a reduced average grating height of 24 nm.

- 1) A razor blade is held perpendicular to the edge of the disc and is scraped around the circumference of the disc to remove the protective sealant. The sealant forms a powder when scraped whereas the polycarbonate forms ribbons. Care should be taken to avoid removing too much polycarbonate or rounding the edge.
- 2) The side opposite the disc label has a scratch resistant coating (~0.1 mm thick) that is typically made of Durabis ©. The film can be removed by first gently rubbing the edge with a finger around the entire disc until the edge of the film begins to roll away from the disc.
- 3) The film should then be peeled towards the disc center and removed in a single piece. Note: The film is easily torn when folded and can leave small pieces behind on the disc.
- 4) The disc must be sonicated in 200mL of 15% nitric acid for 10 min. in a 125 mm diam. recrystallization dish. The solution should be replaced at least once and sonicated for another 10 min. or at least until the metal film has been removed.
- 5) The disc half should be rinsed with a copious amount of DI water and blown dry with a stream of nitrogen or compressed air. Visually inspect the disc to

ensure no metallic particulate remains. Repeat step 4 or rinse again in DI water if the user observes particulate.

Following the processing of both discs, a commercial Innova AFM system was used to obtain the surface profiles of the gratings. The surface profiles shown in Fig. 2-3 are from a cleaned Blu-ray disc and an HD DVD. The grating dimensions of the HD DVD were confirmed to have a pitch of $\Lambda = 400$ nm and a grating height of $h = 60$ nm while the Blu-ray grating had a pitch of 320 nm and a grating height of 33 nm.

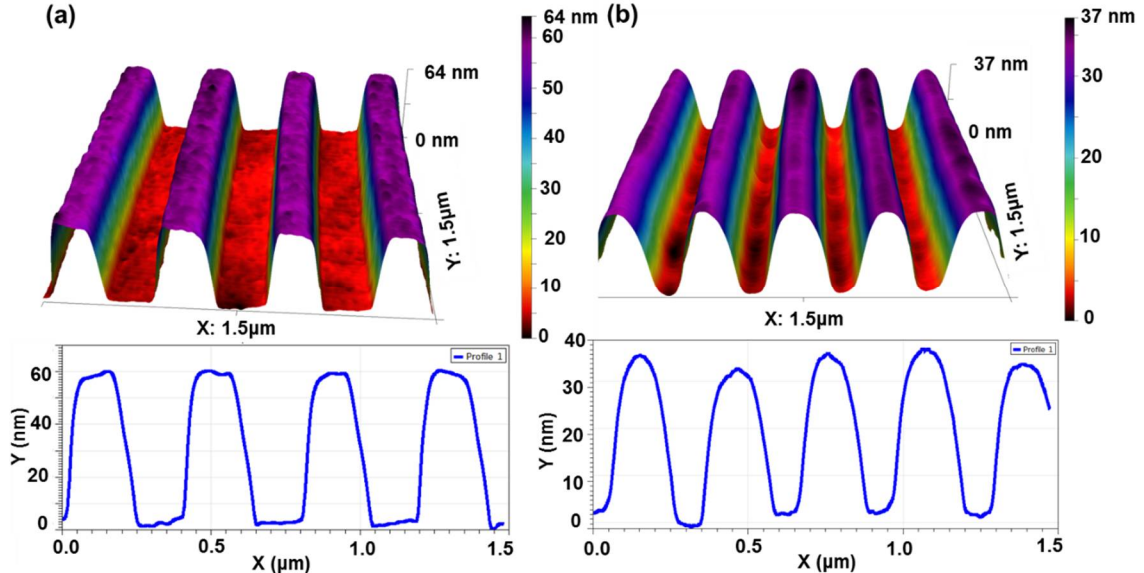


Figure 2-3. 3D rendering of the surface of polycarbonate gratings and corresponding 2D topographical profiles below for (a) HD DVD and (b) 6x LTH Blu-ray disc obtained through AFM.

2.3. Polydimethylsiloxane (PDMS) Stamp Fabrication

Once the optical media has been rendered to a PC master mold, it can be cast using polydimethylsiloxane (PDMS), a type of silicone rubber, and be used as a “stamp” in a μ -contact lithography process. This polymer is also heavily utilized in the semiconductor and microfluidic industries for its ease of casting it into various

shapes and its capability to conform to micro/nano-scale features. As the PDMS will be used as a “stamp,” the flexibility of the stamp can play a critical role in the defect-free release of the ink onto the glass slide or silicon wafer. The flexibility of the PDMS is dependent on the degree of crosslinking which is influenced by the base:curing agent ratio, relative humidity during curing, and the temperature. To better understand the crosslinking of PDMS, the chemical structure of the components need to be understood.

The most common formulation of PDMS sold to researchers is Sylgard-184 PDMS (Gelest, Inc.) and has four main components: base resin, resin accelerator, curing agent, and a platinum catalyst. Upon mixture of these components, the “base resin,” dimethyl vinyl-terminated dimethylsiloxane, reacts with the crosslinking agent, tetra(trimethyl siloxy)silane, in the presence of a platinum catalyst, such as the Karstedt’s catalyst (H_2PtCl_6), via the hydrosilylation reaction seen in Fig. 2-4.[49] The presence of silica fillers in the base mixture of 184-Sylgard ensures a certain degree of uncrosslinked PDMS.

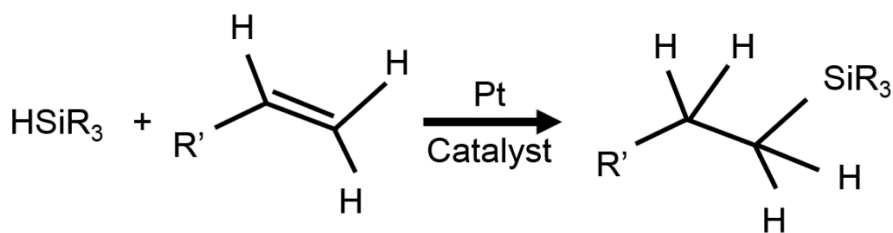


Figure 2-4. General hydrosilylation reaction diagram.

While platinum is the primary catalyst for this reaction, water, in the form of vapor in the air, is also necessary to the progression of crosslinking. If curing PDMS below 30% relative humidity (RH) or in a vacuum desiccator, crosslinking times

can be extended substantially and even prevent crosslinking altogether. Thus it is crucial that the RH be well controlled during crosslinking to obtain reproducible mechanical properties. For this research, a custom humidity control chamber was constructed that maintained the RH between 60-65%.

Several Base:curing agent ratios were used in the fabrication of mechanical testing samples to determine the Young's modulus of elasticity of PDMS. All samples were cured over 72 hours at 60% RH and 25°C before testing. Semicircular 4 cm diameter punches were made at the center of rectangular samples (1.5 cm x 4 cm) to form a stress concentration and loaded onto the Instron machine. The resulting tensile loading plots have been provided in Fig. 2-5(a). Young's modulus or the stress divided by the strain of the sample was extracted for each base:curing agent sample and plotted in Fig. 2-5(b). Other mechanical properties have also been provided in Table 2-2.

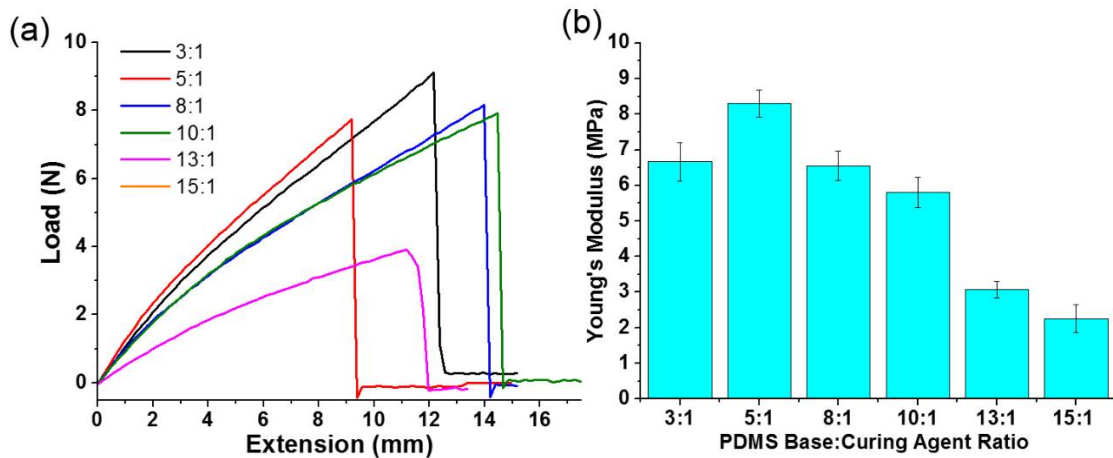


Figure 2-5. Tensile loading results for PDMS samples with different base:curing agent ratios. (b) Young's modulus of elasticity for samples tested in (a).

PDMS Ratio (Base:Curing Agent)	Young's Modulus (MPa)	Max Tensile Stress (MPa)	Max Tensile Strain (%)
3:1	6.664	0.910	16.521
5:1	8.303	0.684	15.865
8:1	6.551	0.741	17.413
10:1	5.811	0.544	21.086
13:1	3.072	0.264	14.148
15:1	2.253	0.244	16.676

A bell curve relationship was found between the PDMS curing ratio and Young's modulus where the ratio with the least ductile PDMS was 5:1. The other PDMS ratios exhibited lower Young's moduli which was caused by either extra cross-linking agent or uncrosslinked or partially crosslinked base trapped in the cured PDMS matrix. There was a similar relationship between the PDMS ratio and maximum tensile stress of the PDMS, where PDMS made from ratios greater than 5:1 resulted in a weaker stamp. However, a trend was not observed between the PDMS ratio and maximum tensile strain. The trend may not be visible due to the large standard error in each measurement likely caused by slipping of the instron grips during loading.

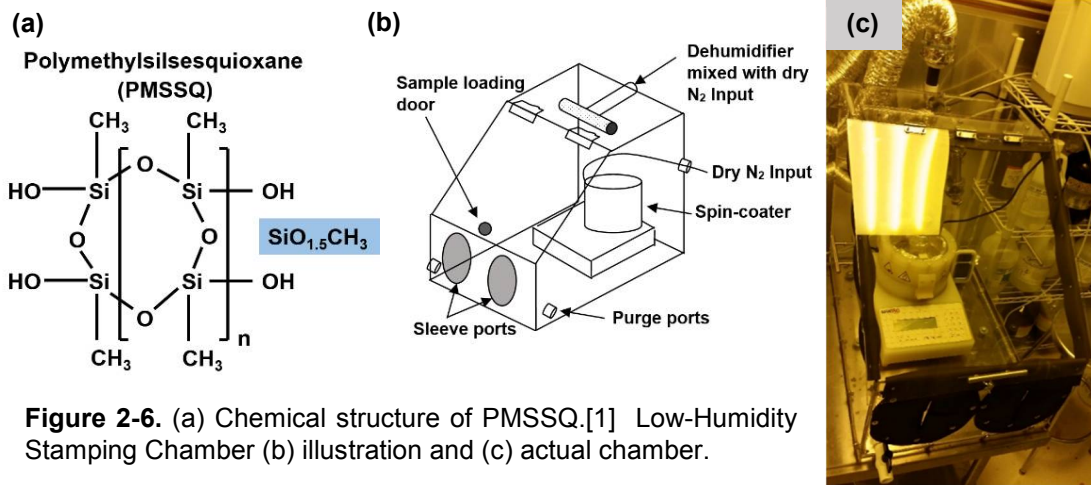
PDMS Stamp Formation: Several PDMS curing ratios (3:1, 5:1, and 10:1) were used to cast PDMS stamps on the PC discs obtained in the previous section. Based on prior research, the ideal stamp thickness ranges from 0.5 to 1 mm. Stamps in this thickness range can be obtained by casting a disc with ~12 grams of PDMS. The process for casting PDMS stamps has been detailed in the protocol below:

- 1) 12 grams total of PDMS should be prepared to cast a single disc in a plastic weigh boat. For example, weigh 10 grams of PDMS base and add 2 grams of curing agent to obtain a 5:1 ratio.
- 2) The base and curing agent must be vigorously mixed for 5-10 min. with a pipette tip. The liquid PDMS should be mixed until an abundance of small bubbles are trapped in the PDMS, and the viscosity appears homogenous.
- 3) The weigh boat with PDMS is placed in a vacuum desiccator for 15 min. Note: The liquid PDMS and bubbles may expand and overflow from the weigh boat. If the PDMS does rise to the edge of the boat, the pressure should be throttled to pop the bubbles then placed back under vacuum.
- 4) After desiccation, the PDMS is poured over the disc in a circular pattern. The weigh boat should be brought close to the disc surface during pouring to avoid bubble formation.
- 5) The discs coated in PDMS are placed in a humidity control chamber (25°C, 60% RH) and left to cure for at least 48 hours.

2.4. Polymethylsilsesquioxane (PMSSQ) Grating Fabrication

The next step after fabrication of the PDMS stamp is to transfer the grating pattern to a more stable surface, such as a glass microscope slide or a silicon wafer. A common method of accomplishing this is through micro-contact lithography which replicates the negative profile of the PDMS stamp using a polymer “ink.” The “ink” used in this process is an organo-silicate polymer known as polymethylsilsesquioxane (PMSSQ). As seen in Fig. 2-6(a), PMSSQ has a silica (SiO₂) backbone with several CH₃ groups that form voids and OH groups that

enable crosslinking. An advantage, and disadvantage of sorts with PMSSQ, is that when exposed water, it rapidly crosslinks. This is advantageous when used as an “ink” as it will quickly solidify and preserve the stamp profile. However, while PMSSQ’s reactive nature with water ensures rapid crosslinking, this makes it difficult to work with in high humidity environments as the working time can be unmanageable.



The inherent sensitivity to water makes it important to have fine control over the humidity at which stamping occurs. The class-100 cleanroom used in this research is susceptible to outdoor fluctuations in relative humidity (RH) which results in a RH between 50-60% in the summer and ~30% in the winter. During the development of the stamping process, it was found that stamping must occur between ~15-35% RH to have a suitable working time (~6 sec.) Above 35% the working time reduces to < 3 sec after removal from the spin-coater and has poor binding to the substrate if performed in a nitrogen purged environment (<10% RH). We obtained better control over the RH through the design and construction of a

transparent humidity control chamber that did not interfere with the dexterity of the user (see Fig. 2-6(b,c)). Using this chamber, the stamping environment was maintained at a RH and air temperature of 20-30% RH and 31°C, respectively. The RH and air temperature in the cleanroom was 57% and 22°C, respectively.

The thickness of the PMSSQ stamp is another critical parameter for accurate replication of the grating pattern. This was optimized using several different %wt. solutions of PMSSQ dissolved in pure ethanol. The spin-coated thicknesses as well as the refractive indices were found using spectroscopic scans with the VASE and provided in Fig. 2-7.

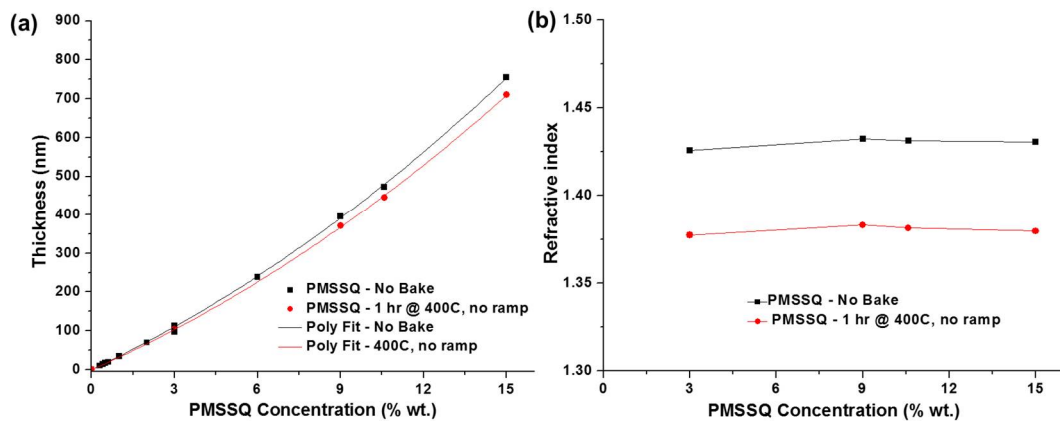


Figure 2-7. (a) Measured and modeled thicknesses and (b) refractive indices for spin-coated PMSSQ films at varying %wt. in pure ethanol with and without curing at 400°C for 1 hour.

*Polynomial fit: PMSSQ - No bake ($Y=33.47808x+1.11497x^2$, $R^2 = 0.9998$), PMSSQ - 400°C bake ($Y=31.2076x+1.06846x^2$, $R^2 = 0.9999$).

Utilizing the thickness plot in Fig. 2-7(a), the 3%wt. solution was selected as the ideal stamp thickness as it is ~2x thicker than the maximum grating feature (55 nm) and provides an adequate thickness to planarize surface imperfections on rougher substrates such as a glass slide. The process for making a PMSSQ

solution, cleaning substrates, and transferal of the grating structure to these substrates has been detailed in the following protocol and illustrated in Fig. 2-8.

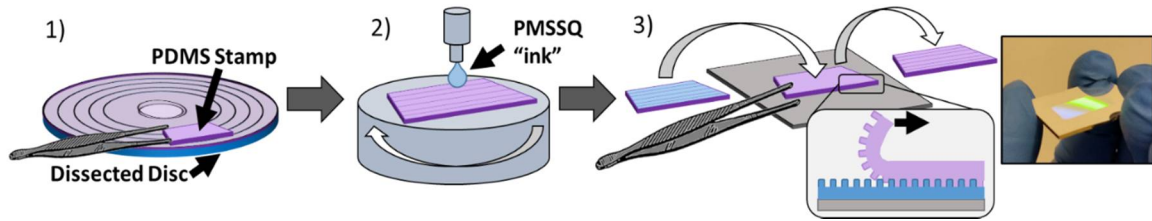


Figure 2-8. Soft lithography process diagram. 1) Cut and remove the PDMS stamp pieces from the disc mold; 2) spin coat PMSSQ “ink” solution onto the PDMS stamp; 3) stamp and peel off the PDMS onto a glass slide or silicon wafer.[42]

PMSSQ “ink” Solution Preparation:

- 1) Add 9.7 g of 200 proof ethanol to a glass 20 mL scintillation vial.
- 2) Weigh out 0.3 g PMSSQ and add to the 200 proof ethanol. PMSSQ aliquots are stored at -18°C and must be warmed to room temperature before opening the container to reduce water contamination.
- 3) The solution is sequentially vortexed for ~ 2 min. and sonicated for ~ 3 min.
- 4) The solution should be stored at -18°C and must be used the same day it was made.

Glass Cleaning Process:

- 1) Glass samples are cut from a microscope slide in 1.5 cm x 1 cm pieces.
- 2) All samples are sequentially sonicated in acetone, methanol, and DI water (AMD) for 5 min. each.
- 3) All samples are placed in a 3:2 Sulfuric acid to hydrogen peroxide (Piranha) solution for 15 min. This removes any remaining organic contaminant and results in a pristine glass surface. Note: Piranha, also known as Jesse’s

solution, is extremely dangerous and should only be handled with the utmost care by trained personnel.

- 4) Samples are rinsed thoroughly in DI water and dried under a stream of nitrogen. Note: Any remaining particulate present on the surface should be removed by sonication in DI water as it can prevent stamp adherence.

Silicon Wafer Cleaning Process:

- 1) Silicon samples are cut from a silicon wafer in ~1.5 cm x ~1 cm pieces.
- 2) All samples are sequentially sonicated in acetone, methanol, and DI water (AMD) for 5 min. each.
- 3) All samples are placed in a 1:10 hydrofluoric (HF) acid to DI water solution for 10 min. This solution etches the native oxide layer and results in a pristine silicon surface. Note: HF, even when diluted, is extremely dangerous and should only be handled with the utmost care by trained personnel.
- 4) The samples are rinsed in DI water and placed in a hot water bath (90°C) for 1 hour to grow a very thin SiO₂ layer. PMSSQ solution adheres to hydrophilic surfaces better than hydrophobic surfaces.
- 5) The samples are then dried under a stream of nitrogen. Note: Any remaining particulate present on the surface should be removed by sonication in DI water as it can prevent stamp adherence.

Micro-contact Lithography Process:

- 1) The nitrogen line connected to the dehumidifier output is opened and allowed to flow for at least 20 min. or until the chamber humidity is <25%.

- 2) Glass and silicon substrates, spare cleaning cloths, syringes, filters, tweezers, and PMSSQ “ink” solutions can be loaded into the chamber at this time.
- 3) The 0.2 μm PTFE syringe filter is primed with 1 mL of “ink” solution and then filled with 1 mL of fresh “ink” solution. This amount of solution is typically sufficient to make 3 gratings.
- 4) A stamp is cut from either an HDDVD or Bluray disc mold with a razor blade in the shape and locations seen in Fig. 2-9. The stamp is placed grating side up onto a 2 cm x 2 cm piece of clean silicon and secured to the spin-coater chuck with vacuum.

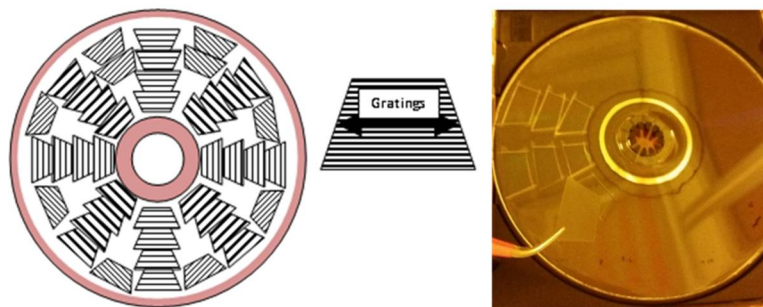


Figure 2-9. Stamp cut pattern for easy identification of grating alignment post stamping.

- 5) The spin-coater chamber is closed, and the chamber is purged with nitrogen for ~30 sec. while the top access port is sealed with the palm of the user’s glove.
- 6) Nitrogen flow is stopped and ~300 μL of the PMSSQ “ink” solution is dripped onto the stamp from the upper port until the solution covers the entire stamp. The spin-coater program is immediately activated with the following

parameters: 3000 RPM for 30 sec. with a 1000 RPM/sec. ramp-up and ramp-down rate.

- 7) Once the program has finished, the stamp is removed with a pair of tweezers and placed grating side down onto the substrate. This step should be conducted as quickly as possible (~5-6 sec.) to reduce PMSSQ crosslinking prior to stamping. The PMSSQ should quickly “wick” across the surface.
- 8) After the stamp has been in contact for 5-8 sec., remove the stamp by lifting one corner of the stamp and peel in a diagonal direction while lifting. Repetitive bending of the stamp should be avoided as it reduces the lifetime of the PDMS and the quality of the PMSSQ grating. A single PDMS stamp can typically stamp 5-10 defect-free PMSSQ gratings.
- 9) The PMSSQ stamp diffraction pattern should be intense and uniform. The color of the stamp, best observed on silicon, should be dark blue in color, which indicates a thickness is 150-250 nm. Gratings with bubbling, diffraction pattern warping, portions of non-adherence, debris, or sky/light blue in color (PMSSQ is too thin) should be discarded.
- 10) Steps 5-8 are repeated for all substrates, and the PDMS stamp is replaced as necessary.

While PMSSQ is excellent at reproducing gratings, it was found that the structure completely degraded over a period of 6 months even when stored in a pure nitrogen environment. To halt the short and long term structural degradation, A 1:1 mole ratio of (3-aminopropyl)triethoxysilane (APTES):PMSSQ was added to

the stamping solution to crosslink the PMSSQ structure. The ethoxy silane group of the APTES reacts with the -OH groups of the PMSSQ to further crosslink the film with Si-O-Si bonds. The structure was further cross-linked by heating the substrates at either 60°C for 20 minutes, 120°C for 20 min., or heated to 400°C at 1°C/min., baked for 1 hour, then cooled to room temperature. The surface energy of the PMSSQ/APTES films was quantified using contact angle measurements for each heating process to determine the process that resulted in a stabilized surface energy. The resulting surface energies have been provided in Table 2-3.

Film Type	Contact Angle Fluids	No Heating	60°C for 20 min on hotplate	120°C for 20 min on hotplate	Ramped to 400°C in furnace (1°C/min., 1 hr. duration)
3% PMSSQ film	1) DI H2O 2) DIM 3) FORM Contact Angle (°)	79.45 ± 1.23 68.98 ± 0.46 56.73 ± 0.10	88.48 ± 1.42 67.92 ± 0.32 59.03 ± 0.13	88.62 ± 0.53 69.17 ± 1.197 72.65 ± 0.66	106.38 ± 1.57 70.57 ± 0.16 88.85 ± 0.48
	Dispersive (dyne/cm)	25.73 ± 2.33	28.97 ± 4.97	22.03 ± 1.27	20.47 ± 2.13
	Polar (dyne/cm)	8.43 ± 1.63	4.90 ± 2.38	4.17 ± 0.72	0.43 ± 0.296
	Total Surface Energy (dyne/cm)	<u>34.17 ± 1.39</u>	<u>33.87 ± 3.53</u>	<u>26.20 ± 0.75</u>	<u>20.90 ± 1.85</u>
3% PMSSQ film + 1:1 mole APTES	1) DI H2O 2) DIM 3) FORM Contact Angle (°)	88.63 ± 0.11 69.08 ± 0.64 80.93 ± 0.42	93.52 ± 0.73 70.95 ± 0.91 77.78 ± 0.49	91.57 ± 0.52 70.40 ± 0.29 76.62 ± 0.42	103.45 ± 0.22 69.82 ± 0.38 88.67 ± 0.29
	Dispersive (dyne/cm)	19.07 ± 4.33	20.83 ± 1.47	20.97 ± 1.73	20.00 ± 3.00
	Polar (dyne/cm)	4.83 ± 2.65	2.80 ± 0.69	3.37 ± 0.87	0.90 ± 0.62
	Total Surface Energy (dyne/cm)	<u>23.90 ± 2.17</u>	<u>23.63 ± 0.93</u>	<u>24.33 ± 1.05</u>	<u>20.90 ± 2.41</u>

*Note: The surface tension (dyne/cm) values used in the model: DI water (Dispersive: 22.10, Polar: 50.70), Diiodomethane (Dispersive: 50.80, Polar: 0.00), Formamide (Dispersive: 39.50, Polar: 18.70).

It was found that the PMSSQ/APTES surface energy remained low and relatively constant despite the different heating steps whereas the PMSSQ film alone was unstable without heating but stabilized after 400°C annealing. Higher ramp rates resulted in polymer flow and flattening of the grating structure as confirmed with AFM. Unfortunately, gratings made with PMSSQ solutions with 1:1 mole APTES developed a white film over the entire grating after 1-2 weeks in a desiccator chamber. The formation of this white film, thought to be caused by excess APTES in the PMSSQ film, resulted in significant grating height variability. As the objective was to fabricate stable PMSSQ films that accurately reproduced the grating structure, the process was adapted to expose the PMSSQ gratings to a saturated vapor of APTES for 1 hour. The vapor process achieved the same surface energy results as the solution APTES but did not develop a white film even after 3-4 weeks in a nitrogen desiccator. The vapor treatment process has been detailed below:

- 1) A 1:1 pure ethanol to APTES solution is made in a low humidity environment. 1.5 mL ethanol is added to a 20 mL scintillation vial and, after all PMSSQ gratings are stamped, 1.5 mL APTES is added to the vial and vortexed for ~1 min.
- 2) All PMSSQ grating samples are arranged in a circular pattern around the Ethanol/APTES vial as seen in Fig. 2-10(a), the vial is uncapped, and the chamber is sealed.
- 3) The house vacuum line is connected to the water trap (Fig. 2-10(b)) and slowly opened to evacuate the trap pressure while the vacuum chamber is still closed.

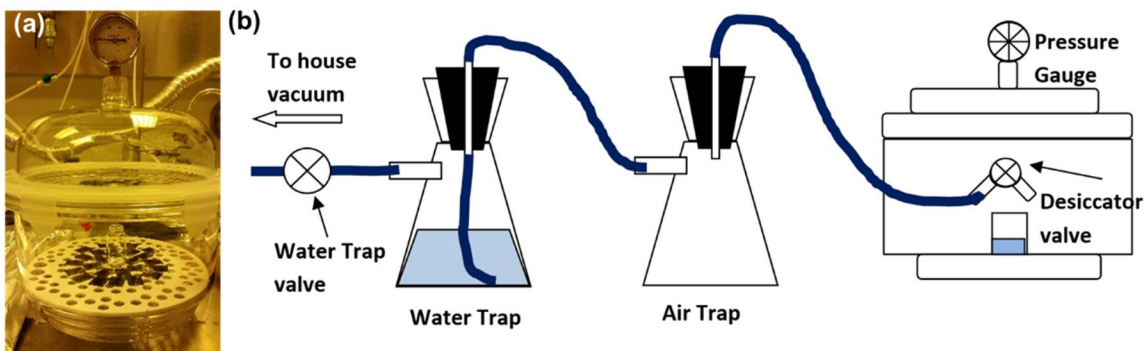


Figure 2-10. (a) Vapor treatment chamber and (b) Illustration of the water and air traps connected to the vapor treatment chamber.

- 4) The desiccator valve is opened to the vacuum slowly and left open until the chamber pressure is -81 kPa (typically ~ 2 - 3 min.) The chamber is then sealed, and samples are left to incubate in the vapor for 1 hour.
- 5) The chamber is slowly opened to atmospheric pressure and fully vented.
- 6) The samples are removed from the chamber and placed on a hotplate for
 After vapor treatment, the PMSSQ gratings must undergo additional heat treatment to stabilize the grating structure. The process for heat treating the gratings has been provided below.
 - 1) All PMSSQ grating samples after vapor treatment are placed on a hotplate set to 60°C for 3 hrs.
 - 2) The samples are then transferred to a silicon wafer as seen in Fig. 2-11 and placed on a high-temperature hotplate with the following settings: Ramp to 400°C at $5^{\circ}\text{C}/\text{min.}$, remain at 400°C for 1 hr., then shutdown to cool samples to 25°C (typically ~ 12 hrs.)

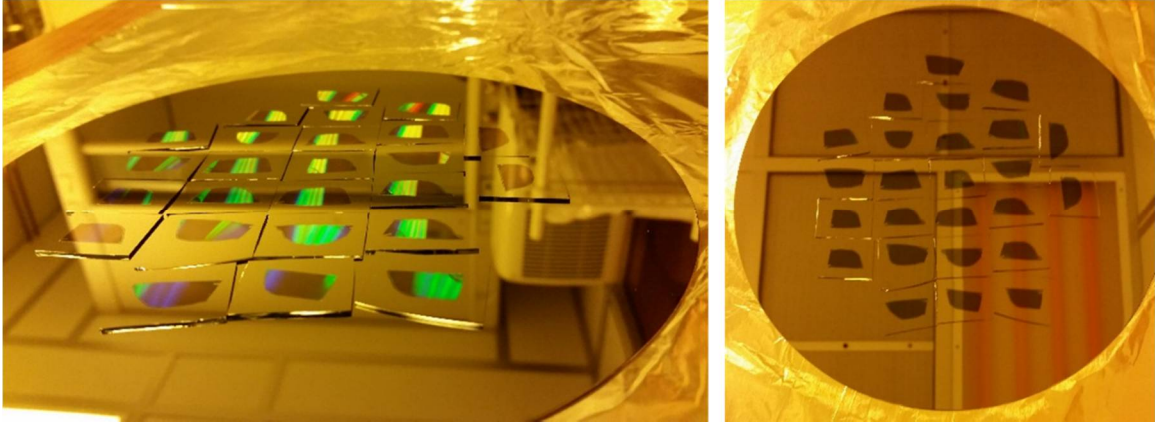


Figure 2-11. PMSSQ gratings on silicon wafer before loading onto the high-temperature annealing plate.

2.5. Metallization and Protective Capping of the Grating

The PMSSQ gratings fabricated in the previous section must be metallized to enable to the formation of SPR and SPCE. Two physical deposition methods were used in this research to deposit metal films: Thermal evaporation and RF/DC sputtering. These methods and the process for depositing a metal film will be explored in this section as well as a separate deposition process, atomic layer deposition, used to deposit a protective ceramic film post metallization. A comparison between the resulting metallic gratings and their corresponding SPR-based fluorescence enhancement in Chapter 3.

Thermal evaporation: This metal deposition method can be used to rapidly deposit materials with melting temperatures much less than the resistive boat or rod used to evaporate the target material, typically made from molybdenum (melt temp.: 2,623°C) or tungsten (melt temp.: 3,422°C). The materials that can be deposited with this method include chromium, silver, and gold. Typically high wattage power supplies are required to deposit materials with higher melting

temperatures, such as platinum or titanium. To deposit these materials, a small lump or pellet of the material is placed in the well of the tungsten boat and the chamber (Fig. 2-12(a,b)) pressure is pumped down to 10^{-8} Torr. High electrical current is run through the boat which generates enough heat to melt the metal pellet as seen in Fig. 2-12(c). The first heating step is performed with a shutter blocking the flux of metal from impinging on the samples as the pellet may have oxides or other contaminants. Many contaminants will burn and be released upon initial melting. The shutter is removed after the metal pellet has been allowed to cool such that it is no longer depositing material and the boat is reheated to begin deposition on the samples mounted above the boat as seen in Fig. 2-12(d).

The distance, L , between the samples and boat is a fixed, but critical, parameter that must be shorter than the mean-free path, or the distance traveled by a moving particle between successive impacts with other particles, to obtain a high-quality metal film. The mean-free path, primarily determined by the vacuum pressure of the chamber, as seen in equation (2.1).[50]

$$\lambda = \frac{RT}{\sqrt{2}\pi d^2 N_A P} \quad (2.1)$$

Where T is the temperature, R is the gas constant, d is the molecular diameter (3.2 Å for silver), N_A is Avogadro's number, and P is the pressure. As distance L is ~27 cm for the chamber used in this research and very high-quality films are desired, the vacuum pressure must be $<10^{-7}$ Torr before deposition. Attaining

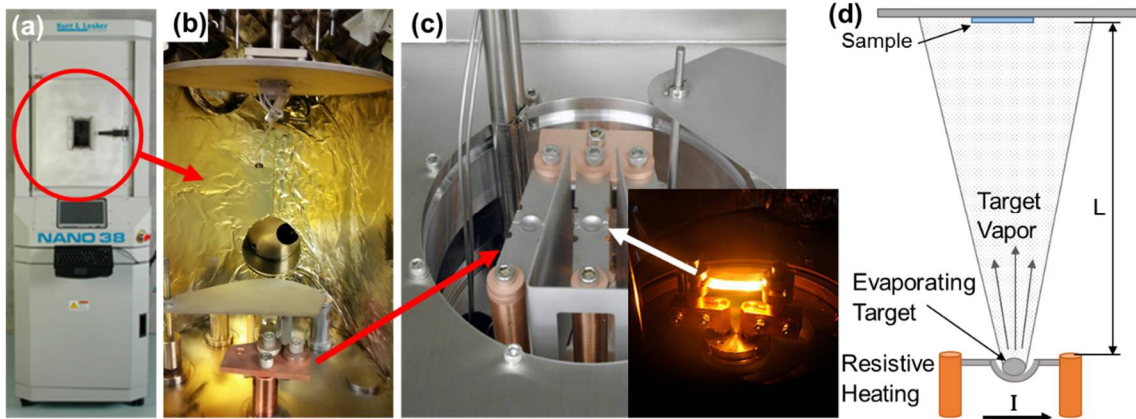


Figure 2-12. (a) Kurt J. Lesker Nano38 thermal evaporation chamber with and (b) an image of the deposition chamber and (c) the resistive boats before and during heating (images courtesy of Kurt J. Lesker Company or Creative Commons BY-SA 4.0.) (d) Thermal evaporation illustration of the resistive heating, evaporation of the target material resulting in a plume of material that is deposited on the sample at distance L above the well.

such low vacuum pressure typically requires the use of a turbomolecular pump with an attached roughing pump.

The rate at which material is deposited is primarily controlled using the power applied to the boat in % of maximum power output. Two methods of evaporation were used in this research, a stepped deposition and a rapid deposition. Before the deposition of the desired metal in both methods, a thin (3-6 nm) film of either chromium or titanium is deposited to enhance the adhesion of the metal to the substrate. In a stepped deposition, the boat is heated until the deposition rate, monitored by a quartz oscillator calibrated to the specific material, reaches 0.1 Å/sec. A total of 10 nm of metal is deposited at this rate. The deposition rate is then increased to 0.45 Å/sec and used to deposit the remainder of the desired film thickness. This deposition method (black lines) can be observed in Fig. 2-13(a) and typically results in very smooth films. However, this method requires a longer deposition time which can lead to additional sample heating.

For a rapid deposition method (red lines), seen in Fig. 2-13(a), the deposition rate is immediately ramped to 0.55 Å/sec, and the entire film is deposited at this rate. While this method results in the fastest deposition, films are often rougher and may contain voids.

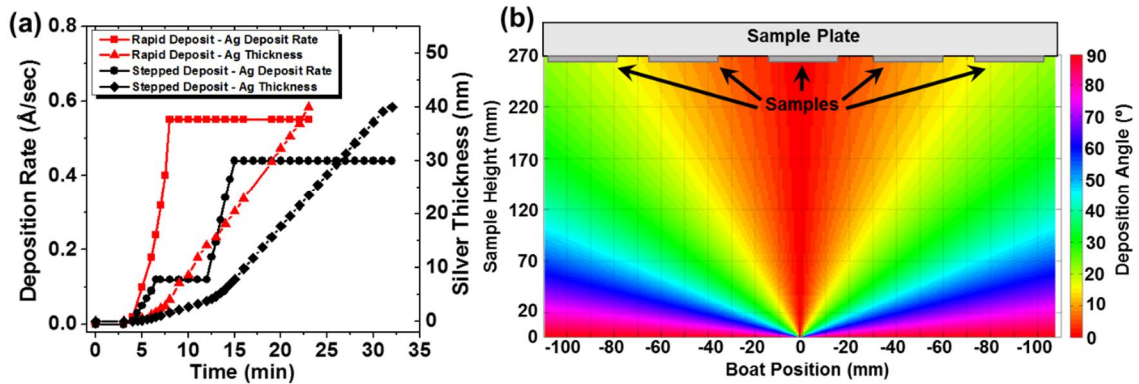


Figure 2-13. (a) Stepped deposition rate (black) and the film thickness of a 40 nm thick silver film in contrast to a (red) rapid deposition rate and the film thickness of a 40 nm thick silver film. (b) Heat map of the deposition angle from the middle boat evaporated onto samples located at sample height = 270 mm.

Another difference between thermal evaporation and other deposition methods is the shape of the deposition plume. For example, the evaporation source can be considered to be a point source where the flux of evaporated material spreads upward in a conical plume. The angle at which the metal flux will impinge on samples mounted at different locations on the sample plate can be modeled for a given distance L such as illustrated in Fig. 2-13(b). As the adatoms impinge the sample surface at specific angles, samples with complex shapes, such as circuits, may “shadow” or block certain locations from being coated. Additionally, the angular deposition model becomes much more complicated when multiple materials are being deposited from boats in different locations, such as the three boats seen in Fig. 2-12(c). The effect of the deposition angle can be reduced by

rotating the sample plate during deposition, for example, at 20 RPM in this research.

It is important to note that energy of the evaporated material is also different between thermal evaporation and sputtering. In thermal evaporation, the energy of the adatoms, or atoms that are adsorbed onto the surface of the sample, is much lower than sputtered adatom which can have a significant effect on the film properties which will be explored in greater detail in Chapter 3.

RF/DC Sputtering: Sputter deposition, unlike thermal evaporation, typically utilizes heavy, charged ions of an inert gas, such as argon, to bombard a target composed of the desired coating material. This bombardment ejects material from the target which is then deposited onto the samples located above the target. The rate at which material is removed from the target is the sputter yield Y which is defined as the ratio of ejected atoms to the number of incident particles or ions. An equation that describes the sputter yield has been derived by many authors including P. Sigmund, whose work has become a standard in the field of sputtering.[51] Based on his work, the sputter yield at low ion energy is:[52]

$$Y = \frac{3}{4\pi^2} \alpha \frac{4M_1M_2}{(M_1+M_2)^2} \frac{E}{U_s} \quad (2.2)$$

Where M_1 and M_2 are the masses of the bombarding ion and the target atom (in amu), E is the energy of the bombarding ion, and U_s is the surface binding energy. The term α is a dimensionless parameter that depends on the mass ratio and ion energy. At ion low energy and a mass ratio $(M_2/M_1) < 1$, $\alpha \approx 0.2$. In equation (2.2), the mass section $\frac{4M_1M_2}{(M_1+M_2)^2}$ describes the momentum transfer between the

bombarding ion and the target atom and is maximum when $M_1 = M_2$. This momentum must then overcome the surface binding energy holding the target atom to the surface and thus the yield is inversely proportional to U_s .

The ions used for bombardment are typically generated by igniting plasma between the target and the sample tray. To generate plasma, the chamber is first pumped down to a pressure of 5×10^{-7} Torr or lower, followed by the introduction of a noble gas, such as argon, into the chamber. A negative voltage, 2000-5000V, is applied to the target, i.e. the cathode, and a positive charge on the sample plate, i.e. the anode, which ignites plasma between the cathode and the anode, see Fig. 2-14(a). The electrons in the plasma bombard the noble gas atoms to form ions. The negative charge of the cathode attracts the positively charged ions towards the target which bombard the target and eject material. This method of sputtering is known as direct current (DC) sputtering and requires conductive target materials to avoid target charge build-up.

An alternative sputtering method uses radio frequency (RF) to ignite plasma and doesn't have the conductive target limitation of DC sputtering. The process for igniting plasma with RF is similar to DC in that the pressure is reduced to high vacuum and a noble gas is flown into the chamber. Unlike DC, high frequency, ~ 13.56 MHz, RF is supplied to the target and the sample plate, see Fig. 2-14(b). Rather than the direct bombardment of electrons to form ions in DC sputtering, the field generated in RF removes electrons from the noble gas to form ions. The rapidly changing field has a much stronger effect on the lighter mass electrons

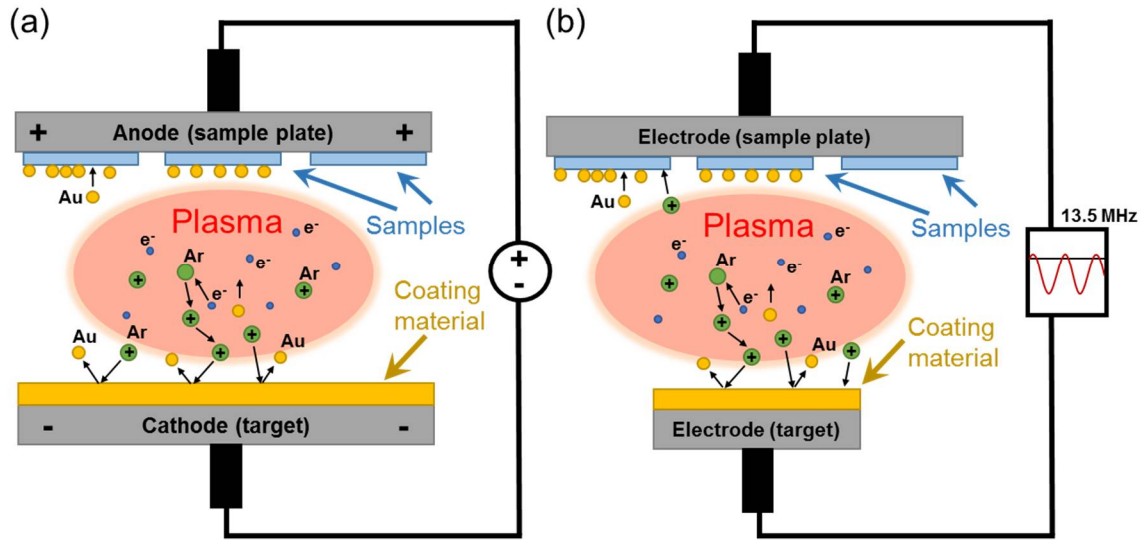


Figure 2-14. Simplified illustrations of (a) DC sputtering and (b) RF sputtering.

which respond nearly instantaneously to variations in the field. However, the larger mass noble gas atoms are inertially confined, i.e. the ion transit time is much less than the RF period, which tends to cause both the target and sample plate to form a negative charge. A neutral charge on both the target and sample plate is maintained by negatively offsetting the voltage applied such that the target and sample plate are positively charged for <1% of the RF period. It is important to note that voltage bias sputtering is necessary when using RF as the average negative voltage of the sample plate will result in ion bombardment of the samples. The substrate voltage can be reduced by increasing the relative size of the sample plate compared to the target where the area, A , and applied voltage, V , are related by:[52]

$$\frac{V_{target}}{V_{sample}} = \left(\frac{A_{sample}}{A_{target}} \right)^m \quad (2.3)$$

Where $m \approx 4$ would be ideal but typically ranges from 1.5 to 2 for most sputtering systems. One drawback to using RF sputtering deposition is that the deposition rate can be much slower than DC sputtering and other deposition methods, such as flash thermal evaporation. However, the higher energy of sputtered adatoms results in much more conformal and smoother films than thermally evaporated films.

For this research, sputtered films were deposited with an AJA International Inc, ATC-2000 V with the following parameters: Three-inch titanium and silver targets (99.999 % purity – Kurt J. Lesker) were mounted to two sputtering guns. Before deposition, the chamber was pumped down to 5.4×10^{-8} Torr and titanium and silver targets were pre-sputtered for 600 sec. at 100 W to clean the target and to remove any pre-existing oxide layer from the target surface. A 5 nm thick adhesion layer (germanium, titanium, or chromium) followed by a 100 nm thick silver layer was deposited with a 100 W RF power at a working pressure of 4 mTorr, ambient temperature (~ 300 K), six-inch throw distance, and 20 RPM sample rotation. Germanium and titanium were deposited at 0.1 nm/s while silver was deposited at 0.17nm/s.

Atomic Layer Deposition: While silver provides the lowest losses in the visible spectrum and correspondingly highest SPR intensities, silver is much more susceptible to corrosion or tarnish than any other noble metal. As the plasmonic gratings will be used in biosensor applications which typically involves immersion in phosphate buffered saline (PBS) and other biological fluids, the silver must be capped with a thin protective layer to prevent silver exposure to such solutions.

However, as SPR is extremely sensitive to minor variations in RI at the interface and the highest E-field intensity is close to the interface, the thickness of the cap should thus be minimized to have the least effect on SPR. The cap should be composed of a thin (<15 nm), optically transparent material that can conformally coat the silver film, such as alumina or silica. Films of this nature can be applied using a process known as atomic layer deposition or ALD.

ALD sequentially exposes samples to reactive chemical precursors to build a conformal film angstrom by angstrom. Silver-coated grating samples were sequentially exposed to water vapor and trimethylaluminum (TMA) in a low vacuum environment to grow an alumina (Al_2O_3) layer. The volume of the gas released in each step, exposure time of the samples to the gas, and chamber temperature (100°C) was calibrated such that a layer, 1\AA thin, of alumina was grown after one cycle, i.e. one exposure to water and TMA. For example, 100 cycles are needed to grow a 10 nm thick film. At the end of the process, the samples are exposed to 10 cycles of just water vapor to create a hydrophilic surface and to ensure that all of the TMA has been reacted.

2.6. Surface and Optical Characterization

As nanofabrication has improved over the past 20 years, so to have advances been made in the characterization of these nanoscale structures. In this research, three characterization techniques were used extensively to evaluate the surface and optical properties of plasmonic gratings including atomic force microscopy (AFM), variable angle spectroscopic ellipsometry (VASE), and fluorescence

microscopy. Each of these techniques will be introduced along with examples of their use on plasmonic gratings.

AFM Characterization: AFM is an invaluable tool for obtaining 3D topographical information about nanoscale structures. It can obtain this information using various scanning modes but all of the modes rely on a common element: the rastering or scanning of a nanoscale “tip” mounted on a deflectable cantilever over the sample to obtain information about the interaction of the tip with the sample. The interaction is monitored by an AFM via a laser reflecting from the top of the cantilever onto a photodetector.

Three general scanning modes are available with AFM: Contact, non-contact, and tapping mode. In contact mode, the tip is lowered onto the sample surface and brought into direct contact with the surface resulting in a measurable tip deflection. One advantage of this scanning mode is that the raw deflection measurements can be easily translated into the surface topography. However, this mode requires stronger and more durable tips which can be quite expensive. The scanning mode may also damage soft sample surfaces or drag nanoparticles across the surface. In contrast to contact mode, non-contact mode never makes physical contact with the surface. The tip is lowered onto the surface but stops once there is any attractive or repulsive forces between the tip and the sample. The height of the tip relative to the sample is modified to maintain the cantilever deflection maintained as it is scanned across the sample. The height adjustments can be directly converted into surface topography. This mode has the lowest chance of damaging the sample but typically results in the lowest resolution scan. The last scanning

mode, tapping, combines the previously discussed modes to obtain the advantages of both. The tip is mounted to a piezoelectric oscillator that oscillates at a frequency only a few Hz less than the resonant frequency of the cantilever and tip. The tip is lowered onto the surface until a minor deflection is detected. The tip is scanned across the sample while oscillating. One of many advantages to this scanning mode is that the tip deflection, relative tip height, phase, and amplitude can be measured and provide valuable information about the tip's interaction with the surface. As the tip oscillates, the tip experiences attractive and repulsive forces that are different than other materials. Thus when two separate materials are present in a scan, such as a metal nanoparticle on a polymer surface, the phase diagram can be used to differentiate the two materials. Two drawbacks of this mode are that it requires a separate scanning cartridge with a piezoelectric oscillator as well as a highly tuned frequency generator.

Due to AFM's ability to provide high resolution, topographical information, it was extensively utilized in this research to obtain surface information about nanoscale gratings. The surface information can be further analyzed using open-source software, such as Gwyddion, to obtain metallic grain sizes, grating height, pitch, and roughness.[53] For example, two Blu-ray gratings coated with 100 nm of silver with either RF sputtering (Fig. 2-15(a-c)) or thermal evaporation (Fig. 2-15(d-f)) were scanned using a commercial Innova AFM system (Bruker Corporation) in tapping mode with a Vista silicon tip ($k = 40 \text{ N/m}$, Resonant frequency = $\sim 295 \text{ kHz}$, length = $125 \text{ }\mu\text{m}$, width = $40 \text{ }\mu\text{m}$, tip height = $14 \text{ }\mu\text{m}$, tip radius $\leq 10 \text{ nm}$). Based

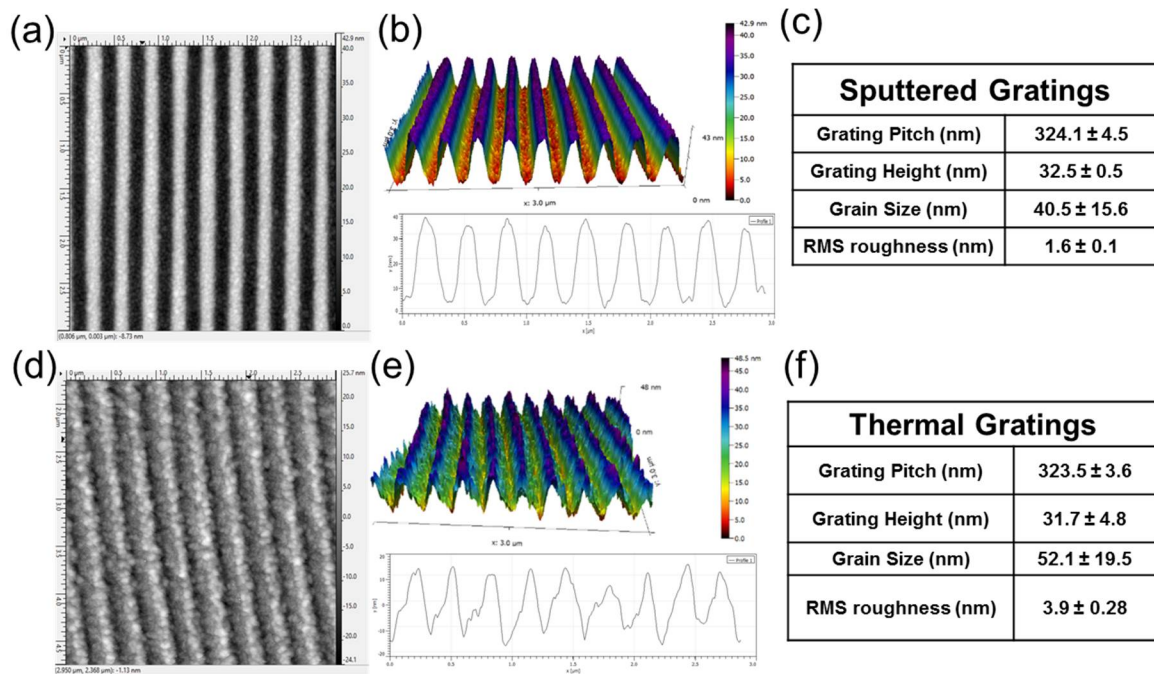


Figure 2-15. 2D topography rendering of a (a) 100 nm Sputter-coated silver and (c) 100 nm thermally evaporated silver Blu-ray grating. Corresponding 3D extrapolation and surface profiles for (b) 100 nm sputter-coated and (d) 100 nm thermally evaporated silver gratings.

on prior experience, better resolution scans are obtained when the tip is scanned in a direction perpendicular to the grating ridge orientation as this allows for the most interaction between the tip and the grating and reduces the blurring observed by scanning the steep edges of the ridges diagonally.

It is important to note that AFM is not a direct measurement of the surface topography, it is an interpretation of the tip interaction with the surface. While the actual surface topography may be very similar to the information provided by the tip interaction, the interpreted surface may include artifacts that are tip, scan, or calibration-based and must be critically evaluated before determining if a structure is actually present on the surface.

Variable Angle Spectroscopic Ellipsometry: As seen previously in Fig. 1-6, reflectivity and transmission measurements are critical to characterizing the light

coupling properties of plasmonic gratings. A J. A. Woollam Variable Angle Spectroscopic Ellipsometer (VASE) was used to conduct these measurements as it allows for finely controlled oblique illumination of samples at user-specified polarizations. The system is capable of detecting minor losses in intensity and changes in polarization after the incident light is reflected or transmitted through the sample.

In this research, the optical properties of gratings were characterized using a VASE in the reflectance mode with TM (P) polarized light incident on the gratings at different angles and wavelengths. This setup is comprised of a Xenon broadband source which directs light through a monochromator via an optical fiber. The light is made incident on the grating sample with the grating ridges aligned

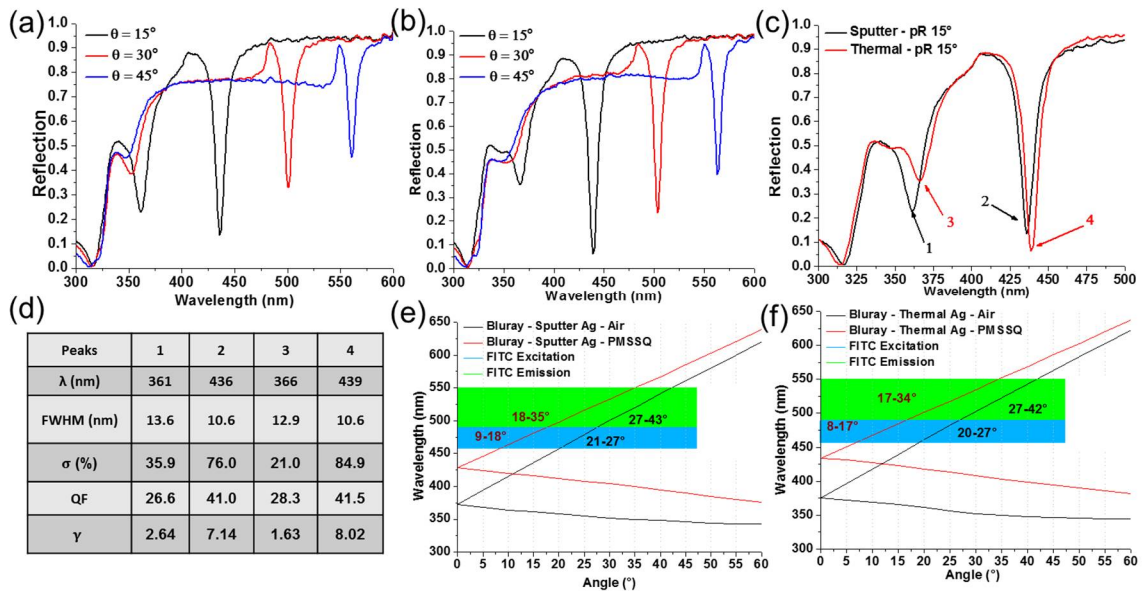


Figure 2-16. Measured reflectance spectra for (a) sputter-coated and (b) thermal evaporated Bluray silver gratings as a function of wavelength for three different incident angles (15°, 30°, and 45°.) (c) Comparison between the 15° reflectivity scans from sputtered and thermal gratings. (d) Table of calculated values for the labeled peaks in (c). SPR dispersion curves (with Air and with a 33 nm thick PMSSQ film on the gratings) with overlaid excitation and emission spectrum location for FITC.

perpendicular to the plane of incidence. The reflected light after reflecting from the silver grating substrate reaches the detector iris and is then passed onto a Si detector (spectral range: 200 nm – 2000 nm).

For example, the silver gratings observed in Fig. 2-15 were scanned in reflectance mode and the resulting data can be found in Fig. 2-16. Based on these reflectivity curves, the two absorption peaks due to SPR coupling can be observed for each incident angle. For every peak, several parameters can be extracted and compared including full width at half maximum (FWHM), peak height also known as coupling strength (σ), and peak wavelength. These parameters can be used to calculate quality factor (QF) and γ , which are defined as:

$$QF = \frac{\lambda}{FWHM} \quad (2.4)$$

$$\gamma = \frac{\sigma}{FWHM} \quad (2.5)$$

Both QF and γ (typically presented as $\gamma * 100$) are used to evaluate the peak shape, where QF is maximum for narrow peaks at longer wavelengths and γ is maximum for narrow, deep peaks. Additionally, an SPR dispersion curve can be calculated using the peak wavelength information as seen in Fig. 2-16(d,e). To determine the optimal coupling angle for SPR and the emission angle of SPCE, the excitation and emission wavelengths of the fluorescent dye fluorescein isothiocyanate (FITC) have also been added to the SPR dispersions. The angular intersection ranges for the silver grating with and without a 33 nm thick overcoat of PMSSQ have also been labeled on the dispersions. The purpose of this PMSSQ film is will be explained in section 2.7.

2.7. Fluorescence Characterization

Determining the SPR field strength of plasmonic gratings was previously demonstrated using FDTD simulations. However, one method of determining the SPR field strength as well as fluorescence enhancement of the grating can be accomplished using fluorescence microscopy. The fundamental principles of fluorescence microscopy, SPR excitation, and SPCE capture was previously explored in sections 1-5, 1-6, and 1-7. Therefore, this section will explore the experimental approach and measurement of fluorescence enhancement using plasmonic gratings.

Fluorescence studies were performed with silver Blu-ray gratings deposited with RF sputtering or thermal evaporation to examine the effect of the deposition methods on the fluorescence enhancement properties with FITC. FITC is a fluorescent dye (488 nm excitation / 519 nm emission) commonly used in biological imaging. FITC was chosen due to the match between the excitation spectrum and the Blu-ray gratings SPR dispersion.

Thin films of PMSSQ doped with FITC were spin-coated onto the gratings to evenly disperse the FITC molecules over the grating surface. Specifically, a 10 μM solution of FITC in a 1%wt. PMSSQ solution in ethanol was spin-coated onto the silver gratings at 3000 RPM for 30 sec. This process produced a thin film (~33 nm thick, RI: 1.41) of PMSSQ with dye molecules embedded in a polymer matrix. Dispersing the dye in a PMSSQ matrix also increases photo-stability and as the photo-bleaching time was much longer than dye molecules in organic solvents or DI water. From the SPR dispersion curves seen in Figure 2-16(e,f), the excitation

spectra of FITC couples at incident angles from 8-18° and the emission is coupled from 17-35° on gratings with a PMSSQ film. As previously determined in Table 1-1, a 20x objective lens with a NA of 0.45 has a maximum incident angle of 26.7°. This angular range includes the θ_{SPR} coupling range for the excitation and half of the emission spectrum of FITC of the Blu-ray gratings.

Fluorescence measurements of the samples were carried out using an Olympus BX51WI epifluorescence microscope with a 300 W Xenon white light source using a FITC filter cube and different magnification objectives (10x, 20x, 40x, and 60x) (Olympus-UPlanApo). A high-resolution CMOS camera (Orca Flash 2.8, Hamamatsu Photonics with an internal gain of 240) was used to obtain the images in Fig. 2-17 with an exposure time of 80 msec.

Fluorescence images were analyzed using ImageJ, an open source image analysis software provided by the National Institute of Health (NIH). The average intensities from all of the images were collected including grating and glass samples without dye coatings. The fluorescence enhancement factor (EF) was calculated using the average fluorescent intensities and equation (2.6).

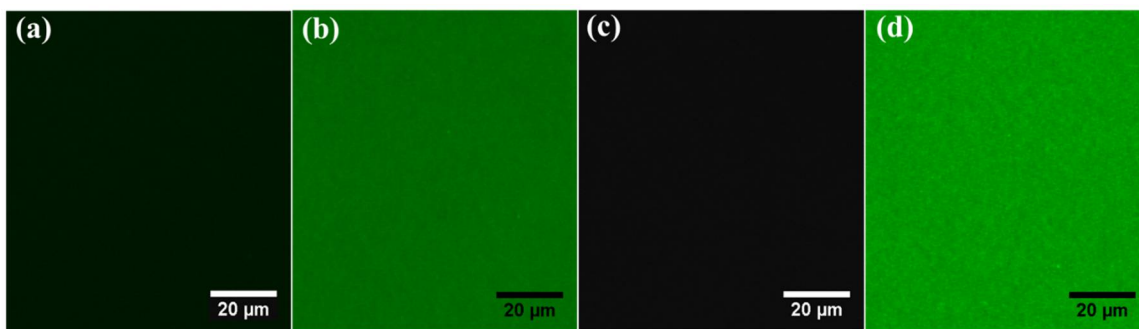


Figure 2-17. Normalized epi-fluorescence micrograph of a 10 μM FITC dye layer on sputter-coated silver (a) flat area and (b) blu-ray grating as well as thermally evaporated silver (c) flat area and (d) blu-ray grating using a 20× objective, 80 ms CMOS exposure and FITC filter set.

$$EF = \frac{I_n - I_{nB}}{I_f - I_B} \quad (2.6)$$

Where I_n is the fluorescence intensity of dye on the grating, I_{nB} is the intensity without dye on the grating, and I_f and I_B are intensities with and without dye and on the compared substrate, in this case, flat silver, respectively. Enhancement factors calculated with equation (2.6) for the sputtered and thermally evaporated silver gratings can be found in Fig. 2-18. It is quite clear from Fig. 2-18 that the thermally evaporated silver gratings have a higher mean enhancement factor than sputtered gratings with every microscope objective tested. Furthermore, the 20x objective showed the best enhancement factors for both types of gratings resulting in a maximum of 22x fluorescence enhancement on the thermal grating and 11x enhancement on the sputtered grating. The increased coupling strength and peak area of the thermal gratings resulted in much better enhancement factors than sputtered gratings.

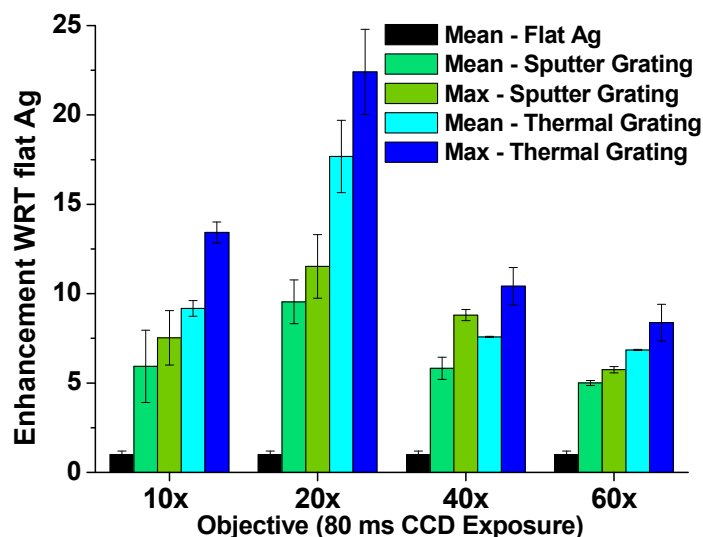


Figure 2-18. Histogram of the mean and maximum enhancement factors of sputtered and thermally evaporated silver Blu-ray gratings coated with a FITC/PMSSQ film compared to flat silver areas next to the gratings.

SPR dispersion in different mediums: As determined in section 1-3, SPR is extremely sensitive to the refractive index of the surrounding dielectric layer. It is also important to consider that most fluorescence assays are conducted in DI water, phosphate buffered saline (PBS), or immersion oil. As such, it is critical that the excitation and emission spectrums of the selected fluorophore match the SPR dispersion of the grating in the desired imaging medium. It also important that the fluorophore spectrums overlap with the SPR dispersion as close to the 0° coupling wavelength as possible. This is necessary for two reasons: 1) The inherently larger illumination intensity at or near 0° from microscopes and plate readers and 2) to ensure that fluorescent photons emitted via SPCE will be near 0° and easily collected by the imaging system.

The VASE system requires that samples be mounted vertically and, as such, it is difficult to take reflectivity and transmission measurements with a fluid (water, oil, etc.) on top of the grating. To take measurements in water or oil, reflectivity or transmission measurements in air should be performed first, the grating sample should then be removed from the sample stage without adjusting the Z-position knob. A drop of water or oil is applied to the sample and a coverslip with slightly smaller dimensions than the sample should be placed over the sample. 5-minute epoxy (for glass substrates) can then be mixed with a pipette tip and immediately transferred to the edges of the coverslip. Note: too much epoxy will block the beam from the VASE. A thin line ~1 mm wide will typically contain the water or oil sufficiently. After waiting 5-10 min. for the epoxy to cure, the grating is then reattached to the sample stage and tilt aligned. Note: The Z-position knob (used

for removing sample during background measurement) should not be adjusted at any time as the light may reflect from the coverslip instead of the grating and yield poor results. Two pictures of grating samples with and without a coverslip for liquid measurement have been provided in Fig. 2-19.

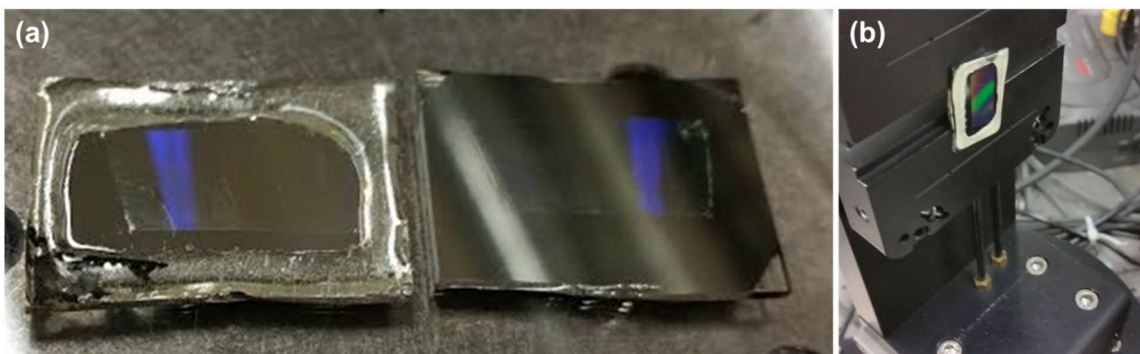


Figure 2-19. (a) HDDVD gratings with (left) and without (right) an epoxied coverslip with immersion oil for reflectivity measurement. (b) grating with coverslip mounted to the VASE sample stage.

For future reference, the SPR dispersions have been provided for 100 nm thick silver HDDVD, Fig. 2-20(a), and Bluray, Fig. 2-20(b), gratings capped in a 10 nm alumina layer with common fluorophore (FITC, R6G, R640, and Cy5) excitation and emission spectrums in air, water, and immersion oil. To demonstrate the variation in fluorescent enhancement in different mediums, fluorescent dyes with various emission spectrums were imaged in air, water, and immersion oil on thermally evaporated silver Bluray gratings (Fig. 2-20(c)).

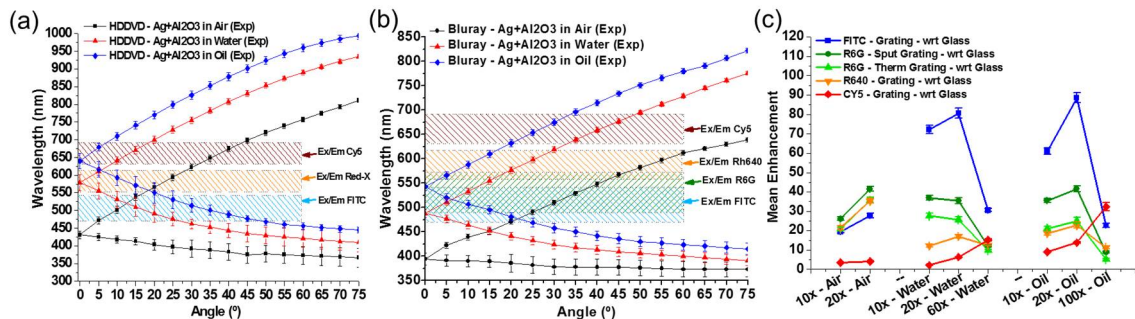


Figure 2-20. SPR Dispersion curves based on coupling peak location from reflectivity data for silver and alumina coated (a) HD DVD and (b) Bluray gratings. The excitation and emission spectrum locations for fluorescein isothiocyanate (FITC), rhodamine 6G (R6G), Rhodamine 640 (R640), and cyanine 5 (Cy5) have also been provided. (c) Mean fluorescence enhancement factor of silver Bluray gratings with respect to dye-coated glass samples for the previously listed fluorophores using different microscope objectives and different imaging mediums including air (RI: 1.000), water (RI: 1.333), and immersion oil (RI: 1.5148).

The enhancement results for each dye will be examined individually below:

FITC: The FITC enhancements were best in DI water (~80 EF with the 20x objective) and oil (~88 EF with the 20x objective). This could be expected as the red shift in the water dispersion curve and the blue shift in the oil dispersion curve would both result in an overlap with the FITC excitation and emission wavelength at $<5-10^\circ$.

R6G: The R6G spectrum is red shifted ~25 nm from the FITC spectrum, and, as a result, the enhancements were more uniform in all imaging media (air, water, and oil) around ~35-41 EF for the 10x and 20x objectives. The sputter deposited Bluray exhibited the same enhancement trend as the thermally evaporated grating.

R640: The R640 spectrum is best overlapped with the oil dispersion curve but, due to the blue shift from the PMSSQ layer, the coupling should be from $7-20^\circ$ in oil. The enhancement in water increased from 12 to 17 EF with the 20x water objective demonstrating that the coupling range is beyond the 20x objective in water. The

EF in oil increased from 18 to 22 with the 20x objective demonstrating that the optimal coupling angle is between the 10x and 20x objectives.

Cy5: The Cy5 spectrum is positioned such that it should couple from 25 - 40° in oil. The enhancement results indicate that the EF increases with the RI of the imaging material, i.e. air to water to oil. The best enhancement seen was with the 100x oil objective at ~33 EF. This indicates that Cy5 is coupling beyond range of the 20x objective but very close to the angle range of the 100x objective.

CHAPTER 3: INFLUENCE OF SILVER DEPOSITION METHOD ON PLASMONIC PROPERTIES

3.1. Abstract

Since the development of fluoroimmunoassays, researchers have sought a method of substantially enhancing fluorescence intensity to extend the limits of detection to new levels sensitivity. Surface plasmon resonance (SPR) and metal enhanced fluorescence has long been a topic of research and has led to the development of prism- and grating-based SPR systems. However, the wide coupling range and ease of exciting SPR on plasmonic gratings with a simple microscope objective, they have tremendous potential for revolutionizing the fields of plasmonics, fluorescence, and sensors. To better understand the influence of grating profile and metal film properties on the extraordinary fluorescence enhancement capabilities of plasmonic gratings, a novel microcontact printing process and different metal deposition techniques were used to fabricate silver gratings with varying grain diameters, roughnesses, heights, and duty cycles using thermal evaporation and RF sputtering. The resulting plasmonic gratings exhibited fluorescence enhancements up to 116× that of dye-coated glass slides using an epifluorescence microscope, much higher than more expensive prism-based SPR systems. This silver grating represents an extraordinary opportunity to quickly and easily enhance fluorescence and widen the detection limits of common fluorescence-based assays with little to no equipment modification.

3.2. Introduction

Surface Plasmon Resonance (SPR) research has grown substantially over the past several years and led to many substantial discoveries in nanotechnology including plasmonic nanoantennas and nanoresolution imaging techniques.^[4-9] SPR is essentially a phenomenon where light can be coupled into a metal/dielectric interface to form a propagating charge oscillation called a surface plasmon polariton (SPP). This method of light coupling only occurs if the wavevector of the incident light matches the wavevector of a SPP. Unfortunately, this does not occur under natural situations, which has led to the development of elaborate systems to form matching conditions that utilize structures such as nanoscale gratings.^[16, 17, 54] The expense of manufacturing platforms such as nanoscale gratings is currently cost prohibitive as it commonly involves the use of electron beam or interference lithography techniques.^[45, 46] To reduce the cost of fabricating nanoscale gratings, a novel soft lithography process was developed that can accurately replicate the gratings found on commercially available HD DVDs in polymethylsilsesquioxane (PMSSQ).^[20] To form SPR, a plasmonic metal coating, such as gold or silver, is required. While gold is typically chosen over silver due to its corrosion resistance, silver can support much higher field strengths due to its inherently lower dielectric losses at optical frequencies.^[21] Using Maxwell's equations, a wavevector matching equation can be derived for a particular metal grating/dielectric interface, seen in equation (1.29).^[20]

$$k_{\text{SPP}} = \frac{\omega}{c} \sqrt{\frac{\epsilon_m \epsilon_d}{\epsilon_m + \epsilon_d}} = \frac{\omega}{c} \sqrt{\epsilon_d} \sin \theta_{\text{SPR}} \pm m \frac{2\pi}{\lambda} \quad (m = \pm 1, 2, \dots) \quad (1.19)$$

Where ω is the frequency of the incident light, c is the speed of light in vacuum, ϵ_m is the dielectric constant for the metal, ϵ_d is the dielectric constant for the medium surrounding the metal, Λ is the grating pitch, k_{SPP} is the wavevector of the surface plasmon, and m is an integer representing the diffraction order. In grating based systems, the diffraction of incident light results in an additional momentum term in the wavevector matching conditions. The range of values at which proper coupling conditions occur can be visualized in a frequency vs. momentum plots, seen theoretically in Fig. 1-4(b) and experimentally in Fig. 1-4(c).[21] Due to this shift in the surface plasmon momentum curve from grating diffraction, multiple frequencies can be used to form SPR at a single angle of incidence. An example of which are the two intersection points with the light line seen in Fig. 1b,c that correspond to the $m=\pm 1$ SPR modes.[24] Furthermore, it can be observed that these two modes converge as the angle of incidence of light approaches $\theta=0^\circ$. The ability to excite SPR at a low illumination angle on gratings has led to the development of systems that, for example, use microscope objectives to excite SPR instead of single angle, laser based systems.

As a better understanding of SPR has been obtained, a unique interaction was observed between the evanescent electromagnetic (EM) field formed during SPR and nearby fluorescent molecules. It was observed that the emission intensity of fluorophores could be drastically enhanced when located between 10 – 100 nm to the metal surface and a phenomenon later called metal enhanced fluorescence.[35] If the frequency of the surface charge oscillation matched the excitation frequency of the fluorophore, the fluorophore would be excited to a

higher energy state. However, due to the proximity to the metal surface, the fluorophore would non-radiatively transfer energy to the metal and form a radiative plasmon with directed photon emission, also known as surface plasmon-coupled emission (SPCE).[36] To maximize fluorescent enhancement of this process, the EM field strength, which is closely tied to the properties of the metal/dielectric layers, must be tuned to be strong in the intended fluorophore excitation spectrum. Grating profile features such as height, pitch, and duty cycle as well as defects in the metal such as large grain boundaries and high roughness can have a strong effect on efficiency on SPR generation and must be further studied.

The objective of this study was to examine the effect of grating structure and silver film properties on SPR generation and fluorescence enhancement. Silver gratings with varying metal film and structural properties were fabricated using the previously mentioned μ -contact stamping process. The surface structure, extent of light coupling, and fluorescence enhancement capabilities of the different silver gratings was then characterized with AFM, VASE, and fluorescence microscopy. To better understand the effect of surface structure on electric field strength, the grating structures were also reproduced in FDTD simulations using FullWave software.

3.3. Silver Grating Fabrication

HD DVD gratings (Height: 60 nm, Λ : 400 nm) were replicated in PMSSQ “ink” with an added crosslinker, 3-aminopropyltriethoxysilane (APTES), using a previously developed μ -contact stamping process and further described in the experimental section.[20] As the gratings were fabricated using the fixed patterns of the HD-

DVD, the capability to change the height, pitch and duty cycle of the polymer layer (PMSSQ) was limited. To study the effect of various parameters discussed above on light coupling and concentration, our novel approach was to control the surface energy of the polymer layer, deposition method (RF sputtering vs thermal evaporation), and the use of different adhesion layers (Chromium (Cr) for thermal evaporation, Germanium (Ge) or Titanium (Ti) for sputtering). The nucleation and growth of thin films relies on the energy of the incoming atoms and their adsorption, diffusion, coalescence/chemical binding to the surface.[55] This was controlled by varying the energy of the incoming atoms, the surface energy of the polymer film, and binding energy of Ge, Ti, and Cr (adhesion layer) to the polymer surface with and without plasma treatment, as well as, the binding energy of Ag-Ag vs. Ag-Ti, Ag-Ge, and Ag-Cr. While varying these parameters, it is important to pay attention to the grain size which should not be too large to increase the scattering losses, but small enough to concentrate SPR field (less than 50 nm). The surface energy of as prepared PMSSQ polymer layer was low (0.024 J m^{-2}) due to the inherent hydrophobicity of the film. Oxygen plasma treatment changes the film to hydrophilic with high surface energy (0.056 J m^{-2}). The hydrophobic and hydrophilic nature of PMSSQ or wettability of the film is then used to control the interaction of the incoming atoms of the seed layers with PMSSQ surface and growth of the adhesion layer. Subsequently, silver atoms will interact with the seed layer and control the growth of silver films. Metal film growth, in general, can be described by three growth modes; the Frank-van der Merwe growth seen in Fig. 3-1(a) (layer by layer growth), Volmer-Weber growth seen in Fig. 3-1(b) (island

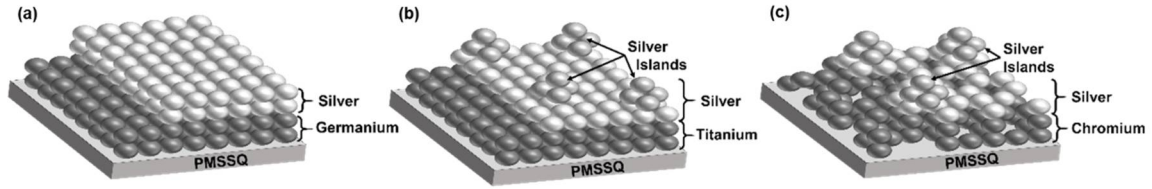


Figure 3-1. Grain and island growth mechanisms for silver films deposited onto (a) germanium, (b) titanium, and (c) chromium adhesion layers.

growth), and Stranski – Krastanov growth seen in Fig. 3-1(c) (layer and island growth).[56] The deposition parameters and surface energy of PMMSQ were varied to control the nucleation and growth processes to achieve films with different silver grain sizes and are discussed in further depth below.

Surface Energy of PMMSQ Films. Plasma treatment of PMSSQ creates a high surface energy surface by forming defects (dangling bonds) and surface bound -OH chemical groups. These sites can act as binding and nucleation sites that reduce the mobility of the adatoms and promote island growth, resulting in the formation of large metal grains. In the case of PMSSQ films without plasma treatment with low surface energy and a low number of defect/binding sites, incident atoms can more readily diffuse to the surface, leading to coalescence, the formation of many new nucleation sites, and ultimately denser, smoother films.

Sputtering vs. Thermal evaporation. The energy of the incoming atoms in a sputter deposition system range from 1-10 eV, whereas, for thermal evaporation, the incoming atoms have much lower energy that ranges from 0.1-1 eV.[57] Due to the low energy of atoms in thermal evaporation, these atoms are less mobile and hence promote island and columnar growth resulting in the formation of large grains. Also, when the low energy atoms with directional flux are deposited by

thermal evaporation onto a grating surface with nanoscale features (60 nm height and 400 nm pitch), the atoms tend to fill the groves and reduce the observed height of the gratings (see Table 3-1). In sputter deposition, the high energy and mobility of incoming atoms promotes layer by layer growth, as seen in Fig. 3-1(a), resulting in smaller grains and smoother films with less groove filling.

Effect of adhesion layer on silver film growth: Both of the two different adhesion layers, titanium and germanium, deposited by sputtering promote layer by layer growth on PMSSQ. However, when silver is deposited on germanium, the higher dissociation energy of Ag-Ge (174.5 KJ/mol) compared to Ag-Ag (162.9 KJ/mol) allows for smoother films with smaller grains than silver deposited on titanium.[58, 59] The Ti-Ti bond dissociation energy (117.6 KJ/mol)[58] is much lower than Ag-Ag, however, the much higher inherent energy of sputtered adatoms vs. thermal evaporation aids in diminishing the effect of the energy mismatch. It is speculated that this is the reason why the RMS roughness of such films is always slightly higher than silver films sputtered onto germanium. By obtaining relatively smooth films despite the substantial mismatch in dissociation energy between Ti and Ag, we also believe that the growth method is closest described by Volmer-Weber growth.[60] In thermal evaporation, Stranski-Krastanov growth is favored for an Ag film deposited onto an adhesion layer of lower dissociation energy, such as Cr-Cr (152.0 KJ/mol),[58] and the substantially lower adatom energy of thermally evaporated silver vs. RF sputtering.

3.4. Surface and Optical Characterization

Surface Structure and Permittivity. The grating surface structure was characterized with AFM and analyzed using Gwyddion to obtain the pitch, height, root mean square (RMS) roughness, duty cycle, and grain diameter tabulated in Table 3-1 and shown in Fig. 3-2(a-f.)

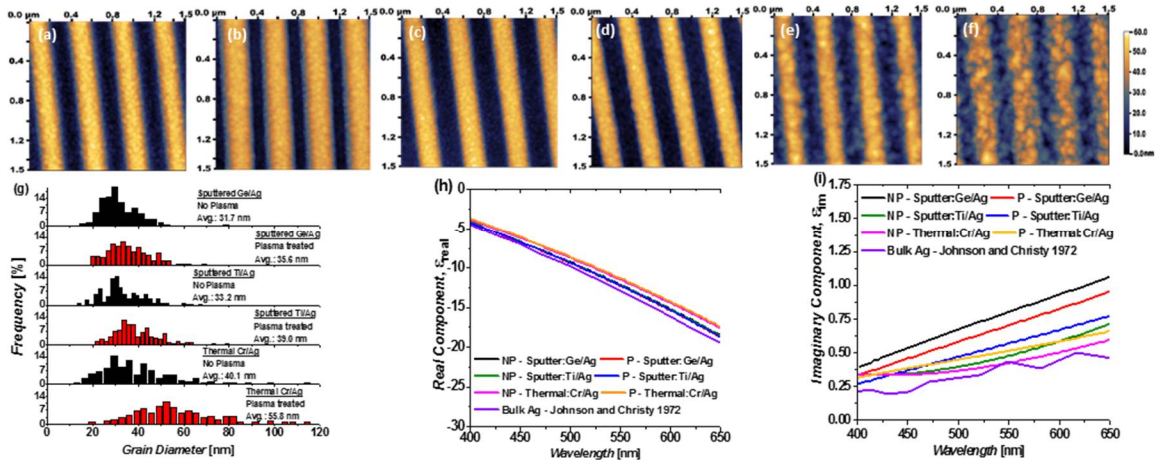


Figure 3-2. Topographical AFM scans ($1.5 \mu\text{m} \times 1.5 \mu\text{m}$) of gratings with (a,b) sputtered germanium and silver, (c,d) sputtered titanium and silver, and (e,f) thermally evaporated chromium and silver. Oxygen plasma treated samples (b,d,f) on average exhibited larger average grain diameters than the (a,c,e) untreated counterparts. All scan heights have been plotted from 0 to 60 nm. (g) Grain diameter histograms from the previous AFM scans. (h) Real and (i) imaginary permittivity components were taken from flat silver films with the same deposition parameters and PMSSQ/APTES film surface energy with bulk silver values from Johnson and Christy.²⁵

Surface Pre-treatment	Deposition Type	Mean Grating Pitch, Λ [nm]	Mean Grating Height [nm]	RMS Roughness [nm]	Mean Grain Diameter [nm]	Duty Cycle
No	Sputtered Ge/Ag	401.4 ± 3.1	52.8 ± 1.9	1.6	31.7 ± 8.2	0.533 ± 0.018
Oxygen Plasma	Sputtered Ge/Ag	400.2 ± 3.5	55.7 ± 1.7	1.7	35.6 ± 9.1	0.552 ± 0.022
No	Sputtered Ti/Ag	401.8 ± 3.4	53.1 ± 0.5	1.9	33.2 ± 9.3	0.512 ± 0.016
Oxygen Plasma	Sputtered Ti/Ag	396.7 ± 3.7	54.8 ± 1.6	2.5	39.0 ± 9.9	0.521 ± 0.018
No	Therm. Evap. Cr/Ag	403.3 ± 5.1	43.9 ± 1.9	4.0	40.1 ± 15.7	0.568 ± 0.027
Oxygen Plasma	Therm. Evap. Cr/Ag	397.3 ± 8.2	42.9 ± 3.5	5.1	55.8 ± 17.5	0.569 ± 0.046

Grain diameter distributions were provided in Fig. 3-2(g). All thermally evaporated samples exhibited larger diameters and wider dispersity than sputtered samples, which is consistent with the previously discussed grain growth mechanisms. Thermally evaporated sample grains also exhibited sharper edges than sputter samples. All plasma treated samples also exhibited increased grain diameters compared to non-treated samples due to the higher surface energy. The effect of the varying deposition techniques on the electric properties of the films was studied by comparing the complex permittivity obtained via spectroscopic ellipsometry for all of the silver films as seen in Fig. 3-2(h,i). Little change in the real component of permittivity was observed between samples; however, the imaginary component associated with energy loss was substantially lower for thermally evaporated samples than sputtered samples.

Reflectivity: The formation of SPR on a metallic grating is commonly seen as a sharp dip in the reflectivity at particular wavelengths and angles of incidence.[20, 61] The depth of the reflectivity dip, also called the coupling strength (σ), is an indicator for how strongly light is coupled to the grating while full width at half maximum

(FWHM) indicates the range of wavelengths that can couple at a particular angle of incidence. The reflectivity of the different grating samples has been plotted in Fig. 3-3(a-f). Two sharp decreases in reflectivity for each angle of incidence correspond to the $m=\pm 1$ SPR solutions that are supported on the grating.[9] For reference, the $m= +1$ SPR coupling wavelength has been indicated for all reflectivity curves in Fig. 3-3(a-f) at $\theta=15^\circ$ and $\theta=45^\circ$. From the $\theta=15^\circ$ reflectivity

of the six grating samples seen in Fig. 3-3(g), a trend of increasing coupling strength with λ grain size can be observed. SPR coupling location found in reflectivity was plotted vs. angle of incidence to obtain a dispersion plot for several angles of incidence and can be seen in Fig. 3-3(h). As the angle of incidence approaches 0° , the SPR coupling wavelengths corresponding to the $m = \pm 1$ solutions converge as seen experimentally in Fig. 3-3(h). Only minor variations were observed between sputtered and thermally evaporated samples which are largely attributed to the similarity in grating pitch between samples.

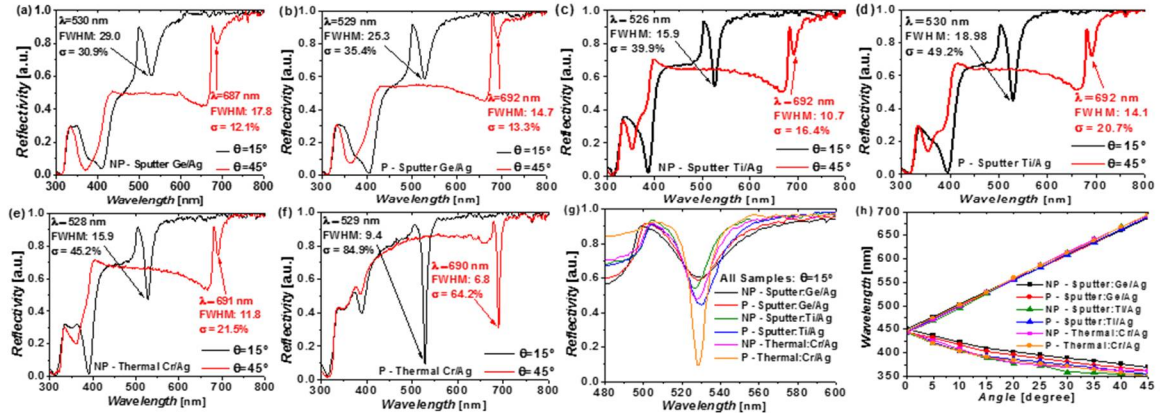


Figure 3-3. TM-polarized reflectivity plots for 15° and 45° angles of incidence of gratings with (a,b) sputtered germanium and silver, (c,d) sputtered titanium and silver, and (e,f) thermally evaporated chromium and silver. Oxygen plasma treated (b,d,f) and untreated counterparts (a,c,e). (g) TM-polarized reflectivity at 15° of silver gratings with plasma, P, and no plasma treatment, NP. (h) Dispersion plot of the $m = \pm 1$ SPR modes derived from reflectivity peak location of silver gratings in air.

3.5. Fluorescent Dye Enhancement

Angled Excitation: Single angle, monochromatic illumination is the most common form of SPR excitation found in literature. While this may be optimal for prism-based systems with narrow coupling ranges, it is much less efficient for systems with wider coupling ranges, such as nanogratings. By exciting SPR on wide coupling range systems with a single wavelength and angle, a large portion of the

SPR coupling range is underutilized. To take full advantage of the wide coupling range, the grating must be illuminated with polychromatic light that matches the excitation spectrum of the desired fluorophore at a range of angles that can couple to form SPR. This type of illumination can already be found in the objective of a simple fluorescence microscope as objectives focus light into a cone with a particular convergence angle as seen in Fig. 3-4(a). The convergence angle of a particular objective can be calculated with equation (1.29):

$$NA = n \sin(\pm\theta) \quad (1.29)$$

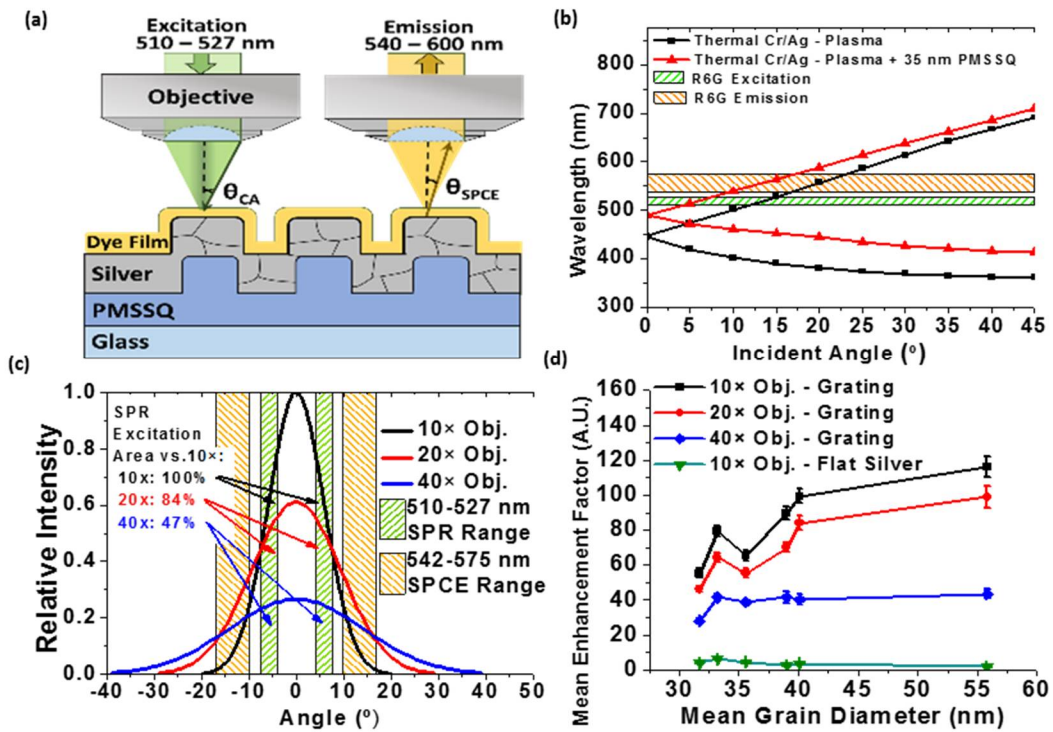


Figure 3-4. (a) Illustration of SPR excitation and SPCE capture from a silver grating with a simple microscope objective. (b) SPR dispersion curve representing SPR coupling peak location with overlay of R6G excitation and emission spectrum. (c) Normalized objective illumination intensity vs. angle for 10x, 20x, and 40x objectives with estimated SPR excitation and SPCE emission angle ranges from (b) for a silver grating coated in 35 nm PMSSQ. (d) Mean enhancement factor of R6G dye coated gratings with different grain sizes as compared to R6G-coated glass substrates using 20 ms CCD exposure.

Where $\pm\theta$ is the maximum convergence angle of the objective from sample normal, NA is the numerical aperture, and n is the refractive index of the imaging medium. The convergence angles were calculated using equation (1.29) for the three objectives: $\theta_{10\times} = \pm 17.45^\circ$, $\theta_{20\times} = \pm 26.74^\circ$, and $\theta_{40\times} = \pm 36.87^\circ$. The angular illumination intensity of an objective is normally distributed with most of the light impacting the sample near 0° and only a small fraction of photons illuminating the sample at the convergence angle.[62]

Dye Selection. The selected fluorophore must have an excitation spectrum that overlaps with the low angle coupling range ($\theta_{\text{SPR}} = < 10^\circ$) of the grating to obtain the highest fluorescent enhancement using gratings and a microscope objective. To accurately determine the SPR dispersion of a dye layer coated grating, a 35 nm thick PMSSQ layer was spin-coated onto the gratings, the addition of which will red-shift the SPR dispersion due to the higher refractive index of the PMSSQ compared to air. Reflectivity measurements were acquired on the PMSSQ coated grating without the fluorescent dye, and the corresponding SPR dispersion has been provided in Fig. 3-4(b). Using this dispersion, the optimal fluorophore must be excited near 530 nm and emit near 550 nm. Rhodamine 6G (R6G) was selected to test the enhancement capabilities of the grating due to its overlap with the low angle SPR dispersion and high photostability.

Fluorescence Microscopy. As previously mentioned in the introduction, fluorophores can non-radiatively transfer energy to metal if the fluorophore is in close enough proximity to the metal surface. The spacing between the fluorophore

and metal determines if the charge oscillation formed on the metal as a result of the energy transfer will be a lossy surface plasmon or a radiative plasmon.[63] If very close (<10 nm), the charge spacing is too small to form a radiative plasmon resulting in the formation of a lossy surface plasmon. However, if the fluorophore is located between 10–100 nm from the surface, a radiative plasmon will form and directionally emit a photon via SPCE. The SPCE wavelength corresponds to the fluorophore emission wavelength and is emitted at the SPR angle. The emission angle of R6G dye was estimated using the SPR dispersion curve in Fig. 3-4(b) to occur between 3.6° and 8° . For an objective to capture SPCE, estimated to emit from the grating from 10° to 17° , the emission angle must fall within the convergence angle of the objective. The SPR coupling and SPCE emission spectrum of R6G were overlaid with the angular illumination intensity of the 10 \times , 20 \times , and 40 \times objectives in Fig. 3-4(c). It can clearly be seen that the 10 \times objective provides the highest intensity excitation in the SPR coupling region while still encompassing the angular range of SPCE. It was calculated that the 20 \times and 40 \times objectives excite the grating with 84% and 47%, respectively, of the illumination area provided by the 10x intensity. It was also calculated that 32.4% of the 10 \times illumination cone is within the SPR excitation angle range while only 28.2% and 24.4% of the 20 \times and 40 \times illumination cones, respectively, is within the SPR coupling range. Dye-coated gratings and glass samples were imaged with all with all three objectives at an exposure time of 20 milliseconds and processed in ImageJ to obtain the raw fluorescence intensity. Fluorescence enhancement factor (EF) of the gratings was calculated using equation (3.1).

$$EF = \frac{I_{R6G,Grating} - I_{Grating}}{I_{R6G,Glass} - I_{Glass}} \quad (3.1)$$

Where I represents the intensity reported by the CCD with and without R6G on gratings or glass substrates. The resulting fluorescence enhancement of the gratings in different microscope objectives compared to dye-coated glass samples has been provided in Fig. 3-4(d). The enhancement factors corresponded well with the estimated objective excitation area for each of the objectives with the 10× objective providing the highest enhancement overall as was expected. The evaporated silver sample with a 55.8 nm mean grain diameter exhibited the highest mean enhancement factor of 116× while the sputtered germanium-silver sample exhibited a mean enhancement factor of 55× compared with dye-coated glass. The high fluorescence enhancement found on these plasmonic gratings is attributed to the combination of using low loss silver films, optimized grating profiles, and a wide angle excitation source.

These fluorescence enhancements are also higher than previously observed values for similar fluorescent dyes on plasmonic grating systems. Table 3-2 has been provided to summarize several recent fluorescence enhancement results on silver and gold gratings with various parameters. The lower fluorescent enhancement seen in previous studies is thought to arise from the small grain sizes obtained through sputter coating, exciting the platform at a narrow-angle range or too far away from the optimal objective illumination range, and incorporation of overly thick capping layers between the silver and the fluorophore. Previously published literature also rarely studied more than two grating parameters and even

fewer characterized the metal film properties where, as this article has demonstrated, several parameters must be properly tuned to obtain high fluorescence enhancements.[61, 64, 65]

Table 3-2. Grating-Based Fluorescence Enhancement Literature Summary

Grating Pitch (nm)	Height (nm)	Duty Cycle	Metal, Thickness, Deposition Method, capping layer	Fluorescent Dye (Ex. λ / Em. λ , nm) and Thickness	Enhancement Factor	Source
400 - 1000	40	~0.5	Gold, 50 nm, not provided, no cap	R6G (530/550), not provided	1.7-36 \times	[66]
480	31	0.40	Silver, 200 nm, RF Sputter, 20 nm SiO ₂ cap	Cy5 (630/650), Surface conjugated	24 \times	[64]
480	20-50	0.40			10 \times	[65]
400	10-30	0.33-0.72			10-40 \times	[61]
300	65	~0.50	Silver, 50 nm, Evaporation, no cap	R6G (530/550), 70 nm film	9-10 \times	[54]
375	65				30-60 \times	
400	65	~0.5	Silver, 100 nm, RF Sputter, no cap	R6G (530/550), 35 nm film	26-36 \times	[20]
400	55	~0.5	Gold, 100 nm, Evaporation, no cap	Cy5 (630/650), Surface conjugated	13.6 \times	[67]
434	20-80	~0.5	Gold, 100 nm, Evaporation, no cap	AF647 (633/670), 6 nm film	~100 \times	[24]
400	52-55	0.51-0.55	Silver, 100 nm, RF Sputter, no cap	R6G (530/550), 35 nm film	55-90 \times	This project
400	42-44	0.57	Silver, 100 nm, Evaporation, no cap		100-116 \times	

3.6. Influence of Grating Properties on SPR

Metal Grain Size. To an extent, grain size has a critical role in determining the complex permittivity of a metal film and ultimately the SPR field strength.[68] To further study the grain –based effects on the fluorescence enhancement, dye coated samples were imaged using a 60x oil immersion objective (1.35 NA) in brightfield and through an R6G fluorescence filter. The resulting images can be found in Fig. 3-5. From these images, the sputter coated silver samples (Ge and Ti adhesion layers) had more uniform fluorescence intensity along the grating ridges while the thermally evaporated silver grating was populated by high-intensity spots located on the top of the grating ridges. These spots correspond to

large, sharp silver grains that concentrate the surrounding SPR field and further enhance the fluorescence intensity. The population of large grains is large enough that when observed on a larger scale, such as using a 10× objective, it is observed as having high intensity, uniform fluorescence. The 60× objective used required that the samples be placed in immersion oil with a refractive index of 1.5. The increase in refractive index caused a large red-shift, much more than the addition of a PMSSQ layer, in the SPR dispersion and moved the R6G excitation/emission coupling range to higher angles. This resulted in less than optimal fluorescence enhancement; however, these imaging conditions were necessary to obtain the resolution to observe the individual grating ridges. Bright field images were taken with a 455 nm high power LED light source to improve the resolution which is estimated to be 166 nm based on diffraction limit theory.[69]

It is important to note that the wide distribution of grain sizes present on the various samples encompassed the estimated 30 nm penetration depth of a photon into silver.[35] As each photon has a high probability of interacting with grain boundaries for all samples, the boundaries play a major role in the losses associated with each silver film and could be studied using the complex dielectric function. In Fig. 3-2(h), it can be seen that increasing grain size had little effect on the real component of permittivity which is often associated with the energy storage of the metal. However, the imaginary component which is related to the loss properties of a metal film shown in Fig. 3-2(i) decreased with increasing grain size. The reduction of the imaginary component primarily arises from the reduction of grain boundary density found on larger grain films.[70] Grain boundaries near the

metal/dielectric interface can also cause greater internal dampening and increased elastic scattering of SPPs.[71] This can have a detrimental effect on SPR propagation length, for example, on copper films and gold nanorods.[6, 72] In both examples, a reduction in grain boundary density, resulted in higher intensity SPR fields, longer propagation lengths, and higher fluorescent enhancements which are consistent with the results seen in Fig. 3-4(d) and Fig. 3-5.

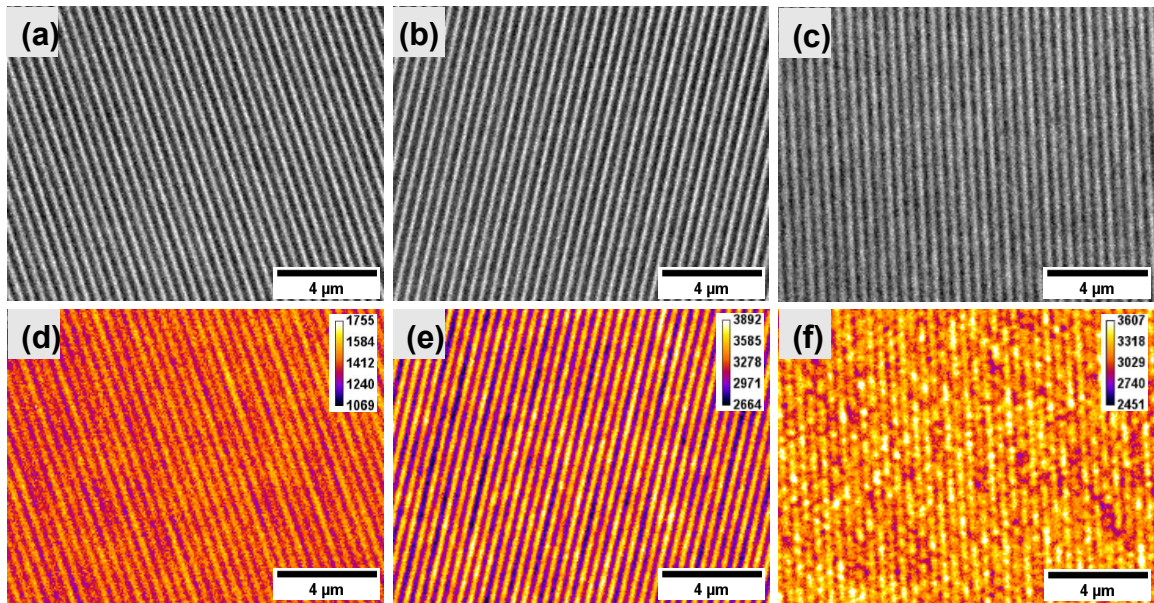


Figure 3-5. Brightfield images and false-colored fluorescence images using a R6G filter taken with a 60x oil immersion objective (NA: 1.35) of R6G dye coated, plasma-treated silver gratings composed of (a,d) sputtered Ge/Ag, (b,e) sputtered Ti/Ag, (c,f) and thermally evaporated Cr/Ag. Bright field images were taken with an exposure time of 200 milliseconds and an Ocean Optics high power 455 nm LED light source. Fluorescence images were taken with a xenon arc lamp and ORCAflash2.8 CCD camera at different exposure times to capture the much lower fluorescence intensity of the sputtered gratings compared to the evaporated gratings: (d) 150 ms, (e) 90 ms, and (f) 50 ms. The fluorescence intensity range for each image has been provided in the top right corner of each image.

Roughness. The adverse effect of roughness including the resulting scattering on SPR strength on flat silver films has been a topic of great interest for many years.[6, 73-76] Despite this attention, little work has been performed to examine the effect of roughness on grating structures. In the few articles that have discussed its effect

on gratings, it was concluded that roughness has a much smaller effect on gratings than on flat films.[76-78] Raether observed that grating RMS roughness had to be 12-25% of the grating height to obtain the same coupling angle shift as 1 nm RMS roughness on a flat film.[77] While roughness can cause surface scattering and SPP loss, it commonly accepted that grain boundary scattering is the dominant scattering mechanism responsible for SPP loss in most cases.[8, 70] It is thought that the walls of the gratings provide an additional means of capturing scattered photons that can result in SPP formation.[77] Sputtered silver gratings exhibited much lower RMS roughness values between 1.6 and 2.5 nm than thermally evaporated silver samples that exhibit much higher roughnesses between 4.0 and 5.1 nm. While these values would be considered too high if used in flat film SPR, the roughnesses are still at or below 10% of the grating height and do appear to have a noticeable effect on the enhancement factor of the various samples, especially in the thermally evaporated silver films.

Grating Profile. The structural profile is possibly the most critical variable in obtaining high electric field strengths as, for example, the grating pitch is responsible for the shifted momentum curve. The pitch was fixed in these experiments as the HD DVD molding process did not allow for this modification. Furthermore, all of the samples exhibited little variability in pitch (Table 3-1) and thus the effect of pitch size on enhancement between samples should be negligible. While grating height is not included in equation (1.19), it has been observed in other literature to have a large effect on SPR field strength and fluorescence enhancement where enhancement factor can range from 15× to 40×

on 10 nm and 20 nm tall grating ridges, respectively.[61] The optimal grating height can vary substantially depending on the variations in the dielectric layer thus it should be optimized for a particular wavelength range and the dielectric layer. As listed in Table 3-1, the grating heights of the four sputtered were much closer to the original PMSSQ HD DVD grating height than the two thermally evaporated samples due largely to their growth kinetics and near vertical deposition angle in thermal evaporation. Despite the 10 nm decrease in height between the sputtered silver and untreated thermally evaporated samples, the coupling strength, Fig. 3-3(a-e), did not exhibit much change indicating that height had less of an effect on this parameter. However, height can have much more of an impact on E-field strength and was examined using FDTD simulations in the next section.

The duty cycle can also have a large effect on the field localization as well as the symmetry of the electric field profile on the ridges or pits of the grating. The gratings deposited by thermal evaporation have a grating height of ~43 nm and duty cycle of 0.56 while the samples prepared by sputtering have a grating height of ~53 nm and duty cycle of 0.52. To better understand the effect that this variation in duty cycle and other grating profile parameters, finite difference time domain simulations were conducted to obtain reflectivity and electric field profiles in the following section.

3.7. EM Field Simulations

Grain Size. To test the effect of grain diameter on light coupling and EM field generation, FDTD simulated profiles for silver gratings with small and large grain sizes were built according to the geometric topography obtained by AFM for

sputtered silver gratings and thermally evaporated samples. As seen in Fig. 3-3(a), larger grain size samples have a smaller FWHM, similar coupling strength, larger gamma value, and larger quality factor. Measurement were taken at 15° angle of TM-polarized incidence in air (see Table 3-3) to compare the simulated and experimental reflectivity intensity for silver gratings with small and large grain sizes.

Table 3-3. Summary of simulated SPR peak parameters at $\theta_{\text{SPR}} = 15^\circ$ for silver gratings with different grain sizes.						
Grain size	Wavelength	FWHM	Quality factor ($\lambda_{\text{SPR}}/\text{FWHM}$)	Coupling strength ($ R_{\text{peak}} - R_{\text{baseline}} $)	Gamma (σ/FWHM)	Peak area
	(λ_{SPR} , nm)	(nm)	(Q, a.u.)	(σ , a.u.)	(γ , 10^{-2})	(a.u.)
small	538	19.3	40.2	84.2%	6.25	20.6
large	536	12.7	42.2	85.0%	6.69	14.7

Notably, the simulated coupling strength (84.2%) of the large grain size gratings was close to the experimental value of 84.9% (see Fig. 3-3(f)); however, the experimental small grain size samples exhibited much smaller coupling strength, less than 40% (see Fig. 3-3(a-c)), than the simulated value (85.0%). This mismatch is attributed to the inability to incorporate grain boundaries into a two-dimensional modeled profile that would introduce a significant loss source as described previously. The same trend of reducing FWHM with increasing grain sizes seen on experimental samples can also be observed in the simulated results in Fig. 3-6(a). Due to the higher grain boundary density as well as the average grain diameter being near the photon penetration depth into the silver, the sputter coated samples had much more loss than the thermally evaporated samples.

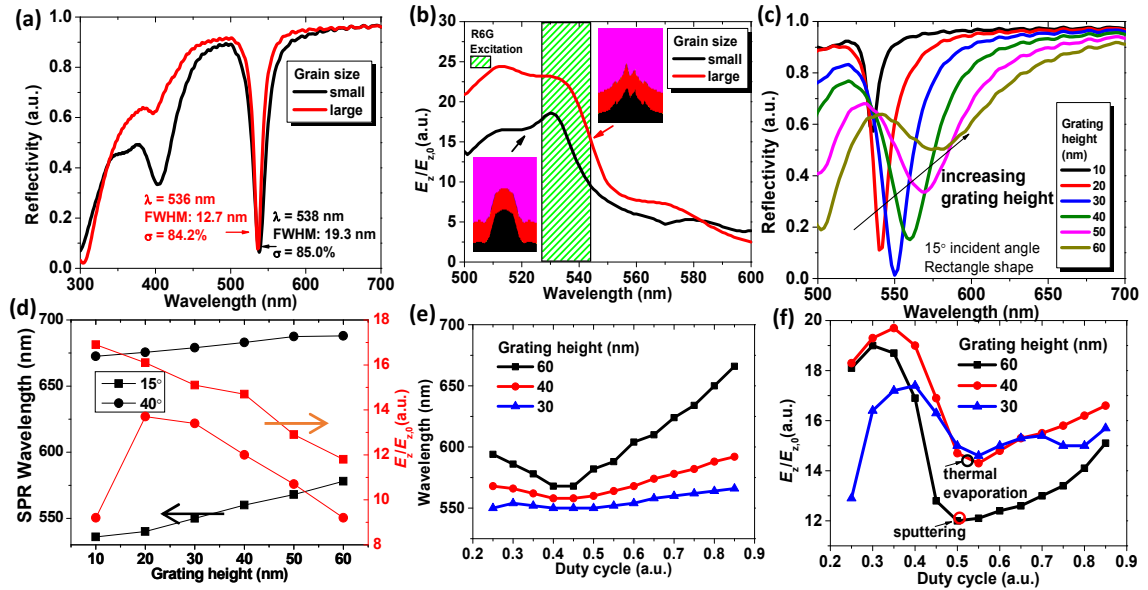


Figure 3-6. Simulations of silver gratings: (a) reflectivity for silver gratings with small and large grain sizes at 15° angle of TM-polarized incidence in air, (b) simulated maximum electric field ($E_z/E_{z,0}$) vs. wavelength for 35 nm PMSSQ-coated silver gratings with small and large grain sizes at 5° angle of TM-polarized incidence in air, (c) simulated reflectivity plots for silver gratings with different grating heights from 10 nm to 60 nm (rectangular shape) at 15° angle of TM-polarized incidence in air., (d) SPR wavelength and maximum electric field vary with grating heights at 15° and 40° angle of incidence, (e) SPR wavelength and (f) maximum electric field at reflectivity dips for gratings with duty cycles from 0.25 to 0.85 with a grating height of 30 nm, 40 nm, or 60 nm.

Simulations were also conducted with the addition of a 35 nm thick conformal PMSSQ film to determine the electric field strength experienced by the dye molecules. In these simulated structures, the maximum electric field (Fig. 3-6(b)) developed at $\theta=5^\circ$ was more intense over a larger range of coupling wavelengths on the large grain size gratings than the small grain size grating. This is primarily due to the localized field enhancement on the sharp asperities and peaks of the larger grains. Similar electric field localization was also observed experimentally

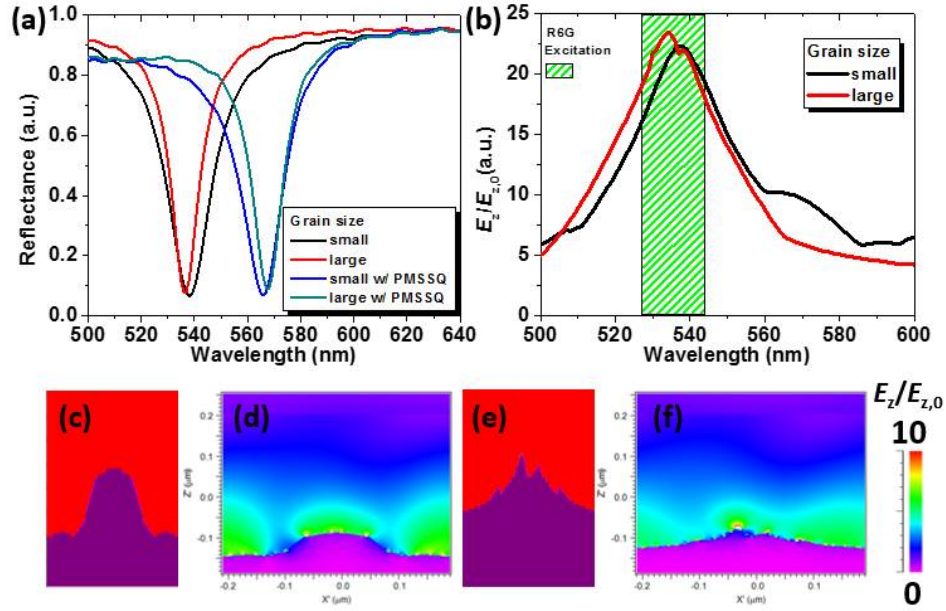


Figure 3-7. (a) Simulated reflectivity plots for silver gratings with small and large grain sizes at 15° angle of TM-polarized incidence in air, with and without conformal PMSSQ coating. (b) Maximum electric field ($E_z/E_{z,0}$) vs wavelength plots for silver gratings. Simulated profiles for (c) small grain size and (e) large grain size, the red region is air and the magenta region is silver and R6G excitation ranges. Electric field distribution for the wavelengths at reflectivity dips for (d) small grain size (538 nm) and (f) large grain size (536 nm), maximum $E_z/E_{z,0}$ is normalized at 10.

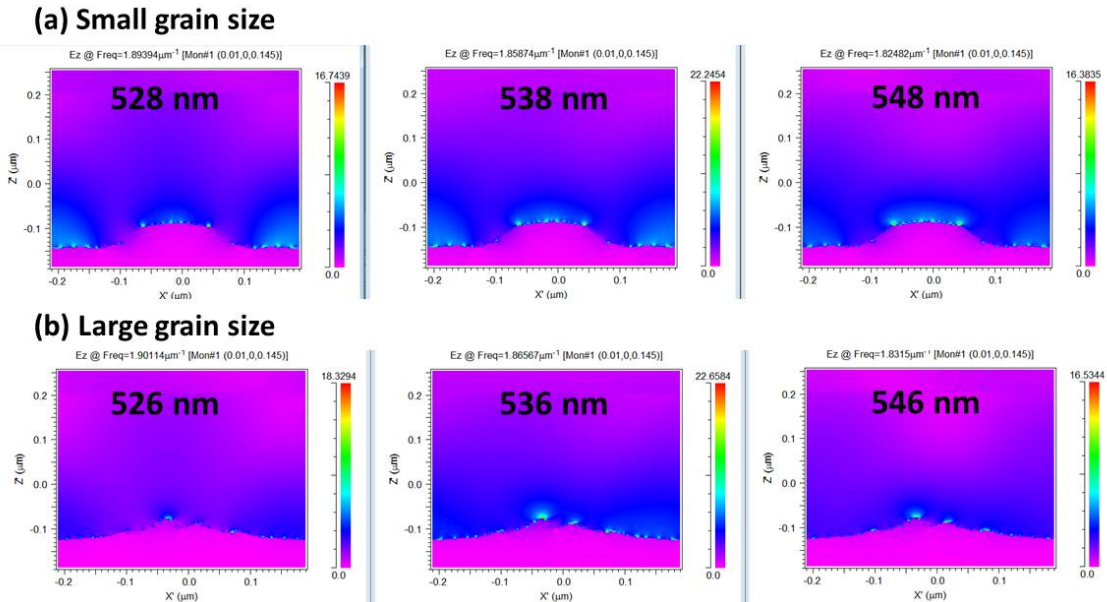
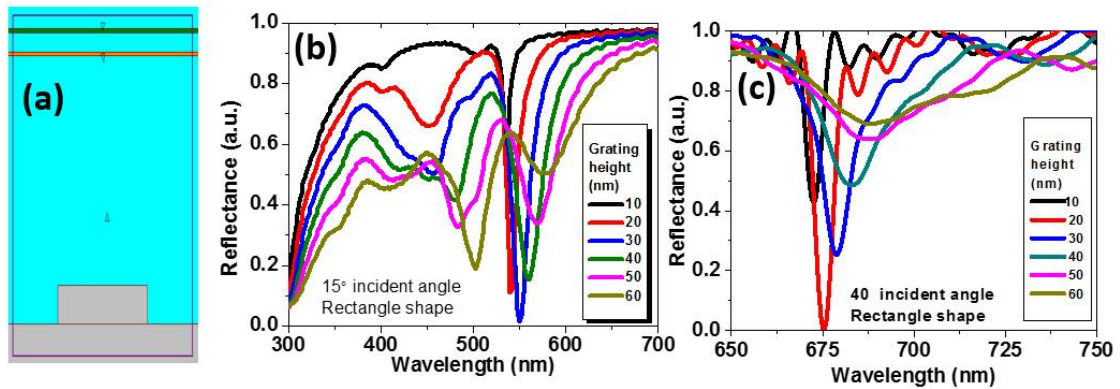
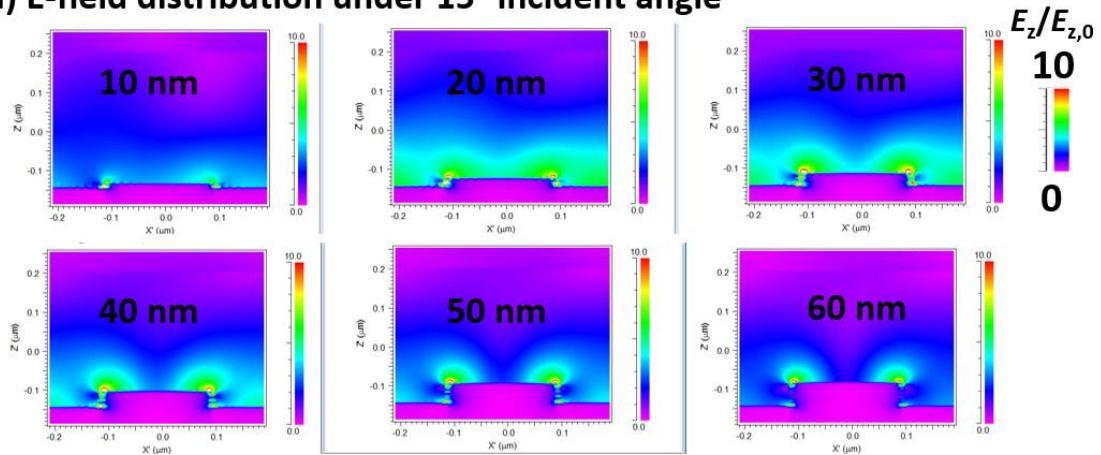


Figure 3-8. Simulated electric field distribution ($E_z/E_{z,0}$) for silver gratings with small and large grain sizes at 15° angle of TM-polarized incidence in air under the wavelengths at reflectivity dips and 10 nm less or more than the SPR wavelength: (a) small grain size and (b) large grain size.



(d) E-field distribution under 15° incident angle



(e) E-field distribution under 40° incident angle

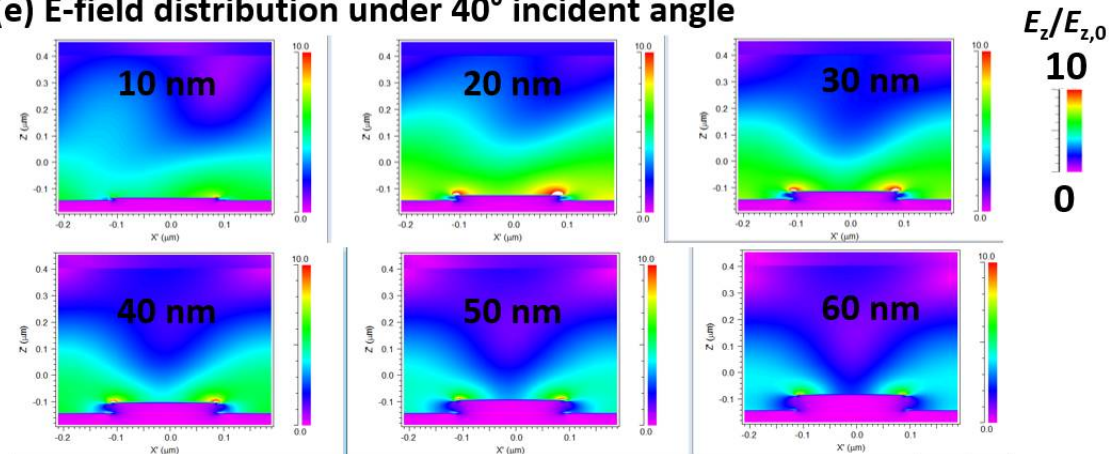


Figure 3-9. (a) 2D simulation window for Ag gratings with rectangular shape varying grating heights from 10 nm to 60 nm. Simulated (b,c) reflectivity and (d,e) electric field distribution ($E_z/E_{z,0}$) for silver gratings with 0.5 of duty cycle at (b, d) 15° and (c, e) 40° angle of TM-polarized incidence in air under the wavelengths at reflectivity dips, maximum $E_z/E_{z,0}$ in scale bar is normalized at 10.

as higher fluorescence intensity of the thermally evaporated silver sample seen in Fig. 3-5(e). PMSSQ layers on top of silver gratings result in red-shift of the SPR wavelength (Fig. 3-7), which makes the plasmonic gratings platforms a better match with the excitation and emission of a fluorophore in the range of 530 – 550 nm as seen from the dispersion curve (Fig. 3-4(b)). These grating-based SPR systems also have broad reflectivity coupling peaks, leading to less angle-dependency in electric field strength (Fig. 3-8 and 3-9) as compared with prism-based SPR systems. This is especially beneficial for fully utilizing the broad excitation and emission peaks of fluorescent dyes for enhancement.

Grating Profile. The influence of grating height on reflectivity and SPR field strength was evaluated for silver gratings with heights between 10 – 60 nm with the pitch and duty cycle maintained at 400 nm and 0.5, respectively. The reflectivity results from varying height samples in Fig. 3-6(c) demonstrate that grating height has a substantial effect on the SPR wavelength, FWHM and coupling strength. The simulated results showed that as grating height increased from 10 to 60 nm, the SPR wavelength red-shifted from 530 to 575 nm and the maximum electric field strength intensity decreased from 17 to 9 at $\theta=15^\circ$ as seen in Fig. 3-6(d). The SPR wavelength at $\theta=40^\circ$ was also red shifted with increasing height and exhibited lower intensity electric fields than at $\theta=15^\circ$ at every height tested. The presence of stronger electric fields at a lower angle of incidence further demonstrates that lower angle illumination should be utilized for higher fluorescence enhancement. The sensitivity of the electric field generation to mismatched coupling wavelength was further evaluated by illuminating the simulated gratings at $\theta=15^\circ$ and 40° but at a

wavelength 10 nm and 5 nm blue-shifted from the peak coupling wavelength, respectively. The simulated electric field strengths have been provided in Fig. 3-9 as well as Table 3-4. Despite an increase in coupling sensitivity at lower incident angles the maximum electric field strength was achieved with a 40 nm grating height. This grating height is closest to the thermally evaporated silver gratings which also exhibited the highest fluorescence enhancement of any of the gratings further supports the simulated result.

Table 3-4. Summary of simulated SPR peak parameters at $\theta_{\text{SPR}} = 15^\circ$ and 40° for silver gratings with different grating heights, with a constant duty cycle of 0.5.

Grating height (nm)	SPR Wavelength (nm)		Max Ez		Ez (less than SPR wavelength)		Ez (change)	
	15°	40°	15°	40°	15°	40°	15°	40°
10	536	672.5	16.9	9.2	6.5	3.8	10.4	5.4
20	540	675.5	16.1	13.7	5.1	7.1	11	6.6
30	550	679	15.1	13.4	12.4	9.8	2.7	3.6
40	560	683	14.7	12	13.6	10.5	1.1	1.5
50	568	687.5	12.9	10.7	11.6	10	1.3	0.7
60	578	688	11.8	9.2	10.7	8.7	1.1	0.5

As shown in Fig. 3-6(e-f), Duty cycle, in a similar manner as grating height, must be optimized for a particular wavelength range and grating height to obtain the highest enhancement factors. Reflectivity and electric field intensity plots were obtained on simulated silver gratings with duty cycles between 0.25 and 0.85. The ideal duty cycle to obtain the highest electric field intensity is 0.4 according to the simulation results, but at the duty cycles found on the experimental gratings, the electric field intensity should be stronger for the thermally evaporated samples than the sputtered silver samples. The reflectivity plots and electric field profiles

provided in Fig. 3-10, further suggest that gratings with 40 nm grating height exhibit higher electric field strengths at most duty cycles.

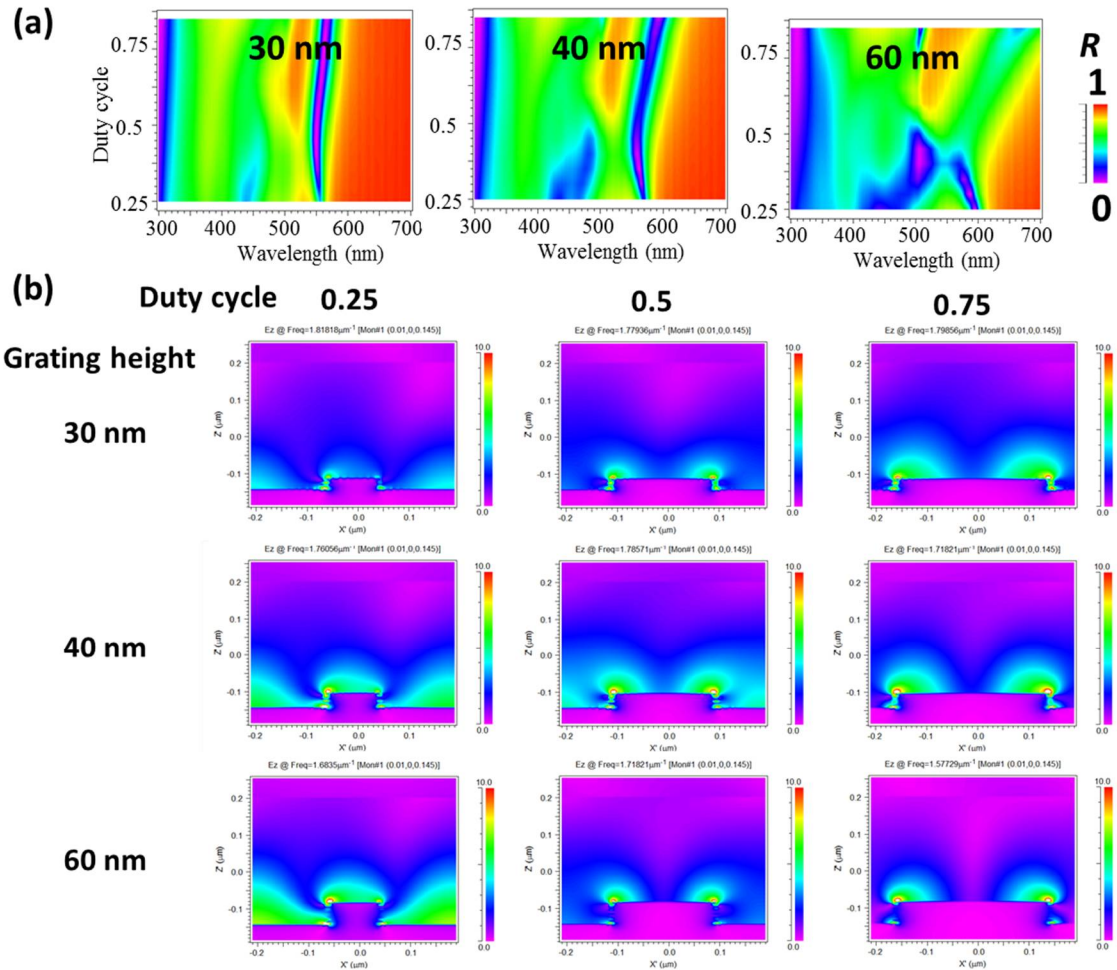


Figure 3-10. (a) Reflectance (R) vs. wavelength for varying grating duty cycles from 0.25 to 0.85 with a constant grating height of 30 nm, 40 nm or 60 nm under each condition. (b) Electric field distribution ($E_z/E_{z,0}$) for silver gratings with varying duty cycle from 0.25 to 0.75 with grating heights of 30 nm, 40 nm and 60 nm, at 15° angle of TM-polarized incidence in air under the wavelengths at reflectivity dips, maximum $E_z/E_{z,0}$ in scale bar is normalized at 10.

3.8. Deposition Alignment Impact on Grating properties

The sensitivity to grating orientation and plate position was also tested with thermally evaporated and RF sputtered gratings, to determine if a radial or circumferential alignment yielded the most consistent enhancement properties. To

do so, gratings were aligned either radially or circumferentially on a silicon wafer and attached with kapton tape. All samples were O₂ plasma treated for 30 sec. at 7 W before deposition. The samples were coated with 100 nm of silver using either thermal evaporation or RF sputtering, and all samples were coated with a 10 nm of Al₂O₃ via ALD. All samples were characterized using AFM to obtain grain diameters, roughness, ridge height, and pitch which are provided in Table 3-5.

A 1% PMSSQ solution with 10 μM R6G in ethanol was spin-coated onto the grating samples and the resulting enhancement was calculated for each sample with respect to a glass sample spin-coated with the same dye solution. The grating ridge orientation (Fig. 3-11(a)) and resulting fluorescent intensity for the thermally evap. gratings has been provided in Fig. 3-11(b) and RF sputtering in Fig. 3-11(c).

Table 3-5. Grating structure summary for various plate positions and orientations.					
	Position and Orientation (C: Circumferential) (R: Radial)	Grating Avg. Height (nm)	Grating Avg. Pitch (nm)	RMS Roughness (nm)	Avg. Grain Diam. (nm)
Thermal Evap.	Center	50.7 ± 2.3	394.8 ± 6.1	3.0 ± 0.2	55.4 ± 17.4
	#1 – C	52.4 ± 4.7	402.2 ± 2.9	3.2 ± 0.2	52.5 ± 14.2
	#2 – C	49.4 ± 3.9	396.0 ± 6.8	2.9 ± 0.2	50.0 ± 13.9
	#3 – C	43.8 ± 2.1	395.5 ± 13.	2.9 ± 0.6	57.8 ± 16.1
	#1 – R	15.2 ± 3.3	401.3 ± 3.7	3.0 ± 0.6	66.4 ± 14.9
	#2 – R	37.9 ± 1.9	399.3 ± 14.0	2.9 ± 0.3	56.5 ± 12.9
	#3 – R	49.9 ± 3.7	403.9 ± 14.5	2.9 ± 0.2	59.7 ± 18.2
RF Sputtering	Center	56.4 ± 2.1	400.67 ± 13.0	2.2 ± 0.2	65.5 ± 21.7
	#1 – C	59.7 ± 3.0	401.17 ± 9.0	2.3 ± 0.1	71.3 ± 20.8
	#2 – C	50.1 ± 3.9	399.33 ± 6.5	2.3 ± 0.3	74.0 ± 18.9
	#3 – C	55.9 ± 2.8	400.03 ± 9.4	2.1 ± 0.2	68.9 ± 19.6
	#4 – C	60.8 ± 2.3	398.67 ± 8.0	2.3 ± 0.1	65.2 ± 14.9
	#1 – R	52.9 ± 2.3	397.33 ± 5.2	2.1 ± 0.3	52.2 ± 13.0
	#2 – R	57.6 ± 2.6	396.67 ± 4.5	2.2 ± 0.2	61.7 ± 16.1
	#3 – R	55.0 ± 1.9	399.00 ± 4.3	2.1 ± 0.2	66.3 ± 18.1
#4 – R	54.7 ± 1.7	398.17 ± 4.3	2.5 ± 0.1	62.4 ± 14.7	

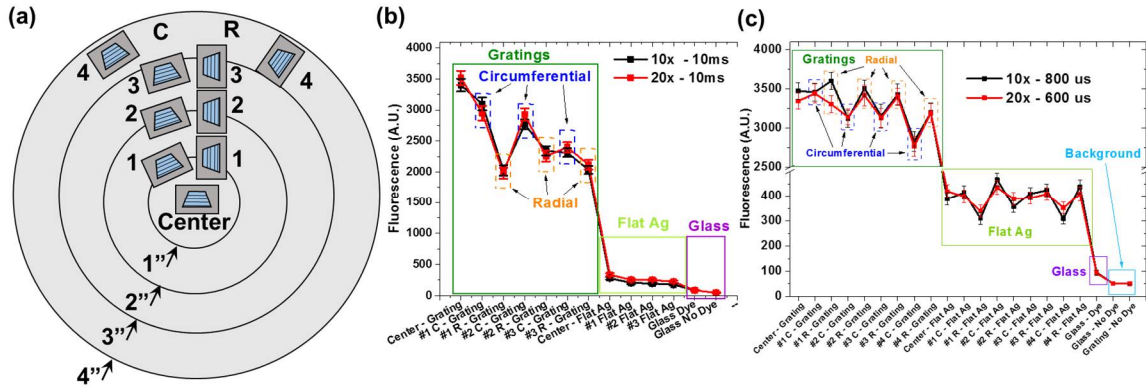


Figure 3-11. (a) Grating orientation and plate position identification diagram on an 8 in. silicon wafer. C: Circumferential, R: Radial. (b) Fluorescence enhancement factors with respect to glass at for silver gratings deposited with (b) thermal evaporation and (c) RF sputtering at different positions and orientations.

Based on Table 3.5, little change can be observed in grating pitch between the deposition methods and orientation. For thermally evaporated gratings, however, the circumferentially aligned gratings exhibited taller ridge heights as well as smaller grain diameters than radially aligned gratings. Thermally evaporated adatoms impinge on the grating at 6° , 12° , and 18° from sample normal at sample positions 1, 2, and 3, respectively, which causes a slight shadowing of the groove region. This results in a higher concentration of adatoms impinging on the ridge and, due to the lower mobility of thermally evaporated adatoms, this increases the metal ridge height of the grating. This is not the case for radially aligned gratings where all sides of the grating are equally exposed to the flux. Due to the rapid deposition of adatoms, the silver film has a tendency to partially planarize the grating by disproportionately filling the grooves of the grating which results in a lower grating height and fluorescent intensity as seen in Fig. 3-11(b).

For RF sputtered gratings, a similar trend with increased ridge height and grain diameter is observed with circumferentially oriented gratings. However, the

preferential deposition of silver on the grating ridges for circumferentially aligned gratings results in more variability in the ridge height as well as an increased grain diameters on the ridges but smaller grains in the grooves. However, radially aligned gratings have more a uniform film thickness, grating heights, and smaller grain size. The variation in the grain size and ridge height of the circumferentially oriented gratings resulted in more variable, and lower fluorescence intensity (Fig. 3-11(c)) than radially aligned gratings. Therefore, if the goal of the deposition is to obtain more uniform grating parameters results across the deposition plate, circumferential alignment should be used for thermally evaporated coatings and radial alignment should be used for sputtered coatings.

3.9. Conclusion

In summary, this paper offers an inexpensive method of fabricating gratings that are capable of enhancing fluorescence emission intensity using a simple epifluorescence microscope. It was found that the silver film properties, such as larger grain sizes, can substantially widen the range of coupled wavelengths, increase the coupling efficiency of light into the grating from 30.9% to 84.9%, and reduce the dielectric losses of the metal film. The sharpness and location of the silver grains also played an important role in concentrating the surrounding electric field formed during SPR. The grating structure, such as duty cycle and ridge height, also played a critical role in the formation of intense, symmetrical electric field profiles that were critical in exciting nearby fluorescent molecules. The wider range and more efficient coupling of light into the grating were better utilized for fluorescence enhancement by illumination the grating with the light cone of

microscope objectives instead of single angle illumination techniques. The results of this paper also demonstrate the importance of characterizing the metal film properties of a plasmonic grating, properties that are often overlooked in many plasmonic grating design literature. By combining the low loss, field localizing properties of large silver grains with a wide range, light coupling properties of plasmonic gratings can result in fluorescence enhancements up to 116× that of dye-coated glass samples. By developing a high fluorescence enhancement plasmonic grating for use in a conventional fluorescence microscope and reducing the expense of its manufacture, it enables the use of this platform in laboratories with little to no system modifications and can be used to replace glass slides and other generic substrates in fluorescence-based assays.

3.10. Experimental Methods

HD DVD Grating Replication. HD DVDs are composed of a metal and light sensitive dye layer laminated between two 0.6 mm-thick polycarbonate (PC) sheets with imprinted gratings (Memorex HD DVDs: 400 nm pitch, 60 nm height). PC gratings were exposed by splitting the HD DVD in half followed by sequential rinses in isopropanol and DI water to remove the organic dye layer. Once exposed, the disc was cast in 5:1 base/cure agent polydimethylsiloxane (PDMS) (Sylgard® 184 silicone elastomer kit, Dow Corning, Inc.) and allowed to cured over 24 hours at 21^oC and 50% relative humidity. PDMS stamps were cut from the mold and spin-coated at 3000 RPM for 30 seconds in a rapidly curing polymer “ink” made from a 3% wt./wt. polymethylsilsesquioxane (PMSSQ, GR650F Techneglass, Inc.) and 0.05% vol. 3-aminopropyltriethoxysilane (APTES) in 100% ethanol. APTES

was added to further crosslink the stamped grating and obtain better adhesion to the substrate. The PDMS was immediately stamped onto a glass slide and removed. Post stamping, all gratings were heat treated at 60°C for 30 min to further crosslink the PMSSQ/APTES grating. Half of the gratings were treated with oxygen plasma for 30 seconds at 7 Watts using a plasma enhanced chemical vapor deposition (PECVD) system immediately before metal deposition.

RF Sputtering of Germanium/Silver and Titanium/Silver films. An AJA International OTC Orion magnetron sputtering system was used to deposit titanium and silver films. Three-inch titanium and silver targets (99.999 % purity – Kurt J. Lesker) were mounted to two sputtering guns. Before deposition, the chamber was pumped down to 5.4×10^{-8} Torr and titanium and silver targets were pre-sputtered for 600 s at 100 W to clean the target and to remove any pre-existing oxide layer from the target surface. A 5 nm thick germanium or titanium adhesion layer followed by a 100 nm thick silver layer was deposited with a 100 W RF power at a working pressure of 4 mTorr, ambient temperature (~300 K), six-inch throw distance, and 20 RPM sample rotation. Germanium and titanium were deposited at 0.1 nm/s while silver was deposited at 0.17nm/s.

Thermal Evaporation of Chromium/Silver films. Chromium and silver films were thermally depositing using a Nano 38 Thermal evaporator from Kurt J Lesker. The chamber was first pumped down to 2.8×10^{-8} Torr. A 5 nm thick chromium adhesion layer and 100nm silver layer were deposited sequentially. Chromium was deposited at the rate of 0.005 nm/s while silver, initially is deposited at the rate of 0.005 ~ 0.01 nm/s for the first 5nm and then increased to 0.05nm/s for the rest of

silver deposition. Deposition thicknesses for the RF sputtering and thermal evaporator were calibrated before deposition and confirmed with an optical profilometer (Wyko NT 9100, Veeco Instruments, Inc.) and step profilometer (Alpha-Step 200, TENCOR Instruments, Inc.).

Surface and Optical Characterization. Surface structure was examined with a Bruker © Innova AFM equipped with an open-loop, small area scanner and AppNano ACTA silicon SPM tips (k: 40 N/m, f: 295 kHz, tip radius: ~6 nm). Reflectivity measurements at different wavelengths and incidence angles as well as spectroscopic scans to obtain the dielectric properties were acquired using a variable angle spectroscopic ellipsometer with a Xeon broadband source (VASE®/HS-190, J.A.Woollam Co, Inc.). Grating ridges were aligned vertically and scanned with transverse-magnetic (TM) light at wavelengths from 200-2000 nm and at angles of incidence from 15-60°.

Fluorescence Enhancement. Silver grating samples were spin-coated at 3000 RPM for 30 seconds with a 1% wt. PMSSQ solution with 10 µM Rhodamine 6G (excitation: 530 nm, emission: 550 nm) in pure ethanol. This produced a conformal, 30 nm-thick layer of fluorophore-laced PMSSQ on top of the gratings. The addition of this layer immediately after metal deposition is also thought to reduce the short term corrosion of the silver layer. The gratings were imaged with an Olympus BX51WI epifluorescence microscope equipped an ORCAFlash 2.8 CMOS camera, 10/20/40× objectives, 60× oil immersion objective, and illuminated with either a xenon broadband light source or high power 455 nm LED light source.

Electric Field and Reflectivity Simulations. Electric field strengths and reflectivity at different wavelengths for different silver grain sizes, grating heights, and duty cycles were simulated using Finite Difference Time Domain (FDTD) software (FullWave by Synopsys.) The configuration used for two-dimensional (2D) models was based on HD DVDs grating with a grating pitch of $\Lambda = 400$ nm with and without a conformal, 35 nm PMSSQ coating. A monitor located above the launch field was used to measure reflectivity while another monitor encompassing the computational window was used to measure the EM field strength. In the x-direction, a periodic boundary condition was selected due to the periodicity of gratings. In the z-direction, PML (perfectly matched layer) and PEC (perfect electric conductor) boundary conditions were used for the maximum and minimum z value boundary, respectively. A uniform grid size of $2 \text{ nm} \times 2 \text{ nm}$ was used for the computational domain for reflectivity measurements and $5 \text{ nm} \times 5 \text{ nm}$ for grain size, grating height, and duty cycle simulations, respectively. A computational stop time of $40 \mu\text{m}$ (in units of cT) was chosen to obtain stability and was excited with a continuous wave (CW) excitation source.

CHAPTER 4: CORTISOL BIOSENSOR

4.1. Introduction

Cortisol is a hormone that plays a critical role in the reduction of inflammation in the body, and its active concentration can be utilized to measure stress levels of patients in a multitude of healthcare settings (Fig. 4-1(a).) The concentration of cortisol in the body follows the circadian rhythm (Fig. 4-1(b)), where cortisol concentration peaks in the morning just after awakening and decreases throughout the day.[79] Elevated cortisol levels impede cell growth and thus contribute to less effective healing. By measuring cortisol levels, the outcomes of these patients can not only be predicted but influenced by adding therapeutic interventions titrated to their cortisol levels.

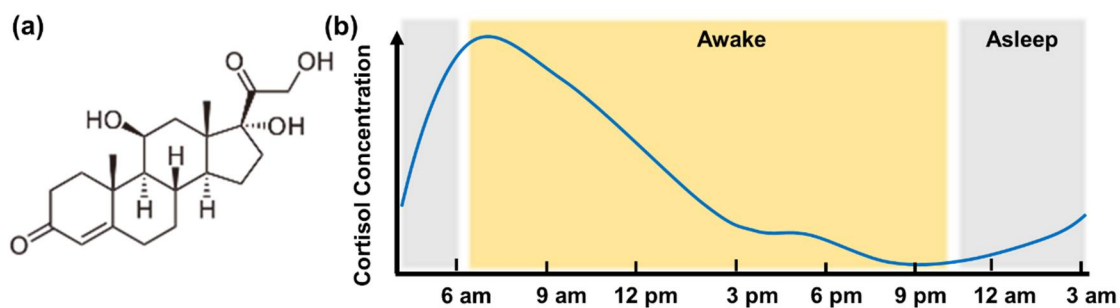


Figure 4-1. (a) Cortisol molecule diagram and (b) cortisol serum concentration throughout a 24 hr. period.

Additionally, patients suffering from psychological conditions such as post-traumatic stress disorder can benefit from cortisol assessment in tandem with interventions to decrease anxiety such as biofeedback in which the patient uses guided thought processes to decrease stress (e.g. cortisol) levels thereby

enhancing the efficacy of cognitive behavioral therapy which is the most commonly used technique in treatment of this disorder.

The current primary method to measure cortisol is an invasive blood test, which is especially difficult to perform on children, as the stress caused by the testing itself can distort the true stress levels of the child.[80-82] Blood is primarily used as the biological fluid of choice as the concentration is very high (Table 4-1) and easily quantifiable with enzyme-linked immunoassay (ELISA) kits. Alternative biofluids for cortisol measurement include urine, saliva, interstitial fluid, and sweat. Saliva is particularly attractive since it is easy to obtain, and saliva cortisol levels are directly proportional to the free cortisol concentration in blood serum. [83] Another advantage of using salivary cortisol is that all of the cortisol is in its unbound state whereas only a small portion of the cortisol is unbound in blood. However, the saliva cortisol concentration (0.5-5 ng/mL) is much lower than in blood (20-250 ng/mL) [80, 84], which is outside the detection capability of many current sensors or requires expensive, bulky detection equipment.

Table 4-1. Normal Adult Physiological Range of Cortisol and Sodium in Body Fluids					
	Blood	Urine	Saliva	ISF	Sweat
Cortisol (ng/mL)	20 – 250 [85]	100 – 1000 (ng/day) [85]	0.5 –5 [80, 84]	0.15 – 15 [86]	8.16 – 141.7 [87]

Over the past few years, a substantial research effort has been made to design high-sensitivity biosensors to quantify low concentrations, even single molecule levels, of target chemicals and other analytes. SPR-based biosensors have been close to the core of this research as they have the capacity to significantly reduce the current limits of detection (LOD) to never before seen concentrations.

An inexpensive soft lithography process was developed in previous chapters that can replicate the gratings found on HDDVD and Blu-ray discs into plasmonic gratings that significantly enhance the emission intensity of any fluorescent dye in the visible light spectrum within a few 100 nm of the grating surface. These plasmonic gratings enhance fluorescence emission intensity to levels high enough that they enable the ability to perform ultrasensitive fluorescence detection of single dye molecules with conventional optics.[88] Prior research has demonstrated that silver produces higher fluorescence enhancement than other metals due to reduced losses in the visible spectrum.[89] However, the vulnerability of silver films to corrosion has severely limited its use in biosensors. This vulnerability has forced most researchers to use only gold at the expense of the SPR-based enhancement.

To protect the unique enhancement capabilities of silver films in biological solutions, we developed thin film coating strategies using a 10 nm thick alumina coating to protect the silver from corrosion with minor effect on plasmonic enhancement. The protected plasmonic gratings were incorporated into two types of immunoassays to quantify cortisol concentration: Sandwich and Competitive binding assays.

4.2. Cortisol Antibody Specificity

Before the development of the assays, a selection of antibodies for cortisol was tested to determine the binding specificity and binding location: XM210 (Monoclonal Mouse α -Cortisol, Pierce), M344 (Monoclonal Mouse α -Cortisol-3CMO-BSA, CalBioscience), 20-CR50 (Polyclonal Rabbit α -Cortisol-3CMO-BSA),

and PA1-85347 (Polyclonal Sheep α -Cortisol-21HS-BSA). There are two primary binding sites on cortisol, location 21 (OH group on the right side of Fig. 4-1(a)) and 3 (carbonyl on the left side of Fig. 4-1(a).) Two forms of cortisol, Cortisol-3, CMO-BSA and Cortisol-21, HS-BSA, were used to determine the binding specificity where either the 21 or 3 location was bound to bovine serum albumin (BSA) which eliminates any antibody binding to the location.

Cortisol-3, CMO-BSA and Cortisol-21, HS-BSA were immobilized onto silanized glass slides (see protocol below) and blocked using BSA alone. All samples were exposed to one of the antibodies mentioned previously and exposed to an AlexaFluor 488-labeled polyclonal antibody that binds to the host of the previously exposed antibody. The fluorescence images and intensity from the specificity assay have been provided in Fig. 4-2.

Specificity Assay Protocol:

1. Glass microscope slides are cleaned by sequential sonication in acetone, methanol, and DI water for 5 min. each and immersed in piranha (3:2 sulfuric acid to hydrogen peroxide (30% active) for 15 min. and rinsed with a copious amount of DI water.
2. Glass samples were immersed in toluene with 2% vol. APTES in a 50 mL centrifuge tube in a nitrogen-filled glove bag for 1 min. Glass slides were then rinsed in toluene followed by ethanol and dried in a stream of nitrogen.
3. Glass samples were then placed in small petri dishes and exposed to 100 μ L of PBS with 0.5% wt./vol. of either Cortisol-3, CMO-BSA and Cortisol-21, HS-BSA for 2 hrs. Glass slides were rinsed three times for 5 min. each

in 1xPBS with 0.1% vol. NP-40 surfactant followed by one 5 min. rinse in 1xPBS.

4. Glass samples were exposed to 2 mL of PBS with 3% wt./vol. BSA for 2 hours to block the surface. Glass slides were rinsed three times for 5 min. each in 1xPBS with 0.1% vol. NP-40 surfactant followed by one 5 min. rinse in 1xPBS.
5. Glass samples were exposed to 2 mL of 1xPBS with 2.5 µg/mL of anti-cortisol antibodies for 2 hrs. Glass slides were rinsed three times for 5 min. each in 1xPBS with 0.1% vol. NP-40 surfactant followed by one 5 min. rinse in 1xPBS.
6. Glass samples were exposed to 2 mL of 1xPBS with 2.5 µg/mL of AF488-labeled anti-host polyclonal antibodies for 2 hours. Glass slides were rinsed three times for 5 min. each in 1xPBS with 0.1% vol. NP-40 surfactant followed by one 5 min. rinse in 1xPBS.
7. Glass slides were imaged in 1xPBS with a glass coverslip and a 20x objective.

The binding results of the specificity assay indicate that XM210 only binds to location 21 of cortisol and exhibited a similar response as M344 but had better surface binding. PA1-85347 had the best reactivity with location 3 and low reactivity with location 21. 20-CR50 had better reactivity with location 21 but also showed cross-reactivity with location 3. Based on these results, XM210 and PA1-85347 were selected as the ideal antibody pair for a sandwich assay and XM210

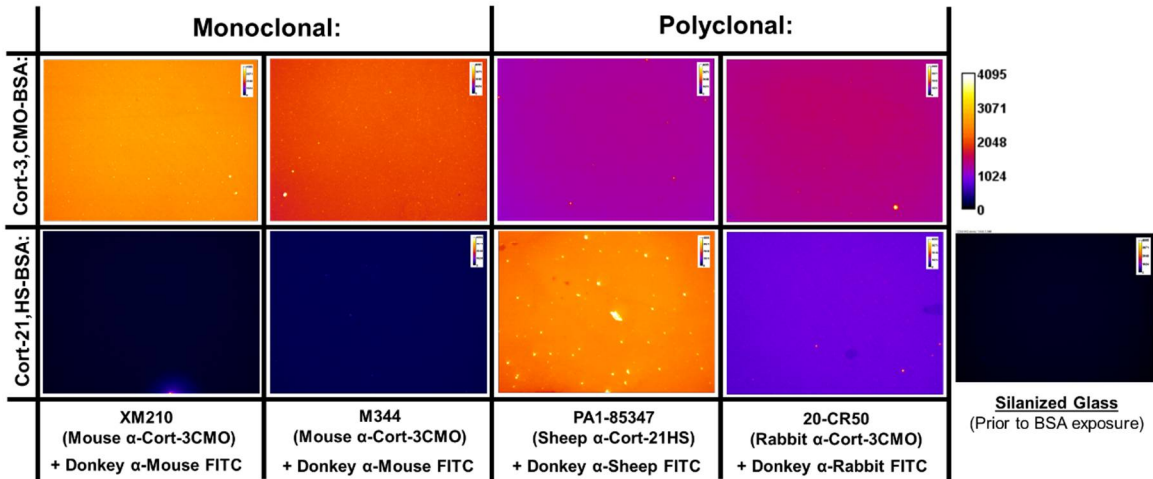


Figure 4-2. Fluorescence images of various cortisol-binding antibodies bound to substrates with either Cortisol-3, CMO-BSA or Cortisol-21, HS-BSA. All fluorescence images were taken with a 20x objective and 2 sec. exposure.

was selected as the antibody for the competitive binding assay.

4.3. Sandwich Fluoroimmunoassay

Sandwich immunoassays use a pair of antibodies that bind to separate sites of an antigen, in this case, cortisol. The assay is composed of a surface-bound antibody, also known as the capture antibody, and a fluorescently-labeled antibody, also known as the detection antibody. A diagram of the sandwich immunoassay has been provided in Fig. 4-3. The assay is conducted in the following order: 1) the capture antibody is immobilized onto the surface, 2) sensor is exposed to the biological fluid containing cortisol, 3) the sensor is exposed to the detection antibody, and 4) the sensor is imaged, and the fluorescent intensity is directly proportional to the cortisol concentration in the biological fluid.

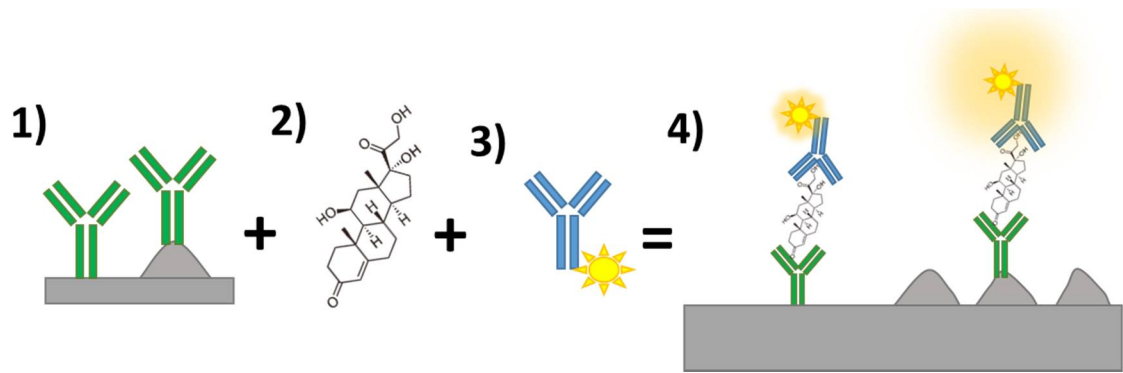


Figure 4-3. Illustration of the Sandwich fluoroimmunoassay for cortisol.

One advantage of a sandwich immunoassay over competitive binding is that the specificity is inherently higher as two antibodies must bind to the target to result in the fluorophore being attached to the surface. Essentially, two keys are needed to open a single lock. However, the use of a sandwich assay may not be ideal as cortisol is a small molecule and the epitope, the binding site, of the antibodies are larger than cortisol. Only one article could be found that used a sandwich immunoassay to detect cortisol but the same pair of antibodies used could no longer be purchased from the original supplier.[90]

Based on the results in Fig. 4-2, XM210 was selected as the capture antibody as it showed the highest binding affinity of any antibody tested and would have the least probability of releasing the cortisol during the rinsing steps. A process was developed to immobilize XM210 onto a silanized glass surface via 1-Ethyl-3-(3-dimethylaminopropyl)carbodiimide (EDC) and N-hydroxysulfosuccinimide (NHS) crosslinking chemistry, detailed in the protocol below. The binding results of the different antibodies are provided in Fig. 4-4.

Antibody Immobilization Assay protocol:

1. Silanized glass slides were exposed to 75 μ L of 0.1 M MES solution at pH 6.0 with 3.2 mg/mL EDC and 8.8 mg/mL NHS for 12 min.
2. 75 μ L of 0.1 M MES solution at pH 8.0 with 2.5 μ g/mL of XM210 was added to the incubation solution and either left to incubate on the shaker table for 2 hrs. or left to incubate overnight at 4°C. Glass slides were rinsed three times for 5 min. each in 1xPBS with 0.1% vol. NP-40 surfactant followed by one 5 min. rinse in 1xPBS.
3. Glass samples were exposed to 2 mL of PBS with 3% wt./vol. BSA for 2 hours to block the surface. Glass slides were rinsed three times for 5 min. each in 1xPBS with 0.1% vol. NP-40 surfactant followed by one 5 min. rinse in 1xPBS.
4. Glass samples were exposed to 2 mL of 1xPBS with 5 μ g/mL of FITC-labeled donkey anti-mouse antibodies for 2 hrs. Glass slides were rinsed three times for 5 min. each in 1xPBS with 0.1% vol. NP-40 surfactant followed by one 5 min. rinse in 1xPBS.
5. Glass slides were imaged in 1xPBS with glass coverslip and a 20x objective.

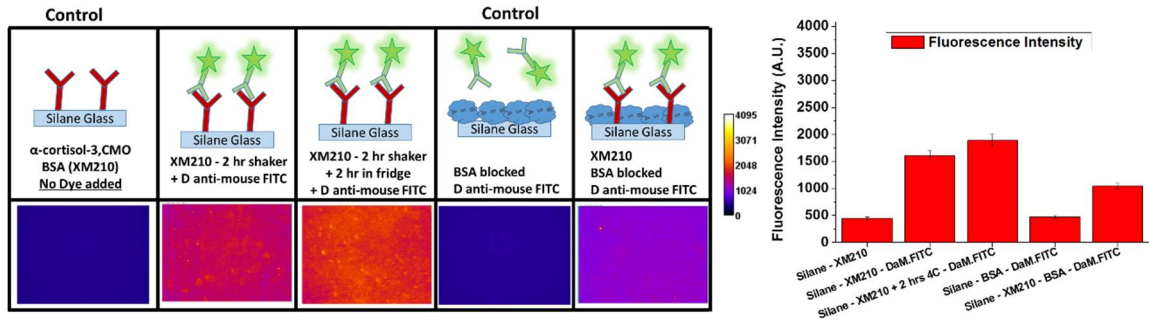


Figure 4-4. Antibody immobilization assay fluorescence images and intensity. All images were taken with a 20x objective and an exposure time of 700 msec.

Based on Fig. 4-4, an improved immobilization efficiency was observed when the capture antibody incubated overnight at 4°C in addition to 2 hrs. on the shaker plate. Thus for all future EDC-based immobilization protocol, antibodies were incubated overnight at 4°C.

After the capture antibody could be immobilized, the detection antibody needed to be fluorescently labeled. PA1-85347 was selected as the detection antibody and was labeled with AF532 (R6G equivalent dye) using a LifeScience labeling kit. We obtained a ~750 μ L of dye labeled antibodies at ~1.26 mg/mL. The labeling efficiency was calculated to be 0.552 mol dye per mol protein which was not ideal but sufficient for preliminary testing. The results of the sandwich assay have been provided in Fig. 4-5.

Sandwich Immunoassay Protocol:

1. Silanized glass slides were exposed to 75 μ L of 0.1 M MES solution at pH 6.0 with 3.2 mg/mL EDC and 8.8 mg/mL NHS for 12 min.
2. 75 μ L of 0.1 M MES solution at pH 8.0 with 2.5 μ g/mL of XM210 was added to the incubation solution and were left to incubate overnight at 4°C. Glass

slides were rinsed three times for 5 min. each in 1xPBS with 0.1% vol. NP-40 surfactant followed by one 5 min. rinse in 1xPBS.

3. Glass samples were exposed to 2 mL of PBS with 3% wt./vol. BSA for 2 hours to block the surface. Glass slides were rinsed three times for 5 min. each in 1xPBS with 0.1% vol. NP-40 surfactant followed by one 5 min. rinse in 1xPBS.
4. Glass samples were exposed to 2 mL of 1xPBS with a cortisol concentration from the standard salivary cortisol ELISA curve. (0, 0.05, 0.12, 0.37, 1.11, 3.33, 10, and 30 ng/mL cortisol) for 2 hrs. Glass slides were rinsed three times for 5 min. each in 1xPBS with 0.1% vol. NP-40 surfactant followed by one 5 min. rinse in 1xPBS.
5. Glass samples were exposed to 2 mL of 1xPBS with 2.5 µg/mL of AF532-labeled PA1-85347 antibodies for 2 hrs. Glass slides were rinsed three times for 5 min. each in 1xPBS with 0.1% vol. NP-40 surfactant followed by one 5 min. rinse in 1xPBS.
6. Glass slides were imaged in 1xPBS with a glass coverslip and a 20x objective.

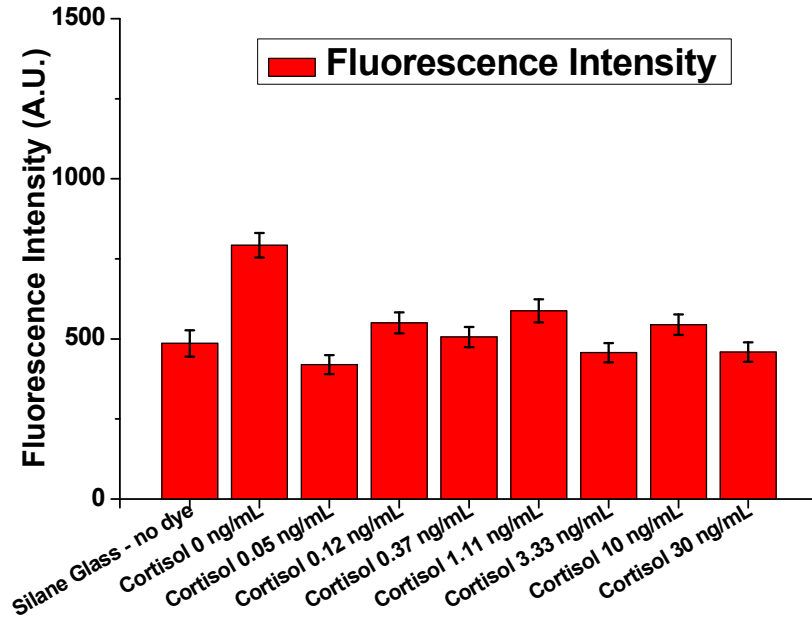


Figure 4-5. Sandwich assay fluorescence intensity results. Fluorescence imaged with the R6G fluorescence filter, 20x Obj., and 2 sec. CMOS exposure.

No observable trend in fluorescence intensity with cortisol concentration was observed with the sandwich assay. It was determined that the antibody pair was not compatible, i.e. both XM210 and PA1-85347 could not both be bound to the same cortisol molecule at the same time. However, the immobilization protocols and XM210 could be easily converted to a competitive binding assay protocol.

4.4. Competitive Binding Fluoroimmunoassay

In a competitive binding assay, a form of the target analyte, in this case, Cortisol-3, CMO-BSA, is immobilized onto the sensor surface instead of the capture antibody. At the same time, a patient sample containing cortisol is incubated with a cortisol binding antibody, XM210, for a set period of time. The XM210 is free to bind to all of the cortisol found in the patient sample. The patient sample with bound XM210 is then incubated with the sensor surface with Cortisol-3, CMO-BSA. Any

free XM210 left in the patient sample binds to the sensor surface. The antibody can either be fluorescently-labeled, or a dye-labeled secondary antibody can be incubated with the sensor surface. The competition between the antibody binding to the patient sample or the surface immobilized cortisol is the reason the assay is referred to as a competitive binding assay. The competition results in an inverse relation between the fluorescence intensity of the sensor and the cortisol concentration in the patient sample. The competitive binding assay process has been illustrated in Fig. 4-6.

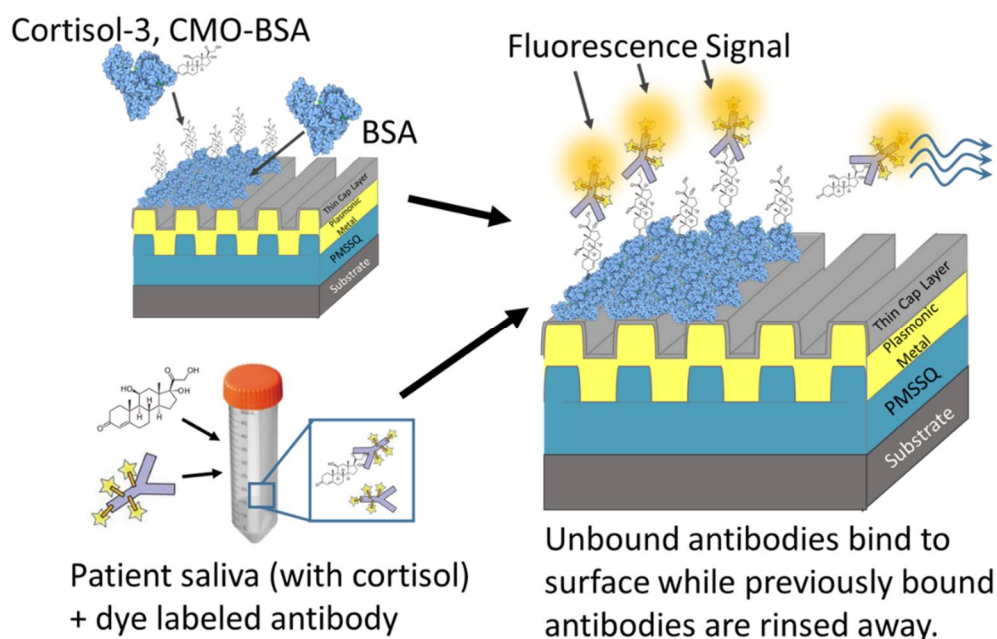


Figure 4-6. Illustration of the Competitive binding fluoroimmunoassay for cortisol.

CO₂ Plasma treatment. While transitioning from plain glass to alumina-coated gratings, the alumina layer on the grating must be functionalized with either carboxylic acid groups or amine groups to obtain the best immobilization efficiency. Gratings were CO₂ plasma treatment using a plasma enhanced chemical vapor deposition (PECVD) chamber. Due to the fragility of the alumina layer, the plasma

exposure time needed to be minimized to reduce the probability for a defect to form in the alumina layer but still long enough to provide an ample number of COOH groups on the surface. A 10 nm thick alumina capping layer was deposited onto both 100 nm thick RF sputtered silver gratings and glass control samples be used to determine the appropriate plasma exposure time. All samples were treated with CO₂ plasma for 0, 30, 60, or 120 sec. at 7 watts and exposed to BSA-FITC for 12 hrs. The fluorescence intensity of all of the samples was measured to determine the exposure time with maximum binding efficiency. The protocol for the experiment can be found below.

Plasma Exposure Optimization protocol:

1. Silver gratings and glass samples were exposed to CO₂ plasma (n=3 for each exposure time) for 0, 30, 60, or 120 sec. at 7 watts.
2. ¼" diameter PDMS wells were punched from 1" x 1" x 1/8" thick PDMS blocks and placed on top of the samples before BSA-FITC exposure.
3. Within 5 min. of plasma treatment, 70 µL of 1x MES buffer at pH 6.0 with 22 mg/mL NHS and 8 mg/mL EDC was added to each well and incubated at 25°C for 12 min.
4. 70 µL of 1x MES buffer at pH 8.0 with 6.6 mg/mL BSA-FITC was added to each well and incubated at 25°C for 1 hr. followed by incubation overnight at -4°C.
7. All samples were rinsed five times for 5 min. each in 1xPBS with 0.1% vol. NP-40 surfactant followed by two 5 min. rinses in 1xPBS.

5. PDMS wells were removed, glass coverslips were cut for each sample, and imaged with the 10x objective.

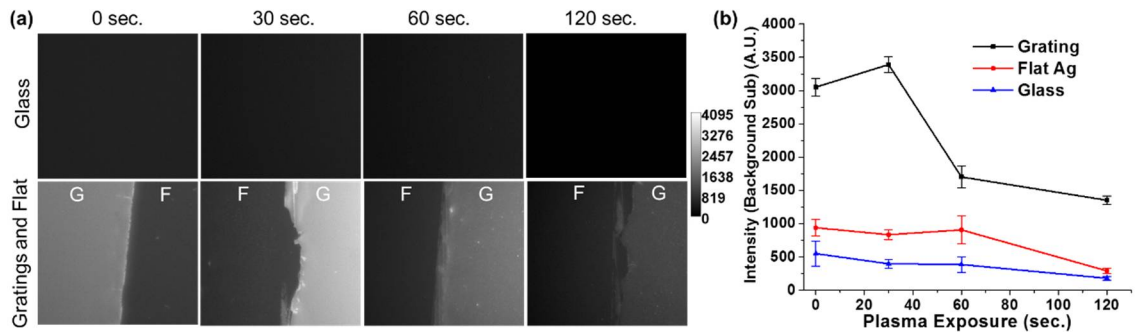


Figure 4-7. (a) Fluorescence Images of gratings, flat silver regions, and glass taken with a 10x objective lens and normalized to 300 ms exposure (Image dimensions: 700 μm x 520 μm .) (b) Fluorescence intensity from alumina-capped gratings, flat silver regions, and glass samples exposed to CO₂ plasma at 7W for 0, 30, 60, or 120 sec. and bound to BSA-FITC.

In addition to the fluorescence images found in Fig. 4-7(a), significant corrosion and peeling of the silver layer was observed for gratings exposed to CO₂ plasma for 60 sec. or more. Based on Fig. 4-7, the optimal plasma exposure time with the least damage to the alumina layer was 30 sec. All future binding experiments will include 30 sec. of CO₂ plasma exposure before protein binding.

PDMS wells and prevention of content leakage. Transitioning from a small petri dishes to PDMS wells for sensor incubations was deemed critical to the long-term survival of the gratings in biological fluids as the alumina on the edges have defects that could be corroded. Thus 1/4" diameter, 1/8" thick PDMS wells were also tested during the previous plasma exposure time studies to determine if the PDMS should or shouldn't be present during plasma exposure. 10 nm alumina capped 100 nm thick silver gratings were exposed to 30 sec. of CO₂ plasma at 7 watts with and without a PDMS well. 150 μL of 1x MES with 0.25% wt./vol. BSA-FITC was incubated in the wells for 18 hours, rinsed three times in PBS+0.1% Tween

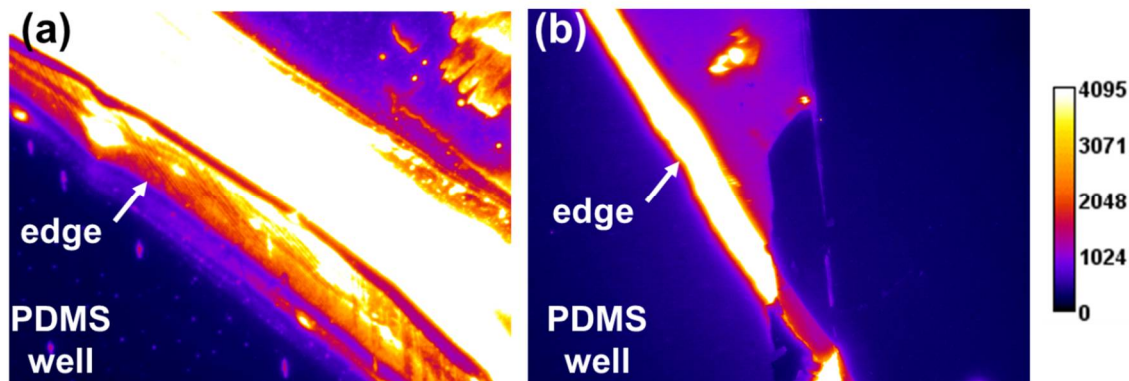


Figure 4-8. Normalized fluorescence images were taken with a 20x objective ($350\mu\text{m} \times 260\mu\text{m}$) of FITC-BSA bound to plasmonic gratings that were exposed to CO₂ plasma with and without PDMS wells during exposure.

20, and PDMS wells were removed immediately before imaging. It should be noted that the PDMS wells had steel spacers (1.5 oz., 3/8" I.D., 1/2" O.D., 1 1/2" long) placed over the top of each well during incubation to press the PDMS into contact with the grating. Fluorescence images of the grating at the edges of the PDMS wells have been provided in Fig. 4-8.

Due to the lack of EDC/NHS during FITC-BSA exposure, the rinsing of the wells with tween-20 resulted in a lack of fluorescence from the well. However, well contents that seeped under the PDMS well would not be removed during rinsing and would appear as a band of bright fluorescence. From Fig. 4-8(a), we find that gratings exposed to plasma with a PDMS well present resulted in substantial seepage of the well contents under the PDMS well. However, in Fig. 4-8(b), we find minor seepage of the well contents when the PDMS well is applied to the grating after plasma exposure. Additionally, the well contents do not spread over the top of the PDMS when applied to the grating after plasma exposure which further reduces the chance of solution loss. Thus, future plasma treatment

protocols will specify that the PDMS wells should be applied after plasma treatment.

XM210 Concentration Optimization: Unlike the sandwich assay, the exact concentration of the antibody is critical to the competitive binding assay. If too high of a concentration of antibodies is added to the patient sample, all of the cortisol will be bound to the XM210 antibodies, and the remaining XM210 antibodies will bind to all of the cortisol on the sensor surface, saturating the binding sites, regardless of the cortisol concentration in the patient sample. If too low of a concentration of antibodies is added to the patient sample, the patient sample will bind to all of the XM210 antibodies and no antibodies will be left to bind to the sensor surface, resulting in no signal from the sensor. As an XM210 antibody is a monoclonal and immunoglobulin type G (IgG), two binding epitopes are present on either branch of the protein. Thus, it is possible that XM210 could bind to more than one cortisol molecule at a time and this should be considered during the selection of XM210 concentration. Varying concentrations of XM210 (1000, 100, 10, 1, 0.1, and 0 nM) were incubated with grating and glass samples with immobilized cortisol-3, CMO-BSA, and the fluorescence response was measured to determine the concentration of XM210 to use during the assay. The protocol for the experiment can be found below.

XM210 Concentration Testing Protocol:

1. 100 nm thick RF sputtered silver gratings and glass samples were capped with a 10 nm alumina layer and exposed to CO₂ plasma for 30 sec. at 7 watts.

2. PDMS wells (cut out of trays and punched with 5/16" punch immediately before plasma) were placed on top of the glass samples and gently pressed to stick to the samples.
3. 75 μ L of 1xMES activation buffer at pH 6.0 with 8.8 mg/mL of NHS and 3.2 mg/mL of EDC was added to each well immediately after plasma treatment and allowed to incubate at 25°C for 12 min.
4. 75 μ L of 1xMES activation buffer at pH 8.0 with 5.5 mg/mL of Cortisol-3,CMO-BSA was added to each well. Samples were placed in a sealed container with a beaker filled with DI water overnight (~15.5 hrs.) at 4°C.
8. The incubation solution was drawn off and samples were rinsed three times with 100 μ L PBS+0.1% Tween 20. 150 μ L of 1xPBS + 5% low fat milk were added to all samples and left to incubate for 15 min. See Fig. 4-9(a).
5. 100 μ L of 1xPBS with a concentration of XM210 corresponding to the concentration curve (1000, 100, 10, 1, 0.1, and 0 nM) was added to each well (n=3 for each concentration) and allowed to incubate for 1 hr. at 25°C. See Fig. 4-9(b).
6. The XM210 incubation solution was drawn off, and samples were rinsed three times with 100 μ L PBS+0.1% Tween 20. 150 μ L of 1xPBS with 5% wt. low-fat milk was added to all samples and rinsed again three times with PBS+0.1% Tween 20.

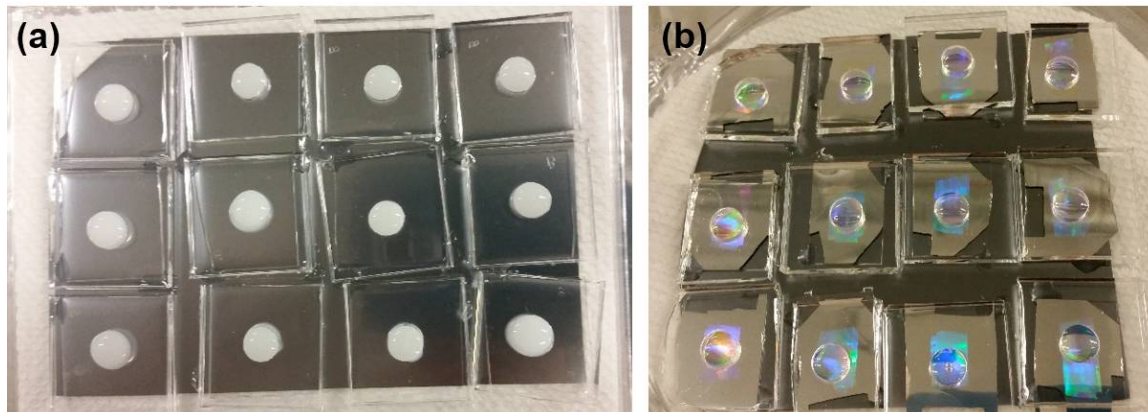


Figure 4-9. (a) Glass samples during exposure to milk blocking solution. (b) Grating samples during exposure to XM210 solution.

7. 100 μL of 1xPBS with 20 $\mu\text{g}/\text{mL}$ of AF568-labeled secondary anti-mouse antibody was added to each well and incubated for 1 hr. at 25°C.
8. The AF568-labeled antibody incubation solution was drawn off and samples were rinsed three times with 100 μL PBS+0.1% Tween 20. 150 μL of 1xPBS with 5% wt. low-fat milk was added to all samples and rinsed again three times with PBS+0.1% Tween 20.
9. 1xPBS was added to every well, and a coverslip was placed on top of each sample for imaging.

The normal salivary cortisol concentration in nM has been overlaid in Fig. 4-10. Several critical parameters can be extracted based on the XM210 binding curve in Fig. 4-10. First, the number of binding sites, Cortisol-3, CMO-BSA, available on both the glass and gratings is slightly higher than 1000 nM as both curves are beginning to taper off near 1000 nM. Second, glass substrates do not exhibit a linear response in fluorescence intensity and is close to the background intensity

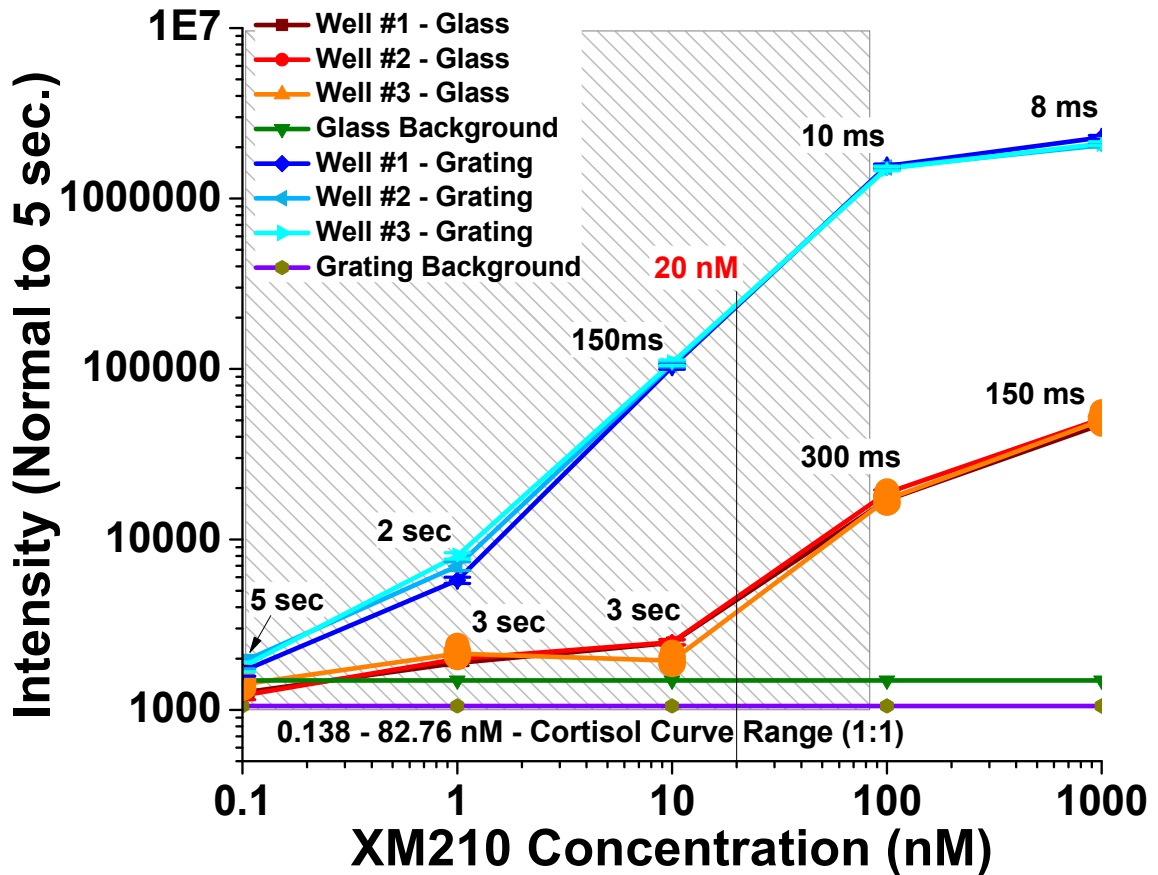


Figure 4-10. Fluorescence intensity (normalized to an exposure time of 5 sec.) at varying XM210 binding concentrations for grating and glass sensors. The original image exposure times are listed by each data point. Fluorescence images were taken with the TRITC filter cube and 10x objective lens.

over most of over the expected salivary cortisol concentration range. Thus, glass should not be able to detect and quantify the normal cortisol concentrations in the saliva. Lastly, a nearly linear response in fluorescence intensity can be observed on grating substrates over the entire cortisol concentration range of interest. Based on this data, an XM210 concentration of 20 nM was selected for future experiments as this concentration would enable fluorescence imaging with exposure times between 100 msec. and 2 sec. for the expected salivary cortisol concentration range. It should be noted that the XM210 binding curve is inversely proportional

to the competitive binding curve, i.e. increased XM210 binding indicates a lower patient cortisol concentration.

Competitive Binding Results: A competitive binding protocol was developed using the parameters obtained in the previous sections for testing with two fluorophores: AF532 and AF568. For testing with AF532 dye, XM210 antibodies were fluorescently labeled using the same type of Lifesciences kit that was used to label PA1-85347 antibodies in the sandwich assay. Despite incubating the antibodies with the reactive dye for 1 hour on a stir plate as recommended by the kit protocol and an additional 3 hours at 4°C the label efficiency was found to be 0.398 mole dye per mole antibody. The label efficiency was sufficient for preliminary testing, but a label efficiency of at least 1 mole dye per mole antibody is necessary for accurate sensing. The protocol for the competitive binding assay with AF532-labeled XM210 can be found below. The resulting fluorescence images of the gratings have been provided in Fig. 4-11(a) and fluorescence intensity in Fig. 4-11(b,c.)

Competitive binding with AF532-labeled XM210:

1. 100 nm thick RF sputtered silver gratings and glass samples were capped with a 10 nm alumina layer and exposed to CO₂ plasma for 30 sec. at 7 watts.
2. PDMS wells (cut out of trays and punched with 5/16" punch immediately before plasma treatment) were placed on top of the glass samples and gently pressed to stick to the samples.

3. 75 μ L of 1xMES activation buffer at pH 6.0 with 8.8 mg/mL of NHS and 3.2 mg/mL of EDC was added to each well immediately after plasma treatment and allowed to incubate at 25°C for 12 min.
4. 75 μ L of 1xMES activation buffer at pH 8.0 with 5.5 mg/mL of Cortisol-3, CMO-BSA was added to each well. Samples were placed in a sealed container with a beaker filled with DI water overnight (~15.5 hrs.) at 4°C.
9. The incubation solution was removed, and samples were rinsed three times with 100 μ L PBS+0.1% Tween 20. 150 μ L of 1xPBS + 5% low-fat milk were added to all samples and left to incubate for 15 min.
5. 1 mL of 1xPBS (mock patient samples) with a concentration of cortisol corresponding to the salivary cortisol ELISA concentration curve (0, 0.05, 0.12, 0.37, 1.11, 3.33, 10, and 30 ng/mL cortisol) was added to 2 mL centrifuge tubes and incubated with 20 nM of XM210 for 2 hrs. at 25°C.
6. 150 μ L of each mock patient sample with a known concentration of cortisol and XM210 was added to each well and incubated for 2 hrs. at 25°C.
7. The incubation solution was removed, and samples were rinsed three times with 100 μ L 1xPBS with 0.1% Tween 20 followed by three rinses with 150 μ L 1xPBS. Coverslips were cut and added to each sample before imaging with a 20x objective lens.

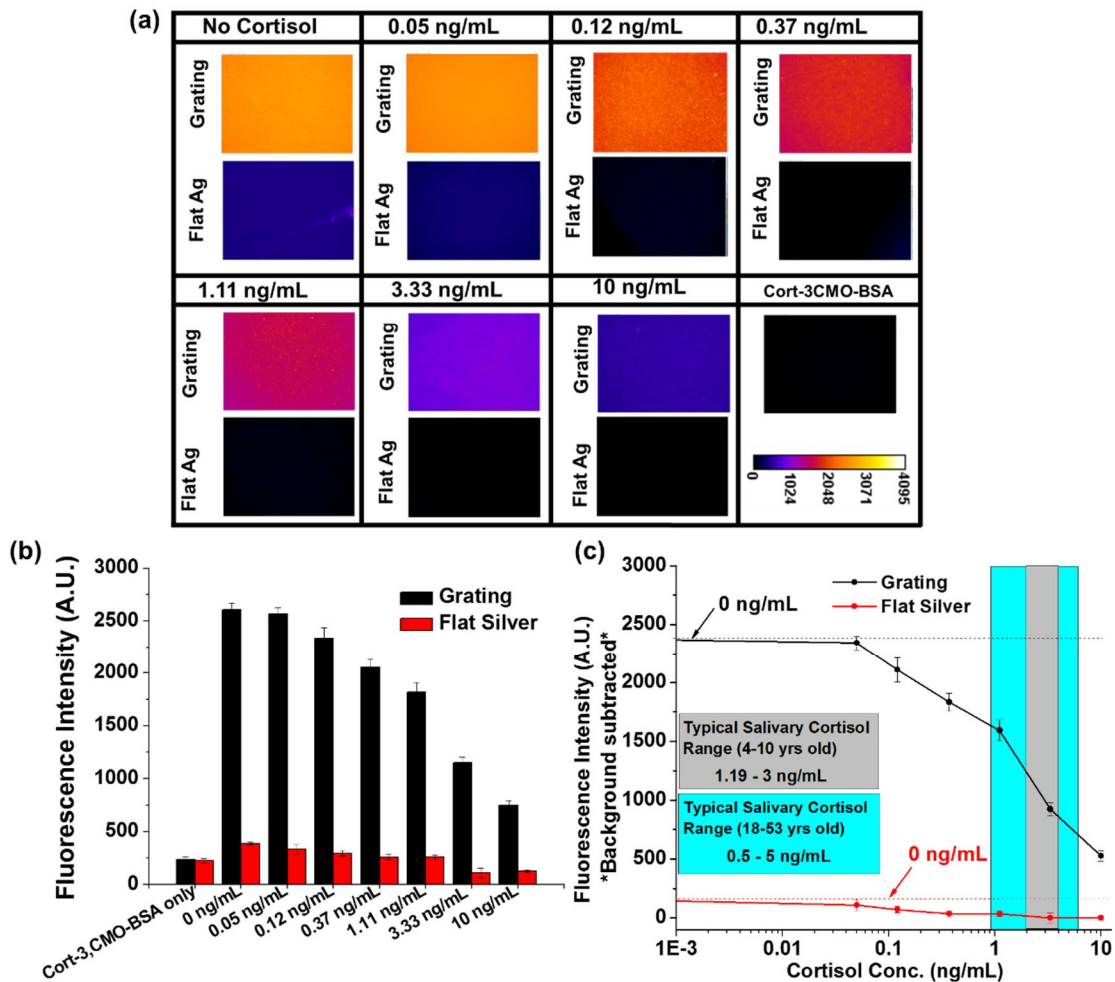


Figure 4-11. (a) Fluorescence images of plasmonic gratings and the surrounding flat silver regions after exposure to different concentrations of cortisol. Images were taken with a 20x objective lens (350 μ m x 260 μ m FOV) with a CMOS exposure of 250 msec. (b) Average fluorescence intensity of the samples in (a). (c) Background subtracted fluorescence intensity plotted with respect to cortisol concentration for gratings and flat silver.

With AF532, the fluorescence response of the grating was \sim 4x more intense than flat silver and exhibited a nearly linear response in the normal salivary cortisol concentration range. The results of this assay could still be substantially improved with a better label efficiency of the detection antibody. Commercially available dye-labeled secondary antibodies have label efficiencies as high as 6-7 dye molecules per antibody. Additionally, based on the SPR dispersion, AF568 would be better

enhanced by the plasmonic grating when the grating is immersed in water or PBS. The competitive binding assay was repeated but the XM210 was not fluorescently labeled and a secondary, AF568-labeled, anti-mouse antibody was incubated with the sensor substrates for 2 hours and rinsed three times with 150 μ L of 1xPBS with 0.1% Tween 20 followed by three rinses with 150 μ L 1xPBS prior to imaging. The number of samples per concentration was increased to n=3 to provide statistically measureable data and the maximum cortisol concentration was increased to include 30 ng/mL. 10 nm thick Alumina coatings were also deposited onto glass substrates and treated the same as the gratings throughout the assay. The results of the assay have been provided in Fig. 4-12.

Significantly higher fluorescence intensities (40-80x higher) were observed on gratings than on alumina-capped glass for every cortisol concentration tested. Additionally, the gratings also exhibited a nearly linear response across the normal salivary cortisol concentration range as well as into the abnormally high cortisol concentrations present in patients with Cushing's syndrome. Cushing's is typically diagnosed when the salivary cortisol concentration measured at 11 pm (lowest cortisol concentration during the circadian rhythm) is 1-1.5 ng/mL.[91]

The increased fluorescence intensity and higher sensitivity of this assay compared to the AF532-labeled assay is due primarily to the proper matching of the SPR dispersion with the labeled fluorophore and the much higher fluorophore labeling efficiency of the secondary antibodies used in the detection step. No statistically significant response was detected from the glass in this concentration range due to the lack of fluorescence enhancement.

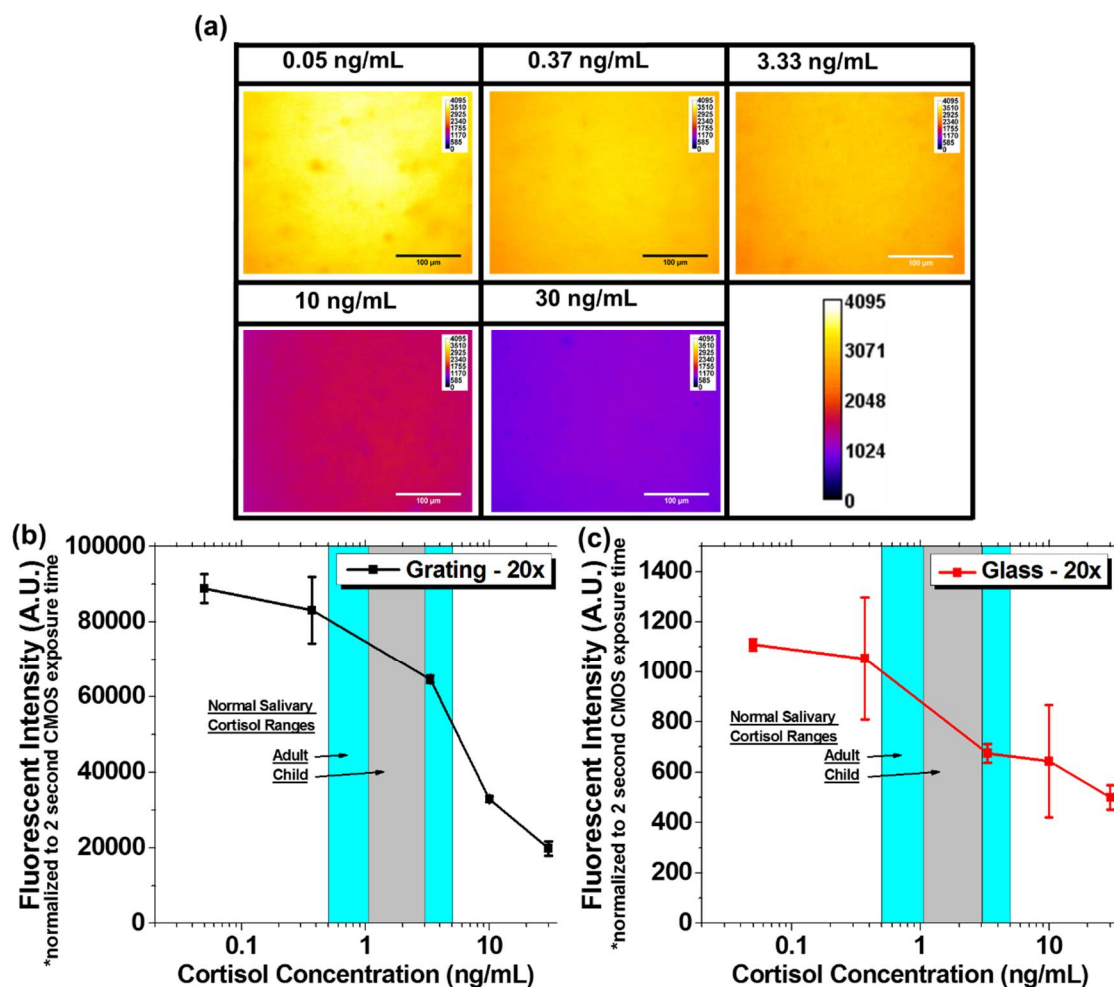


Figure 4-12. (a) Fluorescence images of plasmonic gratings and the surrounding flat silver regions after exposure to different concentrations of cortisol. Images were taken with a 20x objective lens (350 μ m x 260 μ m FOV) with a CMOS exposure of 100 msec. Background-subtracted fluorescence intensity normalized to 2 sec. CMOS exposure plotted with respect to cortisol concentration for (b) gratings and (c) alumina-coated glass samples.

XM210 Binding Relationship with Cortisol: Using the XM210 surface binding curve in Fig. 4-10 and the competitive binding results for gratings in Fig. 4-12, the binding relationship between cortisol and XM210 can be estimated. The molar concentration of XM210 free to bind to the sensor surface from the competitive

binding assay was calculated using a molecular weight (MW) estimate of 150 kDa and 120 kDa for IgG. The MW of IgG is estimated in literature to be 110-150 kDa depending on a specific IgG. The surface bound concentration of XM210 at specific binding ratios to cortisol in the patient sample, i.e. 1:2 indicates one XM210 antibody binds to two cortisol molecules, was plotted against the XM210 binding curve found in Fig. 2-10 to obtain Fig. 4-13. The molar concentration of XM210 requires the MW of antibody and thus two estimates of MW were used to generate Fig. 4-13(a) and Fig. 4-13(b).

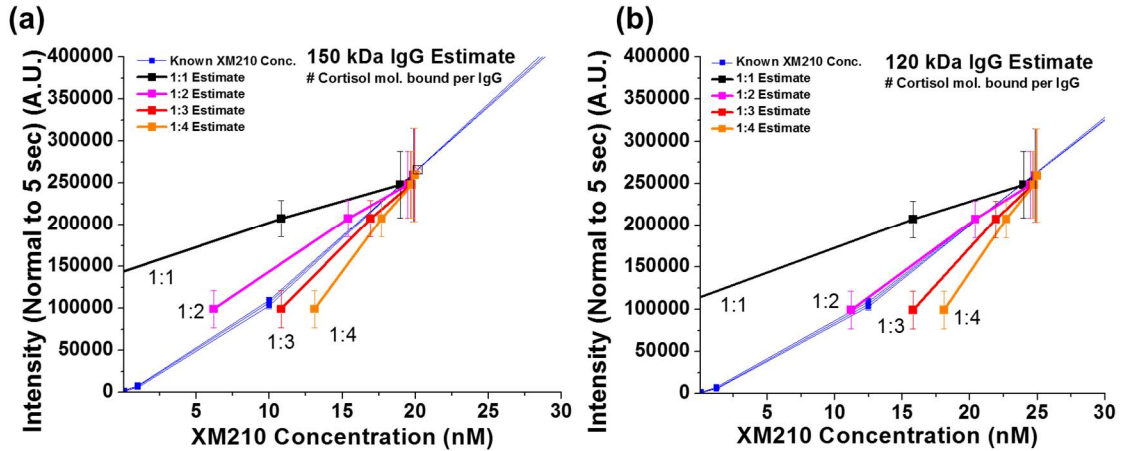


Figure 4-13. Normalized fluorescence intensity of estimated XM210 concentrations given specific binding ratios to cortisol in the patient sample before surface exposure plotted against the normalized fluorescence intensity of known surface-bound XM210 concentrations with a molecular weight estimate of (a) 150 kDa and (b) 120 kDa.

Additional binding ratio curves were generated for MW estimates of 140, 130, and 110 kDa; however, 120 kDa exhibited the most overlap with any binding ratio estimate. Based on Fig. 4-13(b), we estimate that the binding ratio is ~1:2 or one mole of XM210 binds to two moles of cortisol. As IgG has two epitopes and cortisol is a small molecule, it is theoretically possible that a cortisol molecule could bind to each of the epitopes.

4.5. Bimetallic Gratings

To further advance the applications of plasmonic grating technology and greatly improve our abilities to quantify patient stress levels via cortisol quantification, we will explore and develop an aptamer-based assay for cortisol quantification using gold-capped silver plasmonic gratings. Recently, a single-stranded (ss) DNA sequence was discovered that binds specifically to cortisol with very low cross-reactivity to similar molecules.[92] An aptamer-based on this sequence will be designed such that the conformational change from binding to cortisol will result in a fluorescent molecule being lifted out of the quenching domain of the gold layer and into the plasmonic enhancement domain of the plasmonic grating (Fig. 4-14). From the preliminary results, we expect to achieve long-term corrosion resistance to biological fluids and accurately quantify physiologically relevant cortisol concentrations (i.e. <math><0.01 - 300\text{ ng/mL}</math>).

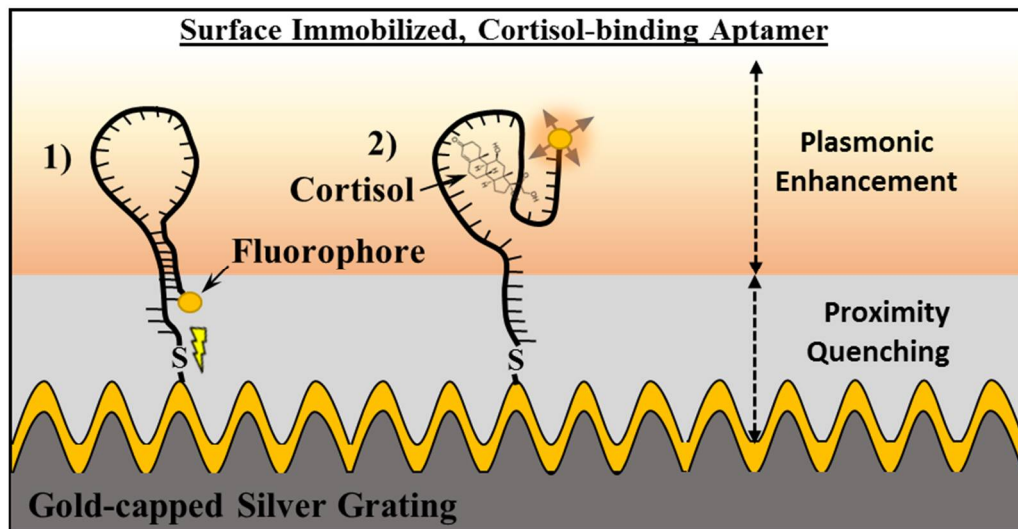


Figure 4-14. (a) DNA-based Cortisol Detection mechanism. 1) Fluorescently-labeled aptamer immobilized onto surface and forms hairpin that brings dye within quenching domain of gold layer. 2) Aptamer binds to cortisol resulting in a conformation change that lifts dye out of quenching domain and into the plasmonic enhancement domain.

Bimetallic Gratings Fabrication and Reflectivity: To demonstrate that gold thin films are capable of improving the corrosion resistance of silver, a thin gold film (10 nm thick) was deposited via RF sputtering onto a 90 nm thick silver grating. Due to the sensitivity of SPR to change at the silver/dielectric interface, reflectivity measurements were taken on silver gratings with and without the gold capping layer and used to make an SPR dispersion plot, see Fig. 4-15. Based on the SPR dispersion, the addition of a 10 nm thick gold layer caused a minimal red shift (1-2 nm) in the 0° coupling wavelength (434 nm vs. 435 nm). However, this red-shift is not as severe as seen on a 100 nm gold grating where the 0° coupling wavelength is located at 440 nm. While an increase in absorption is seen between 300 to 500 nm with the addition of the gold, the coupling strength, i.e. the depth of the SPR peaks is much stronger on the gold-capped grating. This indicates that the bimetallic grating is capable of converting more incident light into surface plasmons and should result in higher plasmonic field strength.

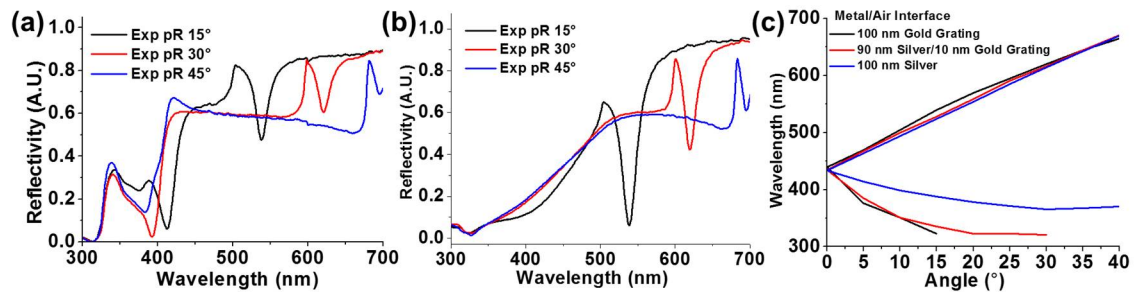


Figure 4-15. Reflectivity measurements at $\theta = 15^\circ$, 30° , and 45° incident light on plasmonic gratings composed of (a) 100 nm thick silver and (b) 90 nm thick silver with 10 nm gold-capping layer. (c) SPR dispersion curves for 100 nm gold grating, 90 nm silver with 10 nm gold capping layer, and 100 nm silver grating in air.

Bimetallic Grating Quenching: Additionally, the gold capping layer can substantially quench the emission intensity of fluorophores very close to the surface. Using plasmonic gratings with 30 nm thick silver and either 5 or 10 nm thick gold layers deposited at glancing angle deposition (GLAD), a process recently developed that produces nanocones among other nanostructures that behave as plasmonic antennas.[93] The plasmonic gratings were spin coated in a 30 nm thick PMSSQ film with 10 μ M Cy5 dye 5 nm thick and imaged using a 60x water immersion objective (Fig. 4-16). We can easily observe the overall reduction in fluorescent signal intensity between the 5 nm and 10 nm gold capping layers. The only sites where fluorescent emission is observed is at the location of the plasmonic hotspots created by the nanostructures grown via GLAD. The widespread quenching effect caused the 10 nm gold capping layer will later be used in the detection mechanism of the cortisol-binding aptamer.

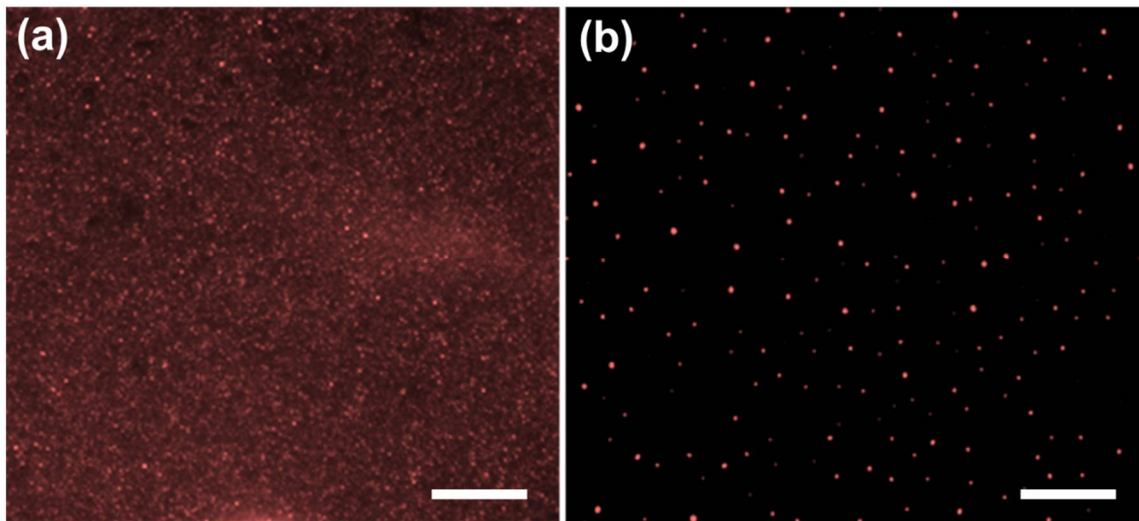


Figure 4-16. Fluorescence images of 30 nm thick silver plasmonic gratings with a (a) 5 nm or (b) 10 nm thick gold-capping layer coated in a 30 nm thick PMSSQ layer with 10 μ M Cy5. Note the metal was deposited via GLAD ($\alpha=76^\circ$). Images taken with 60x WI objective lens. Scale bar: 20 μ m.

Bimetallic Grating Corrosion Resistance: The corrosion of the silver grating, observed as low intensity spotting in brightfield images and development of autofluorescence in the UV and the visible spectrum, particularly strong from $\lambda=350$ to 500 nm, which encompasses the emission wavelength ranges of the DAPI and FITC fluorescence filter cubes. 30 nm thick silver gratings with a 10 nm gold-capping layer were exposed to T50 buffer solution (10mM Tris-HCl, pH 8.0, 50mM NaCl) for 24 hours to observe the corrosion resistance provided by the gold cap. The brightfield images taken before and after T50 exposure, see Fig. 4-17(a,b), don't exhibit any of the common indicators of corrosion such as dark

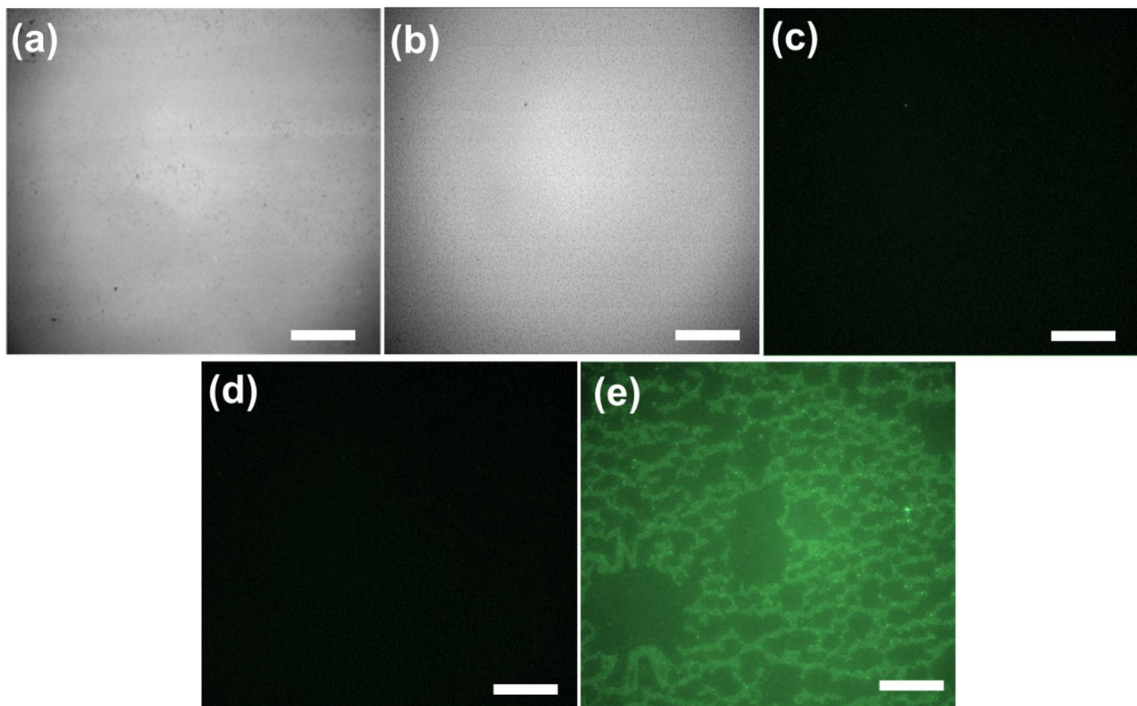


Figure 4-17. Brightfield images of 30 nm thick silver plasmonic gratings 10 nm thick gold-capping layer (a) before and (b) after immersion in T50 buffer solution for 24 hrs. Fluorescence images of the same plasmonic grating after immersion in T50 buffer for 24 hours taken with the (c) DAPI and (d) FITC filter cubes. (e) Fluorescence image of a 40 nm thick silver grating without gold cap in the FITC filter after 1 hour of exposure to T50 buffer. Note the metal was deposited via GLAD ($\alpha=76^\circ$). All fluorescence images taken with a 60x W1 objective and 2 sec. CMOS exposure time. Scale bar: 20 μm .

spotting. Likewise, no autofluorescence was observed in the DAPI and FITC fluorescence images (Fig. 4-17(c,d)) of the gold-capped grating after exposure to T50. Little to no autofluorescence indicates that silver oxidation is minimal and the grating remains largely intact. Unprotected silver gratings exposed to T50 for only 1 hour exhibit intense autofluorescence seen in the FITC filter cube (Fig. 4-17(e).)

Bimetallic Grating Simulation: The impact of a thin gold film added to silver gratings on the E-field strength and Dispersion was determined using FullWave FDTD simulations. A 4 nm grid size was used along with continuous wave excitation from $\lambda = 300\text{-}900$ nm for all simulations. A periodic boundary condition was used for the X-boundaries (left and right) and a PML boundary was used for the Z-boundaries (top and bottom). A 90 nm thick silver grating, 90 nm thick silver with 10 nm thick gold capping layer, and a 90 nm thick gold grating were built in the software and simulated (Fig. 4-18). The corresponding reflectivity results for each type of grating in air, water, and immersion oil have been provided in descending order below each grating type. The reflectivity of 100 nm silver and 100 nm thick gold has been provided in Fig. 4-19(a) and the SPR dispersion based on the reflectivity measurements for each grating type has been provided in Fig. 4-19(b).

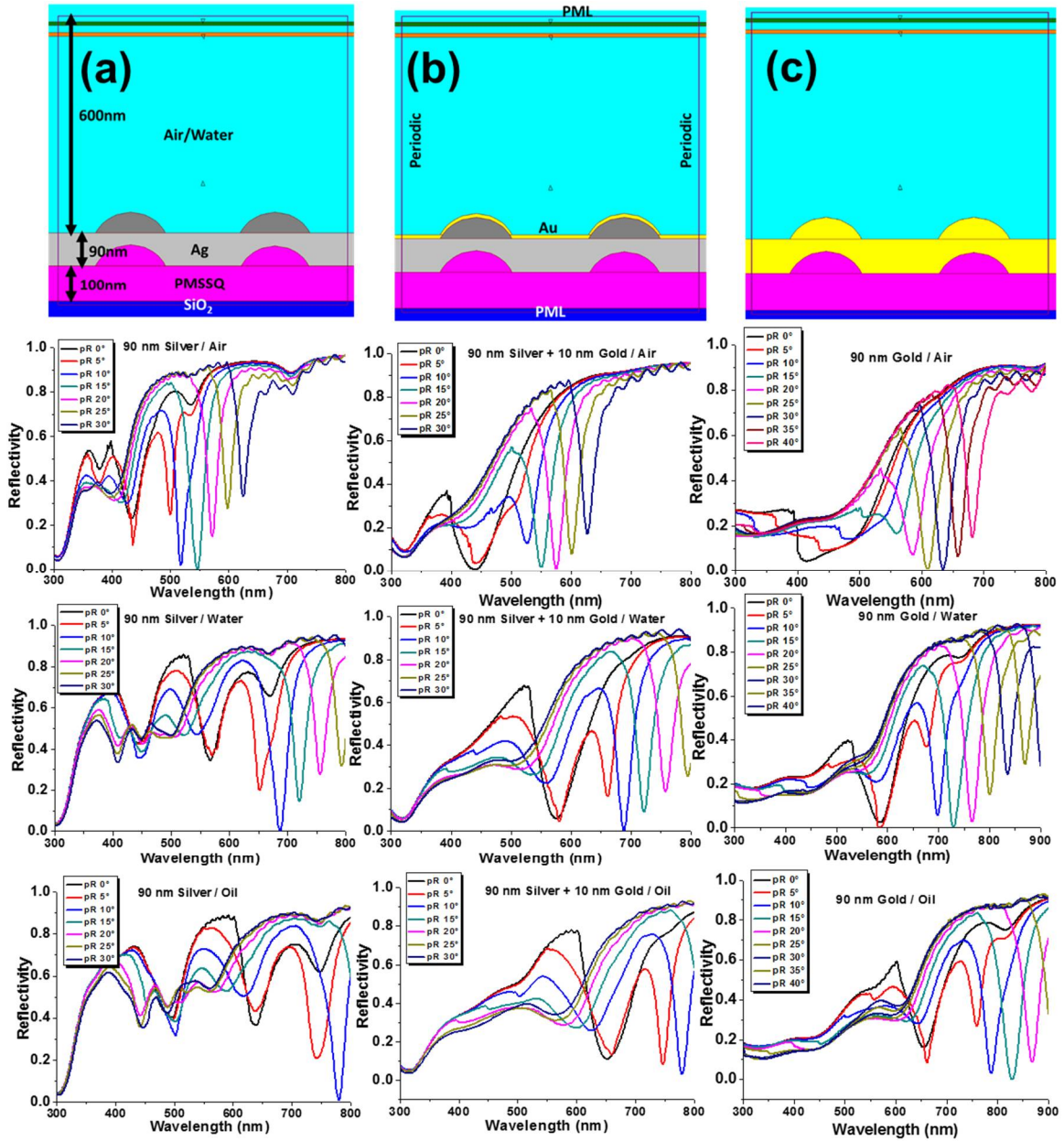


Figure 4-18. FDTD simulation windows for a (a) 90 nm thick silver grating, (b) 90 nm thick silver grating with 10 nm thick gold capping layer, and (c) 90 nm thick gold grating. The reflectivity measurements obtained from the simulation have been provided in (top row) air, (middle row) water, and (bottom row) immersion oil.

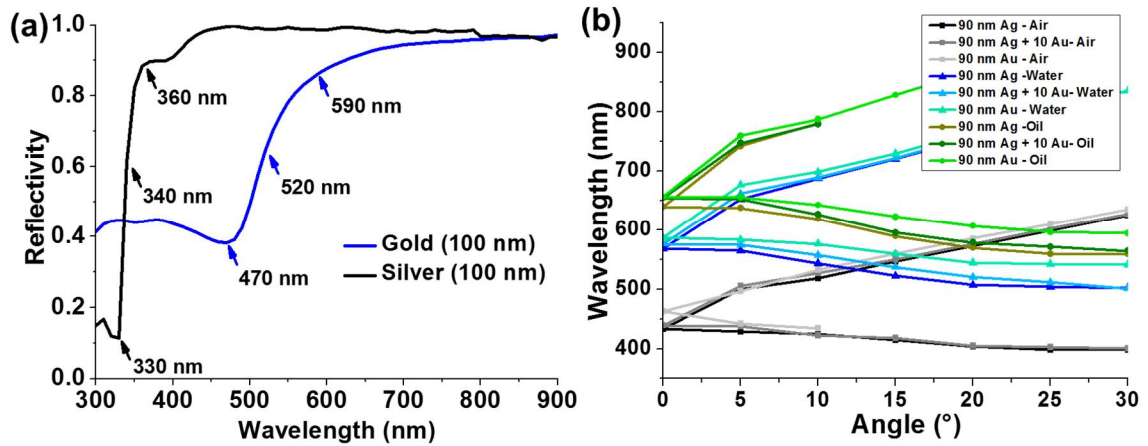


Figure 4-19. (a) Reflectivity measurements from 100 nm thick, flat silver and gold films. (b) SPR dispersion for all gratings simulation in all mediums (air, water, and oil) from the reflectivity measurements in Fig. 4-18.

Based on these simulated reflectivity data, very little change was observed in the SPR dispersion between silver and gold gratings. The lower resonance mode was hindered with the addition of gold in every simulation below ~ 530 nm, regardless of imaging medium (air, water, and oil.) When a 10 nm Gold capping layer is added to a silver plasmonic grating, we don't observe a substantial shift in the upper resonance SPR modes which are represented as the upper line in the SPR dispersion. Below 450 nm, we do see an increase in absorption that can be attributed to the absorption of the gold. This makes it difficult to observe the lower resonance mode peaks and makes the SPR dispersion curve less accurate in this region as seen in the variation of the lower line of the dispersion. The upper resonance mode was less effected but gold-capped and gold gratings exhibited lower field strengths when the peak was also below ~ 530 nm. The effect of the different gratings simulated on the E-field has been provided in Fig. 4-20.

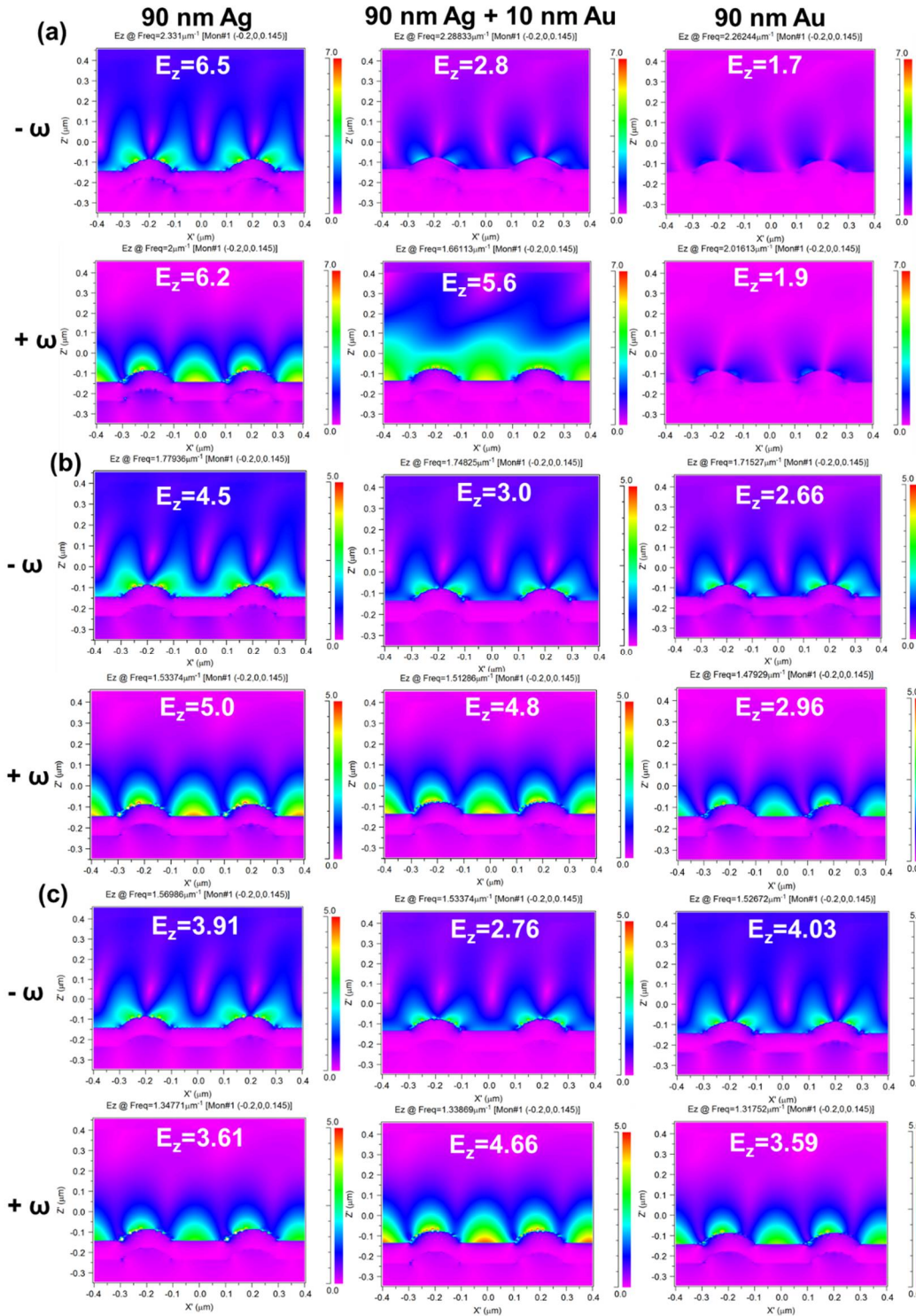


Figure 4-20. E_z field intensities with maximum field intensity listed in each plot for the $\pm\omega$ SPR modes generated at $\theta=5^\circ$ on a 90 nm thick silver grating, 90 nm thick silver grating with 10 nm thick gold capping layer, and 90 nm thick gold grating immersed in (a) air, (b) water, and (c) immersion oil.

The lower resonance mode was lower in both air and water for the gold and gold capped silver gratings due to the absorption of the gold films. However, both the lower and upper resonance mode electric field values in oil were similar between the three gratings. For the lower resonance mode in water, the z-component of the E-field decreased from 4.5 to 3.0 with the addition of the gold capping layer but not as substantially as a pure gold film ($E_z = \sim 2.7$). However, for the upper resonance mode in water, the addition of the 10 nm gold capping layer had a minimal impact on the z-component of the E-field as only a slight decrease was observed from 5 to 4.8. In summary, the addition of a gold capping layer has a minimal impact on the upper resonance SPR mode when the gratings are immersed in water and oil.

4.6. Cortisol Binding Aptamer

The interaction between a fluorophore and metal surface was modeled in section 1.6 and yielded the optimal spacing from the metal surface for complete quenching (< 3 nm) and for maximum emission intensity (>10 nm). Thus, a cortisol binding aptamer was designed based on these distances such that in the unbound state, the aptamer would form a hairpin structure that would bring the fluorophore close enough to the surface to quench the fluorescence. However, in the bound state, the cortisol aptamer would extend the fluorophore at least 12 nm from the surface. To design the aptamer sequence, the sequence was divided into four separate regions 1) fluorescent dye label, 2) cortisol binding sequence, 3) spacer and stabilization sequence, and 4) surface immobilization group. In section 4.4, the dye that provided optimal fluorescence enhancement was AF568 will be used to label the 5' terminus of the aptamer.

Cortisol Binding Sequence: The cortisol binding sequence will be based on the newly discovered set of cortisol binding sequences found in Martin et.al.[94] During their testing, the aptamers were screen against several chemically similar molecules to cortisol, including progesterone, cholic acid, norepinephrine, and epinephrine. Five aptamers were discovered that bind specifically to cortisol but not to the other previously listed molecules. These aptamers are listed in Table 4-2 with the % total of the remaining DNA after the non-specific binding screening process.

Table 4-2. Cortisol binding sequences with highlighted sequence similarities. [94]		
Sequence Label	Binding Sequence	% Total
A	5'-ATG GGC AAT GCG GGG TGG AGA ATG GTT GCC GCA CTT CGG C-3'	66.91 %
B	5'-GGG GGT TGG AAG GGG GGG CCG CGG GGT GGG CCA TCG TTC G-3'	7.58 %
C	5'-GGG GTG GTT TGG GGA CCG TGG GGA GTG TGT GGA GGG GGA TGA G-3'	6.51 %
D	5'-GAC GGG TTG TGG GAA GGG TGT CCC GTG AAT GGG GTG C-3'	3.58 %
E	5'-GAC ACT GCG CGT GTG GAG TTA AAT GTG CGC GCG GCT CGC G-3'	0.13 %

Sequence A from Table 4-2 exhibited a much higher binding affinity for cortisol as seen in Martin et. al. [94] By comparing sequence A to the sequences B-E, ~5-6 similar nucleotide sets (red) can be observed which may bind to the five charged groups found on a cortisol molecule. Given the exact shape of cortisol, **Fig. 4-21(a)**, the location of cortisol's charged groups relative to the nucleotide sets found in cortisol binding aptamers, and the length of the binding sequence (40 bp ssDNA = ~28 nm), we believe that the aptamer spirals at least twice around cortisol.

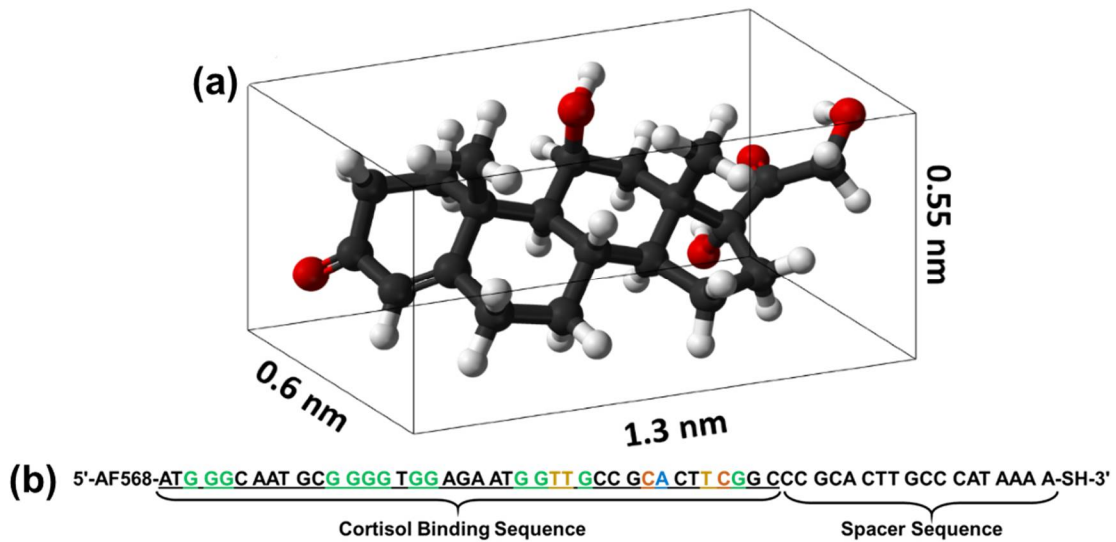


Figure 4-21. (a) Cortisol molecule dimensions. Cortisol 3D model made via Accelrys DS Visualizer. (b) Aptamer sequence including cortisol binding sequence with the sequence sections that are similar to other cortisol binding aptamers highlighted and spacer sequence.

Spacer Sequence: The spacer sequence has two purposes: 1) it must hybridize with the cortisol binding sequence to form a stable hairpin that brings the 5' terminus with dye label within 3 nm of the metal surface and 2) it must provide 10-13 nm distance between the cortisol binding sequence and the metal surface when the aptamer is bound to cortisol. First, the spacer sequence length was fixed at 18 bp to provide 12.6 nm of distance between the start of the cortisol binding sequence and the metal surface when the aptamer is bound to cortisol. This spacer sequence will place the dye molecule 12.6 – 13.2 nm from the metal surface when the aptamer is bound to cortisol. Based on the modeling results found in Fig. 1-14, the dye molecule should experience the most intense E-field of the grating but far enough that non-radiative transfer will lead to the formation of a radiative plasmon. Second, the sequence was selected to be complementary for 17 bp with a 1 bp mismatch to the cortisol binding sequence to stabilize the hairpin conformation of

the aptamer but not stabilize enough to prevent the aptamer from unfolding in the presence of cortisol. A 4 bp poly-A tail was incorporated into the sequence to improve solution stability and fix the location of the dye molecule labeled to the 5' terminus in hairpin conformation 2.6 nm from the metal surface. This short separation distance between the dye and metal surface will ensure that any non-radiative transfer of energy from the dye to the plasmonic grating will result in the formation of a lossy surface wave instead of a radiative plasmon.[35]

The stability and conformation of the aptamer, Fig. 4-21(b), alone was examined using the IDTDNA OligoAnalyzer 3.1. The top four predicted hairpin conformations with corresponding Gibb's free energy (ΔG) and melting temperature (T_M) have been provided in Fig. 4-22. These four conformations have relatively large ΔG values (-11.67 to -13.94) and high melting temperatures (54.2 to 62.6°C) which indicates that the hairpin is very stable and that the dye will remain close to the

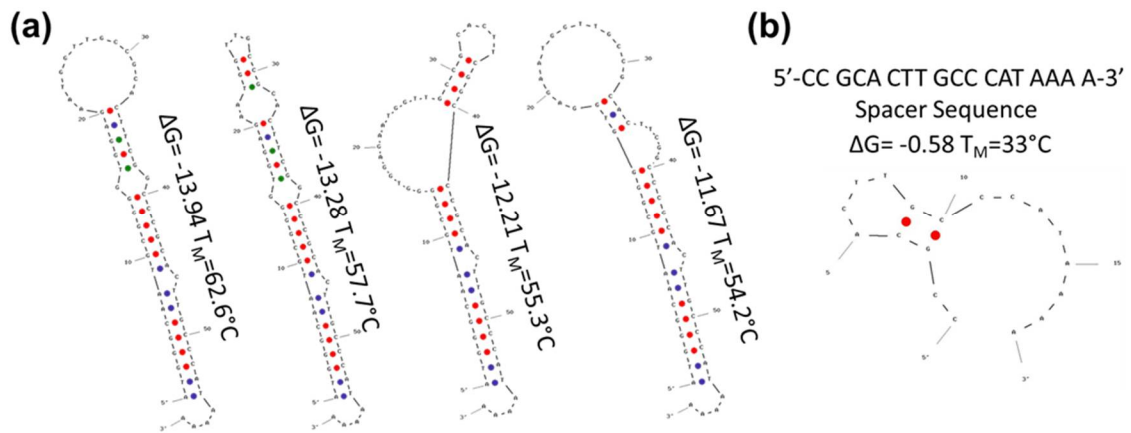


Figure 4-22. Minimum free energy structures (ΔG) predicted by IDTDNA OligoAnalyzer 3.1 for the (a) 58 bp aptamer and (b) the spacer sequence of the aptamer alone. The 58 bp aptamer exhibits very stable hairpin structures that should place the dye label within 3-4 bp (~2.1 - 2.8 nm) of the gold surface. The 18 bp spacer sequence only exhibits one secondary structure but has very high free energy / low melting temperature and thus has a low probability of self-hybridizing when unbound.

surface when the aptamer is not bound to cortisol. The spacer sequence alone was also analyzed using the same analysis technique and found to have only one hairpin conformation that has a very poor ΔG value (-0.58) and low melting temperature (33°C). This indicates that there is a low probability of this hairpin conformation occurring when the aptamer is bound to cortisol. This should result in a minimal reduction in the dye/metal spacing in the cortisol bound aptamer conformation.

The immobilization group was selected to be a thiol group due to its high binding affinity for freshly deposited gold surfaces. The binding of DNA to gold surfaces is further explored in Chapter 5.

In summary, the cortisol binding aptamer sequence designed in this section should change conformation from a hairpin to an elongated conformation that will result in the high intensity, fluorescent emission of the AF568 label.

Designed Aptamer Sequence: 5'-AF568-ATG GGC AAT GCG GGG TGG AGA
ATG GTT GCC GCA CTT CGG CCC GCA CTT GCC CAT AAA A-SH-3'

4.7. Conclusion

A competitive binding fluoroimmunoassay was developed that utilized the enhancement provided by plasmonic gratings to provide better detection capabilities of cortisol than glass substrates. We performed a preliminary study using cortisol-spiked PBS in place of patient samples and compared the response of the plasmonic gratings to glass substrates. The plasmonic gratings exhibited much higher signal intensity and better sensitivity than glass at all of the tested cortisol concentrations (0.05 – 30 ng/mL). This cortisol concentration range

encompasses the typical saliva cortisol levels for adults (0.5 – 5 ng/ml) and children (1.19 – 3 ng/mL). The results of this assay demonstrate that plasmonic gratings could enhance the sensitivity of almost any fluoroimmunoassay by immobilizing the target on the surface and changing the detection antibody.

4.8. Future Work

Cortisol Binding Aptamer Testing: Cortisol in PBS and simulated biological fluids will be flown over a bimetallic grating surface with immobilized cortisol binding aptamers. The resulting fluorescent response imaged with a 20x objective and high resolution, 100x OI objective is expected to yield a faster and more sensitive response to cortisol concentrations typically found in saliva than the competitive binding fluoroimmunoassay.

96-Wellplate Plasmonic Grating Prototype: As most immunoassay kits utilize 96-wellplate readers to speed up sample processing, the plasmonic gratings could be fabricated according to a 96-wellplate template and attached to bottomless well plates such as the grating array seen in Fig. 4-23. Fluorescent plate readers typically use a fiber-optic cable as an excitation source that provides an angular excitation pattern similar to a 10x microscope objective lens. With tuning,

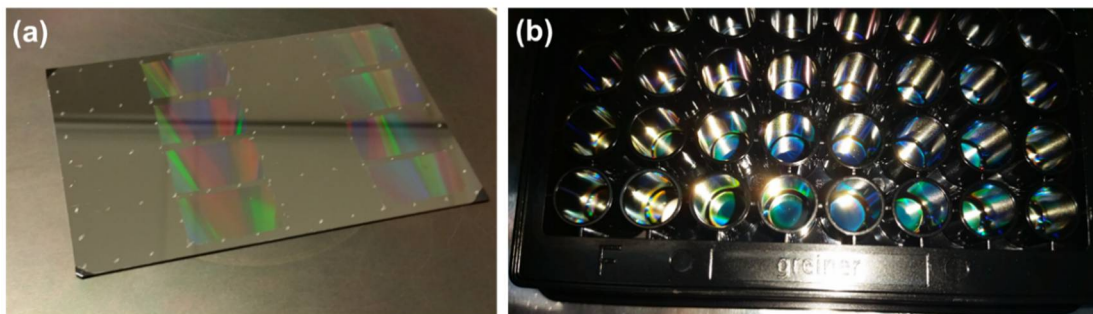


Figure 4-23. (a) 8 cm x 11 cm plasmonic grating array with alignment markings for attachment to a bottomless 96-wellplate. (b) Gratings attached to a bottomless 96-wellplate.

plasmonic gratings could use the angled excitation of the plate reader to enhance the fluorescent signal intensity and improve the sensitivity of the assay.

CHAPTER 5: ENHANCED DNA DETECTION THROUGH THE INCORPORATION OF NANOCONES AND CAVITIES INTO A PLASMONIC GRATING SENSOR PLATFORM

5.1. Abstract

In this chapter, a novel plasmonic grating sensor platform was developed and tested for feasibility using a “lights-on” fluorescence-based DNA assay. The sensor platform combined the fluorescence enhancement of a grating-based plasmonic platform with the electric field intensifying effects of nano-scale cones and cavities. The gratings were made through a microcontact printing process that replicated HD-DVD discs in polymethylsilsesquioxane (PMSSQ) and coated with a thin gold film. Nanocavities were incorporated into the sensor platform during the printing process and nanocones were incorporated during the 100 nm gold deposition process. Fluorescently-tagged single-strand (ss) DNA molecules were immobilized onto the surface and were designed such that the molecules would fluoresce when bound to a complementary sequence. Sensor substrates were imaged after exposure to a mismatched and matched ssDNA to quantify the fluorescence enhancement of the sensor. Exposure to matched ssDNA resulted in fluorescent emission from the grating that was 13.6x brighter than flat gold while the nanocones and nanocavities were 37.5x and 47.4x brighter than flat gold, respectively.

5.2. Introduction

As sensor technology has progressed, many novel methods have been developed for detecting ever smaller concentrations of analytes. Throughout the progression, sensors based on plasmonics and surface plasmon resonance (SPR) have proven their usefulness in applications that reduce the lower limits of detection (LOD).[95, 96] In SPR based sensors, light is coupled to a metal/dielectric interface, creating intense electromagnetic fields at the interface which can be used to excite nearby fluorescent molecules. Coupling occurs at an interface when the tangential momentum of incident light (k_{light}) is equal to the SPR momentum (k_{SPR}) of a metal/dielectric interface, see equation (1.13).

$$k_{\text{SPR}} = \frac{\omega}{c} \sqrt{\frac{\epsilon_d \epsilon_m}{\epsilon_d + \epsilon_m}} \quad (1.13)$$

Where ϵ_d and ϵ_m are the permittivities of the dielectric and metal, respectively. Under normal circumstances, the two momentum components never match thus complex optical systems were needed in order to obtain a momentum match.[16, 17, 20, 22] However, periodic perturbations in the surface profile, such as grating structures, alter the scattering properties and adds a momentum component to the light coupling conditions such that light can be coupled to a surface without the need for prisms and complex optical systems, see equation (1.19).

$$k_{\text{SPR}} = \frac{\omega}{c} \sqrt{\frac{\epsilon_d \epsilon_m}{\epsilon_d + \epsilon_m}} = \frac{\omega}{c} \sqrt{\epsilon_d} \sin \theta_{\text{SPR}} \pm m \frac{2\pi}{\Lambda}, \quad m = \pm 1, 2, 3, \dots \quad (1.19)$$

Where the θ_{SPR} is the incident angle of the illuminating wave to create a surface plasmon and Λ is the grating pitch. Recently, an inexpensive soft lithography

process was developed to produce plasmonic gratings with nano-scale cavities or “nanogaps” and nanoconical structures (Fig. 5-1) that provide the ability to perform ultrasensitive fluorescence detection using conventional optics. The process replaces expensive traditional e-beam lithography techniques by taking advantage of commercially available master molds in the form of CDs, DVDs, HD-DVDs, and Blu-rays with the robustness of the gratings in physiological conditions allowing us to use them as fluorescence sensors.[20, 97, 98]

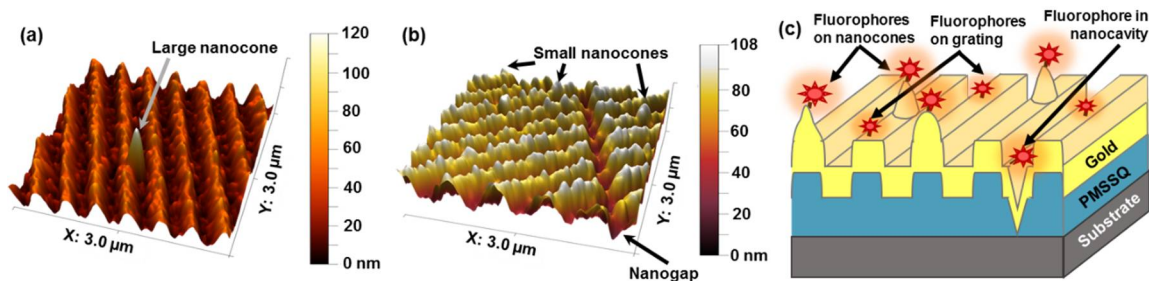


Figure 5-1. AFM rendering of a plasmonic grating with (a) nanocones and a (b) nanogap. (c) The plasmonic grating cross section with incorporated nanocones/gaps with immobilized fluorophores.

Plasmonic gratings were fabricated as hybrid soft/hard nanostructures by nano-imprinting a polymer ink using the existent grating structures on commercially available HD-DVDs followed by thermal deposition of a thin plasmonic metal layer such as silver and gold. Gold was ultimately selected as the plasmonic metal of choice due to its ability to form a strong bond to thiol molecules and its corrosion resistance. Control over the metal deposition rate and stresses incurred during nano-imprinting results in patterned, nanoscale surface structures such as nanocones and nanogaps that serve as sites for extraordinary concentration of incident light (Fig. 5-1). The intensified evanescent field has a profound impact on the excitation of surface-bound fluorophores, enhancing the excitation and

emission intensities many orders of magnitude higher than flat metal surfaces. When combined with a fluorescence-based sensor assay, the enhanced signal enables detection with a much higher signal-to-noise ratio, which is a topic that has become an important focus in fluorescence-based biosensors design in recent years.[99, 100]

Experiments with a “lights-on” fluorescence-based DNA assay using our fabrication methodology have demonstrated the feasibility of the platform as a fluorescence enhancement platform. A dye-labeled single-strand (ss) DNA was attached to a prototype gold grating via thiol-gold binding. The ssDNA molecule initially adopted a collapsed, unstructured conformation or “hairpin” that brought the dye into proximity with the gold surface which effectively quenched the fluorescence, see Fig. 5-2(a.)[101] When the complementary ssDNA was introduced, hybridization resulted in duplex formation, extending the 5'-labeled dye away from the gold surface and allowing plasmonic-enhanced dye fluorescence to occur. With proper tuning and functionalization for bioconjugation, the presented platform could achieve much higher enhancement of fluorescent signals, leading to lower limits of detection and high sensitivity as biological sensors.[20, 96, 97, 102]

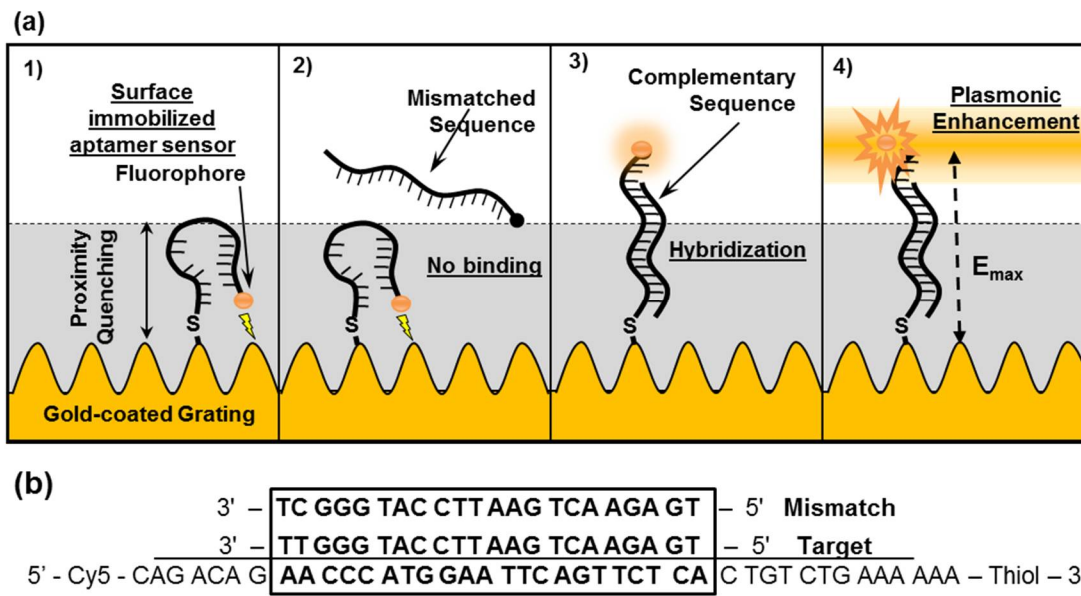


Figure 5-2. (a) Single-stranded DNA (ssDNA) aptamer 1) immobilized via thiol binding to a gold plasmonic grating with a fluorescent dye molecule on the 5' end that is quenched due to folding of the DNA and proximity to the gold surface; 2) exposure to a mismatched aptamer does not result in hybridization; 3) complementary ssDNA binds and hybridizes the DNA, extending the dye molecule out of the quenching region; 4) due to hybridization, the dye molecule is extended into the plasmonic enhancement region of the grating resulting in much more intense fluorescence. (b) ssDNA aptamer sequence compared to the mismatch and target oligomers.

5.3. Materials and Methods

Materials and Reagents: Commercial HD DVD-R discs were purchased from Memorex. Polydimethylsiloxane (PDMS) was ordered from Dow Corning Corporation (Sylgard 184-PDMS). Polymethylsilsesquioxane (PMSSQ) was purchased from Techneglass, Inc (GR650F). Phosphate buffered saline (PBS) tablets and Tris-EDTA (TE) buffer solution were obtained from Sigma-Aldrich. Three custom made ssDNA molecules were manufactured by Integrated DNA Technologies, Inc. A 42 base pair (bp) ssDNA “hairpin” aptamer was bound to Cyanine 5 (Cy5), a fluorescent molecule (excitation: 650 nm, emission: 670 nm), at the 5' terminus and a thiol group at the 3' terminus. The ssDNA aptamer had the following sequence: 5'-Cy5-CAGACAGAACCCATGGAATTCAGTTCTCACT

GTCTGAAAAAA – SH – 3'. Two, 22 bp ssDNA oligomers were also manufactured, one being a perfectly matched sequence to the sensor aptamer (5' – TGAGAACTGAATTCCATGGGTT– 3') while the other ssDNA molecule had a single base mismatch (5' – TGAGAACTGAATTCCATAGGCT – 3'). To better illustrate the binding sites between the ssDNA strands a binding diagram has been provided in Fig. 5-2(b).

The sequence was designed such that the hybridized length of the 5' terminus would be outside of the proximity quenching region of gold (<10 nm) but still within the plasmonic enhancement region, which is estimated to be between 10 and 100 nm from the surface.[35] Ideally, the hybridized DNA strand would place the Cy5 molecule very close to 10 nm from the gold surface to experience the highest field strength of the evanescent field. However, due to the variability in field intensity on the plasmonic grating/nanocones and possibility of DNA bending in fluid shear, the sequence was designed to extend farther than 10 nm from the surface. When hybridized, the Cy5 dye molecule attached to the 5' terminus was estimated to be 21 nm from the immobilized 3' end given that double-stranded (ds) DNA is 0.34 nm in length per base pair and ssDNA is 0.7 nm in length per base.[103]

Grating Fabrication and Characterization: PMSSQ gratings were created through the same microcontact stamping process developed in previously published work.[20, 97, 98] The process replicates gratings found on commercially available HD DVDs. PMSSQ was selected for its stability and robustness at room temperature as well as its ability to quickly crosslink when exposed to moisture/air. Gratings were coated with a 5 nm thick chromium adhesion layer and 100 nm thick

gold layer deposited at a rate of 0.1 Å/sec. for the first 5 nm followed by a rate of 0.5 Å/sec. for the remaining deposition using a NANO 48 thermal evaporation system (Kurt J. Lesker Company). Grating structure was monitored throughout the production process with an atomic force microscope (AFM) (Innova®, Bruker Biosciences Corporation) that used AppNano ACTA silicon SPM tips (k: 40 N/m, f: 295 kHz, tip radius: ~6 nm).

The extent of light coupling to the grating was quantified through reflectivity measurements taken with a variable angle spectroscopic ellipsometer (VASE) system equipped with a xenon broadband source (VASE®/HS-190, J.A.Woollam Co, Inc.). Measurements were taken using transverse-magnetic (TM) light at a range of wavelengths ($\lambda=200 - 2000$ nm) and angles of incidence ($\theta=15 - 60^\circ$). Typically, SPR-induced light absorption is observed as a sharp drop in reflectivity that exhibits strong angular dependence as seen in Fig. 5-3(a).

Sensor Design: Freshly deposited gold gratings were incubated with 5 μ M ssDNA aptamer in 1xTE buffer (1 M NaCl added, titrated to pH 7.5) for 24 hours at room

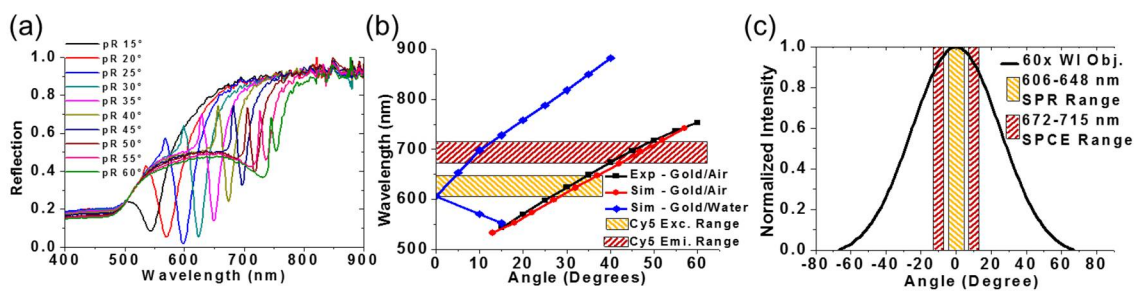


Figure 5-3. (a) Reflectivity measurements on a plasmonic gold grating with nanocavities at difference angles of incidence. (b) Experimental and simulated SPR dispersion plot of plasmonic gold grating indicating the wavelength/angle pairs that result in high, SPR-based absorption as well as the excitation and emission spectrums for the Cy5 filter cube. (c) Objective illumination angle distribution for a 60x water-immersion objective with SPR excitation and SPCE emission ranges from the overlap between Cy5 filter cube spectrum and SPR dispersion of the gold grating in water from (b).

temperature. Semi-covalent bonding between freshly deposited gold surfaces and thiol functional groups is well studied and provides a stable immobilization mechanism that can be used to attach ssDNA to gold surfaces.[101] Sensors were rinsed three times in 1x TE buffer after every incubation step to remove unbound ssDNA. Sensors were then exposed to 100 μ M mismatched ssDNA in 1xTE buffer for 45 minutes at room temperature. Following rinsing, sensors were imaged with an epifluorescence microscope equipped with a 60x water-immersion objective, ORCA Flash 2.8 CMOS camera, and Cy5 fluorescence filter cube (band pass excitation filter: 606-648 nm, dichroic mirror: 665 nm, bandpass emission filter: 672-715 nm). Sensors were then exposed to 100 μ M perfectly matched target DNA in 1xTE buffer for 45 minutes at room temperature. Samples were then rinsed and imaged as previously described.

5.4. Grating Topography

Grating shape and size remained very close to the original HD DVD grating dimensions (60 nm height, 400 nm pitch) throughout the replication and deposition processes. AFM topographical information of the 100 nm gold coated HD DVD grating has been provided in Fig. 5-1(a,b). Surface roughness increased due to the formation of large metal grains on the surface (RMS: 3.92 nm, Grain size: 24.8 nm). Large grain growth on the gratings is attributed to the lower adatom energy which limits atomic mobility.[104] Increased grain size as well as the directional influence of grain growth on grating ridges and pits collectively formed large conical grains that extended far above the grating ridges (Avg. height above ridges: 39.8 \pm 15 nm). The resulting nanoconical structures behave as plasmonic antennas that

concentrate the surrounding electromagnetic (EM) field. The increased field strength at these locations will result in an increase in excitation intensity of nearby fluorophores and ultimately more intense fluorescent emission.[93, 98]

Unequal forces in the PDMS peeling step produced a shear force on the PMSSQ ink giving rise to the formation of nanogaps whose width ranged from 200 – 400 nm and were wide-spread throughout the grating. Nanogaps typically form perpendicular to the peeling direction of the PDMS stamps. The PDMS used to manufacture the gratings in this study were peeled parallel to the grating orientation which resulted in nanogaps cutting perpendicular to the gratings as seen in Fig. 5-1(b). The sharp discontinuity in the grating profile from nanogaps concentrates the surrounding EM field and increase fluorophore emission intensity.[20, 93, 98]

5.5. Optical Properties

Reflectivity scan results in Fig. 5-3(a) indicate that light can be coupled to the gold gratings at wavelengths between 530 – 750 nm at angles of incidence between 15° - 60° in air. The VASE system used to record reflectivity was not capable of measuring low incidence angle reflectivity on liquid samples. However, the SPR dispersion curves of gold gratings in air and water were calculated using Finite Difference Time Domain (FDTD) simulations using FullWave software (Synopsys). Simulated curves were plotted with experimental reflectivity measurements in Fig. 5-3(b). The excitation and emission spectrum of Cy5 dye was not well coupled in the air as it requires a high coupling angle but can couple at the lower angle, upper-frequency SPR mode in water.

To couple light at the required wavelengths, a form of angled excitation and imaging is required. The range of excitation angles present in higher numerical aperture objective provides angled excitation from a simple microscope setup. The range of angles provided by an objective are normally distributed centered at 0° and contained within the convergence angle (θ_{CA}). [42, 62] The convergence angle can be calculated based on the imaging medium refractive index and the numerical aperture of the lens, see equation (1.29).

$$NA = n \sin(\pm\theta_{CA}) \quad (1.29)$$

The objective used in this experiment was a water-immersion 60x objective with a numerical aperture of 1.2. Based on this information, a normal distribution was fitted to the calculated convergence angle ($\theta_{CA}=\pm 64.16^{\circ}$) and plotted in Fig. 3(c). It is clear from this plot that the majority of light is located near 0° and that only a small fraction of light is at the convergence angle. To maximize SPR excitation, the fluorophore excitation and SPR coupling spectrums must both be located near $\theta_{SPR} = 0^{\circ}$.

After fluorophores are excited by the evanescent SPR field, a unique phenomenon has been observed called surface plasmon-coupled emission (SPCE). [35] The phenomenon occurs when the excited fluorophores within 200 nm of the metal surface non-radiatively transfer energy to the metal and where it is converted into a directed emission. SPCE enables far better fluorescence collection as long as the detector can collect the directed emission.

Based on the dispersion of the grating in water and Cy5 filter cube parameters, SPR was generated with excitation light (606 – 648 nm) with incident angle, $\theta = 0$

– 4.2° . SPCE (672 – 715 nm) was emitted from the grating from $\theta = 7.2 - 12.7^\circ$. When compared to the angular illumination range of the 60x objective in Fig. 5-3(c), the objective illuminated the sample in the correct SPR angle range and was able to collect light over the entire SPCE angular range. This precisely designed platform allowed extraordinary fluorescence enhancement from fluorophore-labeled DNA as described in the next section.

5.6. DNA Detection and Fluorescence Enhancement

Brightfield, Fig. 5-4(a), and fluorescence images, Fig. 5-4(b-d), demonstrate the enhanced fluorescence, Fig. 5-5, due to targeted DNA binding on the grating platform and other incorporated nanostructures. The fluorescence images seen in Fig. 5-4(b) demonstrates that ssDNA does not properly bind to the mismatched sequence as only a minor increase in fluorescence intensity was detected over the unexposed ssDNA coated grating. Furthermore, the lack of fluorescence signal from the mismatch exposed DNA sample indicates that little to no surface clumping occurred as clumped DNA has restricted mobility and less accessible binding sites leading to the presence of fluorescent spots.

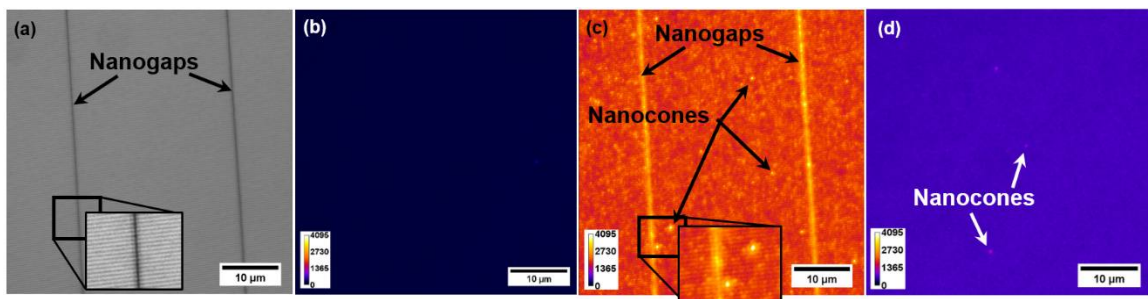


Figure 5-4. (a) Bright-field micrograph of nanocones/gap-embedded gold gratings using a 60 \times water-immersion objective. (b-d) Normalized epi-fluorescence micrographs (0.1 second CCD exposure time) of 0.5 μ M immobilized ssDNA aptamer samples incubated with: (b) no complement (negative control) and perfect DNA complement on (c) gratings and (d) flat gold.

Once exposed to the target sequence the fluorescence intensity from the grating, Fig. 5-4(c), increased to 13.6x brighter than flat gold, Fig. 5-4(d). Nanocones and nanogaps also increased in fluorescence intensity to 37.5x and 47.4x brighter than flat gold, respectively, due to the concentrated EM field. Small nanocones were observed on the flat gold but were much lower intensity than grating-localize nanocones due to the absence of a strong EM field. Due to the range in nanocone height and corresponding EM field concentration, the fluorescence intensity varied between nanocones. With further deposition tuning, nanocone growth can be more controlled and produce more uniform enhancement values. Nanogaps exhibited less variability in enhancement than nanocones, however, more control over orientation and force applied during stamping is necessary to achieve higher and more uniform enhancement values.

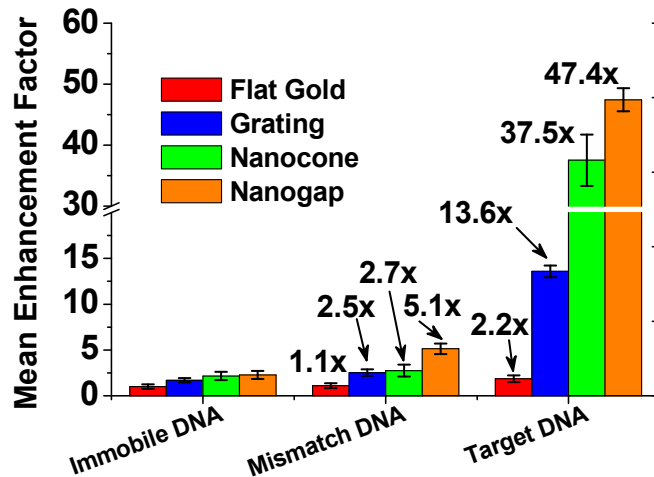


Figure 5-5. Fluorescence enhancement factors of gold gratings, nanocones, and nanogaps with respect to flat gold after exposure to the mismatched and complementary DNA sequences.

5.7. Conclusion and Future Direction

In conclusion, a plasmonic grating-based sensor platform was presented that combined the fluorescence enhancement of grating-coupled SPR with the fluorescence enhancement that arises from intense, localized electric fields that surround nanocones and nanogaps. The resulting high fluorescence enhancement on the platform could easily be used to enhance previously low-intensity signals and detect lower concentrations of oligomers. Future work includes obtaining a concentration dependent fluorescence response curve as well as modification of the aptamer sequence to detect oligomers from analytes of interest. With tuning, the platform could be multiplexed to detect multiple analytes through the immobilization of different aptamers linked to independently distinguishable fluorophores.

CHAPTER 6: SINGLE-MOLECULE SURFACE PLASMON- COUPLED EMISSION WITH PLASMONIC GRATINGS

6.1. Introduction

The ability to image single molecules (SM) was the dream of scientists for centuries and, thanks to substantial advances in high-resolution microscopy, individual fluorescent molecules can now be observed on a regular basis. However, the development of such imaging systems was not without dilemmas such as the detection and separation of the individual fluorescent emissions. One such method used to solve this problem utilized surface plasmon resonance (SPR) to interact with and enhance the emission intensity of SM.

However, while enhancing SM emission intensity has yielded promising results, it does not fully utilize the unique plasmonic properties that could vastly improve the SM imaging capabilities. Here, we use SPR excitation as well as surface plasmon-coupled emission (SPCE) from an HDDVD grating structure to image and identify different fluorophores, fluorescein isothiocyanate (FITC), rhodamine 6G (R6G), and cyanine 5 (Cy5), using the angular emission of SM. Our results have important implications for research in multiplexed SM spectroscopy and multiplexed SM fluorescence imaging.

6.2. Wide Concentration Range Fluorescence Imaging

SPR is a unique phenomenon where a resonant charge oscillation forms at the surface of a metallic grating structure as a result of light impinging on the surface

at a specific angle of incidence. This charge oscillation and the resulting high-intensity EM field can interact with and excite nearby dipoles, such as fluorescent molecules, to much higher energy levels than the incident light alone. In our case, we obtained our nanoscale gratings ($\Lambda = 400$ nm, $H = 55$ nm) from a microcontact printing process using HDDVDs. This process yields very similar results as other grating fabrication methods, such as E-beam lithography, but is much less expensive and less time consuming. After applying a thin, 100 nm silver coating, the gratings have the capability to enhance the fluorescent intensity of R6G and Cy5 dye films by 100-200x vs. glass substrates using a relatively simple epifluorescence microscope.[20, 42, 93] Additionally, these gratings can couple wavelengths of light over a much wider angular range than prism-based SPR platforms. This is advantageous for microscopy as the microscope objective provides the necessary angular illumination for generating an enhanced EM field that encompasses the entire field of view of the microscope and resulting in the ability to observe several molecules in a single image.[42, 93]

Many imaging systems that are used to observed single molecule behavior, such as confocal or TIRF microscopy, are limited to a narrow range (2 nM to 1 pM) of molecular concentrations.[105] The upper concentration imaging barrier is primarily due to the inherent diffraction limitations of such optical systems. However, imaging a concentration below the lower imaging barrier is considered impractical as it often requires the use of time-consuming and expensive techniques.

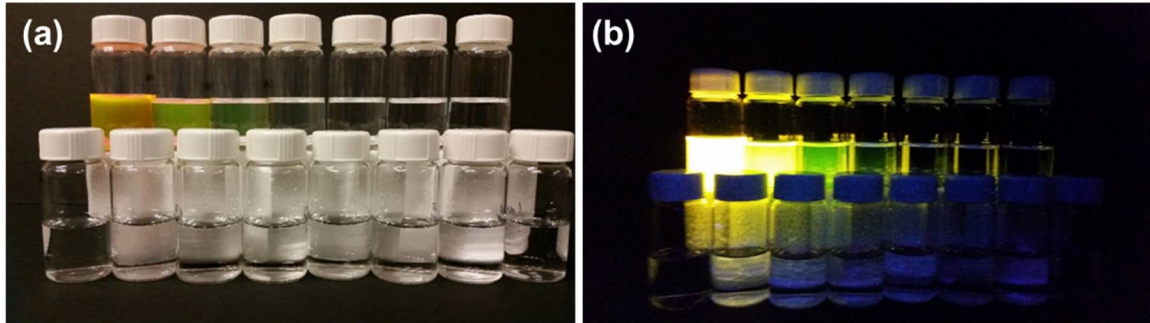


Figure 6-1. Decreasing concentration of R6G dissolved in ethanol under (a) ambient illumination and (b) UV excitation. Top (L to R): 100 μ M, 10 μ M, 1 μ M, 100 nM, 10 nM, 1 nM, 100 pM. Bottom (L to R): 10 pM, 1 pM, 100 fM, 10 fM, 1 fM, 100 aM, 10 aM, 1 aM.

Due to the significant enhancement of single molecule emissions, the increase in signal to noise ratio (SNR), and the resolution enhancements, plasmonic gratings are capable of greatly widening the lower and upper concentration limitations. To test the imaging limits of the plasmonic gratings, 100 nm thick silver gratings with a 10 nm Al₂O₃ spacer deposited via ALD were coated with a 30 nm thick spin-cast PMSSQ film laced with different concentrations of R6G dye (100 μ M – 1 aM, seen in Fig. 6-1) and imaged.

The images were taken with the 100x OI objective. Two distinct imaging domains were observed, the images exhibited either bulk fluorescent emission behavior (100 μ M to 100 nM) or single molecule behavior (10 nM – 1 aM.) The transition between the two domains can be seen in Fig. 6-2.

The increased SNR of the plasmonic gratings enables the identification of single molecules at concentrations up to 10 nM; 5 times more concentrated than the upper concentration limits of TIRF and confocal. Typically, the overlap of SM emissions at the upper concentration limits makes it very difficult to identify the location of a SM. Diffraction limitations play a role as the minimum resolvable

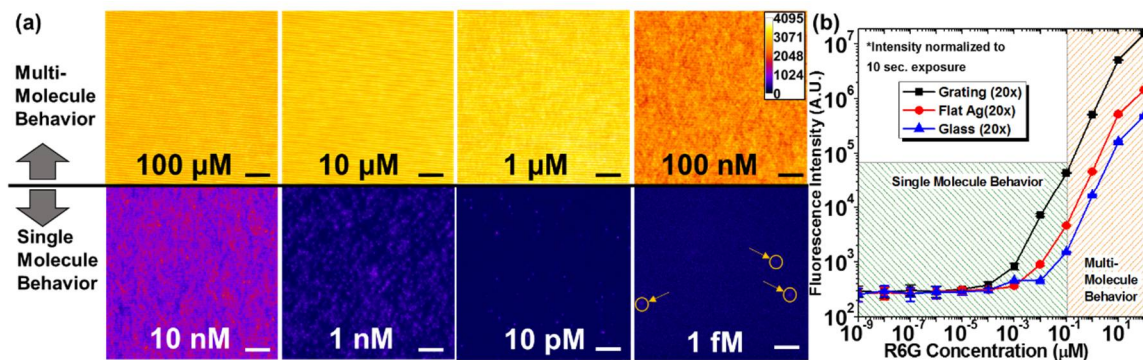


Figure 6-2. (a) False-colored fluorescence images taken with a 100x (1.4 NA) oil-immersion objective of the plasmonic gratings with decreasing concentrations of R6G at different exposure times. 100 μM–0.012s, 10 μM–0.05s, 1 μM–0.5s, 100 nM – 1.5s , 10 nM–4s, 1 nM–8s, 10 pM–10s, and 1 fM–10s. Scale bar: 4 μm. (b) Fluorescence intensity of R6G dye films at different concentrations normalized to 10 second exposure on plasmonic gratings, flat silver, and glass with a 20x (0.45 NA) objective.

distance between molecules is large at optical frequencies (200-400 nm). The plasmonic grating behaves as a far-field superlens (FSL) that can project the sub-diffraction information in the near-field out to the far-field as well as enhance the emission intensity of each molecule, thus increasing the SNR.[93]

For single molecule imaging, the SNR can be further improved by using photo-bleached background subtraction. This image analysis method subtracts the background signal specific to the area being imaged to decrease the standard deviation of the background noise with a small decrease in single molecule emission intensity. In contrast with other background subtraction methods, such as the mean of the background signal being subtracted from the raw image, can actually result in a reduced SNR. If the mean background signal, which has a value of 1201 in Fig. 6-3(a), is subtracted from the raw image, the overall image and the single molecule intensity decreases substantially without a corresponding decrease in the standard deviation of the background noise. This results in a SNR

that decreases proportionally to the strength of the background being subtracted. As seen in Fig. 6-3(c), the SNR decreased from 23.4 to 10.9. However, while the mean background signal is only a specific value, the photobleached sample image contains the background signal specific to area being imaged, including solution background, scattering, unbleached fluorophores, CMOS electrical noise, etc. By subtracting this bleached image, the noise specific to the imaging location is greatly reduced which results in an enhanced SNR, or an increase in SNR from 23.4 to 26.6. The intensity histograms of The image subtraction process can be performed using the “image calculator” built into ImageJ (Process < Image Calculator) to subtract the image frame of the photobleached sample (Fig. 6-3(b)) from the image frame of the raw sample (Fig. 6-3(a)) to give Fig. 6-3(d). The photobleached background subtraction method was used to analyze the SM images obtained from samples spin-coated in PMSSQ

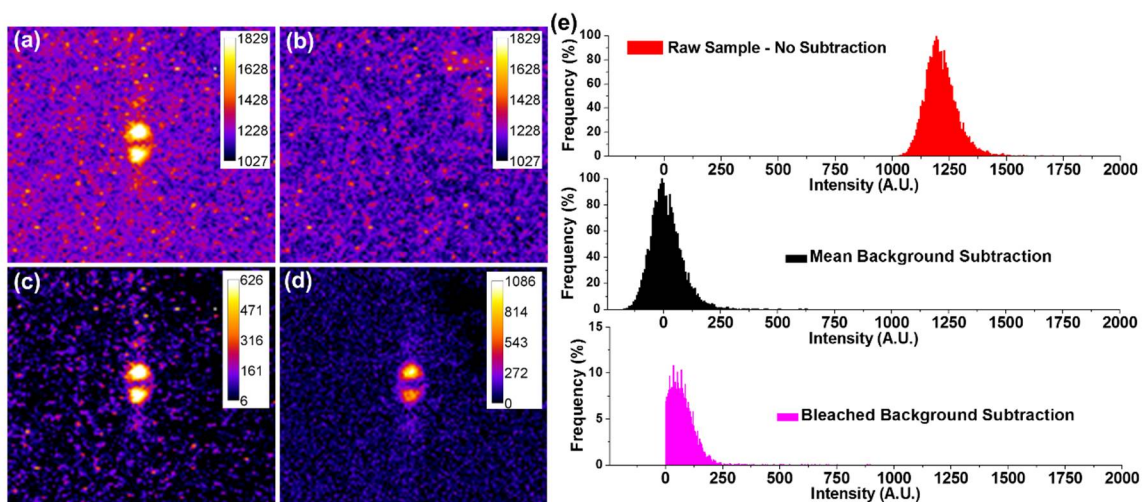


Figure 6-3. Raw fluorescence images of a SM of R6G exhibiting a split-emission pattern from an image sequence (a) before (frame 9) and (b) after photobleaching (frame 33). Each frame had an exposure time of 10 sec. and were taken with a 100x OI objective. (c) Mean background-subtracted fluorescence image where the mean background signal of 1201 was subtracted from the image in (a). (d) The photobleached sample image in (b) was subtracted from (a).

with less than 10 nM R6G. As the concentration decreases below pM, the SNR tends to decrease until the emission signal is within the background noise level.

To extract the emission signal, unique excitation and imaging techniques are often used to increase SNR but are typically time-consuming and expensive. Based on the single molecule emission intensities compared to the noise, we can obtain a SNR between 5 to 13 at R6G concentrations in the single molecule imaging range (1 nM – 1 aM) as seen in Fig. 6-4(a). It can also be seen that the SNR does not significantly change at lower concentrations. The ability to identify and count the number of molecules in a specific area has several uses in research, especially in biosensor research, as the number of molecules bound to a specific area can be directly correlated to the concentration of the molecule in the incubation solution.[106] In this case, the number of molecules per unit area were counted

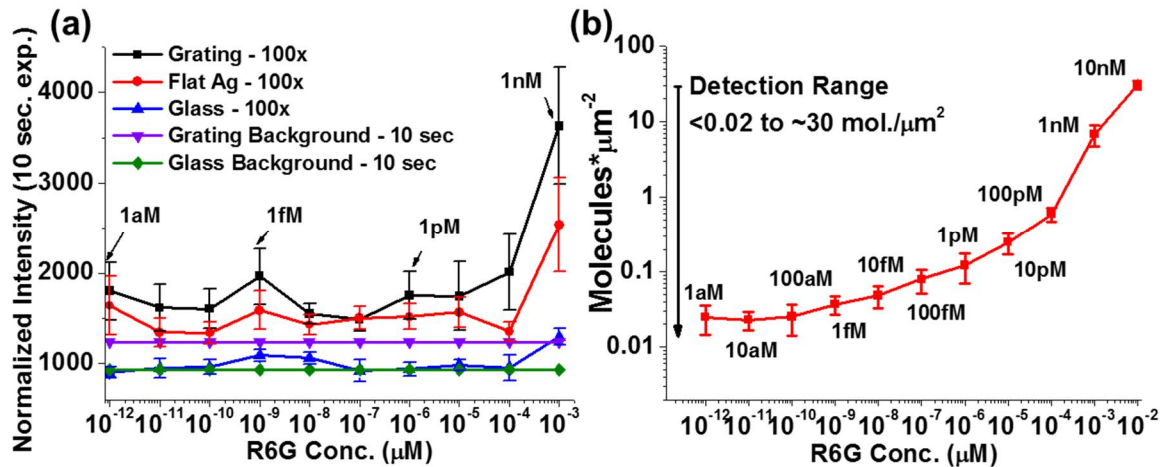


Figure 6-4. (a) Normalized fluorescence intensity of single molecules imaged with a 100xOI objective and 10 sec. exposure time on silver gratings, flat silver, and glass samples coated with R6G over the SM behavior concentration range. (b) Calculated quantity of dye mol. μm^{-2} for various R6G dye concentrations. The estimated upper detection limit is 30 mol./ μm^2 where the SM emission is too overlapped to separate. The estimated lower limit is less than 0.02 mol./ μm^2 and is primarily limited by the field of view of the objective rather than the objective's resolution and CMOS sensitivity.

over the entire SM behavior range using ImageJ and overlaid grids of known dimensions. The number of molecules per μm^2 was tabulated and plotted in Fig. 6-4(b). The number of dye molecules per μm^2 was found to increase with increasing R6G concentration until the SM signals were too overlapped to separate. The maximum number of molecules found to be separable was ~ 30 mol. per μm^2 which represents the upper detection limit. At the lowest concentration tested (1 aM), the SM emissions were well above background (2-3x background signal) but are spaced far apart, 0.02 mol. per μm^2 , or 1 SM per $5 \times 10^4 \mu\text{m}$ region. As the single molecule emissions are easily distinguished even at the lowest concentration tested, the primary limitation in SM detection is the field of view of the camera systems and the ability to find individual molecules over a large sample area.

In this experiment, the relationship between the number of mol. per μm^2 was not linearly correlated with the R6G dye concentration (Fig. 6-4(b).) This non-linearity is caused by the influence of the grating structure on the PMSSQ film during spin-coating, e.g. dye molecules can be trapped and concentrated in the grating grooves instead of freely flowing with the PMSSQ. However, the relationship is expected to be directly proportional when the influence of the grating structure on surface concentration is removed, such as molecules diffusing to the surface out of a solution.

6.3. SPCE Fluorescence Imaging

An interesting observation was made when examining the SM fluorescence on silver gratings with different polarization filters and at different focal heights. The emission intensity of a large SM population was found to exhibit angular emission and, upon further examination, the angular emission was strikingly similar to the emission angle range predicted by SPCE, as illustrated in Fig. 6-5(a.)

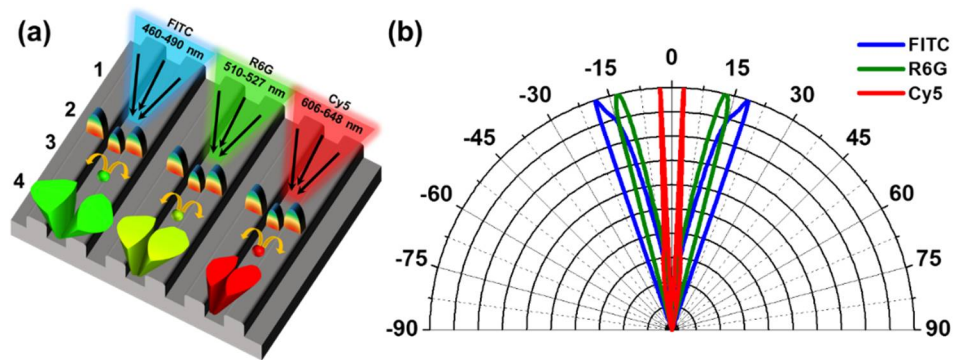


Figure 6-5. Single molecule SPCE on a plasmonic grating. (a) Formation of SM SPCE 1) Excitation light is incident on the grating. 2) Photons converted into SPR evanescent field that excites a nearby fluorescent molecule 3) Excited fluorescent molecule vibrates and non-radiatively transfers remaining energy to the grating 4) Radiative plasmon emitted from grating at the SPCE emission angle (θ_{SPCE}). (b) Calculated θ_{SPCE} range for FITC, R6G, and Cy5 fluorescent dyes based on SPR dispersion, emission wavelengths of each dye, and emission filter transmission spectrum.

To date, SPCE is primarily studied at the macroscale using the projected emission pattern from flat metal films and hemispherical lenses.[36, 107, 108] Correspondingly, very little to no information was available on SPCE imaging at the SM scale.[109] As SPCE and SPR are, in a sense, opposites of each other, where light is coupled at a specific angle to form SPR and radiative surface

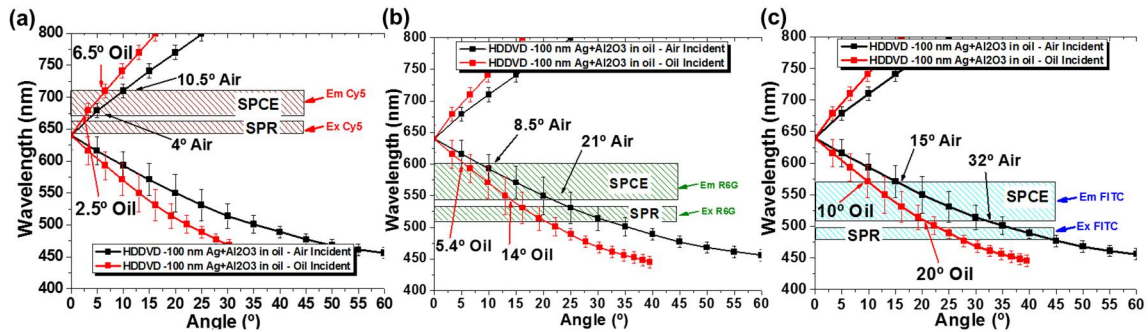


Figure 6-6. SPR Dispersion of the plasmonic grating with light incident in air (black) and oil (red) and excitation (SPR) /emission (SPCE) wavelength ranges for (a) Cy5, (b) R6G, and (c) FITC, respectively.

plasmons are emitted at a specific angles in SPCE, we can use the SPR dispersion (Fig. 6-6) to predict the angular emission of a specific fluorophore (Fig. 6-5(b).) Additional information on the fitting of the angular emission has been provided in the methods sections as well as the determination of the theoretical SPCE emission ranges. By studying the SM emission from SPCE, it is possible to not only obtain emission angle but substantially more information about the molecular position in the EM field and dipole orientation. As the emission angle range is also unique to the fluorophore emission spectrum, it can also be used to identify the fluorescent molecules if, for example, they are part of a multi-labeled fluorescent sample.

SMs of R6G embedded in a 33 nm PMSSQ thin film were imaged using an excitation polarizer and a rotating polarized emission analyzer to determine if the angular emission was due to SPCE and not from dipole-related phenomena. Given the much longer exposure time of the SM images (~10 sec., see Methods), the resulting images will contain the full angular emission range for each SM.[110] During imaging, we observed two populations of SM emissions (Fig. 6-7): the first

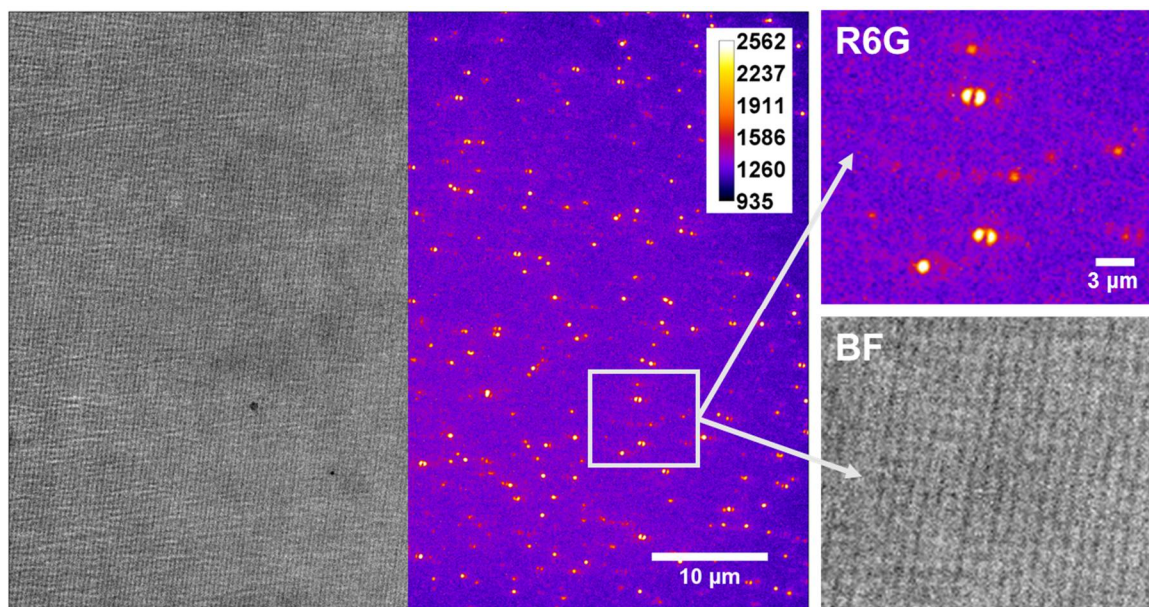


Figure 6-7. Bright field and false-colored fluorescence image (100xOI objective, 10 sec. exposure) of a plasmonic grating with a spin-casted 33 nm thin fluorescent PMSSQ film (10^{-14} M R6G) with expansions of the same location.

and largest population exhibited the response as seen in Fig. 6-8(a) while the second, much smaller population exhibited the response seen in Fig. 6-8(b.) In Fig. 6-8(a), two lobes or a “split emission” per molecule can be observed where the intensity was primarily P-polarized. The absence of S-polarized light in the emission is in agreement with SPCE theory as it is known that P-polarized light is the only polarization that can be emitted by a radiative surface plasmon on a grating.[36] If the emission was due to the dipole orientation alone, we would expect the orientation of the split emission to rotate with the analyzer as was the case for the second, smaller population.[111] The difference in polarization of the emissions also enables easy separation between the two emission types.

A difference in emission shapes between the two populations can also be observed by increasing the height of the objective’s image plane relative to the

sample as seen in Fig. 6-8(b). The split emission SM seen in Fig. 6-8(c) spreads outward from the molecule whereas the second population SM (Fig. 6-8(d)) displayed an inverted, conical emission similar to that observed by Böhmer with defocused images.[112] Two additional fluorophores were imaged, FITC and Cy5, at concentrations within the SM behavior range (1 μ M - 1 pM) to further test if the split emission observed in first population is the result of SPCE. Based on the SPR dispersion and excitation/emission ranges of the two dyes, FITC is expected to

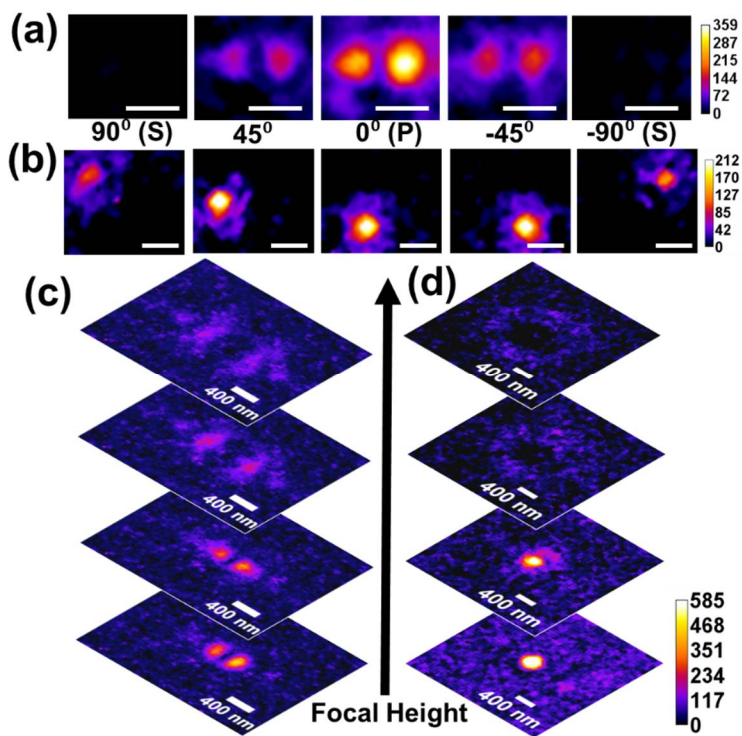


Figure 6-8. Polarization and Emission Angle of Single Molecules. (a) Fluorescence images of single R6G molecules with a polarized emission analyzer rotated from S-P-S polarization. Separate dye molecules exhibiting (Top) P-polarized SM SPCE behavior and (Bottom) Dipole-oriented emission behavior that rotates with polarization angle. (b) Stacked fluorescence images taken at increasing focal plane height above the plasmonic grating. (Left) Angled SPCE and (Right) Airy disc pattern from the isotropic emission of a SM spreading with increasing focal height. Scale bar: 400 nm. Image exposure: 10 sec.

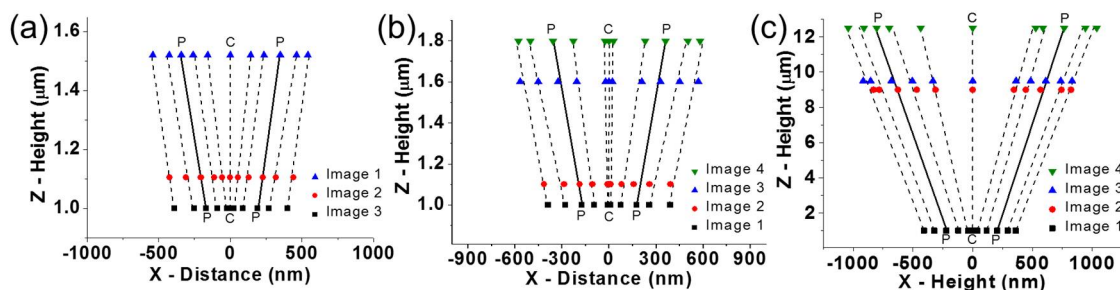


Figure 6-9. Fitted Intensity Profiles. Fluorescence intensity profiles with fitted points of interest (P: peak, C: center) at varying focal heights for (a) FITC, (b) R6G, and (c) Cy5.

have a wider and Cy5 a narrower emission angle range, respectively. As anticipated, the split emission patterns were also observed with FITC and Cy5 that had different angular emission ranges (Fig. 6-9).

The angular emission profiles were obtained using the intensity profiles at known focal heights. Furthermore, points of interest such as the peaks, FWHMs, and valleys of the profiles, at different heights were fitted using linear models for each fluorophore. The resulting angles for each linear model were then applied to the in-focus intensity profile to obtain an emission angle vs. intensity relation for FITC (Fig. 6-10(a)), R6G (Fig. 6-10(b)), and Cy5 (Fig. 6-10(c).)

The obtained emission profiles for each dye correspond well with the predicted SPCE emission range (gray lines) but with variations in intensity between the two lobes of the split emissions. In theory, an excited dye molecule located in the middle of a grating groove has an equal probability of non-radiatively transferring

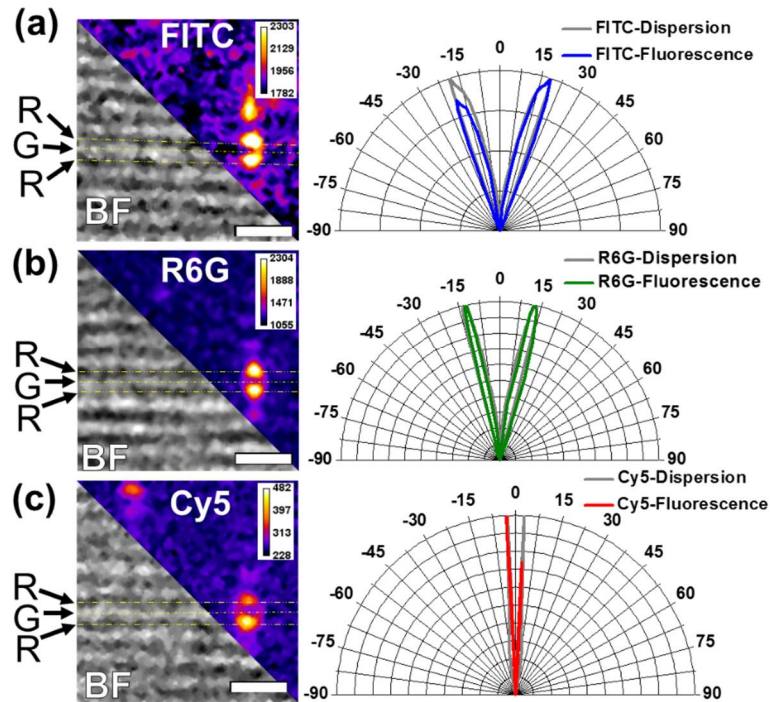


Figure 6-10. Single molecule SPCE on a plasmonic grating. Overlaid brightfield and fluorescence images of PMSSQ coated gratings with 1 fM (a) FITC, (b) R6G, (c) and Cy5. The normalized emission angle range for each respective fluorescence image has been plotted with the emission range predicted by the SPR dispersion to the right of each image. Scale bar: 1 μm . Grating Ridge (R) and Groove (G).

its energy to either grating ridge paralleling the groove. However, closer proximity to either ridge will result in a higher probability of energy transfer according to the surface energy transfer (SET) model.[41] As the placement of the dye molecule is random within the pits of the grating structure, the molecular position may be located closer to one side of the groove than the other. It may be possible to locate the precise XYZ-location of a molecule within the grating groove based on the relative intensity of the two lobes and focal plane location, but this requires a secondary localization precision method beyond the scope of our current measurement capabilities.

The intensity profiles of two representative SM for each population were also compared to determine the image resolution in Fig. 6-11. Based on the intensity profile for the diffraction-limited population (Fig. 6-11(a)), the FWHM was found to be ~ 327 nm. Given that the wavelength of most of the photons collected in these images are between 542 and 600 nm and that an airy disc pattern with distinct 0- and 1st-order diffraction modes can be seen, this population is certainly diffraction-limited. However, the lobes of the split emission (Fig. 6-11(b)) have much better resolution with a FWHM of ~ 233 nm and ~ 217 nm for each lobe, respectively. Additionally, the spacing between the two lobes was smaller yet at ~ 164 nm. The diffraction limit can be roughly estimated to be between 230-260 nm based on the Rayleigh criterion, which is larger than the FWHM and much larger spacing of the split emission pattern. If the split emission is due to SPCE, this confirms that sub-diffraction limit information is being transmitted into the far-field.

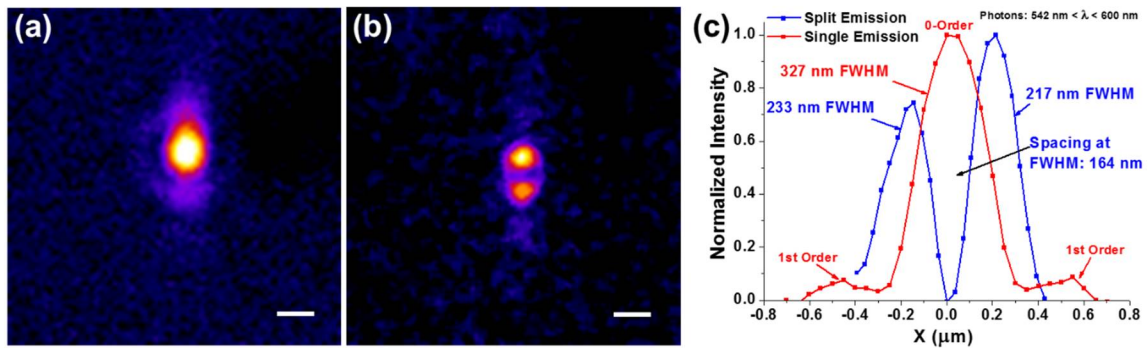


Figure 6-11. Background-subtracted Fluorescence images of single molecules of R6G on a plasmonic grating exhibiting a (a) diffraction-limited airy disc and (b) split emission due to SPCE. 100x Objective (NA 1.49), 10 sec. exposure, Scale bar: 400 nm. (c) Cross-section of the SM in (a) and (b) with calculated FWHM and separation distance of the split emission lobes.

6.4. Conclusion

In summary, silver plasmonic gratings enable enhanced fluorescence-based detection, including single molecule, over a much wider fluorescent dye concentration range, 100 μM - 1 fM, than traditional substrates. We have also demonstrated that it is possible to image SM SPCE from plasmonic gratings using a simple epifluorescence microscope. From these images we can extract the angular emission profiles for individual dye molecules that can be used to identify the type of fluorophore and improve localization precision. The plasmonic gratings can also be used to improve the image resolution to below the diffraction limit. This imaging technique can be easily applied to other SM research applications by substituting glass or quartz substrates for plasmonic gratings to greatly improve fluorophore identification, emission intensity image resolution.

6.5. Experimental Methods

Grating fabrication: PMSSQ gratings were fabricated using a microcontact lithography process with cleaned HDDVD (Memorex) halves as master molds to cast polydimethylsiloxane (PDMS, Sylgard-184, Gelest) stamps. The grating profile was transferred to silicon wafers by spin-casting (3000 RPM, 30 sec.) a 3% wt. solution of polymethylsilsesquioxane (PMSSQ, Techniglass) dissolved in pure ethanol on the PDMS stamp and placing the stamping in contact with the wafer for ~5 seconds before removal. PMSSQ Gratings were cured at 60°C for 3 hours on a hotplate. Gratings were coated with a 5 nm thin titanium film followed by a 100

nm thin silver film using DC Sputtering. Silver was protected from corrosion using a 10 nm thin Al₂O₃ film deposited via atomic layer deposition (ALD).[42]

Fluorescent sample preparation and analysis: Fluorescein isothiocyanate (FITC), rhodamine 6G (R6G), and Cyanine 5 (Cy5) were diluted to 10⁻¹⁵ M in 200 proof ethanol with 1% wt. polymethylsilsesquioxane (PMSSQ) and spin-cast onto the finished gratings to yield a 33-nm PMSSQ thin film and cured at 60°C for 10 min. The fluorophore density of the film was measured to be ~4 molecules per 10 μm x 10 μm area.

Reflectivity peak position and FWHM were used to form the air-incident SPR dispersion ($\theta_{SPCE, air}$) which was converted to oil-incident (n=1.518) SPR dispersion. The normalized emission spectrums ($I_{Fluorophore}$) for FITC, R6G, and Cy5 were multiplied by the respective bandpass emission filter transmission spectrums ($T_{em filter}$), the microscope objectives transmission spectrum ($T_{Objective}$), and the spectral sensitivity of the camera (q_{CMOS}). The resulting spectrums were multiplied by the oil-incident SPR dispersion to convert the intensity related to wavelength into angular emission ($I_{emission}(\theta)$), see equation (6.1).

$$I_{emission}(\theta) = I_{Fluorophore}(\lambda) * T_{em filter}(\lambda) * T_{Objective}(\lambda) * q_{CMOS}(\lambda) * \theta_{SPCE,oil}(\lambda) \quad (6.1)$$

ImageJ software was used to obtain the intensity profiles of individual fluorophores at known focal plane heights. The intensity profile points were fitted across all of the image planes to determine the angular spread of the intensity profile as the SM was defocused.

Experimental set-up: Grating reflectivity was captured using a variable angle spectroscopic ellipsometer. Samples were imaged using an Olympus BX51WI

epifluorescence microscope equipped with a Lambda XL light source, excitation polarizer, fluorescence filter cubes for FITC, R6G and Cy5, rotatable, polarized analyzer, UAPON 100xOI TIRF objective (1.49 NA), and an ORCAFlash 2.8 CMOS camera. Fluorescence videos were captured with an exposure time of 10 seconds.

CONCLUSION

In Chapter 1, the plasmonic dispersion equations were derived based on Maxwell's equations. Using these equations, the theory behind the generation of SPR and similar phenomenon was explored using both prism and grating-based systems. The sensitivity of grating-coupled SPR was modeled using FDTD simulation and studied experimentally. The generation of fluorescence and interaction between fluorescent molecules and SPR was explored to maximize fluorescent emission enhancement and better understand SPCE.

In Chapter 2, a novel micro-contact lithography process was developed that extracts the grating structures found in optical media, HDDVDs and Blurays, and replicates these structures on microscope slides and silicon wafers. The reproducibility and flexibility of the PDMS stamps used in this process was optimized for ease of producing the grating structure in PMSSQ. The crosslinking and long-term stability of the PMSSQ grating structure was studied and optimized with exposure to APTES vapor and heat treatment temperature and duration. The theory behind two metal deposition systems and a ceramic deposition technique was explored to optimize the properties of the resulting alumina-capped metal films.

In Chapter 3, the surface and optical properties of silver films deposited by either thermal evaporation or RF sputtering were modeled and characterized. The influence of metal film properties on SPR was evaluated using fluorescence microscopy to determine the optimal deposition parameters including PMSSQ surface energy, deposition rate, and grating orientation.

In Chapter 4, a fluorescence biosensor process for the detection of cortisol was developed using plasmonic gratings to enhance the fluorescence response.

In Chapter 5, gold plasmonic gratings with incorporated nanostructures, nanocones and nanogaps, were used to enhance the detection of the binding of complementary ssDNA sequences to surface immobilized DNA sequence.

In Chapter 6, the capability of an alumina-capped silver grating to enhance fluorescence over a wide concentration range from bulk fluorescence (10^{-4} M) to single molecule detection (10^{-18} M) was evaluated. The angular emission profiles of single molecule SPCE were also studied using various fluorophores. Based on the emission profiles for individual molecules, the plasmonic grating improved the localization precision and enabled the identification of fluorophore molecules.

In summary, the plasmonic gratings developed in this research can significantly improve the fluorescent emission intensity and resolution of fluorescence imaging across the entire visible spectrum and, as a result, have enormous potential for applications in any fluorescence detection system, including microscopes, plate readers, spectrometers, and biosensors.

PUBLICATIONS AND PRESENTATIONS

Publications – Journal Articles

- 1) A.J. Wood, M.J. Cozad, D.A. Grant, A.M. Ostdiek, S.L. Bachman and S.A. Grant. (2013). Materials characterization and histological analysis of explanted polypropylene, PTFE, and PET hernia meshes from an individual patient. *Journal of Materials Science: Materials in Medicine*. 24(4), 1113.
- 2) R.M. Dolazza, A.J. Wood, S.A. Grant and C.L. Lorenzen. (2014). Comparison between a functionalized glass slide biosensor with fluorescently labeled Calpastatin antibodies and the traditional Calpastatin activity assay. *Meat Science*. 96(1), 450.
- 3) A. J. Wood, S. Basuray, S. Bok, K. Gangopadhyay, S. Gangopadhyay, and S. Grant. (2015). Enhanced DNA Detection through the Incorporation of Nanocones and Cavities into a Plasmonic Grating Sensor Platform. *Sensors Journal, IEEE*. PP (99). pp. 1-1.
- 4) A. J. Wood, B. Chen, S. Pathan, S. Bok, C. J. Mathai, K. Gangopadhyay, S. A. Grant, and S. Gangopadhyay. (2015). Influence of silver grain size, roughness, and profile on the extraordinary fluorescence enhancement capabilities of grating coupled surface plasmon resonance. *RSC Advances*. 5 (96). pp. 78534-78544.
- 5) B. Chen, A. Wood, A. Pathak, J. Mathai, S. Bok, H. Zheng, et al. (2016). Plasmonic gratings with nano-protrusions made by glancing angle deposition

for single-molecule super-resolution imaging. *Nanoscale*. 8. pp. 12189-12201.

*B. Chen and A. Wood have joint first authorship

- 6) A. Wood, B. Chen, J. Mathai, S. Bok, S. Grant, K. Gangopadhyay, P. V. Cornish, and S. Gangopadhyay. (2016) Super-Resolution Light Microscopy Using Plasmonic Gratings. *Microscopy Today*. To be published Jan. 2017.
- 7) A. Wood, C. J. Mathai, K. Gangopadhyay, S. Grant, and S. Gangopadhyay. Single-molecule surface plasmon coupled emission with plasmonic gratings. Submitted to Nature Photonics.

Publications – Conference Proceedings

- 1) A. Wood, S. Grant, S. Basuray, A. Pathak, S. Bok, C. Mathai, K. Gangopadhyay, and S. Gangopadhyay. (2014). Enhanced fluorescence through the incorporation of nanocones/gaps into a plasmonic gratings sensor platform. *IEEE Sensors Proceedings*. pp. 1479-1482. *Won best student paper in Track 3 (Biosensors) at the conference.
- 2) S. Bok, S. Pathan, A. J. Wood, B. Chen, C. J. Mathai, K. Gangopadhyay, S. Grant, C. McArthur, and S. Gangopadhyay. Highly sensitive plasmonic grating platform for the detection of a wide range of infectious diseases, *Transducers 2015, IEEE, Anchorage, AK, 2015*, pp. 1573 - 1576.
- 3) A. Wood, S. Bok, C. J. Mathai, B. Chen, D. Suresh, K. Gangopadhyay, S. Grant, A. Uprendran, R. Kannan, S. Gangopadhyay. (2016). Anti-Corrosive films on Silver Plasmonic Gratings for Fluorescence Imaging of Single Molecules and Cancer Cells. *Conference on Lasers and Electro-Optics, OSA Technical Digest (2016) (Optical Society of America)*

Podium Presentations

NSF Plant Sciences and Bioengineering Colloquium. Oct. 29, 2014, Columbia, Missouri.

- A. Wood, S. Grant, S. Basuray, A. Pathak, S. Bok, C. Mathai, K. Gangopadhyay, and S. Gangopadhyay. (2014). Enhanced fluorescence through the incorporation of nanocones/gaps into a plasmonic gratings sensor platform.

IEEE Sensors Annual Conference, Valencia, Spain. Nov. 2-5, 2014 – Conference Paper and Podium Presentation

- A. Wood. Development of a grating-coupled surface plasmon resonance sensor platform for use in highly sensitive point-of-care diagnostics.
*Won best student paper in Track 3 (Biosensors) at the conference.

Conference on Lasers and Electro-Optics (CLEO), San Jose, CA. Jun. 7-9, 2016

- A. Wood, S. Bok, C. J. Mathai, B. Chen, D. Suresh, K. Gangopadhyay, S. Grant, A. Uprendran, R. Kannan, S. Gangopadhyay. (2016). Anti-Corrosive films on Silver Plasmonic Gratings for Fluorescence Imaging of Single Molecules and Cancer Cells.

REFERENCES

- [1] P. Lazzeri, L. Vanzetti, E. Iacob, M. Bersani, M. Anderle, J. Park, Z. Lin, R. Briber, G. Rubloff, and R. Miller, "Material Characterization and the Formation of Nanoporous PMSSQ Low-K Dielectrics," in *AIP Conference Proceedings*, 2003, pp. 551-555.
- [2] A. Hessel and A. A. Oliner. (1965). A New Theory of Wood's Anomalies on Optical Gratings. *Applied Optics*. 4 (10). pp. 1275-1297.
- [3] U. Fano. (1941). The Theory of Anomalous Diffraction Gratings and of Quasi-Stationary Waves on Metallic Surfaces (Sommerfeld's Waves). *Journal of the Optical Society of America*. 31 (3). pp. 213-222.
- [4] J. Chen, P. Albella, Z. Pirzadeh, P. Alonso-González, F. Huth, S. Bonetti, V. Bonanni, J. Åkerman, J. Nogués, P. Vavassori, A. Dmitriev, J. Aizpurua, and R. Hillenbrand. (2011). Plasmonic Nickel Nanoantennas. *Small*. 7 (16). pp. 2341-2347.
- [5] D. K. Gramotnev and S. I. Bozhevolnyi. (2010). Plasmonics beyond the diffraction limit. *Nat Photon*. 4 (2). pp. 83-91.
- [6] M. Bosman, L. Zhang, H. Duan, S. F. Tan, C. A. Nijhuis, C. W. Qiu, and J. K. W. Yang. (2014). Encapsulated Annealing: Enhancing the Plasmon Quality Factor in Lithographically-Defined Nanostructures. *Scientific Reports*. 4 p. 5537.
- [7] T. Ming, L. Zhao, M. Xiao, and J. Wang. (2010). Resonance-Coupling-Based Plasmonic Switches. *Small*. 6 (22). pp. 2514-2519.
- [8] M. Kuttge, E. J. R. Vesseur, J. Verhoeven, H. J. Lezec, H. A. Atwater, and A. Polman. (2008). Loss mechanisms of surface plasmon polaritons on gold probed by cathodoluminescence imaging spectroscopy. *Applied Physics Letters*. 93 (11). p. 113110.
- [9] W. L. Barnes, D. AlainEbbesen, and W. Thomas. (2003). Surface plasmon subwavelength optics. *Nature*. 424 (6950). p. 824.
- [10] L. N. Binh, "*Wireless and Guided Wave Electromagnetics: Fundamentals and Applications*": Taylor & Francis, 2013.
- [11] D. J. Griffiths and R. College, "*Introduction to electrodynamics*" vol. 3: prentice Hall Upper Saddle River, NJ, 1999.
- [12] E. Hecht. (2002). Optics Pearson Education. *Inc., San Francisco*.

- [13] P. J. Mohr, B. N. Taylor, and D. B. Newell. (2008). CODATA recommended values of the fundamental physical constants: 2006*. *Reviews of Modern Physics*. 80 (2). pp. 633-730.
- [14] A. P. Hibbins, "Grating coupling of surface plasmon polaritons at visible and microwave frequencies," Doctor of Philosophy in Physics, University of Exeter, 1999.
- [15] H. Raether, "*Surface plasmons on smooth and rough surfaces and on gratings*". Berlin ; New York: Springer-Verlag, 1988.
- [16] A. Otto. (1968). Excitation of nonradiative surface plasma waves in silver by the method of frustrated total reflection. *Zeitschrift für Physik*. 216 (4). pp. 398-410.
- [17] E. Kretschmann and H. Raether. (1968). Radiative decay of nonradiative surface plasmons excited by light. *Z. Naturforsch. A*. 23 p. 2135.
- [18] J. W. Goodman, "*Introduction to Fourier optics*": Roberts and Company Publishers, 2005.
- [19] J. Homola, I. Koudela, and S. S. Yee. (1999). Surface plasmon resonance sensors based on diffraction gratings and prism couplers: sensitivity comparison. *Sensors and Actuators B: Chemical*. 54 (1). pp. 16-24.
- [20] K. Bhatnagar, A. Pathak, D. Menke, P. V. Cornish, K. Gangopadhyay, V. Korampally, and S. Gangopadhyay. (2012). Fluorescence enhancement from nano-gap embedded plasmonic gratings by a novel fabrication technique with HD-DVD. *Nanotechnology*. 23 (49). p. 12.
- [21] P. R. West, S. Ishii, G. V. Naik, N. K. Emani, V. M. Shalaev, and A. Boltasseva. (2010). Searching for better plasmonic materials. *Laser & Photonics Reviews*. 4 (6). pp. 795-808.
- [22] H. Shinji and O. Takayuki. (2012). Plasmonics: visit the past to know the future. *Journal of Physics D: Applied Physics*. 45 (43). p. 433001.
- [23] W. Knoll. (1998). INTERFACES AND THIN FILMS AS SEEN BY BOUND ELECTROMAGNETIC WAVES. *Annual Review of Physical Chemistry*. 49 (1). pp. 569-638.
- [24] M. Bauch, S. Hageneder, and J. Dostalek. (2014). Plasmonic amplification for bioassays with epi-fluorescence readout. *Optics Express*. 22 (26). pp. 32026-32038.
- [25] S. Enoch and N. Bonod, "*Plasmonics: From Basics to Advanced Topics*": Springer, 2012.

- [26] Y. Wang, W. Knoll, and J. Dostalek. (2012). Bacterial Pathogen Surface Plasmon Resonance Biosensor Advanced by Long Range Surface Plasmons and Magnetic Nanoparticle Assays. *Analytical Chemistry*. 84 (19). pp. 8345-8350.
- [27] K. Toma, J. Dostalek, and W. Knoll. (2011). Long range surface plasmon-coupled fluorescence emission for biosensor applications. *Opt. Express*. 19 (12). pp. 11090-11099.
- [28] J. Dostálek, B. Menges. (2011). Evanescent Wave Optics. *Max-Planck Insitute*.
- [29] A. Taflove and S. C. Hagness. (1995). Computational electrodynamics: the finite-difference time-domain method. *Norwood, 2nd Edition, MA: Artech House, 1995*.
- [30] K. S. Yee. (1966). Numerical solution of initial boundary value problems involving Maxwell's equations in isotropic media. *IEEE Trans. Antennas Propag.* 14 (3). pp. 302-307.
- [31] G. G. Stokes. (1852). On the Change of Refrangibility of Light. *Philosophical Transactions of the Royal Society of London*. 142 pp. 463-562.
- [32] L. D. Landau, E. Lifshitz, and L. Pitaevskii. (1980). Statistical Physics (Course of Theoretical Physics, Volume 5). *3rd. Edition*.
- [33] J. W. Lichtman and J.-A. Conchello. (2005). Fluorescence microscopy. *Nat Meth.* 2 (12). pp. 910-919.
- [34] J. Franck and E. Dymond. (1926). Elementary processes of photochemical reactions. *Transactions of the Faraday Society*. 21 (February). pp. 536-542.
- [35] J. R. Lakowicz. (2005). Radiative decay engineering 5: metal-enhanced fluorescence and plasmon emission. *Analytical biochemistry*. 337 (2). pp. 171-194.
- [36] J. R. Lakowicz. (2004). Radiative decay engineering 3. Surface plasmon-coupled directional emission. *Analytical Biochemistry*. 324 (2). pp. 153-169.
- [37] B. W. Van Der Meer, G. Coker, and S.-Y. S. Chen. (1994). Resonance energy transfer: theory and data.
- [38] J. R. Lakowicz, "*Principles of fluorescence spectroscopy*": Springer Science & Business Media, 2013.

- [39] J. Zhang, Y. Fu, and J. R. Lakowicz. (2007). Enhanced Förster Resonance Energy Transfer (FRET) on Single Metal Particle. *J Phys Chem C Nanomater Interfaces*. 111 (1). pp. 50-56.
- [40] H. Kuhn. (1970). Classical aspects of energy transfer in molecular systems. *The Journal of Chemical Physics*. 53 (1). pp. 101-108.
- [41] C. J. Breshike, R. A. Riskowski, and G. F. Strouse. (2013). Leaving Förster Resonance Energy Transfer Behind: Nanometal Surface Energy Transfer Predicts the Size-Enhanced Energy Coupling between a Metal Nanoparticle and an Emitting Dipole. *The Journal of Physical Chemistry C*. 117 (45). pp. 23942-23949.
- [42] A. J. Wood, B. Chen, S. Pathan, S. Bok, C. J. Mathai, K. Gangopadhyay, S. A. Grant, and S. Gangopadhyay. (2015). Influence of silver grain size, roughness, and profile on the extraordinary fluorescence enhancement capabilities of grating coupled surface plasmon resonance. *RSC Advances*. 5 (96). pp. 78534-78544.
- [43] S. T. Kochuveedu and D. H. Kim. (2014). Surface plasmon resonance mediated photoluminescence properties of nanostructured multicomponent fluorophore systems. *Nanoscale*. 6 (10). pp. 4966-4984.
- [44] M. Jahn, S. Patze, I. J. Hidi, R. Knipper, A. I. Radu, A. Muhlig, S. Yuksel, V. Peksa, K. Weber, T. Mayerhofer, D. Ciolla-May, and J. Popp. (2016). Plasmonic nanostructures for surface enhanced spectroscopic methods. *Analyst*. 141 (3). pp. 756-793.
- [45] H. Hori, K. Tawa, K. Kintaka, J. Nishii, and Y. Tatsu. (2010). Surface profile dependence of the photon coupling efficiency and enhanced fluorescence in the grating-coupled surface plasmon resonance. *Journal of Applied Physics*. 107 (11). p. 114702.
- [46] X. D. Hoa, A. G. Kirk, and M. Tabrizian. (2009). Enhanced SPR response from patterned immobilization of surface bioreceptors on nano-gratings. *Biosensors and Bioelectronics*. 24 (10). pp. 3043-3048.
- [47] D. Gaoliang, Z. Fan, H. Markus, F. Georg, B. Thomas, K. Samuel, and F. Jens. (2015). Development and characterisation of a new line width reference material. *Measurement Science and Technology*. 26 (11). p. 115006.
- [48] P. Goel, K. Singh, and J. P. Singh. (2014). Polarization dependent diffraction from anisotropic Ag nanorods grown on DVD grating templates by oblique angle deposition. *RSC Advances*. 4 (22). pp. 11130-11135.

- [49] D. Ortiz-Acosta and C. Densmore. (2012). Sylgard® Cure Inhibition Characterization. *Los Alamos National Laboratory (LANL)*.
- [50] H. A. Jakobsen. (2008). Chemical reactor modeling. *Multiphase Reactive Flows, Berlin, Germany: Springer-Verlag*.
- [51] P. Sigmund. (1969). Theory of sputtering. I. Sputtering yield of amorphous and polycrystalline targets. *Physical review*. 184 (2). p. 383.
- [52] D. Depla, S. Mahieu, and J. Greene. (2010). Sputter deposition processes. *Handbook of deposition technologies for films and coatings: science, applications and technology*. pp. 253-296.
- [53] D. Nečas and P. Klapetek. (2012). Gwyddion: an open-source software for SPM data analysis. *Central European Journal of Physics*. 10 (1). pp. 181-188.
- [54] Y. Jiang, H.-Y. Wang, H. Wang, B.-R. Gao, Y.-w. Hao, Y. Jin, Q.-D. Chen, and H.-B. Sun. (2011). Surface Plasmon Enhanced Fluorescence of Dye Molecules on Metal Grating Films. *The Journal of Physical Chemistry C*. 115 (25). pp. 12636-12642.
- [55] J. A. Venables, G. D. T. Spiller, and M. Hanbucken. (1984). Nucleation and growth of thin films. *Reports on Progress in Physics*. 47 (4). p. 399.
- [56] J. E. Greene, "Chapter 12 - Thin Film Nucleation, Growth, and Microstructural Evolution: An Atomic Scale View," in *Handbook of Deposition Technologies for Films and Coatings (Third Edition)*, P. M. Martin, Ed., ed Boston: William Andrew Publishing, 2010, pp. 554-620.
- [57] K.-H. Müller. (1987). Role of incident kinetic energy of adatoms in thin film growth. *Surface Science*. 184 (1–2). pp. L375-L382.
- [58] Y.-R. Luo, "Bond Dissociation Energies," in *CRC Handbook of Chemistry and Physics*, W. M. Haynes, Ed., 96 ed: CRC Press, 2015.
- [59] W. Chen, M. D. Thoreson, S. Ishii, A. V. Kildishev, and V. M. Shalaev. (2010). Ultra-thin ultra-smooth and low-loss silver films on a germanium wetting layer. *Optics Express*. 18 (5). pp. 5124-5134.
- [60] R. Lazzari and J. Jupille. (2001). Silver layers on oxide surfaces: morphology and optical properties. *Surface Science*. 482–485, Part 2 pp. 823-828.
- [61] X. Cui, K. Tawa, H. Hori, and J. Nishii. (2010). Tailored Plasmonic Gratings for Enhanced Fluorescence Detection and Microscopic Imaging. *Advanced Functional Materials*. 20 (4). pp. 546-553.

- [62] J.-Y. Laluet, A. Drezet, C. Genet, and T. W. Ebbesen. (2008). Generation of surface plasmons at single subwavelength slits: from slit to ridge plasmon. *New Journal of Physics*. 10 (10). p. 105014.
- [63] Y. Li, J. Ren, H. Nakajima, N. Soh, K. Nakano, and T. Imato. (2007). Surface Plasmon Resonance Immunosensor for IgE Analysis Using Two Types of Anti-IgE Antibodies with Different Active Recognition Sites. *Analytical Sciences*. 23 (1). pp. 31-38.
- [64] K. Tawa, H. Hori, K. Kintaka, K. Kiyosue, Y. Tatsu, and J. Nishii. (2008). Optical microscopic observation of fluorescence enhanced by grating-coupled surface plasmon resonance. *Optics Express*. 16 (13). pp. 9781-9790.
- [65] A. Naoko, T. Keiko, T. Yoshiro, K. Kenji, and N. Junji. (2009). Grating Substrates Fabricated by Nanoimprint Lithography for Fluorescence Microscopy. *Japanese Journal of Applied Physics*. 48 (6S). p. 06FH17.
- [66] Y.-J. Hung, I. I. Smolyaninov, C. C. Davis, and H.-C. Wu. (2006). Fluorescence enhancement by surface gratings. *Optics Express*. 14 (22). pp. 10825-10830.
- [67] A. J. Bandothkar and J. Wang. (2014). Non-invasive wearable electrochemical sensors: a review. *Trends in Biotechnology*. 32 (7). pp. 363-371.
- [68] V. Lozanova, J. Tasseva, and R. Todorov. (2013). Grain size effect on the optical properties of thin silver films. *Bulgarian Chemical Communications Special Issue B*. 45 pp. 43-46.
- [69] Z. Liu, S. Durant, H. Lee, Y. Pikus, Y. Xiong, C. Sun, and X. Zhang. (2007). Experimental studies of far-field superlens for sub-diffractive optical imaging. *Optics Express*. 15 (11). pp. 6947-6954.
- [70] J. R. Sambles. (1984). Grain-boundary scattering and surface plasmon attenuation in noble metal films. *Solid State Communications*. 49 (4). pp. 343-345.
- [71] P. Dawson, K. B. Alexander, J. R. Thompson, J. W. Haas, and T. L. Ferrell. (1991). Influence of metal grain size on surface-enhanced Raman scattering. *Physical Review B*. 44 (12). pp. 6372-6381.
- [72] H. S. Lee, C. Awada, S. Boutami, F. Charra, L. Douillard, and R. E. de Lamaestre. (2012). Loss mechanisms of surface plasmon polaritons propagating on a smooth polycrystalline Cu surface. *Optics Express*. 20 (8). pp. 8974-8981.

- [73] P. Berini. (2009). Long-range surface plasmon polaritons. *Adv. Opt. Photon.* 1 (3). pp. 484-588.
- [74] Dror Sarid, Robert T. Deck, Alan E. Craig, Robert K. Hickernell, Ralph S. Jameson, and J. J. Fasano. (1982). Optical field enhancement by long-range surfaceplasma waves. *APPLIED OPTICS.* 21 (22).
- [75] J. Jaewook, S. Kim, C. Junhee, and H. Yongtaek. (2009). Stable Stretchable Silver Electrode Directly Deposited on Wavy Elastomeric Substrate. *Electron Device Letters, IEEE.* 30 (12). pp. 1284-1286.
- [76] H. Raether. (1983). The dispersion relation of surface plasmons on rough surfaces; A comment on roughness data. *Surface Science.* 125 (3). pp. 624-634.
- [77] H. Raether, "Surface Plasmons on Smooth and Rough Surfaces and on Gratings": Springer, 1988.
- [78] T. Shibata, H. Ikeda, H. Nishiyama, K. Tawa, and J. Nishii. (2013). Optimization of Metal Quality for Grating Coupled Surface Plasmon Resonance. *Physics Procedia.* 48 (0). pp. 179-183.
- [79] B. Sherman, C. Wysham, and B. Pfohl. (1985). Age-Related Changes in the Circadian Rhythm of Plasma Cortisol in Man. *The Journal of Clinical Endocrinology & Metabolism.* 61 (3). pp. 439-443.
- [80] A. M. McCarthy, K. Hanrahan, C. Kleiber, M. B. Zimmerman, S. Lutgendorf, and E. Tsalikian. (2009). Normative salivary cortisol values and responsivity in children. *Appl Nurs Res.* 22 (1). pp. 54-62.
- [81] E. B. Schwartz, D. A. Granger, E. J. Susman, M. R. Gunnar, and B. Laird. (1998). Assessing Salivary Cortisol in Studies of Child Development. *Child Development.* 69 (6). pp. 1503-1513.
- [82] R. I. Gafni, D. A. Papanicolaou, and L. K. Nieman. (2000). Nighttime salivary cortisol measurement as a simple, noninvasive, outpatient screening test for Cushing's syndrome in children and adolescents. *The Journal of Pediatrics.* 137 (1). pp. 30-35.
- [83] Q. Zhang, J. Dou, W. Gu, G. Yang, and J. Lu. (2013). Reassessing the reliability of the salivary cortisol assay for the diagnosis of Cushing syndrome. *Journal of International Medical Research.* 41 (5). pp. 1387-1394.
- [84] D. E. Polk, S. Cohen, W. J. Doyle, D. P. Skoner, and C. Kirschbaum. (2005). State and trait affect as predictors of salivary cortisol in healthy adults. *Psychoneuroendocrinology.* 30 (3). pp. 261-72.

- [85] A. Kaushik, A. Vasudev, S. K. Arya, S. K. Pasha, and S. Bhansali. (2014). Recent advances in cortisol sensing technologies for point-of-care application. *Biosensors and Bioelectronics*. 53 (0). pp. 499-512.
- [86] M. Venugopal, S. K. Arya, G. Chornokur, and S. Bhansali. (2011). A realtime and continuous assessment of cortisol in ISF using electrochemical impedance spectroscopy. *Sensors and Actuators A: Physical*. 172 (1). pp. 154-160.
- [87] E. Russell, G. Koren, M. Rieder, and S. H. Van Uum. (2014). The detection of cortisol in human sweat: implications for measurement of cortisol in hair. *Ther Drug Monit*. 36 (1). pp. 30-4.
- [88] M. Del Re, R. Gouttebaron, J. P. Dauchot, P. Leclère, R. Lazzaroni, M. Wautelet, and M. Hecq. (2002). Growth and morphology of magnetron sputter deposited silver films. *Surface and Coatings Technology*. 151–152 (0). pp. 86-90.
- [89] R. H. Ritchie. (1957). Plasma Losses by Fast Electrons in Thin Films. *Physical Review*. 106 (5). pp. 874-881.
- [90] N. M. M. Pires and T. Dong. (2014). Measurement of salivary cortisol by a chemiluminescent organic-based immunosensor. *Bio-Medical Materials and Engineering*. 24 (1). pp. 15-20.
- [91] J. Findling. (2014, Nov. 9, 2016). Diagnostic Testing for Cushing's Syndrome. Available: <https://csrf.net/understanding-cushings/diagnostic-testing/>
- [92] M. O. van Aken, J. A. Romijn, J. A. Miltenburg, and E. G. W. M. Lentjes. (2003). Automated Measurement of Salivary Cortisol. *Clinical Chemistry*. 49 (8). pp. 1408-1409.
- [93] B. Chen, A. Wood, A. Pathak, J. Mathai, S. Bok, H. Zheng, S. Hamm, S. Basuray, S. Grant, K. Gangopadhyay, P. V. Cornish, and S. Gangopadhyay. (2016). Plasmonic Gratings with Nano-protrusions Made by Glancing Angle Deposition for Single-Molecule Super-Resolution Imaging *Nanoscale*. 8 pp. 12189-12201.
- [94] J. A. Martin, J. L. Chávez, Y. Chushak, R. R. Chapleau, J. Hagen, and N. Kelley-Loughnane. (2014). Tunable stringency aptamer selection and gold nanoparticle assay for detection of cortisol. *Anal Bioanal Chem*. 406 pp. 4637-4647.
- [95] A. Wood, S. Grant, S. Basuray, A. Pathak, S. Bok, C. Mathai, K. Gangopadhyay, and S. Gangopadhyay. (2014). Enhanced fluorescence

through the incorporation of nanocones/gaps into a plasmonic gratings sensor platform. *IEEE Sensors Proceedings*. pp. 1479-1482.

- [96] J. Homola. (2008). Surface plasmon resonance sensors for detection of chemical and biological species. *Chem Rev.* 108 (2). pp. 462-93.
- [97] C. M. Darr, V. Korampally, B. Chen, K. Gangopadhyay, and S. Gangopadhyay. (2014). Plasmonic-enhanced conjugated polymer fluorescence chemosensor for trace nitroaromatic vapor. *Sensors and Actuators B: Chemical.* 202 (0). pp. 1088-1096.
- [98] B. Chen, C. J. Mathai, S. Mukherjee, and S. Gangopadhyay. (2014). Indium Tin Oxide Photonic Crystal for Controllable Light Coupling in Solar Cells by an Inexpensive Soft Lithography with HD-DVD and Blu-ray. *ECS Transactions.* 61 (18). pp. 69-82.
- [99] J. A. Schuller, E. S. Barnard, W. Cai, Y. C. Jun, J. S. White, and M. L. Brongersma. (2010). Plasmonics for extreme light concentration and manipulation. *Nat Mater.* 9 (3). pp. 193-204.
- [100] X. Zhu, Y. Zhang, J. Zhang, J. Xu, Y. Ma, Z. Li, and D. Yu. (2010). Ultrafine and Smooth Full Metal Nanostructures for Plasmonics. *Advanced Materials.* 22 (39). pp. 4345-4349.
- [101] C. E. Immoos, S. J. Lee, and M. W. Grinstaff. (2004). Conformationally Gated Electrochemical Gene Detection. *ChemBioChem.* 5 (8). pp. 1100-1103.
- [102] J. W. Attridge, P. B. Daniels, J. K. Deacon, G. A. Robinson, and G. P. Davidson. (1991). Sensitivity enhancement of optical immunosensors by the use of a surface plasmon resonance fluoroimmunoassay. *Biosensors and Bioelectronics.* 6 (3). pp. 201-214.
- [103] S. B. Smith, Y. Cui, and C. Bustamante. (1996). Overstretching B-DNA: the elastic response of individual double-stranded and single-stranded DNA molecules. *Science.* 271 (5250). pp. 795-799.
- [104] K. S. Harsha, "*Principles of vapor deposition of thin films*": Elsevier, 2005.
- [105] P. Holzmeister, G. P. Acuna, D. Grohmann, and P. Tinnefeld. (2014). Breaking the concentration limit of optical single-molecule detection. *Chemical Society Reviews.* 43 (4). pp. 1014-1028.
- [106] R. Schmidt, J. Jacak, C. Schirwitz, V. Stadler, G. Michel, N. Marmé, G. J. Schütz, J. D. Hoheisel, and J.-P. Knemeyer. (2011). Single-Molecule Detection on a Protein-Array Assay Platform for the Exposure of a

- Tuberculosis Antigen. *Journal of Proteome Research*. 10 (3). pp. 1316-1322.
- [107] I. Gryczynski, J. Malicka, Z. Gryczynski, and J. R. Lakowicz. (2004). Radiative decay engineering 4. Experimental studies of surface plasmon-coupled directional emission. *Analytical Biochemistry*. 324 (2). pp. 170-182.
- [108] S.-H. Cao, W.-P. Cai, Q. Liu, and Y.-Q. Li. (2012). Surface Plasmon-Coupled Emission: What Can Directional Fluorescence Bring to the Analytical Sciences? *Annual Review of Analytical Chemistry*. 5 (1). pp. 317-336.
- [109] S. Z. Uddin, M. R. Tanvir, and M. A. Talukder. (2016). A proposal and a theoretical analysis of an enhanced surface plasmon coupled emission structure for single molecule detection. *Journal of Applied Physics*. 119 (20). p. 204701.
- [110] M. P. Backlund, M. D. Lew, A. S. Backer, S. J. Sahl, and W. E. Moerner. (2014). The Role of Molecular Dipole Orientation in Single-Molecule Fluorescence Microscopy and Implications for Super-Resolution Imaging. *ChemPhysChem*. 15 (4). pp. 587-599.
- [111] E. Betzig and J. K. Trautman. (1992). Near-Field Optics: Microscopy, Spectroscopy, and Surface Modification Beyond the Diffraction Limit. *Science*. 257 (5067). pp. 189-195.
- [112] M. Böhmer and J. Enderlein. (2003). Orientation imaging of single molecules by wide-field epifluorescence microscopy. *Journal of the Optical Society of America B*. 20 (3). pp. 554-559.

VITA

Aaron J. Wood was born to Lisa and Warren Wood in Kansas City, Missouri. He completed his elementary and secondary education in Columbia, Missouri under the tutelage of his mother and father. He earned the rank of Eagle Scout in the Boy Scouts of America on Nov. 23, 2006. He was the state champion in the National Christian Forensics and Communications Association Team Policy Debate in Missouri (2004 & 2005), Kansas (2007), and the Region V (Missouri, Kansas, Minnesota, and Nebraska) Team Policy Debate champion in 2007. He attended Moberly Area Community College obtaining an Associates of Science in General engineering in spring 2010 graduating with a perfect 4.0 GPA. He was awarded the Alfred and Hazel Parrish Award for academic excellence, leadership skills, and community service and the David W. Stamper Memorial Scholarship upon graduation from Moberly Area Community College. He spent the fall of 2009 and spring of 2010 at Moberly Area Community College in Moberly, Missouri, as an undergraduate lab assistant in the biology laboratory of Dr. Suzanne Martin.

He attended the University of Missouri obtaining a Bachelor of Science in Biomedical Engineering in fall 2012 graduating Summa Cum Lauda and with honors. He spent the summer of 2012 as a research intern in the Biosensor and Biomolecular Engineering Laboratory at Iowa State University in Ames, Iowa. He pursued a Doctor of Philosophy in Biological Engineering at the University of Missouri from January 2013 through December 2016. His Ph.D. research included developing a novel microcontact lithography process to transfer the grating structure of HDDVDs and Bluray discs to glass and silicon substrates,

convert the gratings into plasmonic substrates, and incorporate the substrates into fluorescence-based biosensors to achieve higher detection sensitivity.